

# **Mechanobiology of Healing and Regeneration of Bone**

## **Dissertation**

zur Erlangung des akademischen Grades  
doctor rerum naturalium (Dr. rer. nat.) im Fach Physik  
eingereicht an der

Mathematisch-Naturwissenschaftlichen Fakultät I  
der Humboldt-Universität zu Berlin

von

Diplom Ingenieur Andreas Christian Vetter  
geboren am 29.08.1980 in Lauf a.d. Pegnitz

Präsident der Humboldt-Universität zu Berlin:  
Prof. Dr. Dr. h.c. Christoph Marksches

Dekan der Mathematisch-Naturwissenschaftlichen Fakultät I:  
Prof. Dr. Lutz-Helmut Schön

Gutachter:   1. Herr Prof. Dr. Peter Fratzl  
                  2. Herr Prof. Dr. Georg Duda  
                  3. Herr Prof. Dr. Igor Sokolov

eingereicht am: 9. April 2010

Tag der mündlichen Prüfung: 14. Juni 2010

**Um ein tadelloses Mitglied einer Schafherde sein zu können, muss  
man vor allem ein Schaf sein.  
(A. Einstein)**

## **Zusammenfassung**

Knochen ist ein multifunktionales Organ und zugleich ein biologisches Material. In dieser Arbeit wird der Heilungsverlauf eines Knochenbruchs (als biologisches Material) näher untersucht mit Hilfe von Computermodellen. Im menschlichen Körper kommt es nach einem Bruch zu einer vollständigen Regeneration des Knochens, ohne dass eine Narbe nach der Heilung zurückbleibt. In grob 10% der Frakturen kommt es jedoch zu Komplikationen bis zu einem Nicht-Heilen des Bruches. Das Ziel von intensiver interdisziplinärer Forschung ist es daher, nicht nur die medikamentöse Behandlung solcher Komplikationen zu verbessern, sondern auch durch externe, biophysikalische Stimulation die Heilung anzuregen. Gewöhnlich heilt ein Knochenbruch nicht direkt (Primäre Knochenheilung), das heißt durch Bildung von neuem Knochen im Knochenspalt, sondern über Sekundäre Knochenheilung. Während der sekundären Heilung bildet sich vorübergehend zusätzliches Gewebe außerhalb des Frakturspaltes, der so genannte Kallus, der die Aufgabe hat, den Bruch zu stabilisieren. Im Kallus werden im Laufe der Heilung verschiedene Gewebearten gebildet (z.B. Bindegewebe, Knorpel und Knochen). Die Gewebe werden von spezialisierten biologischen Zellen gebildet. Die spezialisierten Zellen entwickeln sich aus mesenchymalen Stammzellen (d.h. sie differenzieren), die in den Kallus wandern.

Die Zelldifferenzierung kann durch biophysikalische Stimulation beeinflusst werden. Hauptziel dieser Arbeit war die Untersuchung, wie sich lokale Stimulation und das daraus resultierende Zellverhalten auf den Verlauf der Heilung auswirkt. Dabei wurde ein einfaches Computermodell implementiert, das das Verhalten der Zellverbände in Folge mechanischer Stimulation und die anschließende Bildung des entsprechenden Gewebes im Kallus beschreibt. Die simulierte Abfolge der Gewebemuster wurde mit experimentell gewonnenen Histologiebildern verglichen. Im Vergleich zu bisherigen Computersimulationen hat sich die Modellentwicklung an physikalischen Vorbildern orientiert, um das Modell mit einer geringen Anzahl von Parametern einfach zu gestalten. Speziell wurde Wert darauf gelegt, neueste Materialdaten in das Computermodell zu übernehmen, und die Simulationsergebnisse direkt mit Ergebnissen von Tierexperimenten zu vergleichen.

Im ersten Teil der Arbeit werden die histologischen Schnitte eines vorhergegangenen Tierexperimentes quantifiziert. In diesem Tierexperiment wurde 64 Schafen durch einen chirurgischen Eingriff die Tibia waagrecht durchsägt und ein 3 mm breiter Spalt (Osteotomie) im Knochen erzeugt. Histologischen Schnitte wurden zu unterschiedlichen Zeiten während des Heilungsverlaufs gewonnen. Anhand dieser histologischen Schnitte und einer neuartigen Mittelungsmethode war es nun erstmals

möglich, einen „Norm“-Heilungsverlauf zu berechnen, der die Knochenheilung in Schafen mit einer Abfolge von 6 Bildern beschreibt, die die Anordnung der unterschiedlichen Gewebe zeigen.

Im zweiten Teil der Arbeit wurden diese Bilder und neue experimentelle Daten der mechanischen Eigenschaften des neu gebildeten Knochens benutzt, um Finite Element (FE) Modelle der 6 Heilungsphasen zu erstellen. Die Rechnungen zeigten, dass die Berücksichtigung der mechanischen Heterogenität des Knochens die lokalen Deformationen beeinflusst und daher für den Heilungsverlauf von Bedeutung ist.

Im dritten Teil der Arbeit wurden die Simulation der Knochenheilung und der Vergleich mit den experimentell gewonnenen Bildern durchgeführt. Im Bestreben das Modell einfach zu halten, wurden beispielsweise biologische Einflussfaktoren zu einem "biologischen Potential" zusammengefasst, welches das lokale Potential zur Heilung beschreibt. In Parameterstudien wurden die wichtigsten Regulationsparameter des Modells, die Aktivierungswerte für Knorpel- und Knochenbildung, studiert. Die Neubildung des Knochens konnte mit diesem einfachen Modell für eine breite Wahl von Parametern simuliert werden. Die Überbrückung des Frakturspaltes durch Knorpel zu simulieren erwies sich als wesentlich herausfordernder. Hier zeigte sich, dass eine starke biologische Stimulierung über das Periost (äußere Knochenhaut) entscheidend ist.

Der vierte Teil abstrahiert die Problemstellung und untersucht, motiviert von der Knochenheilung, das Verhalten eines selbst-heilenden Materials. Biologischen Zellen werden in dem Modell durch dynamische Sensoren ersetzt, die auf Stimulation mit einer Änderung der Materialeigenschaften reagieren. Untersucht wurde die Fragestellung, wie solche Sensoren auf physikalische Stimulation reagieren müssen, damit ein indirekter Weg der Heilung über eine äußere Überbrückung einer Fraktur erfolgt. Das Modell zeigte, dass eine Koppelung zwischen der Sensoraktivität und den lokalen Materialeigenschaften elementar für eine solche indirekte Heilung ist.

Die Arbeit zeigte das Potential mechanobiologischer Modelle für das Verständnis der Knochenheilung, wenn die gewonnenen Ergebnisse direkt mit quantitativen, experimentellen Daten verglichen werden. Besser fundierte mechanobiologische Theorien der Knochenheilung sind aber ihrerseits wiederum Grundlage für ein gezielteres Eingreifen bei problematischen Heilungsverläufen.

Schlagwörter: Knochenheilung, Simulation, Gewebemuster, Mechanobiologie

## Abstract

Bone is a multifunctional organ, a biological material and is able to fully restore bone fractures without leaving a scar. However, in about 10% of the bone fractures, healing does not lead to a successful reunion of the broken bone ends. Intensive interdisciplinary research therefore looks for new ways to promote healing not only by medication, but also by external biophysical stimulation. Usually, bone fractures do not heal by a direct bridging of the fracture gap with newly formed bone (primary bone healing). Instead, secondary bone healing proceeds indirectly via the formation of an external callus (additional tissue). Within the callus, intricate tissue type patterns are formed, which evolve during the healing progression. Stem cells differentiate into specialized cells, which lay down different tissues such as fibrous tissue, cartilage and bone. This cell differentiation can be biophysically stimulated, e.g. by mechanical deformation of the cytoskeleton. The main aim of this thesis was to connect the microscopic cell response to mechanical stimulation with the macroscopic healing progression. Simple rules for cell behaviour were implemented in a computer model, the progression of healing was simulated and the outcome of the simulations was compared to results from animal experiments. In comparison to existing simulations of bone healing, this study approached the problem from a more physical viewpoint and linked experimental *in vivo* data and computer modelling.

The first part of this work was to calculate an averaged healing progression (in terms of a succession of images) as such data has not been available so far. A novel averaging procedure was implemented and applied to the data of a previous animal study comprising 64 sheep with a 3 mm osteotomy (surgical cut through the bone) at the tibia. Six distinct healing stages could be defined according to topological criteria of the observed tissue patterns. Based on this classification, an averaged image showing the spatial arrangement of the different tissues was obtained for each healing stage.

These images and experimental data of the time-evolving stiffness of the hard callus (newly formed bone) were used to calculate the local deformations within the callus at the six healing stages. The hard callus was modelled as a heterogeneous, porous material. It was found that the heterogeneity of the hard callus influenced strongly the local deformations. In particular, the results suggest that the hard callus heterogeneity is crucially affecting the formation and the consequent resorption of the cartilage in the fracture gap during bone healing.

The next step was to simulate the progression of secondary bone healing. Here, a mechanobiological model was developed including one mechanical stimulus, which

controlled the biological cell differentiation and, consequently, the formation of different tissues. A simplistic model was required to reduce the number of simulation parameters. The model, for example, summed up the different biological influencing factors on bone healing as a net influence (or “biological potential” to heal). Comprehensive parameter studies were performed to understand the role of two key mechano-regulatory parameters, which regulated the formation of cartilage and bone (hard callus) formation, respectively. It was found, that the formation of the hard callus is reproduced *in silico* for a wide range of parameters. The experimentally observed bridging of the fracture gap by cartilage, crucial for the healing *in vivo*, was far more challenging to simulate. Assuming a strong biological source of biological stimulation at the periosteum was important for an agreement with the experimentally found formation of cartilage.

In the last part of the thesis, the process of bone healing was investigated from a broader perspective. The process of healing of a fracture was modelled assuming a self-healing material, where biological cells were abstracted as dynamical sensors (black boxes). The main question was how the sensors have to response to a physical stimulation so that healing occurs in an indirect way by forming an external bridge. Different realizations of the feedback between physical stimulation and local responses were tested. It was found that the response of the sensors (in case of bone healing: cells) has to be dependent on the local material property for simulating an indirect healing progression.

This work showed the importance of a stringent comparison between computer simulations of bone healing and spatial experimental data. Understanding the response behaviour of cells can be used to improve mechanobiological theories of bone healing and hence our treatment of problematic bone fractures.

Keywords: bone healing, simulation, tissue pattern, mechanobiology

## Table of contents

Zusammenfassung .....	iii
Abstract .....	v
Table of contents .....	vii
List of figures.....	ix
Abbreviations.....	xi
1. Introduction.....	1
2. Background.....	4
2.1. Tissues involved in secondary bone healing.....	4
2.2. The biology of fracture healing in long bones .....	8
2.3. Animal experiments on bone healing .....	10
2.4. Influences on bone healing .....	11
2.5. Mechanobiological theories on bone healing .....	16
2.6. Existing computer models of bone healing .....	19
2.7. Aims and structure of this work.....	23
3. Available experimental data used for this work.....	26
I. Quantifying experimental data .....	29
4. Histological analysis .....	30
4.1. Identification of the tissue types .....	30
4.2. Hard callus and cortex.....	31
4.3. Local densification of the hard callus close to cortex .....	34
4.4. Stiffening of the hard callus .....	36
4.5. Conclusions .....	37
5. Calculation of an averaged healing progression.....	39
5.1. Problems.....	39
5.2. Classification into healing stages .....	40
5.3. Averaging procedure .....	41
5.4. Averaged progression of ovine bone healing .....	45
5.5. Average growth of hard callus.....	47
5.6. Conclusions .....	48
II. Static bone healing simulations .....	50
6. The heterogeneity of the hard callus - mechanical implications.....	51
6.1. Mechanical heterogeneity of the hard callus .....	51
6.2. Finite element simulations .....	54
6.3. Strains within the hard callus .....	57
6.4. Strains within the fracture gap .....	58

6.5.	A "local interfragmentary strain theory" .....	60
6.6.	Influence of the hard callus heterogeneity on the strains.....	62
6.7.	Conclusions .....	64
III.	Dynamic bone healing simulations .....	67
7.	Mechanobiological simulation of bone healing .....	68
7.1.	Experimental data on maturation of tissue .....	69
7.2.	Basic mechanobiological bone healing model.....	70
7.3.	Implementation of the model (for a 3 mm sheep osteotomy) .....	73
7.4.	Comparison of experimental data and simulation results .....	75
7.5.	Results.....	78
7.6.	Conclusions .....	84
IV.	Simulating a self-healing material .....	88
8.	Exploring the cell sensitivity.....	89
8.1.	Reduction of the model complexity.....	90
8.2.	Substitution of the mechanical system .....	91
8.3.	Implementation and dimensionless parameters .....	92
8.4.	Feedback of the system.....	94
8.5.	Results.....	98
8.6.	Conclusions .....	103
9.	Summary and outlook.....	105
	References .....	109
	Appendix.....	119
	Glossary .....	121
	List of publications .....	123
	First manuscript (Vetter et al. 2010a) .....	125
	Second manuscript (Vetter et al. 2010b).....	139
	Danksagung .....	156
	Eidesstattliche Erklärung.....	157



## List of figures

Figure 2.1: Overview of a long bone osteotomy .....	5
Figure 2.2: Three phases of secondary bone healing.....	8
Figure 2.3: Progression of secondary bone healing .....	9
Figure 2.4: Time evolution of the fracture stiffness .....	16
Figure 2.5: Qualitative mechanobiological theories on bone healing.....	17
Figure 2.6: Interfragmentary strain theory of Perren and Cordey. ....	18
Figure 2.7: Quantitative mechanobiological theories on bone healing .....	19
Figure 3.1: Example for a stained section (Safranin Orange/von Kossa).....	27
Figure 3.2: Histograms representing the frequency of the nano-indentation modulus of the hard callus .....	28
Figure 4.1: Box plots of the hard callus area of the rigid and lateral side and both fixator types at 2, 3, 6 and 9 weeks post-op. ....	31
Figure 4.2: Box plots of the bone area fraction (BA/TA) of the whole hard callus for rigid and lateral side and both fixator types at 2, 3, 6 and 9 weeks post-op... ..	33
Figure 4.3: Bone area fraction ( $BA/TA$ ) close to the periosteum. ....	35
Figure 4.4: Mechanical development of the hard callus.....	37
Figure 5.1: Classification of the histological images into defined healing stages. ....	41
Figure 5.2: Flow chart of the nine steps during the averaging procedure.. ....	45
Figure 5.3: Images of the averaged spatial tissue information at different healing stages. ....	46
Figure 5.4: Estimation of the hard callus growth .....	47
Figure 6.1: Processes influencing the stiffness of the hard callus.....	51
Figure 6.2: Maps of the elastic modulus of the callus .....	53
Figure 6.3: Semi-logarithmic plot of the mean value of the elastic modulus of the cortex and the hard callus. ....	54
Figure 6.4: Spatial distributions of the maximal shear strain (left) and comparison between the heterogeneous case and the two homogeneous cases as reference. ....	57
Figure 6.5: Local maximal shear strain plotted over the local elastic modulus of the hard callus elements at stage IV. ....	58
Figure 6.6: Calculated IFS during normal bone healing based on FEM.....	59
Figure 6.7: Interpretation of the mechanical stimulus in terms of tissue differentiation.....	61
Figure 6.8: Schematic of the influence of the hard callus heterogeneity on the local strains before bridging, during bridging and after bridging. ....	63
Figure 7.1: Iterative implementation of the mechanobiological bone healing model..	70
Figure 7.2: Mechanobiological tissue maturation and differentiation model. ....	72

Figure 7.3: Geometry of the modelled osteotomy and the boundary conditions. ....	74
Figure 7.4: Comparison of the experimental images with the simulated images performed at each iteration step of the simulation. ....	78
Figure 7.5: Phase diagrams of the mismatch mtt between experimental images and simulation results based on spatial tissue type comparison. ....	79
Figure 7.6: Two phase diagrams of the mismatch between simulation and experiment. ....	81
Figure 7.7: Phase diagrams of the mismatch of cartilage pixels between simulation and experimental stage III. ....	83
Figure 8.1: Schematic of tissue adaptation models. ....	89
Figure 8.2: Reduction of the complexity of the problem. ....	91
Figure 8.3: Scheme of the geometry. ....	93
Figure 8.4: Example for a basic feedback function ....	95
Figure 8.5: Estimated dependency of the sensor`s sensitivity. ....	97
Figure 8.6: Dimensionless stimulus $S_d$ at the initial time point. ....	99
Figure 8.7: Simulations <i>without</i> coupling between feedback and local material properties. ....	100
Figure 8.8: Simulations <i>with</i> coupling between feedback and local material properties. Different ways of gap bridging depending on the according feedback function (left) ....	101
Figure 8.9: Simulations (with coupling between feedback and local material properties) with a positive maximal feedback between $0.6 S_0$ and $1.9 S_0$ . ....	102
Figure 8.10: Development of the stimulus $S_d$ within the fracture gap. ....	103
Figure 8.11: Incorporation of the investigated feedback function into the mechanobiological model of Chapter 7. ....	104

## Abbreviations

$BA/TA$	Bone area fraction (Bone area over tissue area)
$BV/TV$	Bone volume fraction (Bone volume over tissue volume)
$c$	Concentration of biological potential
$D$	Diffusive constant (for biological potential)
DIC	Digital Image Correlation
$E$	Elastic modulus
ESPI	Electronic Speckle Pattern Interferometry
$F$	Mechanical force
FE	Finite Element
FEM	Finite Element Method
IFM	Interfragmentary movement
IFS	Interfragmentary strain
IST	Interfragmentary strain theory
$j$	Heat flux
$k$	Tissue maturation rate
$L$	Thermal conductivity
$MS$	Mechanical stimulus
MSC	Mesenchymal stem cell
$T$	Temperature
$T$	Time
$X$	Location
$\varepsilon$	Mechanical strain
$\mu\text{CT}$	Micro-Computed Tomography
$\tau$	Mechanical stress



## 1. Introduction

### Motivation

Bone is a fascinating organ and material with the unique capability of scarless self-repair. Due to its hierarchical architecture, bone succeeds to be a very stiff yet tough material (Peterlik et al. 2006). However, fractures of bone occur not only due to excessive loads, but also in non-traumatic situations due to an impaired mechanical performance of bone caused by diseases. Clinical studies estimate the percentage of eventful (problematic) fracture healing cases between 5-20% including fractures due to bone diseases such as osteoporosis (Coles and Gross 2000; 2000; Lynch et al. 2008). As the average human life time increases, the percentage of people with bone diseases will increase. Therefore, the issues arising with regards to eventful bone healing are becoming more urgent (Gruber et al. 2006; Jakob et al. 2007). The number of fractures in the European Union due to osteoporosis was estimated at 3.8 million in the year 2000 with related costs for clinical treatment at 32 billion Euros (Reginster and Burlet 2006). Therefore, insights into the process of fracture healing as well as a better understanding of bone as a material and its organisation are desirable in order to improve the prevention and treatment of patients, reducing the resulting costs. The behaviour of cells is very difficult to measure *in vivo*. Computational modelling is an important tool to gain a better understanding of the cell behaviour during bone healing. As a long term goal, these insights into regenerative processes of the human body could be further used in other fields of medicine.

Bone has several tasks besides the “mechanical engineering” tasks of shaping our body (by preventing bending and buckling of our extremities, e.g.) and protection of other organs. The main tasks of bone as an organ are providing a calcium reservoir for the body and producing different types of blood cells (within the bone marrow). The aim of this study was to understand better the biological or biochemical and mechanical influences on the progression of bone healing. To start with, the aim was to understand the “normal” progression of healing in healthy sheep. Accordingly, the influence of the bone’s organ tasks on the healing progression were neglected in this work. Bone healing is controlled by a myriad of influences (smokers, for example, face more probably difficulties during healing). The main task of this thesis was to filter the important influences on a normal healing progression. This task was tackled from a physical viewpoint by post-processing available experimental data, using mechanobiological computer simulations and representing the comprehensive computational results in phase diagrams.

Mechanobiology is a rather young research field which is closely related to the older research field of Biomechanics. This introduction aims to clarify the difference between Mechanobiology and Biomechanics and outlines the benefit and the inherent inter disciplinaryity of these two akin research fields. The link between these two research fields is a process called "Mechanotransduction".

Biological processes are generally very complex, specifically fracture healing. Therefore, significant background knowledge is required in order to model bone healing. Chapter 2 aims to provide knowledge of bone fracture healing and the underlying processes followed by the formulation of specific aims of this thesis. Chapter 3 gives a summary of the available experimental data which was used in this thesis for computational modelling. Chapters 4 to 9 comprise the work which has been carried out in the framework of this thesis. A glossary of biological and clinical terms can be found in the appendix.

### **Biomechanics**

Biomechanics investigates the whole body or parts of the body and their functions from a mechanical viewpoint or in other words, "biomechanics seeks to understand the mechanics of living systems" (Fung 2004). Already in 17<sup>th</sup> century, Galileo Galilei compared the diameter of leg bones of different animal species and estimated the demanded ratio of the diameter depending on the weight of the animal (Galilei 1638). Recent achievements of applied biomechanics have helped to solve problems not only in orthopaedics but in various other areas of regenerative medicine. Biomechanical research labs have designed and optimized artificial heart valves, stents and hip implants, just to name some examples. Biomechanical research labs also measure the material properties of different tissues, which is an important input for mechanobiological studies. The material properties together with the load determine the stresses, interstitial fluid flow and strains within the tissue which can be sensed by biological cells. For example, shear strains are often considered as mechanical stimulus which can stimulate or activate a cell to produce tissue.

### **Mechanotransduction**

In general, the cellular process of response to an activating mechanical stimulus such as strain is called mechanotransduction, meaning the transcription of a mechanical signal into a biochemical signalling cascade (Morgan et al. 2008). A certain signalling cascade is the response of the cell to a stimuli which leads to a specific biological process, for example, differentiation of the cell (transformation of a cell into a more specialized cell). During "normal" fracture healing, several tissue types develop and each tissue matrix is laid down by specialized cells. These specialized cell types all stem from one type of progenitor cell, the mesenchymal stem cells (MSC), which

eventually differentiate according to mechanical, biological, chemical, or electrical stimulation.

### **Mechanobiology**

Tissues with cells are living materials which have the ability to sense their physical environment and react with an adaptive response. The rather young field of mechanobiology wants to “predict growth and differentiation [of tissue and cells – the author] in quantitative terms, based on a given force exerted on a given tissue matrix populated by cells” (van der Meulen and Huiskes 2002). Naturally, “mechanobiological research” is based on a very interdisciplinary approach. One of the early mechanobiological studies was made by the medical doctor Julius Wolff in the late 1800s. Wolff investigated the architecture of trabecular bone by applying engineering methods and hypothesised what is now called functional adaptation of bone (Wolff 1892). Accordingly, bone trabeculae are built at locations where they are mechanically required and removed where they are not required (Robling et al. 2006). Hip implants can be optimized following Wolff’s law. The lifetime of hip implants were significantly increased by avoiding a stress-shielding of the bone surrounding the implant (Huiskes et al. 1992). Too low mechanical stimulation leads to bone resorption and ultimately to a loosening of the implant.

With increasing experimental data, theoretical mechanobiological theories were suggested for different endogeneous processes with the main aim to better understand the mechanical influences on the process and the cells by modelling the cellular behaviour *in silico*. Several studies showed the potential impact of mechanobiological simulations. For example, computational models on bone remodelling were able to predict the natural aging of trabecular bone and provided evidence for the existence of a threshold value above which bone deposition by the cells is activated (Weinkamer et al. 2004; Dunlop et al. 2009).

The main aim of this thesis is to examine to which extent a basic mechanobiological model can explain the local development of different tissue types in a fracture site during bone healing.

### 2. Background

Primary bone healing, also called direct or osteonal healing, occurs in the rare situation when there is no motion of the fracture ends which are compressed onto each other minimizing the gap between the bone ends (Willenegger et al. 1971). In this case, the formation of new osteons (bone packages) proceeds directly through the fracture crack. No external callus is formed which is typical for the more common type of fracture healing, called secondary or indirect bone healing. The following hypothesis of Perren can serve as a guideline to understand the way of secondary bone healing: only tissue can be formed which sustains the local deformation (Perren 1979). Accordingly, secondary bone healing occurs via a “geometrical detour” by formation of an external callus (additional material), which is laid down at the outer side of the fractured bone, a region with low strains. Additionally, a “material detour” occurs by the formation of rather soft tissues like cartilage, which sustains higher strains and is replaced by bone afterwards. The aim of both detours is to stabilize the fracture ends reducing the local strains so that the final material bone can be built within the initially highly loaded gap area. It is thought that these detours also avoid premature decisions where and how healing should proceed (Fratzl and Weinkamer 2007).

#### 2.1. Tissues involved in secondary bone healing

The materials used by the body (tissues) to repair the fracture via secondary healing are bone, cartilage and soft tissue. Tissue consists mainly of cells and intercellular matrix including a system of fibres and interstitial fluid.

Nature's materials in animals and plants are hierarchically organized and based on basic building blocks, mainly fibres, which are restricted in size (Vincent 1990; Fratzl and Weinkamer 2007). Nature assembles these building blocks on several hierarchical levels into whole structures, such as wood, shells or tissues. This organization affects strongly the material properties of the tissues and, therefore, the local stresses and strains. This, again, influences the mechanical stimulation of the cells and, consequently, the mechanotransduction.

#### Basic anatomy of long bones

Long bones, for example the tibia, consist of trabecular and cortical bone. Trabecular bone, found close to the joints (Figure I.1, right), is a network of bone struts with a porosity of about 80%. Trabecular bone is light in weight but still suited for transmission and damping of various mechanical load types, as required for example in the femora head or in the vertebrae. Cortical bone is very dense with a low porosity of about 6%, mainly due to blood vessels, and provides high mechanical



stability. Therefore, cortical bone is found in the shafts of long bones to prevent buckling of the long bone (Figure I.1, left). The two ends of the bone are covered with articular cartilage which provides the interface to the joint. The inner part of the long bone is filled with bone marrow. Both, the outer and inner surface of the cortical bone, are covered by a sheet of fibrous connective tissue. The outer layer is called periosteum and the inner layer endosteum. Both layers contain diverse cell types including mesenchymal stem cells (McKibbin 1978), however, the anatomy and structure of long bones can differ considerably in different mammal species (Locke 2004). Bone is a striking example of a material which combines two properties, which are contradicting from the conventional engineering viewpoint: stiffness and toughness. The organized structure of stiff mineral particles glued together with protein molecules and the interfaces between different hierarchical levels make this combination of both properties within a material possible (Jager and Fratzl 2000; Gao et al. 2003; Gupta et al. 2006).

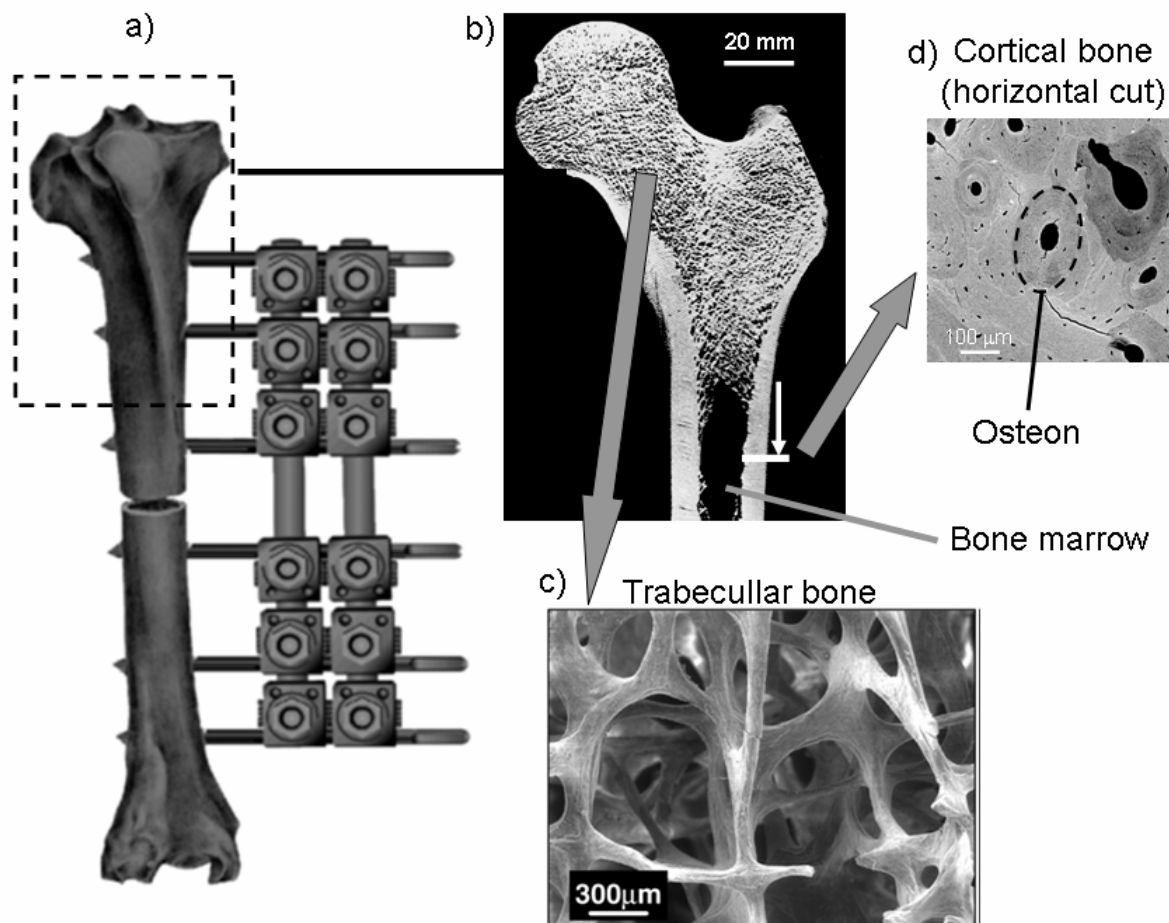


**Figure I.1: Overview of a long bone osteotomy**

**Overview of a long bone osteotomy and the different length scales of the material bone. a)** Sketch of an osteotomy of a long bone stabilized by an external fixator. Figure adapted from (Schell et al. 2005). **b)** Cross section of a femoral head showing cortical and trabecular bone. **c)** Zoom into trabecular bone. Figures b-d adapted from (Fratzl and Weinkamer 2007).

### **Hierarchical structure of bone**

As with other biological tissues, bone is highly hierarchical and heterogeneous in structure (Rho et al. 1998; Weiner and Wagner 1998; Fratzl et al. 2004; Fratzl and Weinkamer 2007). Its basic building blocks are fibrils which contain mainly tough but soft collagen molecules and stiff but brittle calcium phosphate particles. The fibrils are of about 100 nm in diameter and a length of about 1  $\mu\text{m}$  to 10  $\mu\text{m}$ . These fibrils form “lamellar units” which are planar layers with a thickness of about 5  $\mu\text{m}$ . These lamellae form osteons, the macroscopical building blocks in cortical bone, with a diameter of around 200  $\mu\text{m}$  (Figure I.1). Osteons are cylindrical structures with a blood vessel in the centre and are generally aligned in the direction of the long bone axis. In trabecular bone, the lamellae form bone packets, which build up the trabeculae. The thickness of the trabeculae (roughly 170  $\mu\text{m}$ ) is similar to the size of the osteons (Figure I.1).

### **Material properties**

The material properties depend on the investigated length scale, as tissues are built by structures of several length scales. A collagen fibril, for example, has an indentation elastic modulus of about 1-2 GPa (Heim et al. 2006) whereas a typical elastic modulus of a macroscopic piece of bone is about 20 GPa. The generally viscoelastic material properties of tissue have been tried to be assessed on the macroscopic level by standard mechanical tests such as compression tests, on the microscopic level by scanning acoustic microscopy (SAM) or nanoindentation and on a even lower level by atomic force microscopy (AFM). However, the measurement of tissue material properties is a very difficult task for several reasons (Fung 2004). Measurements are generally carried out *ex vivo* to access the desired tissue which, as a result, leads to non-physiological conditions. Severe differences between wet and dry tissue specimen have been observed, e.g. (Seto et al. 2008). The material properties of tissues have been found to be non-linear which is generally neglected to simplify matters. Additionally, the anisotropy due to the hierarchical organization raises the complexity of the experiments and the theoretical description of the material (Zysset 2003). Finally, tissue is a living material and the material properties can change considerably over time depending on mechanical or biological influences. Material properties change as the tissues mature, which is valid in particular during fracture healing (Manjubala et al. 2009). In the following, the mechanical properties of tissues occurring during “normal” fracture healing are summarised.

### **Bone**

It has been known for a while that the mechanical properties of cortical bone can vary remarkably depending on the site (Cowin 2001; Currey 2006). As an example, the tensile strength for the human femur and tibia, both located at very similar

positions, namely the leg, differ considerably from each other (Femur: 124 MPa  $\pm$ 1.1, Tibia: 174 MPa  $\pm$ 1.2) (Yamada 1970). Results for the elastic modulus of human femur showed the macroscopic anisotropy along the long bone axis (longitudinal direction:  $E = 18.2 \text{ MPa} \pm 1.01$ , transversal direction:  $E = 11.7 \text{ MPa} \pm 0.85$ , both cases under compression) (Reilly and Burstein 1975). Recent studies suggest, that the anisotropy can even be much more pronounced on lower hierarchical levels. For example, the elastic modulus of cortical bone packages in fibrolamellar bovine bone (length scale  $\sim 100 \text{ }\mu\text{m}$ ) assessed by micromechanical testing differed by 20-fold or so, depending on the orientation of the fibrils (Seto et al. 2008). The compressive elastic modulus of cortical bone is around 20 GPa (Currey 2006), to give an impression of the stiffness of bone.

Trabecular bone can be modelled as a foam like structure. The elastic modulus of the trabecular bone material is similar to the elastic modulus of cortical bone material. The bulk elastic modulus of trabecular bone was experimentally found to be dependent on the bone volume fraction by a power law (Carter and Hayes 1978). Using beam theory, Gibson and Ashby investigated additionally to the density also the influence of the shape of bone trabeculae on the stiffness (Gibson and Ashby 1999). Accordingly, the (bulk) elastic modulus depends on the elastic modulus of the material  $E_{mat}$  and the bone volume fraction  $BV/TV$  (1). The exponent  $\kappa$  is dependent on the trabecular architecture (Woesz et al. 2004). Several groups experimentally determined  $\kappa$  for trabecular bone at different sites in the body and the values for  $\kappa$  were generally found to be slightly smaller than 2 (Morgan et al. 2003; Gibson 2005).

$$E = E_{mat} \cdot \left( \frac{BV}{TV} \right)^\kappa \quad (1)$$

$E$	Bulk elastic modulus of the hard callus
$E_{mat}$	Elastic modulus of the bone material
$BV/TV$	Bone volume fraction

### Cartilage and soft tissue

The measurement of the material properties of cartilage and soft tissue face severe problems, in particular when trying to assess the properties during the healing process. One of the few nanoindentation studies with the aim to assess the material properties of tissue within the fracture callus points out a main difficulty: "The results reveal that the callus exhibits a wide range of indentation moduli, which is due in large part to the heterogeneous mixture of the tissues present" (Leong and Morgan 2008). This mixture and the maturation of the tissues itself leads to the fact, that values describing soft tissue or cartilage fluctuate strongly.

## 2. Background

---

After clotting of the blood (haematoma), granulation tissue is the first tissue formed in the callus. Nanoindentation tests on one rat sample showed a mean elastic modulus of 0.99 ( $\pm 0.2$ ) MPa (Leong and Morgan 2008). Generally, fibrous tissue replaces the granulation tissue over time. Fibrous connective tissue shows fibrillar elements and was mechanically tested after the regeneration of a complete joint replacement. Fibrous tissue specimens of six dogs were collected and the elastic modulus was found to be around 1.9 MPa (at 0.5 MPa) under unconfined uni-axial compression (Hori and Lewis 1982). Most experimental studies on cartilage were carried out for articular cartilage and the range of its elastic modulus for cartilaginous tissue starts from 1 MPa (Wei et al. 1998) to 11.8 MPa (Setton et al. 1997).

### 2.2. The biology of fracture healing in long bones

The progression of uneventful secondary bone healing is an organized process showing intricate patterning of different tissues. Secondary healing can be divided into three successive and overlapping phases, (i) the inflammatory phase, (ii) the reparative phase and (iii) the remodelling phase, see Figure I.2 (Cruess and Dumont 1975; Buckwalter 1996; Sfeir et al. 2005).

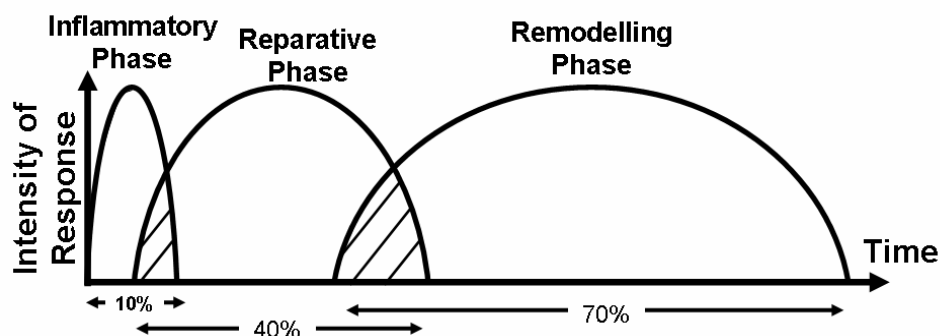


**Figure I.2: Three phases of secondary bone healing**

Three phases of bone healing and their overlap in healing time (100% indicates a completely repaired fracture). Figure adopted from Cruess and Dumont (1975).

#### Inflammatory phase

Besides breaking the bone, a fracture usually leads to the disruption of the periosteum and the endosteum including the damage of cells, blood vessels and the surrounding soft tissue (Buckwalter 1996). The bleeding causes a lifting of the periosteum and an inflammatory response is initiated (Figure I.3). The inflammation causes pain and hydrostatic swelling, both reducing the movement of the fracture ends (Madison and Martin 1993). Clotting of the blood occurs and a large number of signalling molecules are released (Bolander 1992; Schmidt-Bleek et al. 2009). The early fracture environment is typically acidic which is an optimal working environment for the macrophages (Hollinger and Wong 1996), including the resorption of necrotic (dead) tissue and the release of cytokines. Hypoxia and

cytokines can stimulate the formation of new blood vessels (angiogenesis) (Rhineland 1968; Glowacki 1998).

Important elements of the repair process are the pluripotent mesenchymal stem cells (MSCs) which respond to and produce cytokines. These cells migrate within the callus, proliferate (reproduce themselves by cell division) and differentiate (become specialized cells). Within the callus, MSCs differentiate into fibroblasts, chondroblasts and osteoblasts. These cells proliferate and lay down the corresponding tissue matrix (Bostrom 1998). The main origin of the MSCs is either a certain layer (the cambium) of the periosteum or the bone marrow, although other sources such as muscle or fat provide a limited source (Yoo et al. 1998; Gerstenfeld et al. 2003; Malizos and Papatheodorou 2005; Colnot 2009). The fracture ends do not serve as a MSC source. Cell division was observed to happen first in the periosteum (McKibbin 1978).

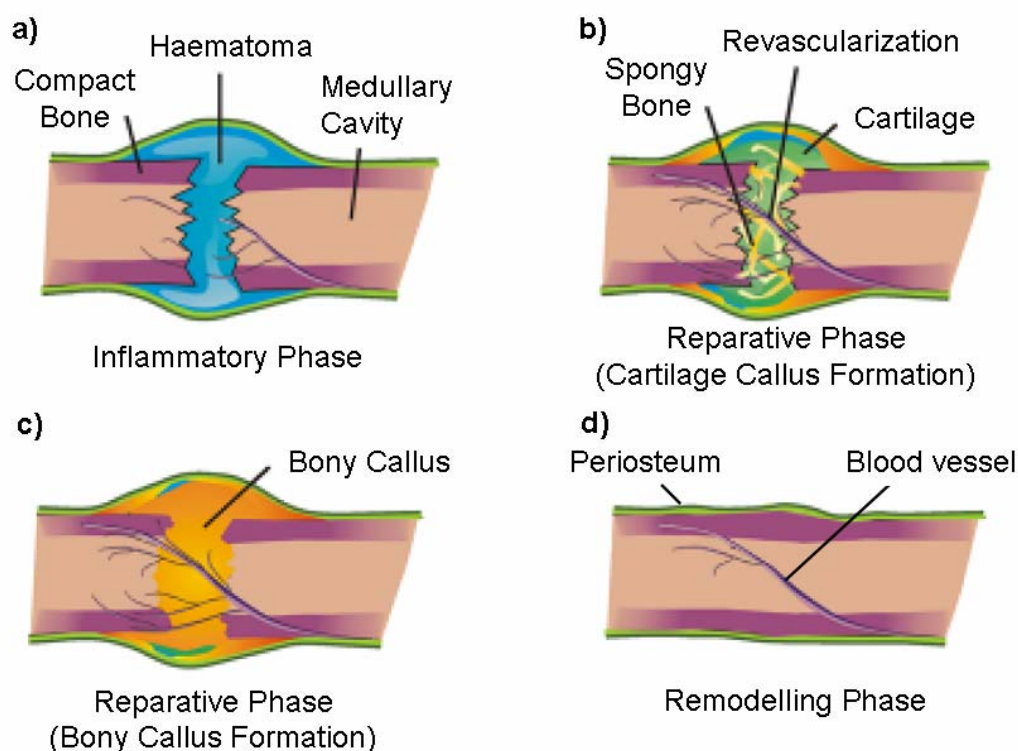


**Figure I.3: Progression of secondary bone healing**

**Schematic representation of the healing progression of secondary bone healing in long bones by formation of an external callus, modified from (Sfeir et al. 2005). The healing proceeds via three overlapping phases starting from a) to d).**

### Reparative phase

The regenerative phase goes together with the restoration of the blood supply (Figure I.3). The pH becomes gradually neutral and then slightly alkine which is beneficial for the mineralisation of woven bone by alkaline phosphatase (Hollinger

and Wong 1996). Woven bone formation begins under the periosteum some millimetres away from the fracture gap by intramembranous ossification (Owen 1970; Einhorn 1998). In that region, osteoblasts excrete un-mineralized bone matrix (osteoid) within the connective tissue and the osteoid mineralizes with time. First, the formation of a fast and “cheap” scaffold of woven bone occurs. Afterwards, the interior of the scaffold is filled with more organized and “expensive” lamellar bone (Liu et al. 2009b). The mineralization process and the maturation results in a fast increase of the stiffness of the bone material (Manjubala et al. 2009). The region comprising the newly formed bone is often referred to as hard callus. Along with the maturation and densification of initially formed hard callus, formation of new hard callus proceeds in the direction of the fracture gap (Einhorn 1998; Vetter et al. 2010a).

As a prerequisite for later ossification and bridging of the fracture gap, cartilage is formed in the periphery of the callus, where a lower oxygen tension is present (McKibbin 1978). Hypertrophic (enlarged) chondrocytes secrete calcium phosphate complexes into the extra-cellular matrix resulting in a calcification of the cartilage (Brighton and Hunt 1986). Calcified cartilage stimulates angiogenesis and the cartilage is eventually replaced by woven bone (Webb and Tricker 2000). This process is called endochondral ossification. Finally, the hard callus bridges the fracture gap and with ongoing mineralization the fracture is considered internally immobilized (Madison and Martin 1993). Recent data suggests, that osteoclastic activity begins already during the reparative phase (Schell et al. 2006).

### **Remodelling**

As the final phase of fracture healing, bone remodelling is initiated after hard callus bridging and reunion of the fracture ends (Figure I.3). Woven bone is replaced by lamellar bone and the edges of the hard callus start to be resorbed (Buckwalter 1996; Hollinger and Wong 1996). The endosteal blood supply is restored with the resorption of the endosteal hard callus (Rhineland 1968). Eventually, the original shape and lamellar structure of the bone is restored without leaving a scar (Owen 1970; Willenegger et al. 1971; Madison and Martin 1993). Nevertheless, it was shown that the remodelling activity at the fractured site in humans may be accelerated for several years (Wendeberg 1961).

### **2.3. Animal experiments on bone healing**

Animal experiments on bone healing have been conducted on small and large animals, comprising mice, rats, rabbits, dogs, pigs, goats and sheep (Jagodzinski and Krettek 2007; Reichert et al. 2009). Large animals such as sheep show more

similarities to human healing than small animals, for example by similar tissue type patterns. Therefore, the conclusions drawn from studies on large animals can be more likely transferred to clinical applications (Auer et al. 2007).

### **Defect models**

The gap between the bone ends (Figure I.1, left) is called the defect and two types of defect models exist, fracture models and osteotomy models. Fracture defect models aim to create real fractures caused by an impact. Fracture models face the difficulty of reproducibility and have been conducted mainly on small animals (Bonnarens and Einhorn 1984; Sturmer et al. 2006; Toben et al. 2009). Most of the animal studies try to circumvent the problem of reproducibility by setting an osteotomy, which is a defined gap. The osteotomy is set by cutting through the bone with a thin saw, extending the gap manually to a desired size and placing a spacer within the gap. Afterwards, a fixation is applied to prevent the bone ends from approaching each other and the spacer is removed. Osteotomy models differ in the complexity of the defect's geometry and the type of damage of the tissue. Therefore, the healing process of similar fracture models and osteotomy models (e.g. same defect size) can differ from each other (Kratzel et al. 2008).

### **Fixation types**

The most basic fixation of the defect is a plaster cast. As it does not provide a precise stabilisation, other fixations are most frequently used for animal experiments, either internally or externally applied. Internal fixation comprises intramedullary nails or bone plates (Tarr and Wiss 1986). Intramedullary nailing has the disadvantage of damaging the bone marrow and therefore influencing the healing process. External fixation comprises rod and ring fixators. Accordingly, screws or pins are inserted in the cortex perpendicular to the long bone axis and connected to each other by rods or rings (Höntzsch 1997; Watson et al. 2000). External fixators can be modified in order to apply cyclic loads (dynamic fixators). A very common model is a tibial sheep osteotomy treated with external fixators with a gap size of 3 mm (Jagodzinski and Krettek 2007). The experimental basis for this thesis stemmed from such an *in vivo* model. As a particular fixation type, interfragmentary compression has to be mentioned. This type applies several fixation types, e.g. tension bands, in order to create absolute stability to achieve primary bone healing.

## **2.4. Influences on bone healing**

The healing time and the pattern of healing depend on the animal species as well as biological and mechanical influences (McKibbin 1978; Duda et al. 2008). Small animals tend to heal faster and more cartilage is generally formed (McKibbin 1978).

More endosteal activation is seen in rats compared to sheep (Mehta et al. 2008). To list just some biological influences, bone healing was shown to be dependent on age, sex (Strube et al. 2008; Mehta et al. 2009), infection of the fracture site, nutrition and soft tissue trauma (Reichert et al. 2009). Several *in vitro* and *in vivo* studies were carried out to investigate the role of diverse growth factors and genes in order to improve the healing process or stimulate healing in case of eventful healing. (Greiner et al. 2007; Barnes et al. 2008; Schindeler et al. 2008; Pauly et al. 2009). The importance of the periosteum as source of the stem cells was studied on animals which had been stripped of the periosteum. Without the periosteum, the probability of a non-union increased significantly (Utvag et al. 1996; Garcia et al. 2008). By cauterization (burning) of the periosteum and removing local bone marrow, the healing could not proceed and a non-union was the result (Kaspar et al. 2008). Furthermore, electric current and the application of electromagnetic fields were found to be capable of stimulating bone healing by affecting the biochemical processes at the fracture site (Ryaby 1998; Park and Silva 2004; Mollon et al. 2008; Victoria et al. 2009).

### **Mechanical influences**

Regarding the mechanobiological viewpoint of this thesis, an overview is provided of several *in vivo* studies which have been carried out in order to investigate the effects of the mechanical influences on the healing process. All these experiments demonstrated the importance of an appropriate mechanical environment to ensure union of the fracture ends and to accelerate the healing process (Reichert et al. 2009). However, it has to be mentioned that there are also in-vitro approaches to study the influence of the mechanical environment on a cellular basis.

*In vivo* studies varied “global” mechanical parameters resulting in different local mechanical environment within the callus. To be more specific, bone healing was found to be dependent on the “global” parameters: (i) magnitude of the relative motion of the bone ends, also called interfragmentary movement (IFM), (ii) fixation type, resulting in different motion types, for example compression or shear, and (iii) timing of motion. In the case of dynamic fixators, the frequency of the actuation (or dose rate) was also varied. Finally, it has to be mentioned that the gap size is also a crucial factor influencing both mechanically and biologically the healing process (Claes et al. 1998; Claes et al. 2003; Mehta et al. 2009).

#### **(i) Magnitude of motion**

The magnitude of motion is generally regulated by the stiffness of the fixator. A “normal” ovine healing process starts with initial axial interfragmentary strains (IFS)



of up to over 30% (Claes et al. 1997). In the same study, high initial IFS (31%) were found to be stimulative compared to low initial IFS (7%). The IFS decreases due to the stiffening of the callus, despite higher limb loading with the advance of the healing process. Furthermore, a bigger external callus forms with increasing IFS (McKibbin 1978; Gardner et al. 1997). However, excessive IFS inhibits the maturation of the callus and non-union occurs (Perren 1979; Harrison et al. 2003; Schell et al. 2008). Callus stiffness and bone mineral density was related to the magnitude of motion (Kenwright and Goodship 1989; Goodship et al. 1993).

### **(ii) Motion modes**

The motion modes are distinguished into axial tension, axial compression, bending and torsion along the long bone axis, and translational shear. In general, a complex combination of these motions is found in the callus despite the classification of an animal experiment in one of the these motion modes (Gardner et al. 1997; Duda et al. 1998).

#### **Axial tension and compression**

During distraction osteogenesis, the fragment ends are pulled slowly apart from each other creating an axial tension in the interfragmentary gap and thereby stimulating bone formation (Morgan et al. 2006). Distraction osteogenesis is clinically used to generate large amounts of new bone that has been lost, e.g. by trauma, infection or cancer (Ilizarov 1989; Richards et al. 1998).

Several studies with static fixators showed that moderate axial interfragmentary motion is beneficial to bone healing (Goodship et al. 1993; Claes et al. 1995; Epari et al. 2006a). Goodship and co-authors concluded: "More flexible fixation may lead to excessive interfragmentary motion ... while too rigid fixation may impair callus formation contributing to ... non-union" (Goodship et al. 1993). For sheep tibia osteotomy models, Claes and co-authors estimated the range of optimal IFM to be between 0.2 mm and 1.0 mm resulting in an IFS range of 10% to 50% for a model with 2 mm gap size (Claes et al. 1998).

#### **Bending**

A special external fixator was implemented to create a specified bending along an ovine long bone axis (Hente et al. 2004). Larger callus formation on the compressed side compared to the elongated side was found. This led the to the conclusion, that axial compression stimulates the formation of an external callus while tension stimulates the formation of fibrous tissue between the bone fragments. A rat model with an alternating bending load resulted in cyclic compression and distraction on both sides of the callus (Cullinane et al. 2003). Under this symmetrical bending

condition, symmetrical callus formation was also found, however, with an increased cartilage formation compared to a rigid control group.

### Translational shear and torsion

Tissue materials are generally softer and more disruptive (can sustain less deformation) under shear compared to axial loading. Therefore, this type of motion is particularly important for the healing progression. Several animal experiments induced shear either by setting an oblique osteotomy or by external loads and high shear loads were found to be detrimental to healing. An early study on rabbits investigated several different shear conditions (Yamagishi and Yoshimura 1955). When applying moderate shear force, the fracture callus showed a higher amount of cartilage and a lower amount of fibrous tissue and the application of high shear loads leads to pseudoarthrosis (non-union). Analysing a sheep osteotomy model, Augat and co-authors concluded that shear movement considerably delayed bone healing compared to axial movement (Augat et al. 2003). However, they applied the same amount of displacement in both directions, shear and axial. Park and co-authors compared oblique fracture healing on a rabbit tibia and found confirmed that shear is stimulative for cartilage formation. They point out that "interfragmentary shear motion is not a principle cause of delayed union or non-union" (Park et al. 1998). Another sheep osteotomy model compared the healing under axial compression and pure torsional shear loads (Bishop et al. 2006). The results for the monitored healing parameters (hard callus density, callus stiffness) and histological analysis support the hypothesis "that interfragmentary shear is not necessarily detrimental to bone healing and can stimulate callus formation" (Bishop et al. 2006).

### **(iii) Timing of motion by inducing micromotion**

With the aim to actively stimulate bone healing, several studies with dynamic fixators inducing micromotion have been carried out where the induced micromotion can be altered in a controlled way. These studies provide an elegant approach to study the effects of the timing of external loading. When the cyclic loading was reduced during the healing progress, faster healing could be achieved (Gardner et al. 1998). Another dynamic fixation model showed, that the benefits of cyclic loading are eliminated if the stimulation is delayed (Goodship et al. 1998). Furthermore, high strains applied in late healing inhibited callus bridging and reduced callus stiffness. In summary, early mechanical stimulation resulting in strains up to 50% is thought to be desirable with a considerable reduction of the strains with the ongoing healing process (Jagodzenski and Krettek 2007).

**Limitations of these studies**

The problem of defining “good” healing is complex. Intuitive definitions or questions such as “when can a patient use the bone again?”, or “when is the original shape and function of the bone restored?”, face the problem that they are difficult to quantify. Several parameters have been proposed with the aim to describe the “quality” or “success” of healing. As a crude parameter, IFM (interfragmentary movement) is often reported. Accordingly, a fast decrease of the IFM indicates fast healing. However, measuring IFM in a living animal raises several technical difficulties and the accuracy is generally a problem, explicitly after bridging of the fracture gap occurred resulting in tiny IFM. Furthermore, IFM can provide information about the bulk stiffness of the callus but no information about the composition or architecture. As a crude architectural parameter, the callus size is often measured or estimated, for example by X-ray. With the rise of high resolution micro-computed tomography ( $\mu$ CT) scanners, architectural data of bone can be gathered for small animals *in vivo* (Waarsing et al. 2004; Lambers et al. 2009). However, the animals still have to be sacrificed (killed) in order for detailed investigations, e.g. precise mechanical testing or histological analysis. Many *in vivo* studies on large animals sacrifice animals only at one or two time points post-operatively in order to reduce the number of required animals. The aim of these studies is often to answer the question if a specific treatment, for example the application of micromotion, shows an effect on the healing outcome. However, the investigated healing parameters constantly change their values during the process of healing. Therefore, a larger number of investigated time points is necessary for more detailed conclusions on the *process* of healing.

Nevertheless, several studies have drawn conclusions about the healing process mainly based on data from a single investigated time point (Claes et al. 2003; Bishop et al. 2006; Gardner et al. 2006; Javadieh et al. 2009). For example, six groups of sheep (three different gap sizes and treated with two different fixators) were compared and conclusions were drawn about which groups healed faster based on the mechanical testing of the bone specimen at 9 weeks post-op (Claes et al. 1997). After some weeks of uneventful healing, the stiffness of the bone typically shows values in the same region or even higher than the non-fractured bone due to the external callus. It is reasonable to assume that the development of stiffness shows an increase to a maximum with a successive decrease to the normal stiffness of a long bone. Without additional data points, one can not find out which animal group showed faster healing (Figure I.4).

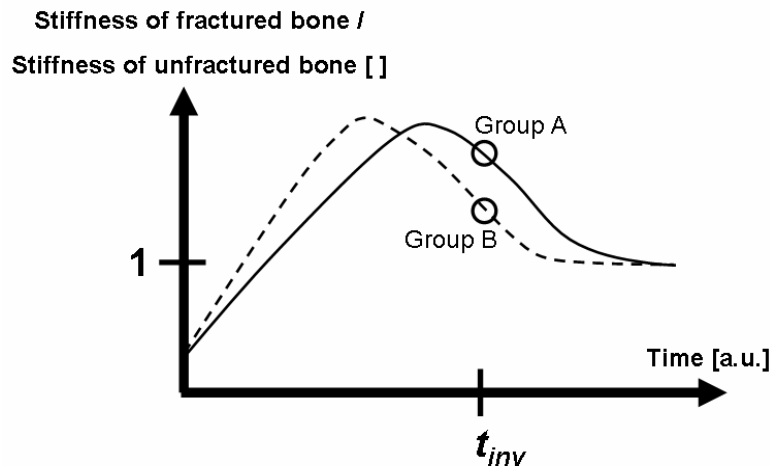


**Figure I.4: Time evolution of the fracture stiffness**

Hypothetical time evolution of the stiffness of the fractured long bone for two animal groups (A, B).  $t_{inv}$  denotes the chosen investigation time point at which the animals are sacrificed, the circles represent the experimentally assessed data. Group B reaches the unfractured stiffness faster than group B. Considering only the amount of gained stiffness at time point  $t_{inv}$  leads to the wrong conclusion that the animals of group A heal faster.

### 2.5. Mechanobiological theories on bone healing

The previous section described animal experiments with different external or “global”, mechanical parameters. Whereas these “global” parameters are useful for clinical applications, e.g. by identifying the best mechanical fixation, mechanobiological theories try to explain the healing (locally) on the cellular level and are accordingly interested in estimating the local mechanical environment within the fracture callus. Mechanobiological theories on bone healing relate, for example, experimentally observed tissue patterns during healing with the local mechanical conditions. The most frequently used tool for the estimation of the local mechanical conditions has been the Finite Element Method (FEM). FEM is a computational method, which has the drawback that it needs accurate material parameters of the different tissues as input parameters (section 2.1). As experimental methods, also digital image correlation (DIC) and electronic speckle pattern interferometry (ESPI) have been applied (Thompson et al. 2007; Bottlang et al. 2008).

The first comprehensive, but only qualitative, mechanobiological theory on bone healing was presented by Pauwels in the early 1960s (Pauwels 1960). He suggested that the local mechanical stresses determine the differentiation pathway of the mesenchymal stem cells (MSCs). Assuming the cell can feel how it is deformed, Pauwels differentiated between stresses which change the cell’s shape and those which change its volume. Accordingly, deviatoric stresses (e.g. caused by tension) stimulate the formation of fibrous connective tissue (Figure I.5, left), which can

sustain well shear deformation. Hydrostatic stresses (in bone healing caused by compression in the gap area) stimulate the formation of cartilage which can sustain well pressure. After the formation of cartilage or connective tissue, formation of bone can occur. A similar, but more detailed, theory, proposed by Carter and co-workers, was based on the history of tensile strain and hydrostatic stress and included the possibility of direct formation of bone (Figure I.5 , right) (Carter et al. 1998). The idea of incorporating the history of mechanical stimulation (instead of the focus on the instantaneous stimulation) was presented by Carter earlier by introducing the “osteogenic index” which is a weighted sum of deviatoric stress history and hydrostatic strain history (Carter et al. 1988). Low values of the osteogenic index were thought to be stimulative for bone formation.

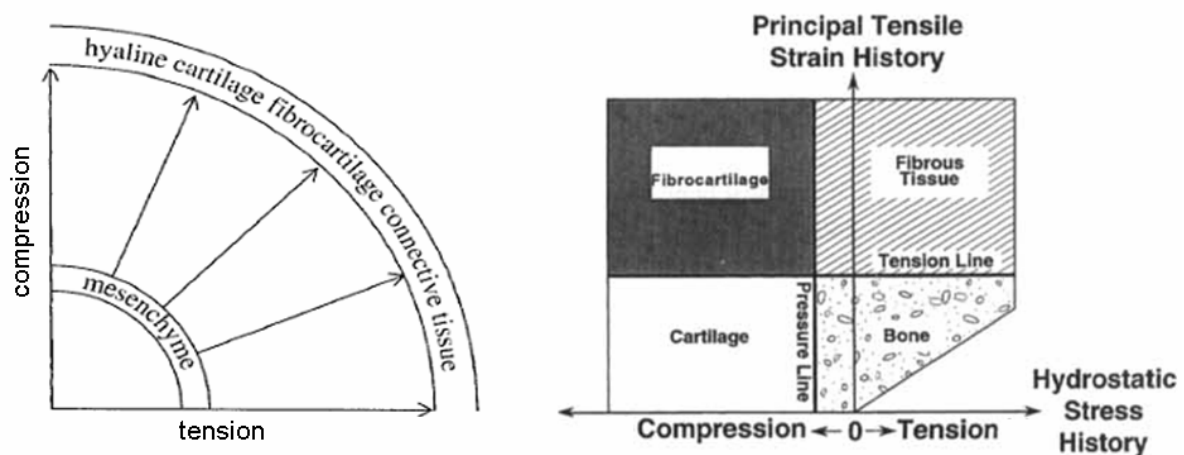


**Figure I.5: Qualitative mechanobiological theories on bone healing**

**Qualitative mechanobiological theories with two mechanical stimuli. Left: theory of Pauwels (1960) (figure adapted). Right: theory of Carter et al. (1998).**

Perren and Cordey (Perren 1979; Perren and Cordey 1980) introduced the interfragmentary strain (IFS) theory. They argued that only that tissue type is formed in the gap which can sustain the current interfragmentary strain and they also quantified their idea (Figure I.6). This theory focuses only on the interfragmentary conditions and does not take the mechanical environment of the callus into account. However, the advantage of this approach is that it can directly be tested as IFM is generally recorded during healing. Due to its simplicity, this theory is also the leading idea for this current work.

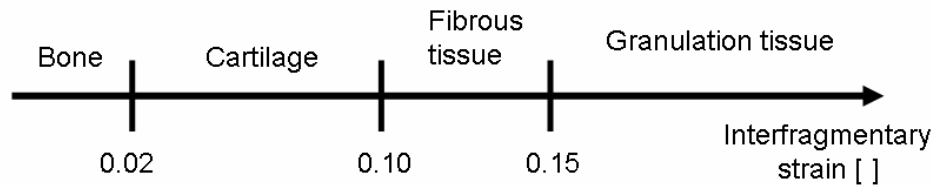


**Figure I.6: Interfragmentary strain theory of Perren and Cordey (1980).**

**This is a basic and quantitative mechanobiological theory on bone healing, which applies only one mechanical signal (stimulus), the interfragmentary strain, as predictor for tissue differentiation.**

In the following years, several quantitative mechanobiological models have been proposed. Claes and Heigele conducted an FE study on idealised sheep osteotomies at three healing time points, at early, intermediate and late healing (Claes and Heigele 1999). They compared the assessed local stresses and strains with the development of the tissue estimated by histological analysis. Based on this comparison, they proposed a mechanobiological theory similar to Carter et al. (1988), employing the axial strain and hydrostatic pressure as mechanical stimuli (Figure I.7, left). Some studies proposed the idea that interstitial fluid flow and the resulting shear of the cells is one main mechanical stimulus. In the following, poroelastic mechanobiological theories were proposed. However, it was shown that solid and poroelastic models on cartilage show very similar results assuming typical loading conditions within the body (Carter and Beaupre 1999). The authors conclude that poroelastic models with low permeabilities only slightly differ from single phase models when slow cyclic loading regimes are investigated. Prendergast and co-authors neglected the differentiation between compressional and tensional deformation and assumed high values of distortional solid strain and/or high fluid velocity stimulative for fibrous tissue formation. Bone formation occurs only if both values are low and cartilage forms for intermediate mechanical environment (Prendergast et al. 1997) (Figure I.7, right). A very similar model was proposed by Kuiper and co-workers based on a FE model of an idealized callus with a 2 mm osteotomy at an early healing time point (Kuiper et al. 1996). The mentioned mechanobiological theories on bone healing are similar to each other and look at the healing process only from slightly different viewpoints. All theories include the idea that only that tissue can form which can sustain the local mechanical environment and, therefore, the current theories can be interpreted as a refinement of the approach of Perren and Cordey (1980). However, a comparison of the different theories is difficult as all theories use different mechanical stimuli, which trigger cell differentiation.

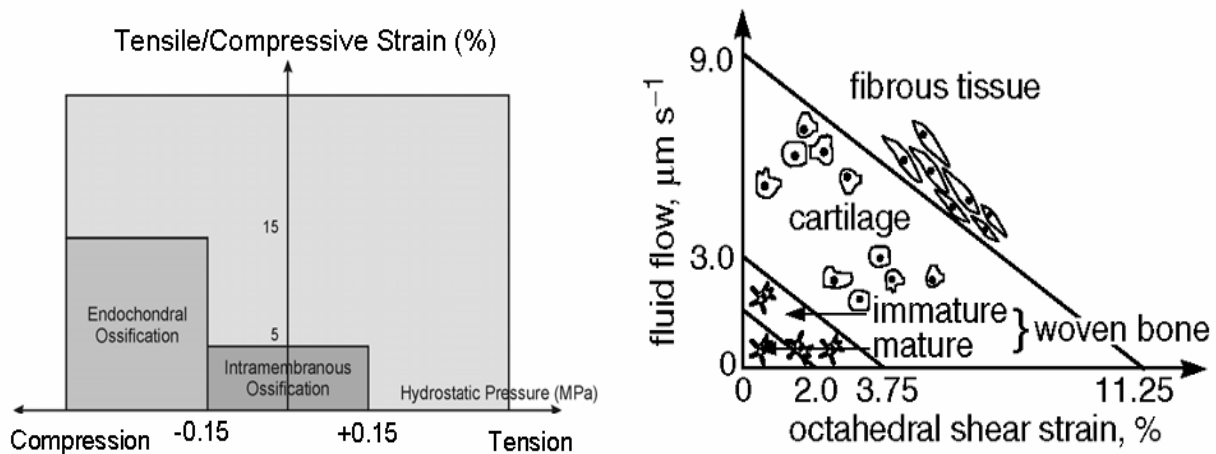


**Figure I.7: Quantitative mechanobiological theories on bone healing**

Quantitative mechanobiological models applying two mechanical signals (stimuli), which regulate the tissue differentiation during bone healing. Left side: theory of Claes and Heigele (1999). Right side: theory of Prendergast et. al (1997). Figure from (Lacroix and Prendergast 2002).

### Limitations

As discussed in section 2.4, the local mechanical environment is generally more complex than just displaying one mode of motion. Therefore, an estimation of the local mechanical environment is desired. To reach this aim, FE models on idealized geometries has frequently been carried out, often assuming rotational symmetry along the long bone axis. Additionally to the idealization of the callus geometry, the mechanical loads are idealized, generally uniformly distributed along the cortex, which is not realistic. Finally, also the input data, time-evolving material properties and loads, are difficult to measure and show high inaccuracies. For this limitation, the results of FEM are only crude estimations. Nevertheless, these studies can provide correct *qualitative* results and have paved the way for computer simulations of bone healing.

### 2.6. Existing computer models of bone healing

Mechanobiological theories on tissue regeneration can be tested by implementing them *in silico* as an iterative tissue adaptation algorithm. Besides bone healing, computer simulations have been carried out on different fields of tissue regeneration such as wound healing, implant osseointegration, or distraction osteogenesis. The models of bone healing can be distinguished into mechano-regulated models, pure biological models and models which consider both, biological and mechanical stimuli (Geris et al. 2009). This section gives a short overview of the work of several groups on mechanobiological bone healing simulations (see also to Table 1 for an overview of the different modelling approaches). To run a simulation, one has to define the geometry and the mechanical loading conditions, the mechanical stimuli

(mechanobiological theory) and the biological influences. Regarding biology, many simulations let cells or/and growth factors migrate into a callus with a stationary, pre-defined geometry. The migration is modelled mostly as a diffusion process on a coarse length scale (continuous model). However, random walk models were also suggested considering a cell-based length scale (Perez and Prendergast 2007; Checa and Prendergast 2009). Other models mimic callus growth which leads to a time-evolving callus geometry (Kuiper et al. 2000; Gomez-Benito et al. 2006).

One of the first bone healing models used a fuzzy logic approach in order to match the lack of precise knowledge about the cellular behaviour during fracture healing (Ament and Hofer 2000). A set of 9 fuzzy logic rules was approximated from medical knowledge. The strain energy density together with the osteogenic factor, or the gradient of bone area fraction, were the parameters deciding on the type of tissue adaptation. Bone was only allowed to form in regions with high osteogenic factor which results in new bone forming only close to existing bone areas. This rule substituted to a certain degree the “biological factor”, or the migration of cells as used in other model approaches. The authors concluded, that “the biological factors play a more dominant role than effects derived from a more sophisticated nonlinear elastomechanic model” (Ament and Hofer 2000).

Prendergast and Lacroix implemented a poroelastic model based on the two mechanical stimuli, interstitial fluid flow and tissue shear strain (Lacroix and Prendergast 2002). The choice of the origin of progenitor cells, either the medullary cavity, the periosteum or the surrounding tissue, was found to fundamentally influence the simulated healing and the decrease of IFS. This model was refined by modelling diffusion, proliferation and differentiation separately for mesenchymal stem cells, fibroblasts, chondrocytes and osteoblasts. A 3D application of this refined model showed asymmetric tissue type distribution in the callus when applying asymmetric loads (Andreykiv et al. 2008).



**Table 1: Overview of several conducted simulations on bone healing.**

Used abbreviations: IFM (IFS): interfracture movement (strain), x: location, t: time, d: displacement, F: force, MSC: mesenchymal stem cells, CC: Condocytes, FB: Fibroblasts, OB: Osteoblasts, CGGF: chondrogenic growth factor, OGGF: osteogenic growth factor, VGF: vascular growth factor, EC: endothelial cell

	Animal model, geometry	Mechanics			Biology			Validation
		Material description	Load case	# Biophysical stimuli	Cells	Source of cells	Growth factors Angiogenesis Tissue growth	
Ament and Hofer (2000)	Sheep, 2D Quarter, 2 mm gap	Linear elastic	$F_{axial} = 500 \text{ N}$ , $d_{max} = 1.3 \text{ mm}$	1: Strain energy density	No cells but osteogenic factor	--	--	IFM (t)
Kuiper et al. (2000)	2D half, 2 mm gap	Linear poroelastic	several d (t), $F_{max} = 1000 \text{ N}$	2: Shear strain and fluid shear stress	No cells	--	Volume growth	Callus composition at 20 and 40 days. Axial stiffness at 4 and 7 weeks.
Lacroix and Prendergast (2002)	Human, 2D Quarter, 1, 3 and 6 mm gap	Linear poroelastic	500 N axial ramp load of 0.5 s	2: Shear strain and fluid flow (Prendergast et al. 1997)	MSC	Marrow, periosteum, surrounding tissue	--	IFS (t), Elastic modulus maps over healing time
Bailon-Plaza and van der Meulen (2003)	Sheep, 2D quarter, 3 mm gap	Linear elastic; conn. tissue hyperelastic	$F_{axial} = 360 \text{ N}$ at 0.5 Hz	2: Deviatoric strain and dilatational strain	MSC, CC, OB	MSC from surrounding tissue and periosteum	CGGF from fracture cut, OGGF from periosteum	Axial stiffness (t), bone mineral content at the osteotomy line (experiment) with average bone density at the osteotomy line (simulation)
Gomez-Benito et al. (2006)	3D half, axial-symmetric; 3 mm gap	Linear poroelastic	$F_{axial} = 500 \text{ N}$ at 1 Hz	1: Second Invariant Of deviatoric strain	MSC, FB, CC, OB	MSC and OB from the periosteum (ratio 4:1)	Volume growth	IFS (t, angle) Cell concentration maps (t)
Isaksson et al. (2006)	2D quarter, 3 mm gap	Linear poroelastic	$F_{axial}$ (t) at 1 Hz; $F_{axial} = 300 \text{ N}$ and 600 N at 1 Hz	1 – 2: Comparison of different theories	MSC	Marrow, periosteum, surrounding tissue	--	Comparison with simulation results of Lacroix and Prendergast 2002 IFM (t), Interfracture stiffness (t), Elastic modulus maps (t)
Andreykiv et al. (2008)	Ovine, 2D Quarter, 3 mm gap	Linear poroelastic	Two bending cases and Two actuation cases	2: Shear strain and fluid flow (Prendergast et al. 1997)	MSC, FB, CC, OB	MSC from medullary cavity and surrounding tissue	--	IFM (t), Cell concentrations (t, x), tissue fractions (t, x), bone fraction (t)
Isaksson et al. (2008a)	Sheep, 2D Quarter, 3 mm gap	Linear poroelastic	Cyclic $F_{axial} = 300 \text{ N}$ , 400 N and 500 N at 1 Hz	2: Shear strain and fluid flow (Prendergast et al. 1997)	MSC, FB, CC, OB	MSC marrow, from periosteum, surrounding tissue and randomly in callus	--	Matrix concentration (t, x) of FT, C and B, cell concentrations (t), Elastic modulus maps (t)
Geris et al. (2008)	Murine model, 2D	Linear poroelastic	Several cases	1: Fluid flow	MSC, FB, CC, OB, EC	Various cells from different sources; e.g. OB from bone ends (at the beginning)	CGGF, OGGF, VGF, Angiogenesis	Tissue fractions (t), Bone density (x, t)

## 2. Background

---

The same basic model of Prendergast and Lacroix was applied and refined in several other studies. In a comprehensive study (Isaksson et al. 2006), the results of the simulations assuming the mechanobiological theories of Carter, Claes and Heigele and Lacroix and Prendergast, as well as assuming only one mechanical stimulus (deviatoric strain, fluid flow and pore pressure) were compared. The study showed that the three theories and the simulation employing only the deviatoric strain resulted in similar results. A different study introduced a cell-phenotype specific model (Isaksson et al. 2008a). The authors were aware of the models` complexity, both mechanically and biologically, mainly due to the increased number of model parameters. Using statistics, only a subset of the possible combinations of the assumed levels of the 26 cellular parameters of the model was investigated. Therefore, a fractional factorial design study was carried out (Isaksson et al. 2008b). They found the matrix production rates of bone and cartilage as well as cartilage replacement rate to be most important for their model. They furthermore concluded that their analyses “establishes the complexity of the mechanobiological process during bone healing” (Isaksson et al. 2008b) which is not a very surprising result considering the complexity of the implemented model. The authors also investigated the influence of the assumed material properties on the simulated healing (Isaksson et al. 2009). Slight variations of the assumed material properties did not significantly alter “the sequence of predicted events during bone healing. However, they did influence the rates of healing and the mechanical stability” (Isaksson et al. 2009).

Kuiper and co-authors suggested a similar mechanobiological model as Prendergast and co-workers (Prendergast et al. 1997). Additionally, they modelled a variable callus geometry by assuming a moving tissue boundary (Kuiper et al. 2000). The boundary velocity increased with an increasing local maximal shear strain up to an assumed maximal velocity of  $10^{-3}$  m/day. Different load cases were assumed and all simulated fractures healed except for the large load case which showed a non-union. The authors discussed the potential importance of incorporating angiogenesis into their model. Another study on a 3D osteotomy included callus growth depending on mesenchymal cell proliferation and chondrocyte hypertrophy (Gomez-Benito et al. 2006). Within the plane of the fixator, this simulation showed a smaller callus size and a delayed fracture gap bridging.

Bailón-Plaza and van-der Meulen started with a pure biological model based on chondrogenic and osteogenic growth factors (Bailon-Plaza and van der Meulen 2001). In a follow-up model, the development of connective tissue, cartilage and bone still depended on the local growth factors, however, the formation of bone was either stimulated or inhibited by local strains. Beneficial effects of moderate loads

were found whilst detrimental effects of excessive loads (Bailon-Plaza and van der Meulen 2003). To improve the results, this model was refined by including angiogenesis (Geris et al. 2008).

### **Limitations**

Computer simulations were able to reproduce basic global variables (variables which describe the whole callus). That included interfragmentary movement or strains (IFM or IFS) and the stiffening of the callus over time. Furthermore, simulations have been successful to show the effects of global load magnitude in terms of predicting non-unions or delayed healing. More detailed, asymmetric tissue type patterns were found for asymmetric loading conditions. However, a quantitative comparison of spatial tissue distribution between experiment and simulation has not been carried out. The simple reason for this lack of comparison between experiment and simulation is that the required experimental data, i.e. a quantitative description of a normal, uneventful healing based on images, did not exist. Therefore, the comparison has been based on basic, scalar values as IFM or rather vague comparisons of tissue type distributions based on personal impressions. Nevertheless, most of the simulation studies claim to reproduce the tissue type distributions “reasonably” or “well”. In fact, that can be doubted. Firstly, the studies did not rigidly distinguish between regions with different (predominant) tissue types. Instead, different amounts of different tissue types in one element were allowed which is useful for smoothing the model but not really realistic. Secondly, when assigning a certain tissue type to an element, for example by the local mechanical stiffness, the simulation results showed differences to the experimentally observed tissue patterns. For example, ovine simulations showed a clear endosteal activation right at the start of the healing process (Isaksson et al. 2006) which was not observed experimentally (Schell et al. 2005; Bishop et al. 2006; Epari et al. 2006a). Theoretical models have recently become more complex, e.g. by incorporation of angiogenesis. It can be speculated, if this is due to the observed lack of prediction capability of the simulations. However, the experimental *in vivo* data delivering the required input parameters are generally missing.

### **2.7. Aims and structure of this work**

Existing mechanobiological models have shown the potential to simulate bone healing *in silico*. However, two main drawbacks of these simulations can be detected as already mentioned in the previous section. First, a stringent comparison of the simulation results with a “normal” progression of bone healing based on tissue types has not been carried out. The reason for this is simple: a normal progression of healing has not been “defined”. In order to allow more specific conclusions based on

computer simulations, the availability of such data is crucial. The second drawback is the complexity of most existing models. The respectable aim to model nature in a very detailed way, e.g. by modelling each cell type, increases the dimensionality of the parameter space to unreasonable values. For the previously cited model (Isaksson et al. 2008b), a complete parameter study with only 2 values for each of the 26 parameters, would lead to  $2^{26}$  or about 67 million simulations. Therefore, the aim of the current work was not to set up another mechanobiological model, but to implement a kind of minimal model guided by simulations in physics and additionally, to link computer models closer to experimental data.

To summarize the main aims: firstly, a quantitative description of a normal healing progression was desired and, secondly, a phenomenological model of bone healing had to be set up with the perquisite to minimize the simulation parameters in order to allow thorough parameter studies. The core question of this thesis is then: to which extend can a basic mechanobiological model reproduce the typical tissue patterns experimentally observed during secondary bone healing?

The experimental data stemmed from a sheep model with 64 sheep providing data at four different time points post-operatively. For a study on large animals, this is a rather big number of time points (and, therefore, animals) and enables detailed and rather unique investigations. The thesis is divided in four parts. Part one through three address the core question of this thesis while the fourth part investigates the process of fracture healing from a broader perspective.

The **first part** analyses the histological data of the underlying animal experiment and is in part published (Vetter et al. 2010a). The quantitative results of standard histological analyses have been generally restricted to scalar variables, as for example the amount of cartilage at a certain time point post-op. As an experimental “foundation” of the following in silico work, an averaged healing progression was calculated representative for a typical sheep. To achieve this, a novel averaging procedure was implemented and applied to the sheep model. The norm healing could be described by means of six tissue type images at six different stages of the healing process.

The **second part** of the thesis uses the images of the averaging procedure and previous experimental material data to calculate the local strains at the six stages during healing. Part of this work was summarized in a manuscript (Vetter et al. 2010b). The aim was to investigate the influence of the heterogeneity of the hard callus on the strain distribution within the callus. Furthermore, these “static

simulations", meaning simulations only at certain healing stages, help to answer the question of which invariants of the strain tensor are suitable to act as mechanical stimulus.

The **third part** consists of the dynamic simulation of normal bone healing in sheep. The aim was to implement a basic phenomenological model with a minimum set of parameters. This was achieved by summing up underlying biological processes (described by a local "biological potential" to heal) and by applying *in vivo* data for the estimation of further simulation parameters. The core question of this thesis was tackled by comparing the simulation results with the experimental images from the first part. This model was also used to investigate the influence of the origin of the biological potential on the healing progression.

The **fourth part** aims to analyse the healing process from a stronger physical perspective, i.e. eliminating the specificities of bone healing from the model. The mathematical complexity of the system was reduced by substituting the mechanical problem by a conductivity problem. This part addresses the question which physical feedback between local stimulus and cell response is necessary to achieve an indirect healing of a fracture.

#### **3. Available experimental data used for this work**

The experimental background for (i) investigating the mechanical influences on bone healing, (ii) implementing a computer model on bone healing and (iii) the successive validation of the simulation results was provided by a previous animal model.

#### **Animal model**

Altogether 64 mature female Merino sheep underwent a 3 mm tibial mid-shaft osteotomy. The sheep were equally divided into two groups, group A and group B, of thirty-two each with the aim to investigate the healing under two different mechanical environments. Therefore, the osteotomies were stabilized with two types of external fixators medially applied (Figure I.8). The fixator of group A was more rigid than the fixator of group B. Both fixators were mechanically characterized beforehand. The medial application of the fixator led to higher deformations at the lateral side compared to the medial side. As investigation time points, two, three, six and nine weeks were chosen. At each time point eight sheep of both groups were sacrificed. The animal model has been extensively reported (Schell et al. 2005; Epari et al. 2006a). For this experimental model, a FE study showed predominantly axial compression in the callus whilst also some shearing was found (Epari et al. 2006b).

#### **Experimental data**

##### **Loading**

During healing, X-ray radiographs were taken and showed that the osteotomy gap was hold constant at 3 mm by the external fixator. Additionally, the interfragmentary movement (IFM) was recorded (Schell et al. 2008). The initial IFM, one input parameter for the computational model of this work, was found to be approximately 0.5 mm. An earlier FE study estimated the maximal force during walking on an unfractured ovine leg to be around 500 N (Duda et al. 1998).

##### **Histology**

After harvesting and mechanical testing, the callus regions of all sheep were sectioned in the frontal plane. Polymethylmetacrylate (PMMA, Technovit® 9100, Heraeus Kulzer, Germany) was used to embed the anterior portion after dehydration and serial histological sections of 6 µm were cut. The histological sections were used for staining. The stainings were Safranin Orange/von Kossa, marking the mineralized tissue (mainly bone material) in black, Safranin Orange/Fast Green marking cartilage in green and Movat Pentachrome marking haematoma in violet. Digital images of all sections were taken (2048x1536 pixels). The region of interest (ROI) had to be constricted to a rectangle comprising  $\pm 6$  mm in vertical direction from the horizontal osteotomy line due to the influence of the fixator screws (Figure I.8).

Histomorphometrical analysis showed more cartilage at 6 weeks post-op in the animal group with the semi-rigid fixator. One interpretation of the previous analyses based on mechanical testing and standard histomorphometry was that instability, due to the semi-rigid fixator, prolongs the healing time (Schell et al. 2005).

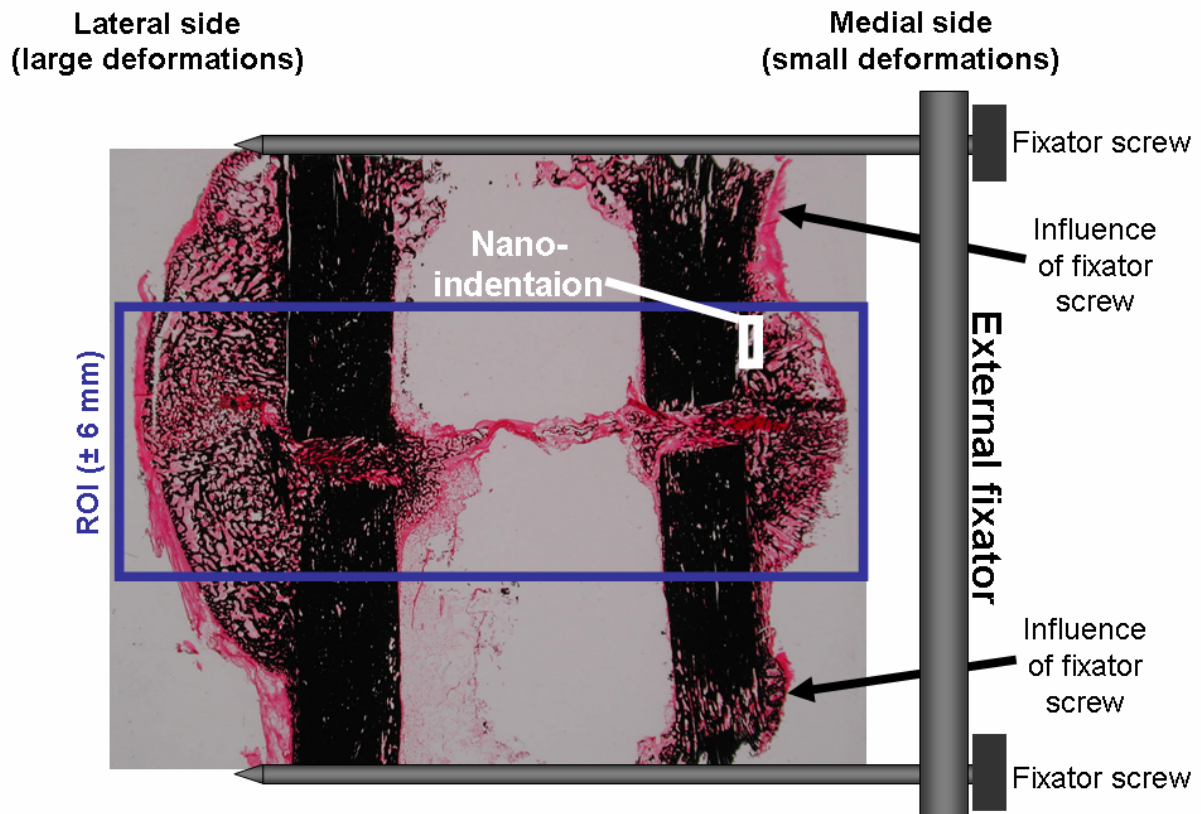


**Figure I.8: Example for a stained section (Safranin Orange/von Kossa).**

The external fixator was applied on the medial side which led to a higher stability at this side which decreases the deformation compared to the lateral side. The blue box comprises the Region of Interest (ROI) which had to be smaller than the whole callus to avoid regions influenced by the fixator screws. The white box comprises the region adjacent to the cortex measured by nanoindentation.

#### Material properties of the hard callus

The remaining blocks were grinded and polished (PM5, Logitech, Glasgow, Scotland) for nanoindentation measurements. Nanoindentation was performed with a scanning nanoindenter (Hysitron Inc., Minneapolis, USA) to determine spatial and temporal distribution of the stiffness of the bone material,  $E_{mat}$ , see Eq. (1) (Manjubala et al. 2009). The experimental nanoindentation results, which were used in this thesis, stemmed from the periosteal hard callus region (rectangle of the size 0.75 mm x 2 mm) adjacent to the cortex and 3 mm away from the osteotomy (Figure I.8). A Berkovich diamond indenter was used and 101 x 11 indents per sheep were performed, with a fixed load function leading to indentation impressions typically

### 3. Available experimental data

---

under the dimension of  $10\text{ }\mu\text{m} \times 10\text{ }\mu\text{m}$ . The indent spacing was  $20\text{ }\mu\text{m}$  between lines and  $75\text{ }\mu\text{m}$  between columns to minimize the influence between neighbouring indents. The hard calli of four sheep (rigid-fixation) were measured for each time point. Figure I.9 shows the histograms of the measured elastic moduli at the four different time points. Averaging the values for each time point, an increase of the average elastic modulus was found starting from about 5 GPa at 2 weeks to about 12 GPa at 9 weeks (Figure I.4, top left). Within the current work, the same region was investigated for the bone area fraction ( $BA/TA$ ) (Figure I.4, bottom left) and both data were used together to calculate the development of the bulk elastic modulus the hard callus using Eq. (1) (Figure I.4, right).

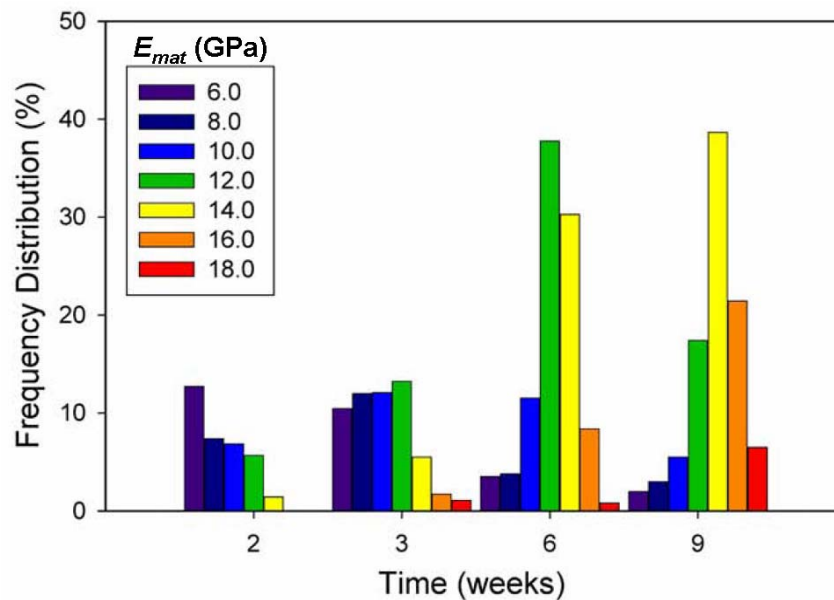


**Figure I.9:** Histograms representing the the frequency of the nano-indentation modulus of the hard callus (bone trabeculae).

The nano-indentation modlus describes the stiffness of the bone material (elastic modlus  $E_{mat}$ ).  
Figure adapted from (Manjubala et al. 2009).



---

## **I. Quantifying experimental data**

In Chapter 4, histological analysis was carried out to identify the different tissue types on the histological sections and separate masks for each tissue type were created for each animal. Furthermore, the formed hard callus during healing was investigated histomorphometrically.

In Chapter 5, the tissue masks were assembled into an image describing the spatial pattern of tissue for each animal. The occurring tissue type patterns or healing stages were identified and the images were classified into six occurring healing stages which were defined by six topological criteria. Based on this classification, an averaged progression of healing was calculated. The progression represents the “normal” healing progression in sheep depending on the fixation type (rigid, semi-rigid) and side of the long bone (lateral, medial).

### 4. Histological analysis

An extensive analysis of the available histological sections was carried out to localize the different tissues followed by a detailed analysis of the development of the bone area fraction ( $BA/TA$ ) over time. Firstly, the development of  $BA/TA$  was investigated on a global level (considering the whole fracture area) and, therefore, the two main regions at the osteotomy site were chosen: the whole newly formed hard callus and the cortex. Secondly, on a local level, only a small part of the periosteal hard callus close to the cortex was investigated. This local data stemmed from the same area as the data of the bone material stiffness measured by nanoindentation (Manjubala et al. 2009).

#### 4.1. Identification of the tissue types

For each animal, one separate binary image or mask for each tissue type was created with an image editing software (KS 400, Zeiss Jena, Germany). The available stained histological sections and digital images were used for this purpose (Schell et al. 2005; Epari et al. 2006a). Staining techniques generally stain certain cellular components and, therefore, the stained regions were only used as an indicator. Stained regions in the histological sections were further investigated using a light microscope with the aim to determine the local predominant cell type and confirm (or reject) the indication. Then, the regions with a predominant tissue type were marked by hand in a separate mask using the image editing software. The masks are binary images marking the regions of the callus where the investigated tissue was found. In doing so, the regions of cartilage, fibrous tissue, haematoma and marrow were identified. The mineralized bone area was identified in the digital Safranin Orange/von Kossa image by thresholding. This image was also used to create a mask of the cortex marking the edge of the cortex by hand.

The masks of the mineralized bone tissue (comprising the hard callus, which is the bone and the “void” space in between) were further investigated. The bone area fraction,  $BA/TA$ , was determined for the whole hard callus and for the same region close to the cortex as for the nanoindentation study. Both areas were located within the same maximal region of interest or ROI ( $\pm 6$  mm from the osteotomy gap), as in the previous study which focused on the tissue areas (Schell et al. 2005; Epari et al. 2006a).

#### 4.2. Hard callus and cortex

First, the development of the whole hard callus and cortex was investigated. The variables tissue area  $TA$  and bone area fraction  $BA/TA$  were investigated for the callus or cortex in a whole (or globally) to describe the healing progression on a first and basic approach. In this animal experiment, the external fixator was medially applied, resulting in lower deformations on that side (see also Figure I.8). This influenced the two investigated variables.

##### Area of hard callus

The box plots in Figure I.1 show the time development of the hard callus area for the four cases (rigid lateral, rigid medial, semi-rigid lateral, semi-rigid medial). The area increases for all four cases till 6 weeks.

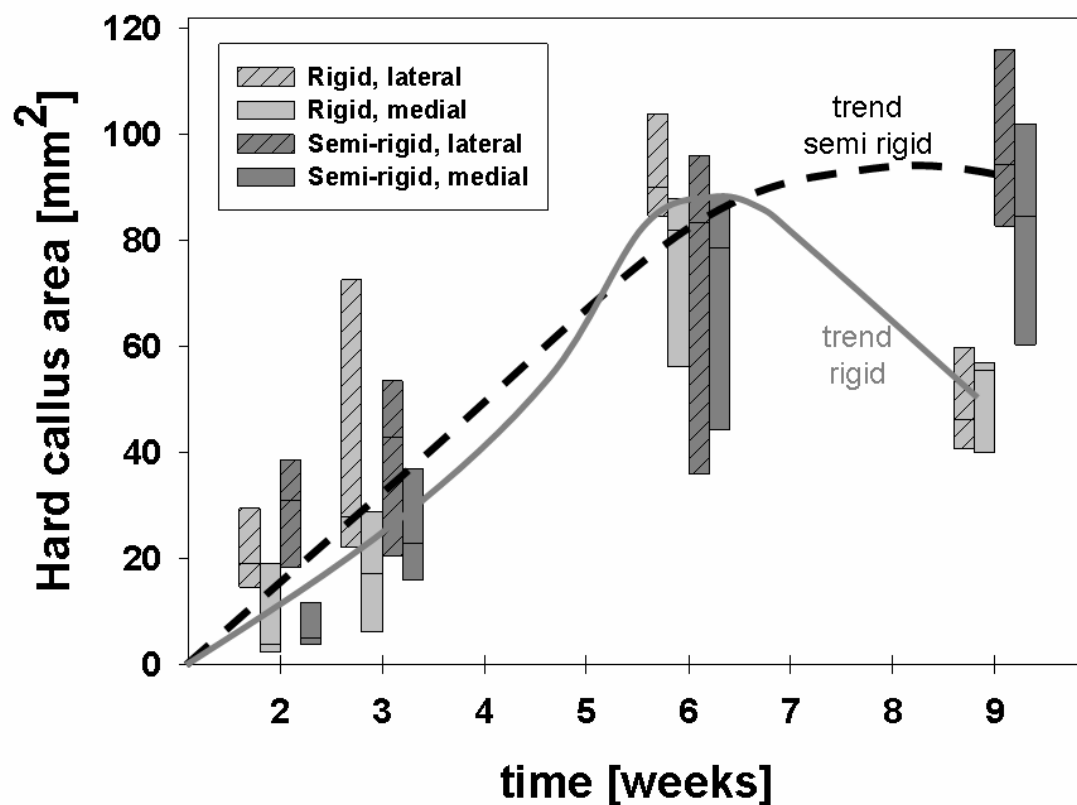


Figure I.1: Box plots of the hard callus area of the rigid and lateral side and both fixator types at 2, 3, 6 and 9 weeks post-op.

The three horizontal lines of each box indicate the upper quartile, the median value and the lower quartile. The solid and the dashed line show the two trends of the bone area fraction ( $BA/TA$ ) for averaged values of the animals with a rigid fixation and averaged values for a semi-rigid fixation (trend estimated by eye).

Comparing the fixation types, one can clearly see two different trends for the rigid and semi-rigid fixation. The rigid fixation shows a decrease of area between week 6 and week 9 (due to remodelling) while this is not the case for the semi-rigid fixation

(Figure I.1). Without the knowledge of the other time points, one would conclude for the 6 weeks time point that both fixations lead to similar results. For the 9 weeks time point, one could even conclude that the semi-rigid fixation is desirable because more hard callus was formed. Taking all four time points into account, the hard callus area data indicates clearly a faster healing for the rigid fixation. The maximum area for the rigid fixation is assumable reached at around six weeks while the maximum for the semi-rigid is probably between six and nine weeks. This also indicates the high variability for semi-rigid fixation at 6 and 9 weeks. This example shows the necessity of investigating several time points when comparing the healing of different animal groups. However, several healing parameters should be investigated to corroborate these conclusions. For this reason, the tissue type pattern will be analysed in Chapter 5.

When comparing the osteotomy site (medial, lateral), all median values were higher for the lateral side, except for the 9 week rigid case. This confirms the histological evidence that the 9 week animals with rigid fixation show a very late stage of healing where remodelling is the dominating process. The influence of the osteotomy site on bone formation seems to be more influential than the fixation type at week 2 and 3. The high variability between the sheep makes definite statements questionable. The lateral side is higher loaded mechanically and this could be a reason for this higher response by means of bone formation. Furthermore, the biological difference between the two sides could be the reason for this observation. It was argued, that the lateral side of the tibia is covered with more tissue providing a higher potential to heal and, therefore, this is the main reason for the faster development on the lateral side (Epari 2006).

#### **BA/TA of hard callus and cortex**

The development of the bone area fraction,  $BA/TA$ , showed two different trends: an increase of  $BA/TA$  for the callus and a decrease of  $BA/TA$  for the cortex (Figure I.2). The median values of  $BA/TA$  for each group (rigid lateral, rigid medial, semi-rigid lateral and semi-rigid medial) could be linearly fitted (the mean increase of the four cases was 4.85% per week) and showed interesting dependencies on the fixation type and side of the bone axis (Figure I.2, top). The decrease of the bone area fraction  $BA/TA$  in the cortex could not be fitted as well (Figure I.2, bottom). The mean decrease of the four cases was 2.61% per week.

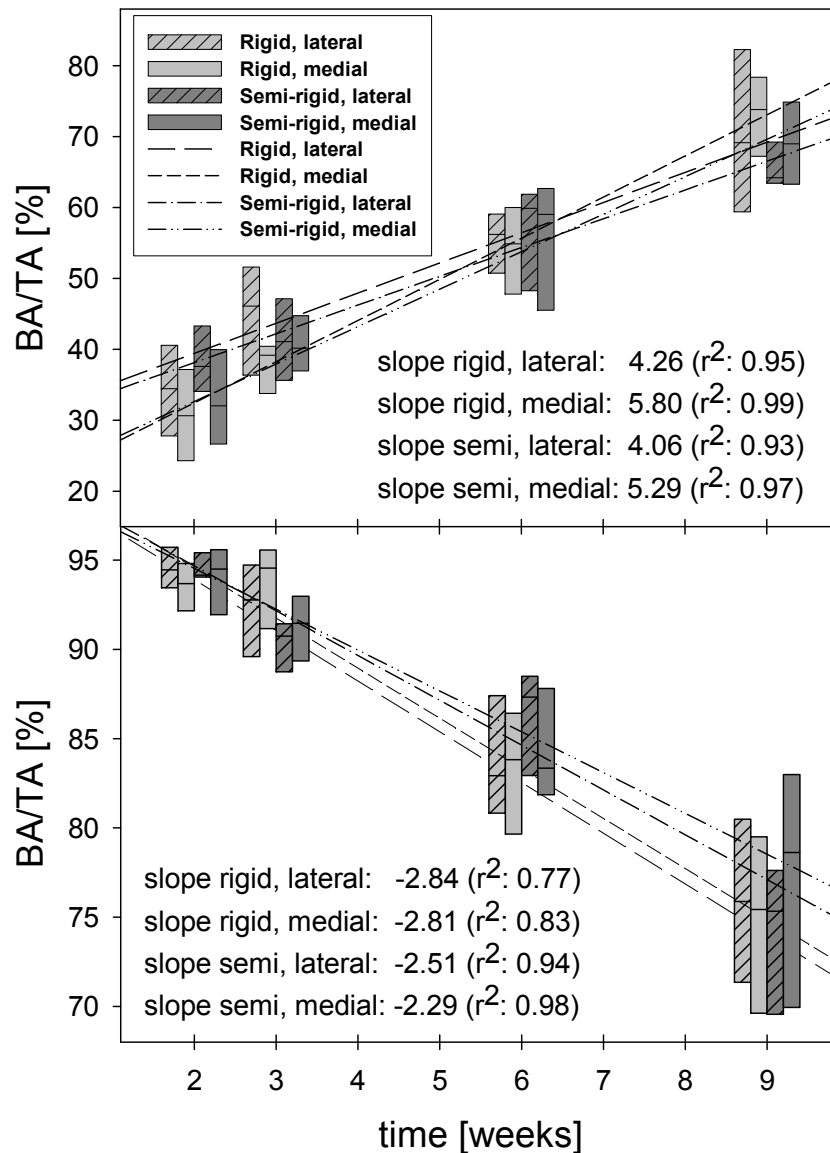


**Figure I.2: Box plots of the bone area fraction (BA/TA) of the whole hard callus for rigid and lateral side and both fixator types at 2, 3, 6 and 9 weeks post-op.**

The three horizontal lines of each box indicate the upper quartile, the median value and the lower quartile. The value of  $r^2$  is the coefficient of determination (for a perfect linear fit,  $r^2$  is equal to 1)..

The fixator was medially applied, resulting in lower deformations on that side (see also Figure I.8). With this information in mind, the results for  $BA/TA$  drive the impression that the mechanical stability is a key parameter for the increase of  $BA/TA$  (densification) of the hard callus. For the case of highest stability, that means the medial side on a rigid fixator, the fastest densification was found and for the case of lowest stability, that means the lateral side on a semi-rigid fixator, the slowest densification was found (Figure I.2, top). Furthermore, the osteotomy site (medial or lateral) was found to be more important for the slope than the fixation type. Neglecting biological influences, this indicates that the mechanical influence on the

healing process depends more on the osteotomy site (due to the asymmetrical applied external fixator) than on the two different fixators.

The decrease of the cortical  $BA/TA$  agrees with the idea of functional adaptation. During the healing process, the cortex is less loaded compared to the un-fractured situation. At the beginning of the healing process, the leg is less loaded due to pain. After the hard callus has bridged the gap, the load is also transmitted via the hard callus and therefore reducing the strains in the “old” cortex. Despite the less precise fitting, two tendencies were found. The decrease of bone area fraction was higher for rigid fixation than for semi-rigid fixation, which is the same tendency as for the densification of the hard callus. However, higher increase of bone area fraction was found for the lateral side compared to the medial side, which is the opposite trend in the hard callus densification.

Surprisingly, both processes, the increase of  $BA/TA$  of the hard callus and the decrease of  $BA/TA$  in the cortex, were found to follow a linear trend. This is probably only valid for the investigated time period between 2 and 9 weeks. The onset of remodelling between 6 and 9 weeks will eventually lead to a stop of further densification.

### **4.3. Local densification of the hard callus close to cortex**

The area fraction of the newly formed bone  $BA/TA$  was assessed within the same ROI (0.75 mm x 2 mm) adjacent to the periosteum as previously used for the nanoindentation measurements (see also Chapter 3). This region shows early and continuous intramembranous ossification. The increase in  $BA/TA$  is initially stronger and is small between 6 and 9 weeks. The bone area fraction showed a continuous increase starting with about 30% at 2 weeks to about 80% at 9 weeks (Figure I.3, left). The following section aims to answer the question if this densification of the hard callus can be modelled by very basic considerations. These basic considerations allow an estimation of the apposition rate of new bone.

### **Simple model for the local hard callus densification**

The following considerations are driven by the observation that the newly formed hard callus is laid down in at least two steps during fracture healing (Liu et al. 2009b). As first step, a framework or “scaffold” of unorganized woven bone is laid down. Bone forming cells (osteoblasts) sit on this scaffold. In a second step, the holes inside the scaffold are filled by depositing the organized lamellar bone.

Driven by investigating the histological sections, the scaffold of the hard callus was assumed to be either a quadratic lattice with a unit length of  $l_0$  (Figure I.3, right). Additionally, a cubic lattice was applied in order to investigate the influence of assuming a 3D model. The osteoblasts were assumed to cover the whole edges (or surfaces) of the square (or cube) and produce constantly bone and, therefore, producing a moving growth front of new bone with the of the constant velocity  $v$  (2). Accordingly, the bone area fraction development depends on the velocity and the unit scaffold length  $l_0$  according to equations (4) and (5). The doubling length  $l_0$  together with doubling the velocity  $v$  results in the same development of  $BA/TA$ .

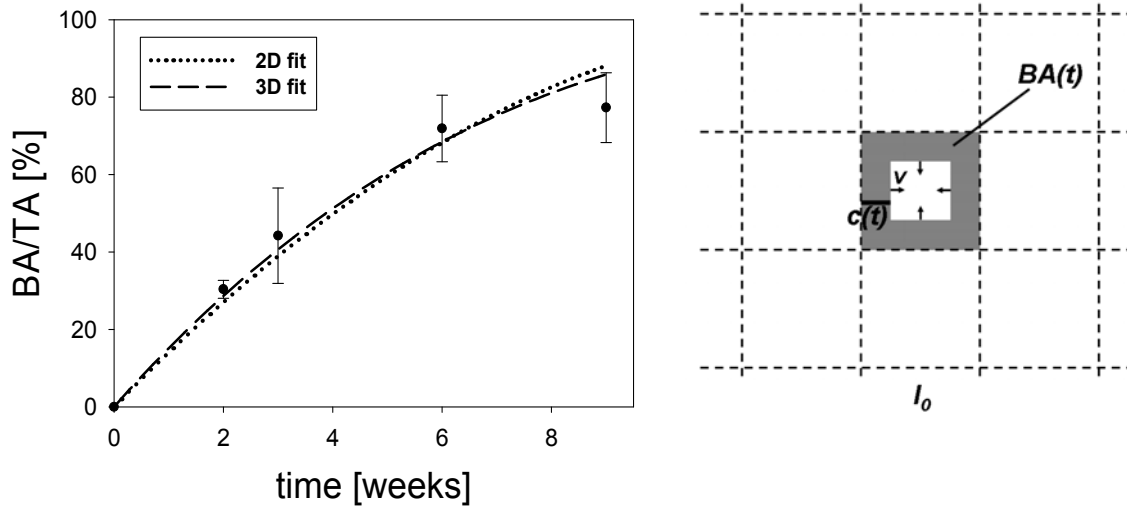


Figure I.3: Bone area fraction ( $BA/TA$ ) close to the periosteum

Densification of the hard callus in terms of the bone area fraction,  $BA/TA$ . Left: Experimental data from a small periosteal region adjacent to the cortex and the fit of this data to a basic theoretical model employing a constant bone apposition rate. Right: The basic lattice model starts with an infinite thin quadratic (or cubic) scaffold (dashed lines), which provides the framework for the cells forming new bone (osteoblasts).  $l_0$  is the unit length of the scaffold,  $A(t)$  is the bone area at time  $t$  and  $c(t)$  is the distance, which the growth front (with the constant velocity  $v$ ) has moved at time  $t$ .

## 2-dimensional calculations

$$c(t) = v \cdot t \quad (2)$$

$$A(t) = A_0 - (l_0 - 2c)^2 = 4l_0vt - 4v^2t^2 \quad (3)$$

$$\frac{BA}{TA}(t) = \frac{A(t)}{A_0} = \frac{4vl_0t - 4v^2t^2}{l_0^2} = 4 \cdot \left(\frac{v}{l_0}\right) \cdot t - 4 \cdot \left(\frac{v}{l_0}\right)^2 \cdot t^2 \quad (4)$$

## 3-dimensional result

$$\frac{BV}{TV}(t) = \frac{V(t)}{V_0} = \frac{6vl_0^2t - 12v^2l_0t^2 + 8v^3t^3}{l_0^3} = 6 \cdot \left(\frac{v}{l_0}\right) \cdot t - 12 \cdot \left(\frac{v}{l_0}\right)^2 \cdot t^2 + 8 \cdot \left(\frac{v}{l_0}\right)^3 \cdot t^3 \quad (5)$$

Two least square fits of with regards to the four experimental mean values were carried out to determine the ratio  $v/l_0$ . The ratio  $v/l_0$  was found to be  $5.16 \cdot 10^{-3} \text{ day}^{-1}$  in 2D (mean error of the fit per data point: 5.9%) and  $3.78 \cdot 10^{-3} \text{ day}^{-1}$  in 3D (mean error of the fit per data point: 4.4%). Both fits could explain the development well. This drives the hypothesis that one main reason for the decrease of the densification with time is the geometrical constriction – with the ongoing densification, the osteoblasts have less amount of surface to work on. The 3D model showed the same tendencies but a better fit of the experimental data and all experimental data points could be better fitted including the time point 9 weeks (error at 9 weeks for 3D: 8.4%; error at 9 weeks for 2D: 10.4%). The fact that the last time point could not be fitted as well as the other time point indicates that either bone formation stopped or bone resorption has started between 6 and 9 weeks. This observation is in agreement with a study on the osteoclastic activity (Schell et al. 2006).

Based on histology, the length of the initial scaffold  $l_0$  was estimated to be 0.5 mm. The according growth velocities or apposition rates were  $2.58 \mu\text{m/day}$  (2D) and  $1.89 \mu\text{m/day}$  (3D) which leads to a estimation of the apposition rate of  $2 \mu\text{m/day}$ . This value is in a reasonable range. It is smaller (about 5 times) than the very fast process of the callus growth itself with an estimated maximal velocity of  $10 \mu\text{m/day}$  (Kuiper et al. 2000). In a clinical study, the mineral apposition rate during normal bone remodelling was measured to be  $0.58 \mu\text{m/day}$  (Eriksen et al. 2002). Accordingly, the bone apposition during bone healing is about 3-4 times faster compared to bone remodelling.

#### 4.4. Stiffening of the hard callus

The experimental data available from two different length scales are now combined to get an estimation of the stiffness of the newly formed bone or hard callus: on the macroscopic scale, the bone area fraction  $BA/TA$  (length scale: 0.5 mm) as described in this chapter and on the microscopic level, the stiffness of the bone material, as previously measured by nanoindentation (Manjubala et al. 2009). The elastic modulus of the bone material,  $E_{mat}$ , characterizes the stiffness of a bone trabecula ( $\sim 170 \mu\text{m}$ ). Due to the incorporation of mineral,  $E_{mat}$  increases in time (Figure I.4, top left).

Applying foam theory, the bulk elastic modulus of the hard callus (on the same length scale as  $BA/TA$  – 0.5 mm) depending on time can be calculated (1). The increase of the elastic modulus is rather small at the beginning of healing due to the power law. Between two and six weeks is a fast increase which slows down after 6 weeks due to the slowing down of densification and further stiffening.



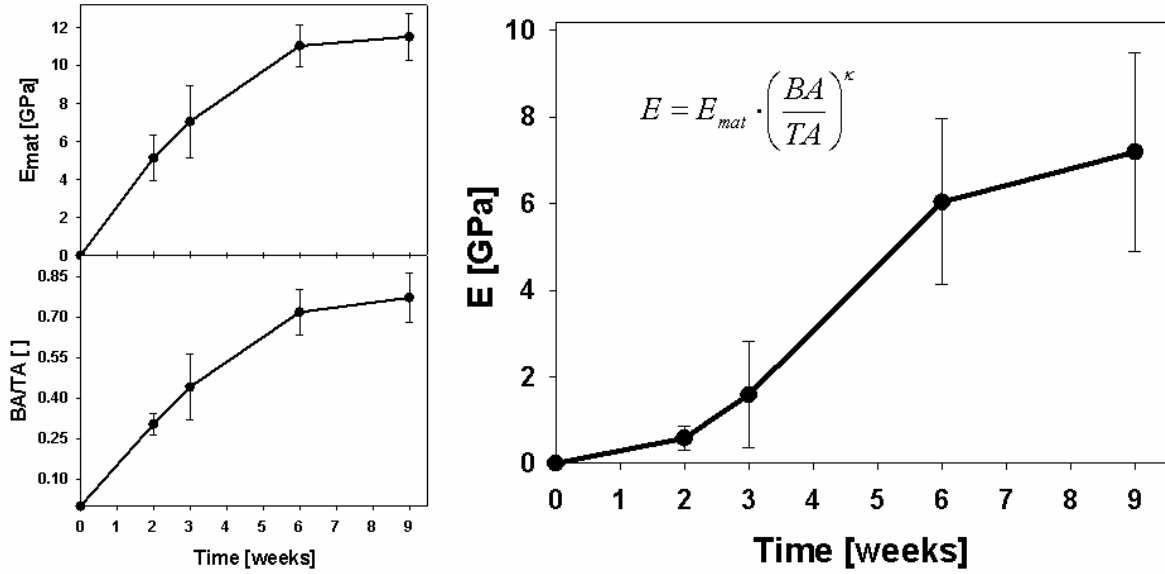


Figure I.4: Development of the hard callus.

The data stemmed from the region adjacent to the periosteum ( $0.75 \times 2$  mm), see also white frame in Figure I.8. Left: The increase of bone area fraction ( $BA/TA$ ) and the increase of the elastic modulus of the bony material  $E_{mat}$  showed strong similarities over time. Right: Resulting bulk elastic modulus  $E$  calculated with the data on the left side employing the Gibson-Ashby equation on porous material (as shown in the figure). The material exponent  $\kappa$  was assumed 1.83 (Morgan et al. 2003).

#### 4.5. Conclusions

The investigated data of the hard callus, the bone area fraction ( $BA/TA$ ) and the hard callus area, suggests that there is a strong mechanical influence on the bone formation process. A linear increase in callus  $BA/TA$  was found and the slope was higher for more rigid fixation. Furthermore, a decrease of about 2.6% per week of the cortical density, assumable due to low loadings in the cortical region, was found.

The local increase in  $BA/TA$  of the hard callus can be explained by a bone growth front produced by osteoblasts. Therefore, the densification process is fast at the beginning and afterwards the densification slows down because the surface, on which the bone lining cells can form bone, becomes smaller with time. Employing a two and a three dimensional model, as well as different sizes of the initial framework, on which the bone lining cells sit, the estimated velocity of the growth front is around  $2 \mu\text{m/day}$ .

Close to the periosteum, the way how the bone area fraction of the hard callus increases was found to be almost identical to the increase of the stiffness of the bone material  $E_{mat}$  (Figure I.4, bottom left). This is remarkable because both

processes, the formation of bone and the stiffening of bone, e.g. by mineralization, work on two different length scales. However, these two processes could be tightly linked to each other. A simple model could possibly explain that link, similar to the densification process explained by geometrical effects.

To summarize, this is the first time quantified data of the time *development* of the bone area fraction of the hard callus was gathered in a study on bone healing in large animals. This was made possible by the large number of animals and the investigation of four different time points. The trends of hard callus area and densification suggest a delayed healing for the sheep treated with a semi-rigid fixator. This suggestion will be further corroborated in the next chapter.

## 5. Calculation of an averaged healing progression

The main aim of this section is to *quantify* the typical topological arrangements of the different tissues during the healing progression. The input data were the obtained tissue masks (Chapter 4.1) from the sheep experiment comprising 64 sheep with a tibial osteotomy treated with two different fixators resulting in two different loading conditions (Schell et al. 2005; Epari et al. 2006a). The output of the novel averaging procedure is a succession of six images, which describes the progression of healing under different loading conditions. These images can be used to validate the results of bone healing simulations which aim to reproduce “normal” ovine bone healing. Previously, such simulations have been quantitatively compared only with global healing parameters that means parameters referring to the whole callus (IFM, stiffness of the callus).

### 5.1. Problems

In order to gain more detailed histological data, sections of the callus are harvested at different sites and different time points post-op. Depending on the harvesting time, these histological sections show an intricate pattern of different tissue types including haematoma, fibrous tissue, cartilage, mineralized cartilage and the newly formed bone. In order to summarise the information of a group of animals, typically only the amount of the various tissue types (area fractions) are reported as quantitative outcome (Claes et al. 1995; Lill et al. 2003; Schell et al. 2005; Bishop et al. 2006). This information is limited for two reasons. Firstly, area fractions are missing important topological information, i.e. they do not provide location and distribution information. The topological information of the tissue type patterns, however, is crucial for a more profound understanding of the healing process. Secondly, individual histological sections have the disadvantage to reflect the healing situations only in single animals. It remains unclear whether they are representative for animal groups and, in addition, data on variability is lacking. Two main problems arise to calculate an averaged healing progression. First, there is the geometrical variability between animals, e.g. different thickness of the cortex. This problem can be solved by rescaling of the histological images. The second problem is the topological variability between the animals and can be solved by classifying the animals into different healing stages with the same topologies. This second problem is discussed more in detail.

The averaging of images of the same healing time is not reasonable as there exist considerable differences in the topology between different sheep at the same healing time point. At three weeks post-op for example, some animals showed strong

formation of cartilage while other animals did not. In addition, the cartilage group also showed a larger hard callus area but with a similar shape as the no-cartilage animals. The assumption is reasonable that some animals heal faster than others but there is no considerable difference in the way of healing (Schell et al. 2005; Epari et al. 2006a). The question then arises is how to average the images of these sheep. For this particular example, one can ask how to average the region where some animals have cartilage and others do not, or in other words, what is an average of fibrous tissue and cartilage? In order to quantify an averaged healing progression, the tissue type maps are not averaged over the same time points (Vetter et al. 2010a). Instead, these tissue type maps are averaged which have similar tissue type patterns. That means the images are classified into different “stages”. However, individual differences lead to a considerable difference in the speed with which the animals advance on the healing path.

### 5.2. Classification into healing stages

Six different successive healing patterns were identified according to the topological criteria summarized in Table 2. All healing patterns were found for all four cases (lateral, medial, rigid, semi-rigid), except for Stage III with rigid fixation on the medial side.

**Table 2: Definition of the criteria of all six observed healing stages.**

**The right column shows their classification in the standard scheme of healing phases to describe the bone healing process, e.g. Sfeir and co-authors (2005).**

Healing stage	Topological criteria	Classification according to healing phases
Stage I	remnants of haematoma still present in the callus	late inflammatory phase
Stage II	remnants of haematoma left, cartilage not yet formed	early reparative phase
Stage III	bridging via cartilage in the outer osteotomy zone, but no bony bridging of the osteotomy gap	reparative phase
Stage IV	formation of a periosteal bony bridge between the proximal and distal parts of the osteotomy callus	late reparative phase
Stage V	formation of an endosteal bony bridge between medial and lateral parts of the osteotomy callus	early remodelling phase
Stage VI	reduced size of the hard callus, resorption of the endosteal bony bridge	remodelling phase

### Estimating the time of the healing stages

The connection of time and healing stages gets lost because the averaging is not carried out at the same time points but at same healing stages (Figure I.5).

However, the time points of sacrifice is known of the sheep which were classified into the same healing stage. This makes a simple estimation of the time for the healing stage possible. The most basic way is to calculate the average time of the animals classified into the same stage. As an example, 2 images of animals sacrificed at 3 weeks and 4 images of animals sacrificed at 6 weeks were classified into the same stage. This results in an estimated time for this stage of 5 weeks  $[(2 \cdot 3 + 4 \cdot 6) / 6 = 5]$ .

The estimated times for the healing stages indicate that Stage II is reached faster under the semi-rigid fixation, both for the lateral and medial side (Figure I.5). However, healing Stage V is reached faster under rigid fixation and more images of animals with rigid fixation fulfil the criteria of the final healing Stage VI. This findings corroborate the previous conclusion that semi-rigid fixation delays the healing. However, the initial healing process seems to be positively stimulated by semi-rigid fixation.

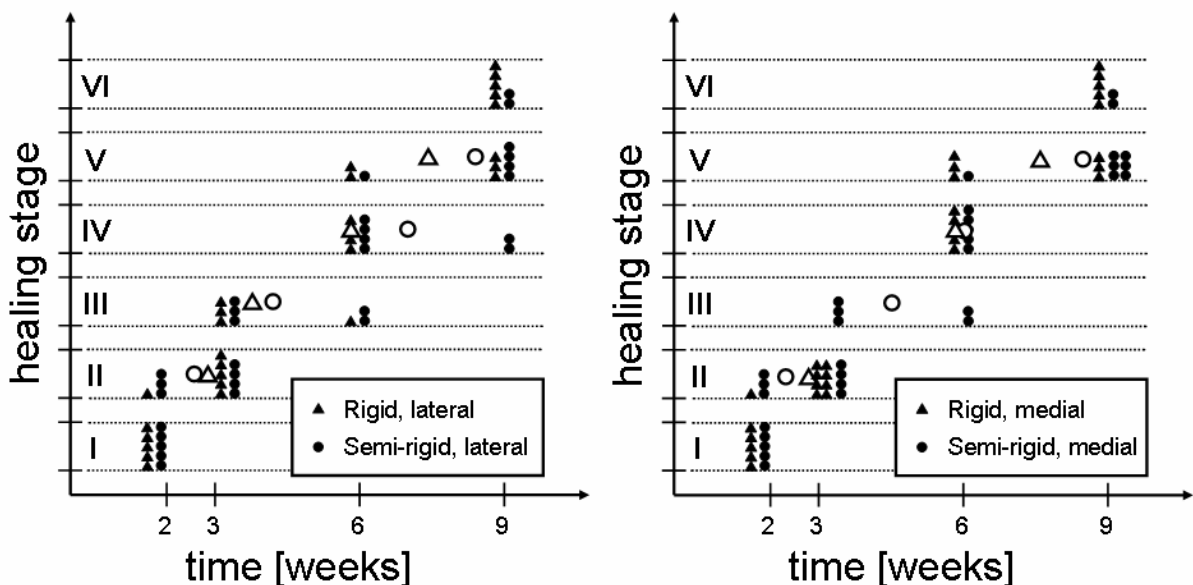


Figure I.5: Classification of the histological images into the six defined healing stages (for the the defined criteria see Table 2).

Each circle or triangle represents one image. Left: results for the lateral side of the callus. Right: results for the medial side of the callus.

### 5.3. Averaging procedure

The spatial information of the different tissue types (tissue masks), see Chapter 3, was used in the averaging method. The method followed nine successive steps and,

as a result, each healing pattern could be described by an averaged tissue type image. The steps are described in the following and a flow chart of the procedure is provided in Figure I.6. The resulting images for the sheep treated with a rigid fixator are found in the next chapter.

### **Step i) Generating of the tissue types maps**

By marking regions of different tissue either by hand based on light microscopy or by using thresholding, discrete information was gathered (e.g. pixel is or is not cartilage) in the form of a binary tissue mask. For each animal, these binary tissue masks were assembled into one tissue type map comprising the whole tissue information (Figure I.6, top). When one pixel was marked in the cartilage mask and the bone mask, the tissue identification by eye using light microscopy (cartilage mask) was preferred to the mask created by thresholding (bone mask). Accordingly, pixels marked as cartilage overwrote pixels marked as bone (Vetter et al. 2010a).

### **Step ii) Identification of the existing tissue type patterns**

The tissue maps were sought for tissue patterns, separately for the medial and lateral side. As described in the previous section, different patterns were identified and the osteotomies with the same pattern were assumed to be in the same “healing stage” based on the tissue pattern.

### **Step iii) Quantifying geometrical information**

The next step is to quantify the information which is assumed to be independent from the healing process. For example, this comprises the cortical thickness  $c.th$  and the bone marrow width  $m.w$ . Furthermore, the fracture gap size  $g$  was measured on the tissue type maps and on X-ray radiographs. Smaller values for the tissue type maps were found, which can be explained by a shrinking of the histological sections during dehydration. The x-ray data showed that the applied fixators, both rigid and semi-rigid, kept the fracture gap size at the initially set osteotomy size of 1.5 mm.

### **Step iv) Defining the averaged target geometry**

The tissue type images show variability due to the data acquisition (e.g. rotation of the histological section) and, additionally, the individual differences of the animals. A desired averaged target geometry (Figure I.6, top right) was defined in order to deal with the geometrical variability. Assuming horizontal axis-symmetry, the geometry consists of a rectangular cortex with the median cortical thickness and a medullary channel with the median bone marrow width as found in Step iii. The target geometry consisted of four sub-target areas, the periosteal area (a), the cortical area (b), the intercortical area (c) and the endosteal area (d). If the actual shape differs from the target geometry considerably, e.g. due to missing parts (see cortex in Figure I.6, top), the transformation into the target geometry can be a complex

problem. The information content was reduced by investigating only bone area fraction on a crude resolution. More precisely, only eight regions of the cortex were distinguished and their  $BA/TA$  values were calculated (Vetter et al. 2010a). Accordingly, the influence of missing parts or pixels was reduced.

#### **Step v) Transformation of the information into the target geometry**

This step transforms the four regions of the tissue image into the according target areas and, in doing so, minimizes the inter-individual geometrical differences which do not depend on the healing process. In the most general case, each of the four sub-regions (a,b,c,d) is transformed into the corresponding region in the averaged geometry (Figure I.6). For the given histological images, the periosteal, intercortical and endosteal region were rotated according to the cortical edges to ensure precise alignment. Afterwards, horizontal scaling for all of the four sub-regions can be carried out. For the given histological images, a common horizontal scaling, according to the cortical thickness, showed good results. Finally, a vertical scaling of the osteotomy region was carried out to transform this region to the gap size of 1.5 mm to match the gap size.

#### **Step vi) Geometrical rescaling within the stages**

A secondary scaling can be necessary due to the fact that, even if grouped into the same stage, the animals show a considerable variability in the size of the callus. After this step, the images have a similar basic geometry and size. For the given histological images, there was only horizontal scaling of the periosteal region (a) carried out according to the median hard callus width of the images of the same stage. The images are now ready to be averaged.

#### **Step vii) Defining and measuring of describing parameters**

The parameters describing each tissue type are defined and measured. The bone area fraction was determined as a scalar field by scanning the images with 50  $\mu\text{m}$  squares, overlapping by 25  $\mu\text{m}$ . The size of one square was chosen so that several trabeculae fit in one square. Furthermore, a threshold of bone area fraction was applied (10%). Haematoma and cartilage regions were described by their centre of area, area and second moment of area  $I$  (6).

$$I_y = \int_A x^2 dA \quad (6)$$

$I_y$	Second moment of area along the vertical axis (y)
$x$	Distance to the vertical axis
$A$	Area

### **Step viii) Averaging of the describing parameters**

In this step, the averaging of the parameters, describing the tissue distribution, is carried out. The median field of the continuous parameter field of the bone area fraction can be calculated directly. The discrete parameters of haematoma and cartilage describe the amount, the shape and the location of the tissue. The shapes of haematoma regions were highly variable but reminded of a circle while the shapes of cartilage regions reminded of an ellipse. The radius of the haematoma region was fit to the median haematoma area. The two elliptic parameters  $r_1$  and  $r_2$  **(7)** were fit to the median values of the cartilage area and moment of area. The averaged haematoma and cartilage regions were located at median of the horizontal centre of mass positions. The vertical centre of mass positions fluctuated around the vertical axis of symmetry. The vertical centres of the haematoma and cartilage region were placed in the vertical axis.

$$A = \pi \cdot r_1 \cdot r_2 \quad (7)$$

A      Area of an ellipse

$r_1$       Major axis of an ellipse

$r_2$       Minor axis on an ellipse

### **Step ix) Assembly of the averaged tissue data**

The final step is the assembly of the averaged data of the previous step. This is carried out in the same way as the tissue maps were assembled in Step i. The result for Stage III is shown in Figure I.6.



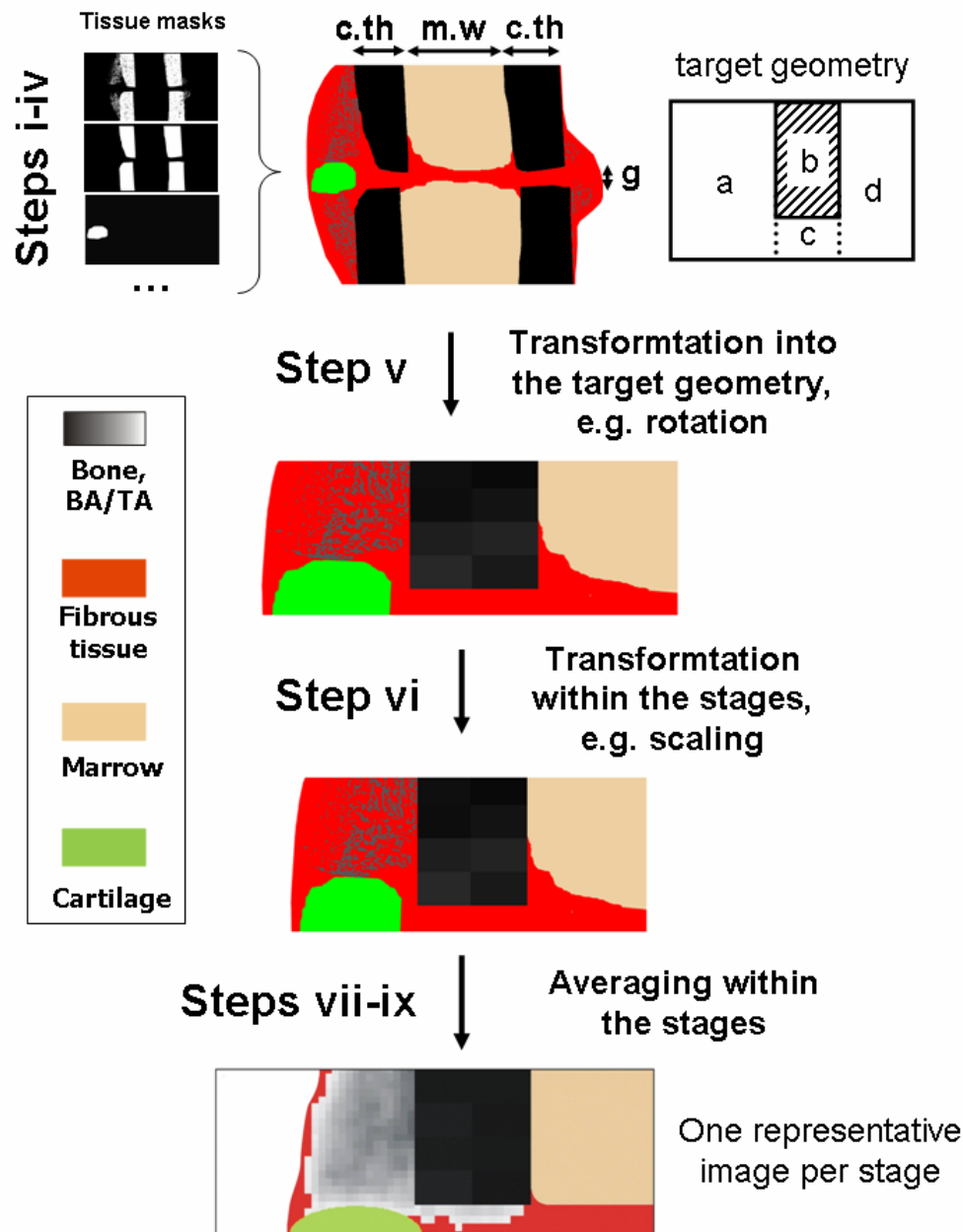


Figure I.6: Flow chart of the nine steps during the averaging procedure.

This flow chart shows the averaging of stage III – all other stages are averaged in the same way. Following abbreviations are used: cortical thickness (*c.th*), marrow width (*m.w*) and fracture gap size (*g*).

#### 5.4. Averaged progression of ovine bone healing

The averaged images were similar for all four cases due to the defined topological criteria. Figure I.7 (left) shows the averaged healing progression for sheep treated with a rigid fixator. Most interestingly, the cartilage region at Stage IV was found to be shifted towards the fracture gap compared to Stage III. The average procedure also provides information on the spatial variation of the bone area fraction *BA/TA*. The standard variation of the *BA/TA* shows, that in particular the edges of the hard

## 5. Calculation of an averaged healing progression

callus differ from animal to animal (Figure I.7, right). The shape of the hard callus differed from sheep to sheep even if classified into the same healing stage.

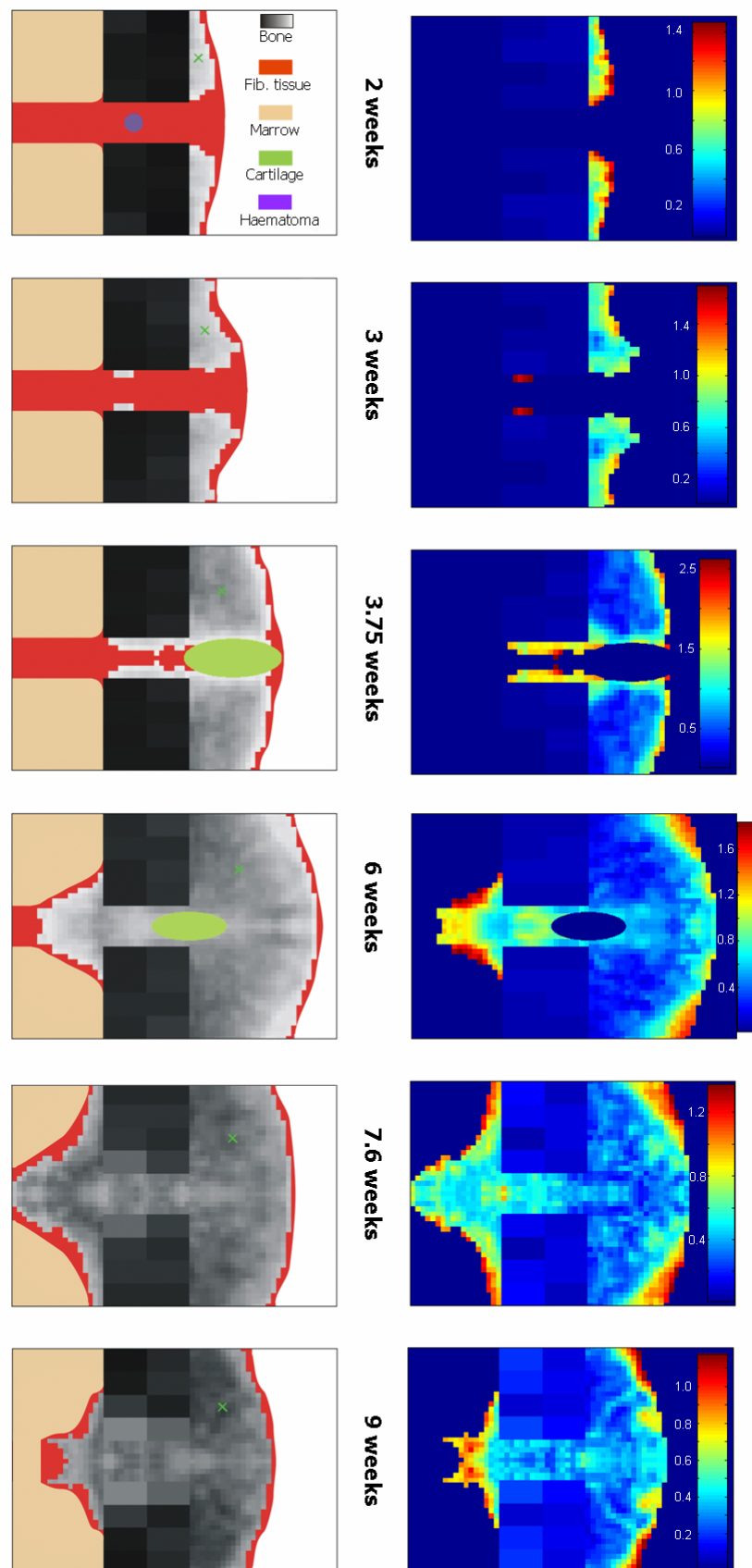


Figure I.7: Images of the averaged spatial tissue information at different healing stages.

Left: averaged progression of the healing, the green x marks the centre of mass for the periosteal hard callus. Right: standard deviations for the bone area fraction ( $BA/TA$ ) of the hard callus.

### 5.5. Average growth of hard callus

With the images of the six successive healing patterns, information is also provided to describe the average growth of the hard callus. Therefore, the edges of the hard callus at each stage are marked manually (Figure I.8, left). The age of the edges is known and the region between two edges is interpolated (Figure I.8, right). This map shows the age of the hard callus pixels at Stage V, therefore at a time point of around 7.8 weeks (rigid fixation, lateral side). The youngest bone is found in the endosteal region because the horizontal bridging of the marrow cavity just occurred. At the periosteal side, the dashed black line indicates the region of hard callus which has been resorbed between Stage VI and V. The dotted line indicates the edge of the further resorbed hard callus at Stage VI. This information is useful for a rough estimation of the age of the local hard callus. With the assumption that the measured stiffening of the bone trabeculae depends only on the time and that the local stiffening process adjacent to the cortex is universal, one can estimate the local material stiffness of the hard callus. This information will be applied in Chapter 6 to calculate more accurately the mechanical strains within the callus.

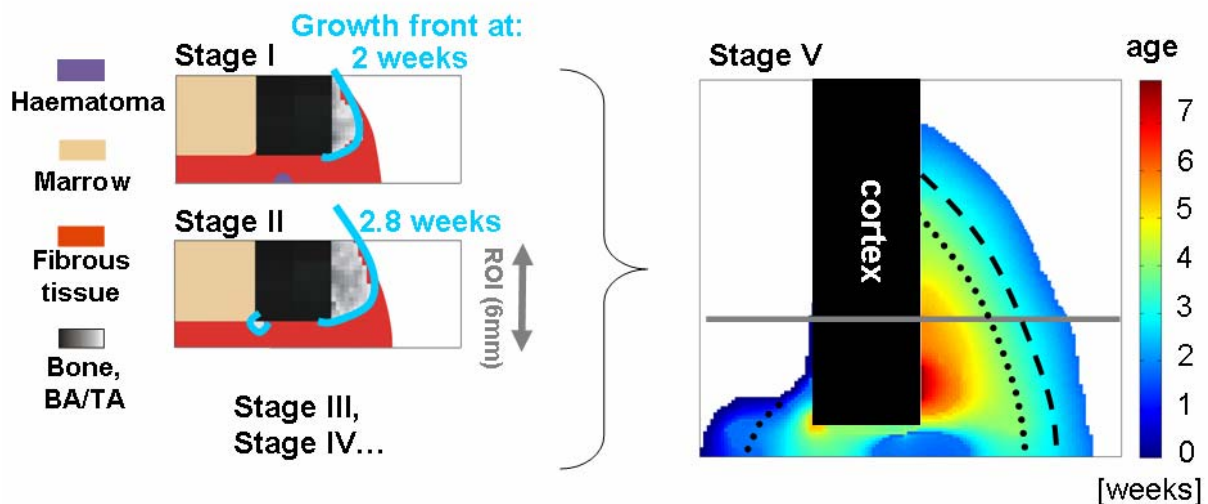


Figure I.8: Estimation of the hard callus growth, rigid fixation, lateral side.

Left: Marking the edges of the hard callus (growth front) at different healing stages. Right: Generating a smoothed growth map of the hard callus based on the marked edges. The map shows the age of the hard callus at Stage V (circa 7.8 weeks). The dashed line indicates the resorped area of the hard callus between Stage IV and Stage V, the dotted line indicates the resorped area between Stage V and Stage VI (resorption starts from the outer edges of the hard callus).

### 5.6. Conclusions

The information of the tissue images describing an averaged healing progression will be used as input data for mechanobiological modelling of bone healing and the validation of the according computer simulations. First, static mechanical simulations will be carried out to estimate the mechanical strains within the callus at the six healing stages (Chapter 6). Secondly, dynamic simulations try to reproduce the full time course of normal bone healing (Chapter 7). A clear advantage of this averaging procedure is that it provides quantitative data on the tissue distributions. A further advantage is that it provides six images instead of four (according the four investigated time points). Instead of “blurring” of the healing progression by a restricted averaging according to the healing time, more and “de-blurred” data is available which can be compared with the simulation results.

The prerequisite for this averaging method is quantified tissue data. Therefore, information of the healing progression of each animal has been localized and converted into spatial tissue data. The tissue information was either binary, as in the case of haematoma or cartilage, or continuous in the case of bone area fraction. The core of this averaging procedure is to get rid of the restriction of averaging parameters at the same time points. Instead of the classification of the animals into the same time points, the animals were classified according to their topological appearance. The applied averaging method quantifies and condenses the information. First of all, this allows the definition of a normal healing progression. This again makes it easier to detect non-normal healing progression or even a singular healing pattern which was not observed in the normal healing. This is explicitly important for studies with a small number of animals where the definition of normal healing is not possible. The condensation of the data makes it possible to distribute the data for comparison with other studies.

As a direct benefit, this procedure indicates that healing process in the animals with the semi-rigid fixation is delayed compared to the rigid fixation. This conclusion is in agreement with previous histological analysis (Schell et al. 2005; Epari et al. 2006a). Also from the histograms of the nanoindentation moduli there is further evidence of similar but delayed healing under semi-rigid fixation compared to rigid fixation (Liu et al. 2009a). However, the classification of the images into the stages suggests that the semi-rigid fixation triggers the healing in the early phase more efficiently compared to the rigid fixation. This conclusion is in agreement with the conclusions drawn from investigating the hard callus area and density (Chapter 4). The same influence of early stimulation of the osteotomy has been found for a sheep model

with a dynamic fixator (Goodship et al. 1998). This study induced larger micromotion during the early phase of healing and smaller micromotion at the later phase.

A sheep study on two rigid fixators, which resulted in the early healing phase in different initial IFM but similar mechanical environment afterwards, showed that the initial stability influenced the amount of hard callus formation (Klein et al. 2003). However, only histomorphometric data at nine weeks post-op is available. It was speculated, that the formation of blood vessels in the initial healing period depends strongly on the mechanical environment (Lienau et al. 2005). As blood supply is essential for bone formation, this could explain to a large degree the differences in tissue formation due to initial stability. A recent study indicates that blood vessel formation starts at the same time but the blood vessel formation regulated by gene expression depends on the mechanical stability (Lienau et al. 2009).

It has to be pointed out, that the high number of animals resulting in information at several time points was the prerequisite for these conclusions in combination with application of several investigation techniques. A smaller number of animal studies, but with more sheep, is therefore desirable for more profound conclusions.

The described averaging method is not the only way to condense and quantify histological data. Variations of this method would result in similar but slightly different images. Future studies could use specialized measurements for localizing particular tissue types. A clear limitation of this study is the constriction to 2D. A rat study showed major changes of tissue type distribution depending on the longitudinal cut through the osteotomy (Gerstenfeld et al. 2006). Therefore, a combination of  $\mu$ CT data and histological investigations based on serial sectioning could provide the basis for defining the normal healing progression in small animals. The condensed information of different studies could be saved in a data base providing the essential information of normal healing in different animals in a first step, and depending on different influences in a second step.

## II. Static bone healing simulations

The in-depth evaluation of the sheep experiment (Chapters 3-5) results in a *quantitative* description of a normal bone healing *progression*. The prerequisite for this description was the availability of data from several time points of the healing progression. The new experimental data provides *quantitative* information in terms of development of the callus geometry, the tissue arrangements with the callus and the stiffening of the bone material. With these new structural data, it is now possible to set up a more precise mechanical description of the process of bone healing compared to previous mechanical models. In our improved model, the development of the heterogeneous hard callus is included. Using this data as input for Finite Element computations, the local strains within the callus due to normal walking at the six healing stages were calculated (described in Chapter 5).

The calculated strains within the callus were tested for their capability to predict tissue differentiation (as it has been carried out by other groups on idealized models of the callus). In this sense, the following calculations can be considered as “static simulations” of bone healing, while Chapter 7 describes “dynamic simulations” of the progression of bone healing. The most basic mechanobiological concept or theory was chosen for the interpretation of these “static simulations”, following the idea of reducing the complexity of the demanded model on bone healing. Therefore, the interfragmentary strain theory of Perren and Cordey (1980) was applied on a local level using one mechanical signal for tissue differentiation. The results showed the potential of applying only one invariant of the strain tensor as mechanical stimulus responsible for the tissue differentiation, especially on the periosteal and intercortical region.

The influence of the mechanical heterogeneity of the hard callus on the strain distribution was investigated. To do so, additional hypothetical FE models assuming a homogeneously stiff hard callus were calculated and compared with the heterogeneous results. The mechanical heterogeneity of the hard callus increased considerably the strains within the osteotomy gap. The FE results indicate that the heterogeneity influences the way endochondral ossification occurs. The stiffening of the hard callus could be an essential factor for the shifting of the cartilage region inwards to the osteotomy gap during healing, similar to what is reported from animal experiments.

## 6. The heterogeneity of the hard callus - mechanical implications

With the available nanoindentation data of the bone material describing the increase of its elastic modulus,  $E_{mat}$ , over time (Manjubala et al. 2009) and the spatial tissue information of the averaged healing progression (Chapter 5), it is possible to characterize the mechanical heterogeneity of the hard callus. The combination of these two data results in an improved mechanical description of the callus during a normal bone healing process represented by six healing stages (Chapter 5).

### 6.1. Mechanical heterogeneity of the hard callus

From the mechanical viewpoint, the process of hard callus development consists of three important sub-processes on three different length scales. From the largest to the smallest length scale, these processes are: (i) hard callus growth, (ii) densification of the existing hard callus by thickening of existing bone struts (trabeculae) and formation of new struts and (iii) stiffening of the existing bone material (Figure II.1). The first two processes were quantified for a normal healing progression in the previous chapter and the stiffening was characterized by nanoindentation (Manjubala et al. 2009), see also Chapter 3.

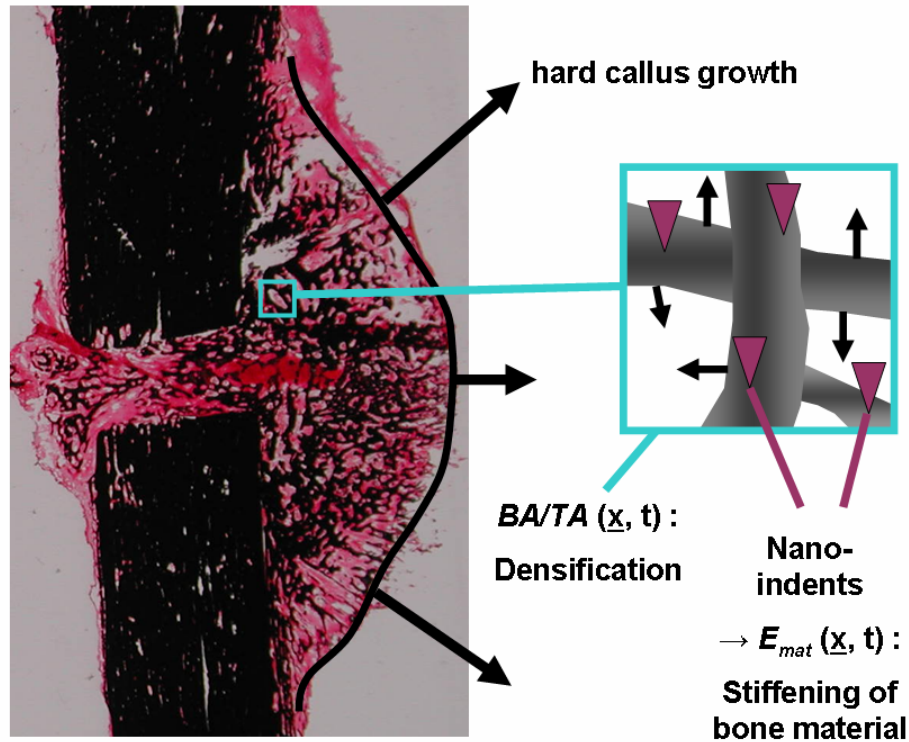


Figure II.1: Processes influencing the stiffness of the hard callus.

Three processes influencing the stiffness of the hard callus at three different length scales: hard callus growth (denoted by black arrows in the left image), densification (black arrows in the inset) and material stiffening. Hard callus growth and bone area fraction ( $BA/TA$ ) can be

## 6. The heterogeneity of the hard callus

---

quantified by histological analysis and the elastic modulus of the bone material ( $E_{mat}$ ) by nanoindentation (indicated by the purple triangles in the inset) (Manjubala et al. 2009).

The hard callus was described as a porous structure according to the Gibson-Ashby formula **(8)**, depending both on the location  $x$  in the callus and the time  $t$ . A time dependent stiffening of the bone material ( $E_{mat}$ ) was assumed as measured previously (Figure I.4) and the local value of  $E_{mat}$  was estimated by knowing the age, or  $t$ , of the local hard callus element (Figure I.8). The bone area fraction ( $BA/TA$ ) data was extracted spatially and temporally from the averaged healing progression. The cortex, which increases its porosity during healing, was described in the same way except assuming a constant value for  $E_{mat}$  of 20 GPa (Claes and Heigele 1999).

$$E(\vec{x}, t) = E_{mat}(t(\vec{x})) \cdot \left( \frac{BA}{TA}(\vec{x}, t) \right)^\kappa \quad (8)$$

E	Bulk elastic modulus of the hard callus
$E_{mat}$	Elastic modulus of the bone material
BA/TA	Bone area fraction

In order to calculate the strains by means of FEM, the whole callus was mechanically modelled in terms of linear elasticity. All tissues were described as isotropic materials, therefore characterized by an elastic modulus and a Poisson ratio. The regions of fibrous tissue, marrow and cartilage were assigned to the corresponding values derived from literature (see also next chapter, Table 3). As an example of an input for the FE-Model, Figure II.2 shows the map of the calculated elastic modulus at stage III (left). In contrast, the map on the right of Fig. 6.2 assumes a homogenous elastic modulus. For this case, the value of the elastic modulus is assumed equal to the averaged elastic modulus of the heterogeneous hard callus.



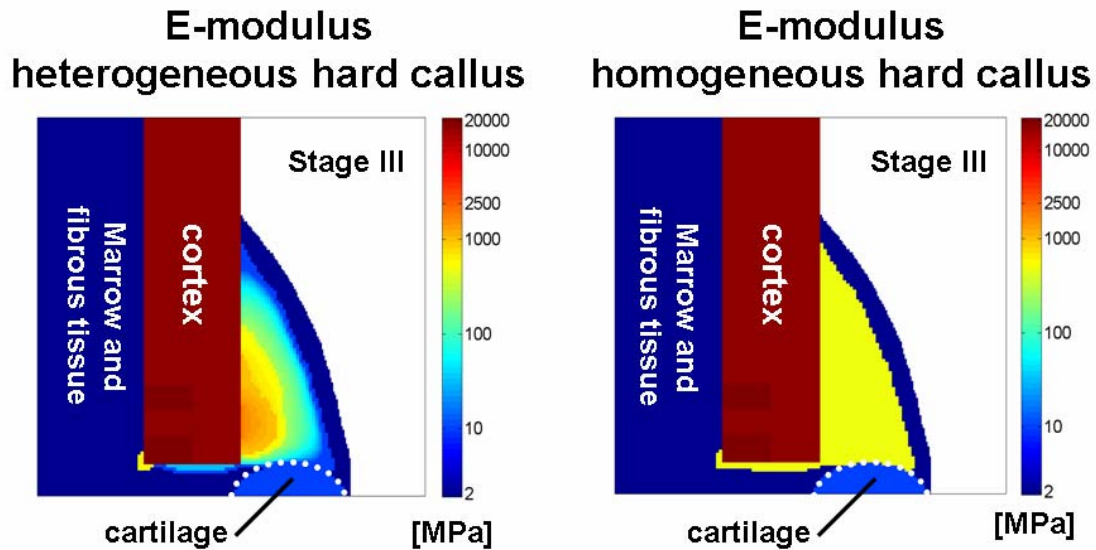


Figure II.2: Maps of the elastic modulus of the callus (Stage III, rigid fixation, lateral side).

Left: The heterogeneity of the cortex and hard callus was considered. Cortex and hard callus are modelled as porous structure according to Gibson and Ashby (8). Cartilage was assigned an elastic modulus of 10 MPa (Schaffler and Burr 1988), fibrous tissue and bone marrow an elastic modulus of 2 MPa (Hori and Lewis 1982; Isaksson et al. 2006). Right: In contrast, the hard callus assumed as a homogeneous material (the assigned elastic modulus was the mean value of the elastic moduli of the hard callus – see left image).

The mean values of elastic modulus of the hard callus showed an exponential increase over time (Figure II.3). In a semi-logarithmic plot, the data could be well fitted by a straight line. The cortical stiffness was reduced over time due to the reduction of  $BA/TA$  with ongoing healing. Compared to the cortex, the variability of the elastic modulus was naturally much higher in the hard callus, especially at Stage IV. Deduced from the variability at Stage V and Stage VI, the hard callus becomes less heterogeneous to the end of the healing progression. The elements of the hard callus reach a similar density and stiffness while the variability of the cortical stiffness increases.

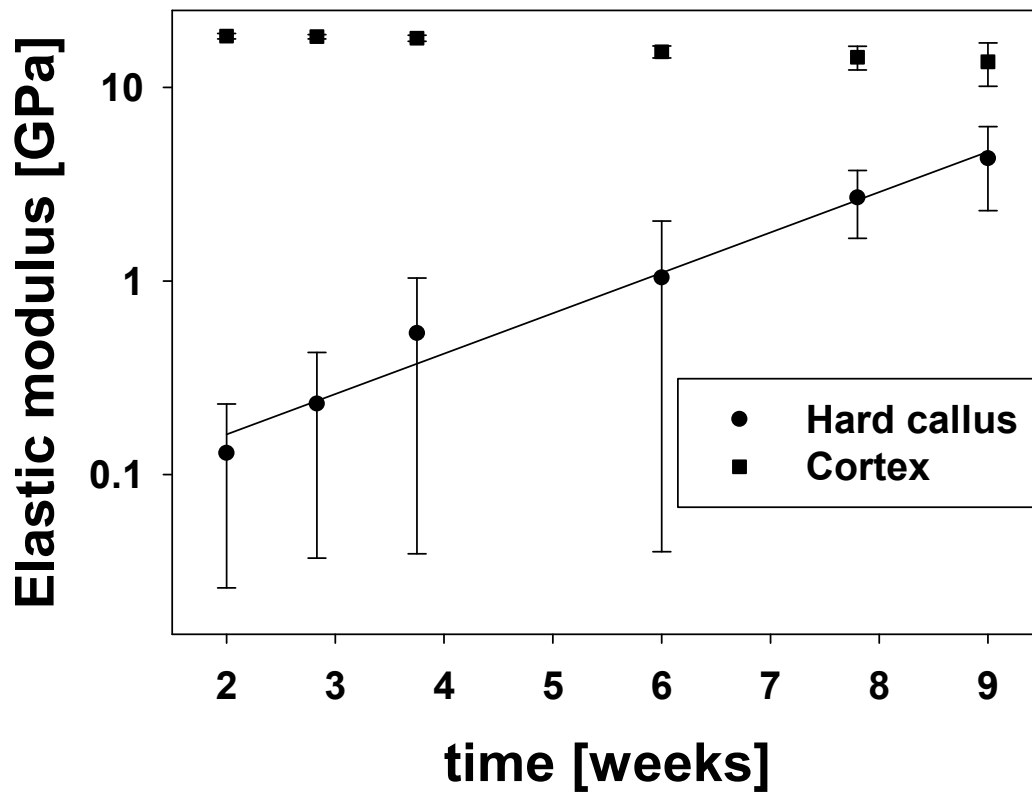


Figure II.3: Semi-logarithmic plot of the mean value of the elastic modulus of the cortex and the hard callus.

The increase in the elastic modulus for the hard callus could be well linearly fitted ( $r^2$ : 0.98, slope: 0.21).

## 6.2. Finite element simulations

The mechanical problem, described by four equations (9) – (12) has to be solved to calculate the local strains within the callus. The geometrical relation between strain and spatial displacement of material is known by assuming infinitesimal strains (9). Additionally, there were no sources of stresses within the investigated callus (10). At the geometric boundaries of the callus, either the displacement or the force were known (11). Linear elastic behaviour (12) of the tissues was assumed for this model. Furthermore, isotropic behaviour was assumed which reduces the non-zero entries within the stiffness tensor  $C$  to two. The two entries are the elastic modulus  $E$  and Poisson ratio  $\nu$ , which are known parameters. The displacement  $u$ , strain  $\varepsilon$  and stress  $\tau$  remain as unknown parameters.

$$\varepsilon_{ij} = \frac{1}{2} \left( \frac{\partial u_i}{\partial x_j} + \frac{\partial u_j}{\partial x_i} \right) \quad \text{Infinitesimal strain} \quad (9)$$

$$\vec{\nabla} \cdot \underline{\underline{\tau}} = \underline{\underline{0}} \quad \text{Mechanical equilibrium} \quad (10)$$

$$\underline{u}_b \text{ or } \underline{F}_b = \underline{\underline{\tau}}_b \cdot \underline{n}_b \quad \text{Boundary conditions} \quad (11)$$

$$\underline{\underline{\tau}}(\vec{x}) = \underline{\underline{C}}(\vec{x}) \cdot \underline{\underline{\varepsilon}}(\vec{x}) \quad \text{Material law} \quad (12)$$

$\varepsilon$	Strain	$x$	Spatial coordinate
$\tau$	Stress	$F$	Force
$C$	Stiffness tensor	$\underline{n}$	Normal vector
$u$	Displacement		

### FE models

A commercial FE solver (ABAQUS v6.6, Hibbit Karlsson & Sorensen, Inc., RI, USA) was used in order to solve the mechanical equations (9) – (12). The details on the FE modelling can be found in the section Material and Methods of the according manuscript (Vetter et al. 2010b), which is found in the appendix. For each of the six healing stages, three models were implemented to study the influence of the mechanical heterogeneity of the hard callus and the softening of the cortex. The first model was the heterogeneous (“normal”) model with the heterogonous mechanical data. Additionally, two *hypothetical* cases for each stage were modelled as references: i) assuming a homogeneous hard callus and ii) assuming a homogeneous cortex. In the case of a homogeneous hard callus (as an example see Figure II.2), the elastic modulus of each hard callus element was set to the corresponding mean value of the hard callus (Figure II.3). In the homogeneous cortex, the elastic modulus of each element in the cortex was set to the corresponding cortical mean value. Other tissue types than hard callus develop during the healing too. Due to the lack of specific material data, the other tissues were described by standard, time-independent literature values for linear elastic behaviour (Table 3).

**Table 3: Elastic modulus of the tissue material  $E_{mat}$ , Poisson ratio  $\nu$  and empirical exponent  $\kappa$ , see (1), of the different tissues within the callus.**

[a] Hori and Lewis (1982), b) Isaksson et al. (2006), c) Schaffler and Burr (1988), d) Claes and Heigele (1999), e) Morgan et al. (2003), f) Manjubala et al. (2009)]

Material	$E_{mat}$	$\nu$	$\kappa$
Fibrous tissue, marrow	2 MPa <sup>(a,b)</sup>	0.167 <sup>(b)</sup>	--
Cartilage	10 MPa <sup>(c)</sup>	0.167 <sup>(b)</sup>	--
Hard callus	$E_{mat}(\hat{t})$ <sup>(f)</sup> – (Figure I.4)	0.3 <sup>(d)</sup>	1.83 <sup>(e)</sup>
Cortex	20 GPa <sup>(d)</sup>	0.3 <sup>(d)</sup>	1.83 <sup>(e)</sup>

### Results

The calculated stress and strain tensors were reduced to a scalar quantity for further investigations. One investigated invariant was the strain energy density (13) which is the product of strain and stress vector and describes the energy uptake of a material during deformation. This value is often used as failure criteria. The second investigated invariant was the maximum of absolute values of the principle strains (14). This value takes only the volume change of an element into account. The third invariant was the maximal shear strain (15). This value describes the shape deformation of an element. The results for the two investigated strain invariants were qualitatively the same.

$$SED = \frac{1}{3} \cdot \varepsilon_i \cdot \sigma_i \quad (13)$$

$$\varepsilon_{mpr} = \max(|\varepsilon_1|, |\varepsilon_2|) \quad (14)$$

$$\gamma_{\max} = \sqrt{(\varepsilon_x - \varepsilon_y)^2 + \gamma_{xy}^2} \quad (15)$$

$SED$	Strain energy density	$\varepsilon_x$	Strain in horizontal direction
$\gamma_{max}$	Maximal shear strain	$\varepsilon_y$	Strain in vertical direction
$\varepsilon_1$	Principle strain 1	$\gamma_{xy}$	Shear strain
$\varepsilon_2$	Principle strain 2		

As an example, the maximal shear strains of the three FE models at stage III are shown in Figure II.4 - a figure with all stages can be found in the attached second manuscript in the appendix (Vetter et al. 2010b, Figure 3). The left image shows the calculated maximal shear strains and indicates a strain in the fracture gap of around 22%. The middle image shows the difference of the strains calculated by the heterogeneous model and the strains calculated by the model assuming a homogeneous hard callus. This comparison shows that the mechanical heterogeneity of the hard callus influences strongly the strains within the cartilage region at this stage of healing. The cartilage close to the gap is higher deformed in the heterogeneous case (strains there are lower about 2.5% - 5%) while the outer part of the cartilage region is less deformed (strains there are higher about 2% - 4%). From a mechanobiological viewpoint, this means that an ossification of the cartilage is more likely to occur at the outer fringe of the cartilage and this tendency is intensified by the heterogeneity of the hard callus. One can speculate that the hard callus heterogeneity is one main factor in the experimentally observed shift of the cartilage towards the fracture gap during the bone healing progression. The same type of comparison was carried out for the FE models assuming a homogeneous

cortex (Figure II.4, right). At stage III, the influence of the mechanical heterogeneity of the cortex is less pronounced than the influence of the hard callus heterogeneity (note the different orders of magnitude in Figure II.4).

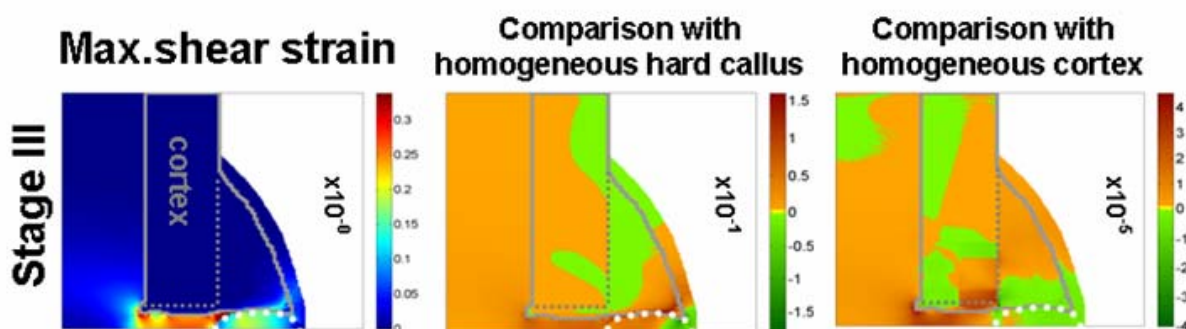


Figure II.4: Spatial distributions of the maximal shear strain (left) and comparison between the heterogeneous case and the two homogeneous cases as reference.

Left: maximal shear strains calculated for stage III during bone healing considering the heterogeneity of the stiffness of the hard callus and cortex. Middle: strain differences of the heterogeneous case and a hypothetical homogeneous hard callus. Right: strain differences of the heterogeneous case and a hypothetical homogeneous cortex. In the comparison between heterogeneous and homogeneous cases, areas with reddish colours indicate higher strains in the heterogeneous case while greenish colours indicate higher strains in the homogeneous case. Grey lines indicate the boundaries of the cortex and the hard callus. The region of cartilage is marked with a white dotted line. The orders of magnitude of the displayed values are provided on the right of each image. All values are given in dimensionless units of strain. To transform to  $\mu$ strain values, the given values have to be multiplied with  $10^6$ .

In the following chapters 6.3 to 6.6 additional data and interpretation of the data concerning the heterogeneity of the hard callus is presented, which is not part of the manuscript (Vetter et al. 2010b). First, the strain distributions calculated with the heterogeneous FE-models are investigated and in Chapter 6.6 the comparison with the homogeneous FE-models is summarized.

### 6.3. Strains within the hard callus

Stage IV was chosen to show the correlation between local strain and stiffness of the element. Stage IV exhibits the biggest size of hard callus of all six healing stages and also the most heterogeneous data. Additionally, no resorption has been observed at Stage IV yet. Figure II.5 shows the local strain within a hard callus element plotted against its local elastic modulus. Except for outliers in the low elastic modulus region, a clear correlation between strain and elastic modulus can be found.

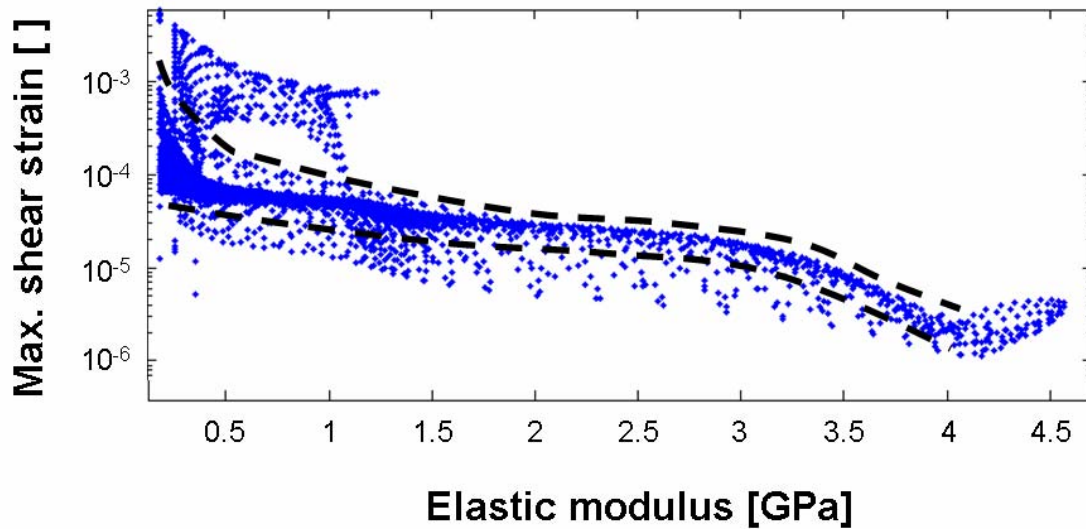


**Figure II.5: Local maximal shear strain plotted over the local elastic modulus of the hard callus elements at stage IV.**

**Stage IV shows the biggest hard callus area and no evidence of resorption of bone.**

### **6.4. Strains within the fracture gap**

Following the reasoning of Perren (Perren 1979), the interfragmentary strains (IFS), i.e. the strains within the fracture gap, were investigated to describe the progress of healing (Figure II.6). The IFS started from around 20% at week 2 and decreased over time to about less than 0.1% at week 9. No decrease was found between 2 and 3.75 weeks due to two reasons. Firstly, the IFM at these times were held constant at the experimentally measured value of 0.5 mm (Schell et al. 2008), although the measurement of IFM is challenging and accordingly the error bars are large. Applying a constant displacement of 0.5 mm corresponds to an increase in load since the overall stiffness of the callus also increases. Secondly, the maturation of soft tissue was not modelled due to the lack of experimental data. In real fractures, the tissue in the fracture gap matures from granulation tissue to fibrous connective tissue and increases its elastic modulus. This, in return, would decrease the IFS (as indicated *qualitatively* by the dotted line, Figure II.6).

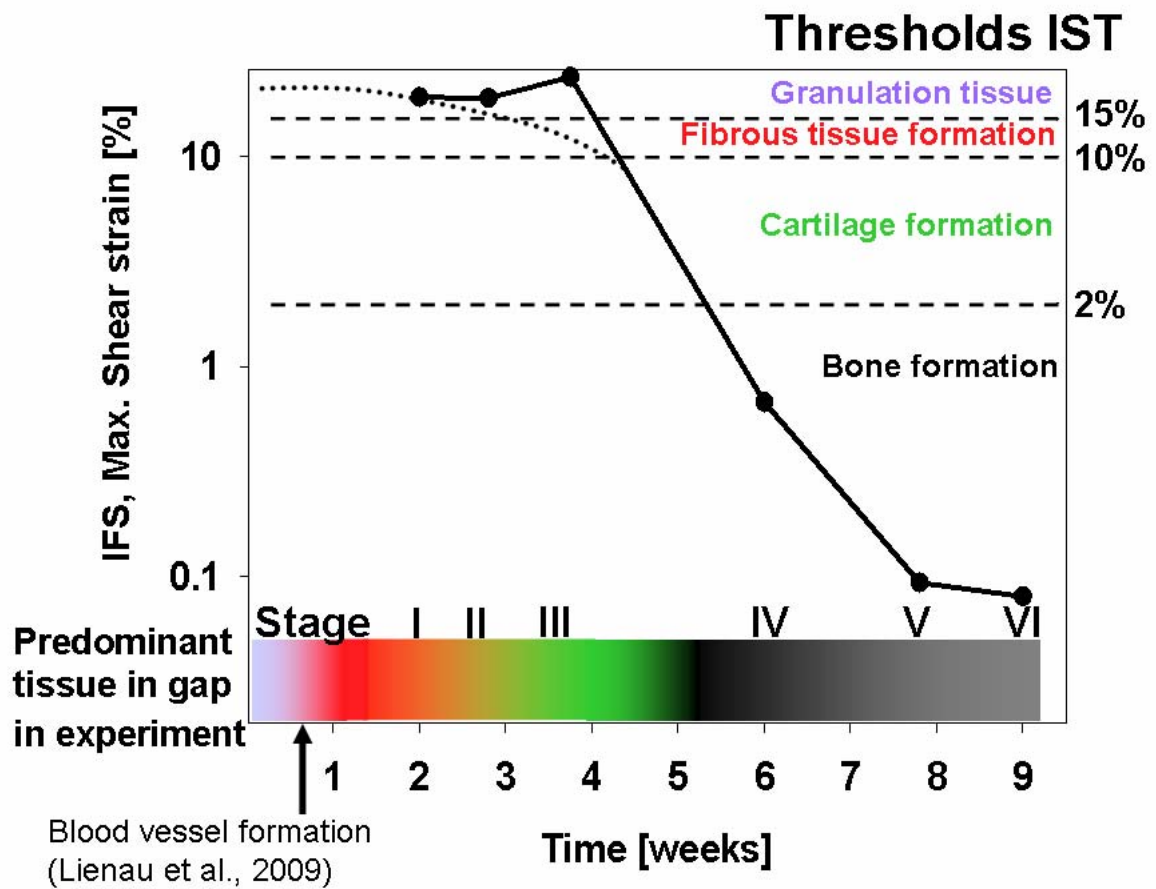


Figure II.6: Calculated IFS during normal bone healing based on FEM

Calculated IFS during normal bone healing based on FEM considering the mechanical heterogeneity of the hard callus. The estimated decrease during the early healing phase is denoted as a dotted line (see text for an explanation). Right side: the prediction of tissue formation according to the interfragmentary strain theory (IST) of Perren and Cordey (1980). The bar on the bottom describes the predominant tissue type in the osteotomy gap for the normal bone healing in sheep (Vetter et al. 2010a). The colours within the bar follow the colour coding of the formation of tissue according to the IST at the right side of the plot.

The development of the IFS shows the typical trend in normal fracture healing. With the measured initial IFM of 0.5 mm, the initial strains are 20% for a 3 mm osteotomy gap. This value is in the range of the desirable initial strains in order to stimulate bone healing. The following comments regard the interfragmentary strain theory of Perren, abbreviated with IST.

The maturation of granulation tissue is not predicted by IST for the initial three stages and, therefore, no formation of fibrous tissue or even cartilage could occur (see strain thresholds on the right side of Figure II.6). The formation of cartilage in the osteotomy gap occurs too early compared to IST, whereas the formation of bone occurred around an IFS of 2%. These predictions of tissue maturation could be due to the basic modelling of fibrous tissue and cartilage (with fixed "mean" elastic

moduli). Explicitly, the maturation of fibrous tissue would lead to lower IFS, and the formation of cartilage could perhaps be predicted by IST at the estimated time.

However, testing the IST beyond a qualitatively comparison faces a severe difficulty: to define precise time ranges when the formation of which tissue was predominant in the osteotomy gap region. As one clear result, the threshold for the formation of fibrous tissue (15%) was found to be too low in IST. Besides these limitations, the IFS showed its potential for explaining the tissue differentiation within the gap for *normal* healing. This fuels the idea of applying IST not only to the fracture gap, but also to the callus as a whole. As a first step, this is carried out “statically” for the six healing stages (see next chapter).

### **6.5. A “local interfragmentary strain theory”**

The aim of this section is to interpret the six calculated strain maps in order to investigate if there is a mechanical signal, which locally predicts the tissue differentiation between two stages. This should be obtained using a single mechanical stimulus leading to a one dimensional tissue differentiating diagram (Figure II.7, bottom). Such a diagram is defined by three different threshold values for the formation of cartilage, for the formation of bone and for the resorption of bone. The following speculative observations should serve as a guideline for the mechanobiological control of tissue differentiation (Chapter 7).

Three mechanical stimuli were tested to predict tissue type differentiation as observed in the averaged healing progression (Chapter 5): the strain energy density (SED), the maximum of the absolute values of the principle strains and the maximal shear strain (13) – (15). The thresholds of the mechanical stimuli were varied and the best tissue prediction map was found manually for each of the three investigated stimuli. In particular, the aim was to predict the formation of hard callus and cartilage. The two strain invariants were found to show better predictions of the tissue differentiation than assuming the strain energy density as mechanical stimulus. The periosteal cartilage formation could less well be predicted with the SED as stimulus. Similar patterns of tissue type differentiation could be reached by scaling the thresholds for the shear strain and the principle strain. The strain energy could be less well scaled to reach a similar differentiation pattern because the strain energy shows different patterns.



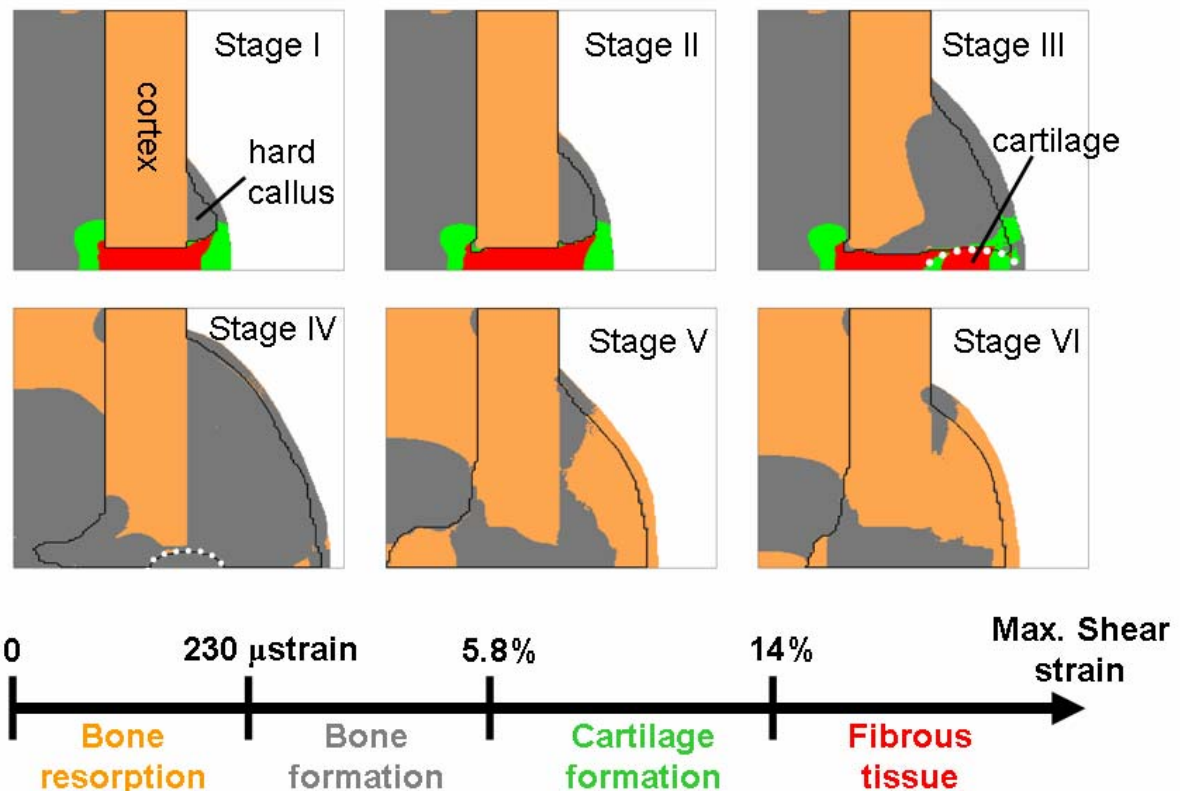


**Figure II.7: Dynamical interpretation of the mechanical stimulus to forecast tissue differentiation.**

The maximal shear strain was assumed as mechanical stimulus.

The threshold values, explaining the experimentally observed tissue differentiation the best, were similar for both strain types. The tissue differentiation could be explained on the periosteal side and also intercortically (Figure II.7). On the endosteal side, the model would predict cartilage formation at the early stages of healing, which is not consistent with experimental data. Biology could be an explanation for the “delayed” endosteal reaction to the local low mechanical stimulus. Some authors even conclude that bone healing in the endosteal region is biology-driven (McKibbin 1978). However, the cells feel the local strains independently on their actual site. Therefore, mechanobiological rules should be valid independently if the cells are in the periosteal or endosteal region. Possible explanations for the endosteal behaviour could be: (biological) inhibitors at the early stages in the endosteal region, or less or delayed migration of mesenchymal stem cells into the osteotomy site from the bone marrow.

### **6.6. Influence of the hard callus heterogeneity on the strains**

After calculation of the heterogeneous FE models for each of the six stages, hypothetical cases were calculated. In the first set of six hypothetical cases, the hard callus at each stage was modelled as homogeneous by assigning the according mean elastic modulus to each element of the hard callus (Figure II.3). Following the same principle, a homogeneous cortex was assumed in the second set of hypothetical cases according to the mean elastic modulus of the cortical region at each stage. Afterwards, comparison of the strain distributions was carried out by calculating the differences of the strain distribution in the heterogeneous case and the strain distribution of the homogeneous case. In total, 12 images of strain differences were available for the six healing stages showing the influence of the heterogeneity of hard callus and cortex. All 12 images can be found in Figure 3 of the manuscript (Vetter et al. 2010b), see appendix. Based on these images, the influence of the heterogeneity on the strain distributions at the stages before, during and after bridging of the gap are summarized in Figure II.8. The effect on the heterogeneity changes the mechanical stimuli in the callus and is therefore potentially important for dynamical simulations of bone healing.

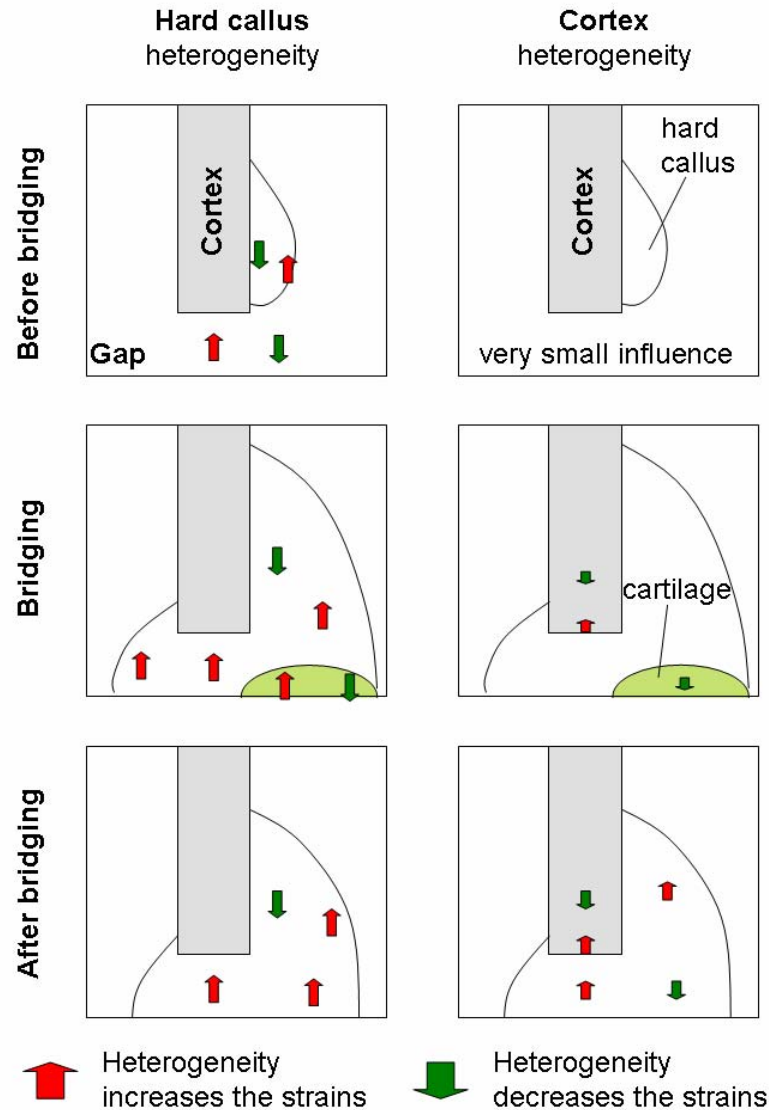


**Figure II.8: Schematic of the influence of the hard callus heterogeneity on the local strains before bridging, during bridging and after bridging.**

The little variation in the stiffness of the cortex, compared to variation in the hard callus, results in a higher influence of the hard callus heterogeneity on the strain distributions, especially in the early healing stages. The influence of the cortex heterogeneity, due to the remodelling of the cortical ends, starts to become important with cartilage bridging and becomes more important with bony bridging. As one main effect of the decrease of the bone area fraction at the cortical ends, the strains in this region are increased compared to the hypothetical homogeneous case. This will eventually cause that the strain threshold for resorption of bone will be exceeded in the cortical end region and further resorption will stop.

Some influences of the hard callus heterogeneity on tissue differentiation are given below, based on the interpretation of the strains from a basic mechanobiological point of view (see Chapter 6.5):

1) The initiation of intramembranous ossification is enhanced by the hard callus heterogeneity. This is due to a mechanically “smoother” interface between hard callus and adjacent fibrous tissue, which leads to lower strains in the fibrous tissue enabling intramembranous ossification.

2) The formation of cartilage in the periosteal gap area is strongly influenced by the heterogeneity. The hard callus heterogeneity reduces the strains further outside the periosteal gap. However, compared to the homogeneous case, higher stiffness close to the cortex increases also the strains not only within the gap but also in the osteotomy region close to the cortex. Therefore, the heterogeneity should shift the cartilage formation towards the outside of the callus.

3) In the same way, the endochondral ossification is influenced. Not only do the strains in the cartilage regions at Stage III depend on the hard callus heterogeneity, but also the strains in the cartilage at Stage IV. In the heterogeneous case, higher strains were seen closer to the fracture gap. Neglecting biological influences, the endochondral ossification, occurring between Stage III and Stage V, seems to be driven by the mechanical stimuli which are a result from the heterogeneity of the hard callus (Vetter et al. 2010b).

4) Finally, the mechanical signal for bone resorption is reduced by the hard callus heterogeneity. The outer regions of the hard callus are less loaded due to the mainly vertical transmission of the load, applied on the cortex. Therefore, the strains are very low in that region for a homogeneous hard callus. In the heterogeneous callus, the stiffness is lower at the outer fringes of the hard callus and, therefore, inhibits early resorption of the outer fringes.

### **6.7. Conclusions**

Over the last decade and more Finite Element models have been used to estimate the local strain, stress and fluid flow within the callus. Patterns of these mechanical parameters have been correlated with the patterns of tissue differentiation (Kuiper et al. 1996; Prendergast et al. 1997; Claes and Heigele 1999; Epari et al. 2006b). This section of the thesis was driven by the same idea. Previous studies based their investigations on assumed homogeneous tissue type distributions within the callus estimated by experimental observations. This study was based on a *quantitative* “norm” healing progression, which was calculated by a well defined method applied to a comprehensive animal study with a large number of animals. Therefore, a more detailed description of the healing progression was available compared to former

studies. In particular, the mechanical heterogeneity of the hard callus could be quantified. It was found that the overall stiffening of the callus described by its averaged elastic modulus increased exponentially during the healing (Figure II.3).

The dynamical interpretation of the mechanical strain pattern was led by the idea of Perren and Cordey (1980). First, the interfragmentary strain theory (IST) was found to be generally capable to describe the tissue differentiation within the osteotomy gap. However, the threshold value for the formation of fibrous tissue was found to be too low. Therefore, fibrous tissue would not have been formed in the osteotomy gap according to the interfragmentary strain theory which is contradicting to the experimental observation. In a next step, the IST was applied on a local basis as a mechanoregulatory model. The results of these “static simulations” showed the potential of applying only one mechanical signal (a strain invariant) as mechanical stimulus driving the tissue differentiation. The tissue differentiation could be well explained on the periosteal side of the callus and in the fracture gap. However, the endosteal tissue differentiation can not be explained by this basic mechanoregulatory model. In a mechanobiological model, the biology probably has to inhibit the mechanical signal for tissue maturation within the endosteal region at the initial healing phases. One main advantage of the IST is that only one mechanical signal determines the tissue differentiation. This reduces the complexity which is a demanded property of the mechanobiological computer model which will be used for dynamical simulations of bone healing (see chapter 7).

The heterogeneity of the hard callus is a crucial factor on the strain distribution within the callus (Vetter et al. 2010b). Therefore, it is also an important factor for mechanobiological simulations on bone healing, as the heterogeneity changes the values of the assumed mechanical stimulus. From a mechanobiological viewpoint, the hard callus heterogeneity is an important factor for the shift of the cartilage from the outer periosteal side inwards to the osteotomy gap over time. This shift occurs between Stage III and Stage IV which is approximately between 3.75 weeks and 6 weeks post-op. The comparison with the hypothetical homogeneous calculations showed the importance to incorporate the hard callus development into dynamical simulations of bone healing.

It is not clear whether the bony bridging occurs via endochondral ossification, intramembranous ossification or both and what causes the cartilage to ossify. Some evidences are in favour for endochondral ossification (Epari 2006). From a mechanobiological viewpoint, one could hypothesise for the healing progression between Stage III and IV: (i) endochondral ossification starting from the outer

periosteal end and processing forward into the intercortical gap and, at the same time, further formation of cartilage towards the intercortical gap; (ii) around the time when cartilage has reached the intercortical region (as seen as cartilage “remnants” in Stage IV) the stability has considerably increased and reduced strains in the gap so strongly, that bone formation in the gap occurs.

Unfortunately, the animal study did not provide data points between 3 and 6 weeks and detailed insight of the healing process (in particular the bony bridging) between this time is limited. Several questions remain unanswered. Further experimental and computational studies focusing on this healing time could help to clarify some of the following questions. How does bony bridging occur on the endosteal and periosteal side? Is it pure endochondral ossification or does also intramembranous ossification play a role? And how important is the endosteal bridging (seen at Stage IV) for the strain distribution and the shift of the cartilage?

---

### III. Dynamic bone healing simulations

This chapter aims to answer a core question of the thesis: to which extend can a basic mechanobiological model explain the experimentally observed succession of tissue patterns (Chapter 5.4)? A new mechanobiological model was implemented which included an iterative tissue adaptation loop. The prerequisite for the modelling was to reduce the number of model parameters to enable extensive parameter studies. Only the *required* details of mechanics and biology should enter the model.

The local application of the Interfragmentary Strain Theory of Perren and Cordey (1980) was tested in “static simulations” (Chapter 0) and showed its potential to explain the tissue differentiation on the periosteal side of the callus and in the fracture gap. In this chapter, this concept was implemented in a dynamical tissue adaptation algorithm and parameter studies were carried out altering the mechanosensitivity (thresholds) of the cells. In the model, different tissue types are clearly discriminated, i.e. no “rules of mixture” of different tissue types within elements were applied (as it is generally the case in existing models on bone healing). An important improvement of our model is to allow new bone to be formed either by intramembranous or endochondral ossification.

The output of the simulations was, according to the set up of the model, “pure” tissue type distributions (or images). The term “pure” means that each pixel within the callus was assigned to a specific tissue type. This made a “one-to-one” comparison between simulation results and spatial tissue data possible. The images of the averaged healing progression (Chapter 5.4) were used for this reason. It was found that this spatial-temporal validation of *in silico* simulations is highly important for the improvement of mechanobiological theories on bone healing.

### 7. Mechanobiological simulation of bone healing

The lack of experimental data is a crucial problem for more detailed conclusions drawn from mechanobiological simulations. This problem becomes even more severe as the complexity of the models increases. Assuming that only 5 different values per parameter of a model should be tested, doubling the number of parameters from 10 to 20, for example, would increase the computational costs of a sensitivity study by a factor of one billion. This basic consideration points out the advantage of a basic model with a reduced number of model parameters. The small number of parameters allows a thorough study of the parameters, which can be summarized in phase diagrams, which describe the agreement between experiment and simulation depending on the value of the simulation parameters.

The approach of this model was to bring experiment and simulation closer together by: (i) gathering *in vivo* data describing the healing progression based on an experimental study comprising a large number of sheep ( $n = 64$ , see Chapter 3) and by (ii) reducing the complexity of the model on the computational side. One key feature of the previous work was the calculation of an averaged progression of the healing, allowing a stringent validation of the simulation results (see Chapter 5).

Bone healing is simulated as a mechanobiological process. Using a lattice model, the local mechanical strains within the callus were calculated by means of the Finite Element Method (FEM). All tissues were modelled as linear elastic materials to reduce the mechanical complexity and the number of material parameters. Additionally, the according developments of the material properties of tissues (maturation or dematuration) during bone healing are fairly unknown which makes a more sophisticated mechanical description not very reasonable. Biology enters into the model via a biological "potential", which migrates from predefined sources into the osteotomy callus. The biological potential describes the potency to form different tissues and includes implicitly mesenchymal stem cells (MSCs), angiogenesis and other biological factors. The migration of the biological potential was modelled as a diffusion process. The diffusion problem was solved on the same lattice as the mechanical problem. The local amount of mechanical stimulus decided if the tissue matured and on the way of ossification (endochondral or intramembranous ossification) of an element. The local amount of biological potential decided on the speed of the maturation or the local increase of the elastic modulus.

Following the idea of simplicity, this model employs linear elastic behaviour of the material and only one mechanical stimulus regulating the tissue adaptation. Tissues,



explicitly soft tissue and cartilage, are biphasic materials with interstitial fluid inside the tissue matrix. Most of the recent bone healing simulations use mechanical poroelastic material behaviour and two mechanical stimuli. These simulations define a loading regime and calculate the local fluid flow as one of the two mechanical stimuli besides the tissue strain or stress. However, for the characteristic slow loading conditions during walking (around 1 Hz), no qualitative differences in the local strains and the local fluid flow were found (Carter and Beaupre 1999). In other words, the mechanical signals provided by fluid flow in a poroelastic model and by strains in a uni-phasic model are qualitatively the same.

### 7.1. Experimental data on maturation of tissue

During bone healing, different tissue types are formed and mature. Generally, the tissues change their appearance, become more isotropic and increase their stiffness. In this model, the maturation of tissue is modelled by an increase of the local elastic modulus. The maturation rates (increase of the stiffness per time) of the tissue type differ from each other. The maturation rates have to be quantified in order to run the simulations and were estimated based on the available vivo data.

The maturation of the hard callus, modelled as a porous material, was based on nanoindentation experiments (Manjubala et al. 2009) and the assessment of the increase of the bone area fraction ( $BA/TA$ ), see Chapter 4.4. The data stemmed from the region where the formation of bone starts and where a continuous maturation of the bone occurs during the reparative phase of bone healing (McKibbin 1978). Accordingly, the assumption was made that the experimentally measured stiffening occurred under optimal conditions, i.e. the mechanical stimulus in this region was continuously in favour for bone formation and the biological potential was maximal. The slope of bulk elastic modulus of a hard callus element (Figure I.4, right) gives therefore the maturation rate for bone,  $k_{bone}$ . A hard callus element, mechanically stimulated and with optimal ("full") biological potential, increases its stiffness with  $k_{bone}$ , which depends on the local elastic modulus of the material.

The maturation rates for fibrous tissue and cartilage was assumed to be linear due to the lack of detailed data. The according maturation rates could be estimated by investigating the histological sections from the animal experiment. First intramembranous bone was estimated to be found around 8 days post op. Assuming full biological potential at this site, the maturation rate for fibrous tissue,  $k_{ft}$ , was set to 1 MPa/day. The process of endochondral ossification for full biological potential was estimated to require around 10 day and, therefore, the maturation rate for cartilage,  $k_c$ , was set to 50 MPa/day.

### 7.2. Basic mechanobiological bone healing model

The mechanobiological model will be generally described in this section while the following section describes the application of the model to the case of ovine osteotomy healing.

#### Iterative tissue adaption loop

The heart of every dynamical simulation of bone healing is the iterative tissue adaptation loop. The loop for this model consists of the calculation of the mechanical stimulus and the migration of the biological potential (Figure III.1). With this information, the tissue (or the elements of the model) matured and differentiated.

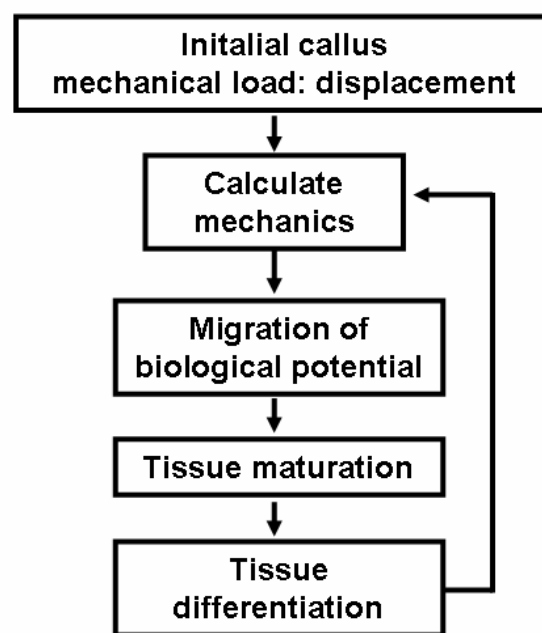


Figure III.1: Iterative implementation of the mechanobiological bone healing model.

#### Biology

The biological cells and other influences are not modelled on a cellular level but on a continuous level (each element consists of several cells). The biological influences are modelled as one net-effect parameter, called "biological potential". This potential describes the ability of an element (with several cells inside) to "heal" meaning to produce additional tissue matrix or increase the element's stiffness. In other words, the biological potential describes the potency to form different tissues and includes implicitly mesenchymal stem cells (MSCs), angiogenesis, nutrition, growth factors and other biological factors. The migration of the biological potential  $c$ , which takes normalized values between 0 and 1, was modelled as a diffusion process (16). The diffusion coefficient  $D$  did not depend on the tissue properties or the mechanical environment.

$$\frac{\partial c(\vec{x})}{\partial t} = D \cdot \nabla^2 \cdot c(\vec{x}) \quad (16)$$

$c$  Concentration of the biological potential  
 $D$  Diffusion constant

### Mechanics

The linear elastic mechanical problem has to be solved to calculate the local mechanical stimulus. The problem is analogue to the static simulations of bone healing (Chapter 6.2). The hard callus was also modelled a porous material (1). The strain tensor  $\varepsilon$  is assumed to carry the mechanical signal or stimulus. The strain energy density ( $SED$ ) was not further investigated due to the results from the static simulations. To investigate the influence of the choice of the mechanical stimulus  $MS$ , three different stimuli were investigated: (i) the absolute value of the vertical strain (17), (ii) the maximal shear strain (18) and (iii) the maximal value of the absolute values of the maximal and minimal principle strain (19).

$$MS = |\varepsilon_{yy}| \quad (17)$$

$$MS = \gamma_{\max} = \sqrt{(\varepsilon_x - \varepsilon_y)^2 + \gamma_{xy}^2} \quad (18)$$

$$MS = \max(|\varepsilon_1|, |\varepsilon_2|) \quad (19)$$

$\varepsilon_x$	Strain in horizontal direction	$\gamma_{\max}$	Maximal shear strain
$\varepsilon_y$	Strain in vertical direction	$\varepsilon_1$	Principle strain 1
$\gamma_{xy}$	Shear strain	$\varepsilon_2$	Principle strain 2

### Tissue maturation and differentiation

The model generally describes the development of tissue starting from granulation tissue to cortical bone (Figure III.2). Each element is assigned to one tissue type and, in particular, no mixture of tissues within one element is allowed. The development or maturation of an element is modelled by changing its elastic modulus  $E$ . The decision, if the tissue element matures or de-matures is received by the amount of the local mechanical stimulus  $MS$ . The actual amount of the increase or decrease of the elastic modulus,  $\Delta E$ , is according to the element's tissue type and to its amount of biological potential  $c$  ( eq ). When an element reached a certain elastic modulus threshold, the element changed its tissue type (Figure III.2).

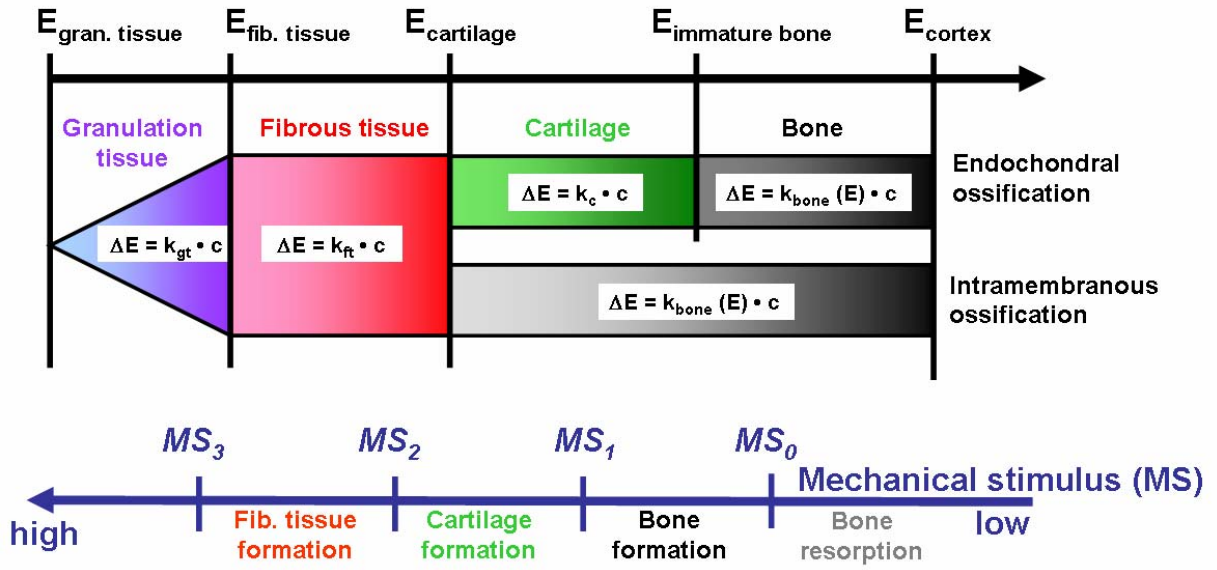


Figure III.2: Mechanobiological tissue maturation and differentiation model.

Each element or pixel was initialised with granulation tissue and matured according to the local mechanical stimulus  $MS$  and the cell concentration  $c$ . The maturation data of bone is presented in Figure I.4.

It is assumed that the cells feel the deformation of their cytoskeleton. Accordingly, strains are assumed as mechanical stimulus. The mechano-regulation of the tissue adaptation follows the idea of Perren (Perren 1979): tissue can only be formed if it sustains the according strain. In the model, tissue at a certain site in the callus matures only when it receives a lower strain than the current tissue at this site can sustain. In other words, a lower mechanical stimulus is required for a local maturation of a tissue as the current tissue “likes”. De-maturation (decrease of the local elastic modulus) is only considered for bone (hard callus). The de-maturation simulates the resorption of bone which is a important process in the regenerative healing phase. For the de-maturation of bone, a very low mechanical stimulus is required. The mechano-regulation was implemented by four thresholds of the mechanical stimulus (20).

The largest threshold,  $MS_{ft}$ , is crucial for granulation tissue elements and decides on its maturation (granulation tissue likes strains of  $MS_{ft}$  or higher). No maturation occurs for elements above  $MS_{ft}$  (20). The next smaller threshold,  $MS_c$ , decides if a fibrous tissue element matures. When a fibrous tissue element is matured the local amount of  $MS$  decides which way of ossification is taken (Figure III.2). For  $MS < MS_b$ , the element becomes a hard callus element (intramembranous ossification) otherwise, the element becomes cartilage.  $MS_b$ , decides on the further maturation of cartilage (endochondral ossification) and the maturation of hard callus or woven

bone (further intramembranous ossification). The smallest threshold,  $ms_r$ , decides, if a bone element decreases its elastic modulus due to the lack of mechanical stimulation causing remodelling or resorption of bone.

$$\Delta E = \begin{cases} 0 & MS > MS_{rt} & \text{No maturation} \\ k_{gt} \cdot c & MS < MS_{rt} & \text{Maturation of granulation tissue} \\ k_{ft} \cdot c & MS < MS_c & \text{Maturation of fibrous tissue} \\ k_c \cdot c & MS < MS_b & \text{Endochondral ossification} \\ k_{bone}(E) \cdot c & MS < MS_b & \text{Intramembranous ossification} \\ -k_{res} \cdot c & MS < MS_r & \text{Resorption/remodelling of bone} \end{cases} \quad (20)$$

### 7.3. Implementation of the model (for a 3 mm sheep osteotomy)

The iterative tissue adaptation loop was implemented using MATLAB (The Mathworks Inc., v 7.1) to carry out the simulations. The same lattice was used for the two problems, the diffusion of the biological potential  $c$  and the calculation of the mechanical strains  $\varepsilon$ . For both, solving the diffusion problem and the mechanical calculations, a non-commercial FE code was applied (DUNE). The code had been optimized for lattice models and the results were tested extensively with the commercial FE toolbox Abaqus (ABAQUS v6.6, Hibbit Karlsson & Sorensen, Inc., RI, USA).

#### Lattice model and iterative tissue adaptation

The lattice model the area of the callus is subdivided into small squares with a side length of 0.15 mm. The model is 3-dimensional, but assuming rotational symmetry along the long bone axis a 2-dimensional cross-section through the callus is representative for the whole system. Computational time is further reduced under the assumption of proximal/distal symmetry along the horizontal osteotomy cut (Figure III.3). The geometry of the callus was derived from the histological image analysis (Vetter et al. 2010a). The mechanobiological model was implemented as an iterative loop in MATLAB (The Mathworks Inc., v 7.1) (Figure III.1). The mechanical FE calculations at each step were carried out using the software DUNE which was accessed as a shared object library within the MATLAB routine. For the mechanical calculations, all tissues were modelled as linear elastic. The assumed typical material properties are summarised in (Chapter 6.2, Table 3). Since the diffusion of the biological potential does not depend on the mechanical properties of the callus, the diffusion equation can be solved beforehand, and the prepared results are then used in the iteration loop. The updates of the elastic moduli of each element were performed as described before (Eq. (2)). The time increment per step corresponded to about one day. The lattice size was 112\*120 square elements with a side length of

0.15 mm. The numerical stability of the results was checked by doubling the resolution of the lattice and decreasing the time step to 0.1 and 0.5 days. For all four source types, a parameter study varying the two mechanical stimuli thresholds was carried out. The range of the thresholds was from 0.005 to 0.2 for bone formation and 0.01 to 0.4 for cartilage formation. The simulated time comprised 60 days for each simulation run.

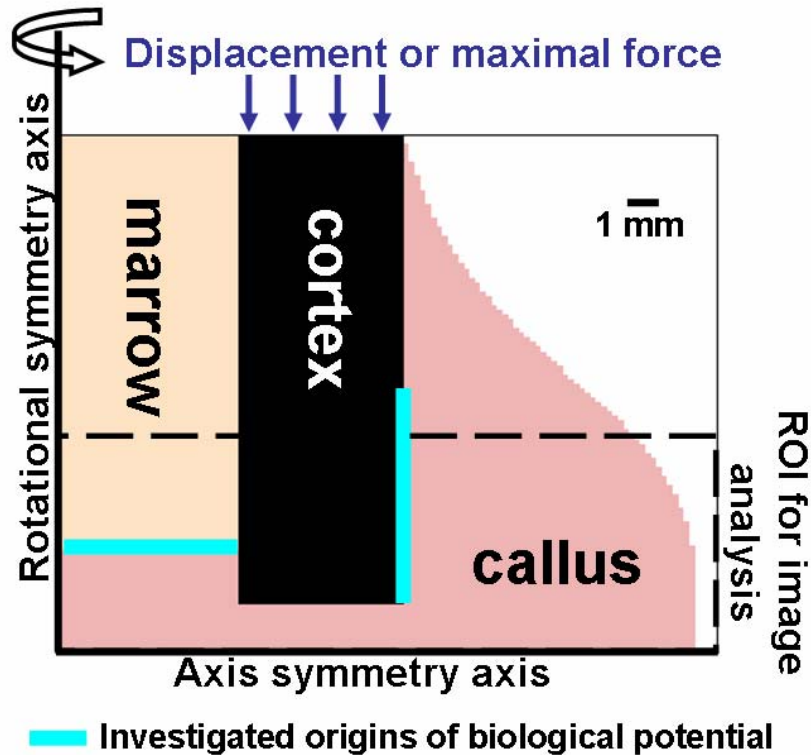


Figure III.3: Geometry of the modelled osteotomy site and the boundary conditions.

The gap size was 1.5 mm which equals to 3 mm in a non axis symmetric model. Two different origins of the biological potential (e.g., cells) were investigated: i) at the periosteum starting from the gap up to 6 mm and ii) the bone marrow interface.

### Boundary conditions

### Biology

We assume that main contributors to the biological potential are mesenchymal stem cells (MSCs) and other progenitor cells migrating into the callus. Based on experimental evidence, the main origins of MSCs are either the cambium of the periosteum or the bone marrow, although other sources as surrounding muscle, fat and synovium provide a limited contribution (Yoo et al. 1998; Gerstenfeld et al. 2003; Malizos and Papatheodorou 2005; Colnot 2009). The fracture ends do not serve as MSC source (McKibbin 1978). In the simulations, the main source of the biological potential was the periosteum, starting from the osteotomy gap up to 6 mm away from it (Figure III.3). Four different source types were implemented to investigate the influence of different origins of the biological potential and the way of

its diffusion. In the first case (source type 1), the biological potential at the periosteum was set equal to 1 resulting in a front of the biological potential migrating into the callus. To produce a steeper front of the biological potential, the strength of the source at the periosteum was set equal to 10 in the second case (source type 2). A steep front of the biological potential is obtained since all elements, which would have values of  $c$  larger than 1 due to the diffusion of the biological potential, are reset by definition to the maximum value  $c = 1$ . In the third and fourth case, the bone-marrow interface was assumed to serve as source, additionally to the periosteal source of  $c = 10$ . The bone-marrow interface was set to  $c = 1$  for the third case (source type 3) and  $c = 0.1$  for the fourth case (source type 4). For all four different choices of the source, the diffusion constant was adjusted so that the biological potential was homogeneous at the end of the simulated healing process.

### **Mechanics**

According to monitored interfragmentary movement (Schell 2008), the cortex was displaced by 0.25 mm (equals to 0.5 mm in a non axis-symmetric model). When the maximal force of 500 N on the cortex (Duda et al. 1998) was reached, the boundary condition was changed from a displacement of 0.25 mm displacement to applying 500 N onto the cortex (Figure III.3).

#### **7.4. Comparison of experimental data and simulation results**

Each simulation run was compared with the experimental data. The comparison between experiment and simulation was based on successive healing stages showing different tissue type patterns. These stages describe the healing progression in a typical sheep (Vetter et al. 2010a). The region of interest (ROI) of these images analysis was limited in their height (Figure III.3) due to the influence of the fixator screws. Only the images of healing stages II, III and IV were used for the comparison (Figure III.4). Healing stage I showed still remnants of haematoma, while stages V and VI showed remodelling of the hard callus. Neither haematoma nor remodelling was incorporated in the first, basic simulations. The experimental images of these three stages were compared with all 60 images of a simulation run. The comparison between experiment and simulation were performed focusing on different aspects of the images.

Firstly, only the area fractions,  $a$ , of the three occurring tissue types in the callus, fibrous tissue (ft), cartilage (c) and hard callus or bone (b), were compared. The mismatch in area fractions for each stage,  $m_{area, stage}$ , was obtained by summing the difference of the area fractions for each tissue type,  $tt$ , and calculating the mean

## 7. Mechanobiological simulation of bone healing

---

value (21). The mean value of the three  $m_{area,stage}$  values,  $m_{area}$  (22) was calculated to describe the mismatch of a complete simulation run.

$$m_{area,stage} = \frac{1}{3} \cdot \sum_{tt=1}^3 |a_{tt,exp} - a_{tt,sim}| \quad (21)$$

$$m_{area} = \frac{1}{3} \cdot \sum_{stage=II}^{IV} a_{area,stage} \quad (22)$$

$m$	Mismatch
$a$	Area of tissue type $tt$
sim	Simulation
exp	Experiment

Secondly, the spatial information of the images was considered by a pixel-to-pixel comparison between two images. Three scalar quantities were calculated based on such a one-to-one comparison between pixels in the experimental and the simulated image. The first quantity,  $p_{tt}$ , considered only the tissue type and was 1 for pixels with a mismatch in tissue type, and 0 for matching tissue type. The second quantity,  $p$ , took into account that elements of the hard callus contain an additional information, their bone area fraction,  $BA/TA$ . A straightforward extension of the pixel-to-pixel comparison is to calculate the difference in the  $BA/TA$  values in case that both compared pixels have the tissue type bone (23). The number of mismatching pixel was summed up and divided by the total number of pixels in the callus (see Appendix for a mathematical definition of the quantities) to quantify the pixel-based mismatch  $m_{stage}$  of experimental and simulated image. Again, the average,  $m$ , of the three values of  $m_{stage}$  was calculated to quantify the pixel-based comparison of a simulation run with the experimental data.

$$p = \begin{cases} 0 & \text{Pixels different type} \\ 1 & \text{Both pixels bone} \\ |(BA/TA)_{sim} - (BA/TA)_{exp}| & \text{Both pixels the same type} \end{cases} \quad (23)$$

$p$	Mismatch of a comparison of two pixels
$BA/TA$	Bone area fraction

To emphasize the importance of amount and location of the formed cartilage, a third quantity,  $p_c$ , was calculated, which takes only the mismatching cartilage pixels into account. Evaluated are only the pixels, which are cartilage either in the experiment or in the simulation. Accordingly,  $p_c$  is defined as 0 if both compared pixels were cartilage, otherwise  $p_c$  is 1. The sum over all  $p_c$  was normalized by the number of



cartilage pixels in the experimental image in order to quantify the cartilage mismatch for an image (or healing stage),  $m_{stage}$  (see Appendix). The estimated overlap of both cartilage areas can be estimated by dividing this value by the factor 2.

Figure III.4 (right) shows a typical plot, which summarizes the comparison between experiment and simulation. On the x-axis, the simulation time is plotted, on the y-axis the mismatch between the experimental and simulated images. The comparison with three experimental images results in three curves. In the beginning, the curve of comparison with Stage II shows the lowest values of the mismatch. With periosteal bone formation in the simulation, the mismatch decreases further until a minimum is reached (marked by a cross in the plot). While in the following the mismatch with Stage II increases, the mismatch with Stage III is still decreasing and taking lower values than the comparison with stage II at some point and finally running through a minimum, too. Shifted in time, the same behaviour of tipping at a minimum is observed for the comparison curve with Stage IV. A general trend is that the minima for the different curves get larger from Stage II, to III and IV. This demonstrates that it becomes more and more difficult to reach good agreement between experiment and simulation at later times. The average value,  $m$ , of the three smallest mismatches,  $m_{II}$ ,  $m_{III}$ , and  $m_{IV}$  (see Figure III.4, right), was calculated. With this scalar quantity  $m$ , the overall agreement between a simulation run and the experiment is quantified. In the following parameter studies this total mismatch  $m$  is plotted to assess which set of parameters produces the best agreement with the experiments.

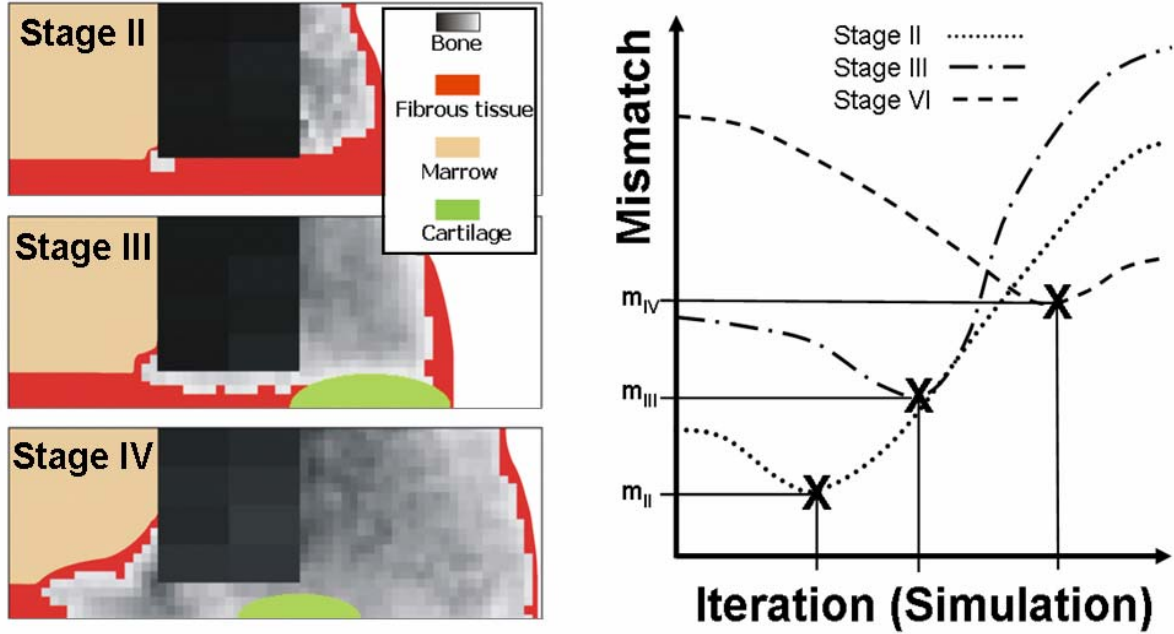


Figure III.4: Comparison of the three experimental images (Stage II, III and IV) with the simulated images performed at each iteration step of the simulation.

Left: the three experimental images with which the comparison is performed (Vetter et al. 2010a). Right: Time evolution of the number of mismatching pixels of the simulated and experimental images. For each healing stage, the curve shows a minimum (marked by a graph). The minima occur in the same order than the healing stages. The average value of the minimal mismatches is the quantity to assess the overall agreement between simulation and experiment for a given set of simulation parameters.

## 7.5. Results

### Influence of different choice for the mechanical stimulus

In a first set of simulation runs, the influence of the choice of the mechanical stimulus was studied. From the local strain tensor, three different scalar mechanical quantities were calculated and used as mechanical stimulus in our computational model: (i) the vertical strain, (ii) the maximum of the absolute values of the maximal principle and minimal principle strain and (iii) the maximal shear strain. For all three stimuli, the threshold values for cartilage formation ( $MS_c$ ) and bone formation ( $MS_b$ ) were independently varied in the range of  $0 \leq MS_c \leq 0.4$  and  $0 \leq MS_b \leq 0.2$ , with  $MS_c > MS_b$  according to fundamental mechanobiological reasoning (Perren 1979). The comparison of experimental and simulated tissue images was performed as described in the previous section, calculating the mismatching pixels,  $m_{tt}$ , as scalar outcome of the comparison. Plotting the quantity  $m_{tt}$  for different choices of the mechanical thresholds  $MS_c$  and  $MS_b$  results in phase diagrams as shown in Figure III.5. Each of these phase diagrams summarizes the outcome of 547 independent simulation runs. The phase diagrams are not only qualitatively, but also

quantitatively very similar. A clear feature, common for all phase diagrams, is the horizontal separation into a region of poor agreement between experiment and simulation for low values of  $MS_b$  (bone formation) and good agreement for larger values. The value for  $MS_b$ , where this horizontal separation occurs, is for the cases of vertical strain and principle strain around 0.05 and, also the position of the minimum of the mismatch (marked by a white cross in Figure III.5) is the same at the same position ( $MS_c = 0.175$ ,  $MS_b = 0.095$ ). The corresponding values for the simulation runs with the shear strain as mechanical stimulus are slightly larger by a factor of 1.15. Also, the stated results in the following chapters were qualitatively, and often even quantitatively, independent of the chosen mechanical stimulus. The reported results in the following were obtained using the shear strain as stimulus since shear strains have been proposed and used frequently as mechanical stimulus (Bailon-Plaza and van der Meulen 2003; Isaksson et al. 2006; Geris et al. 2009).

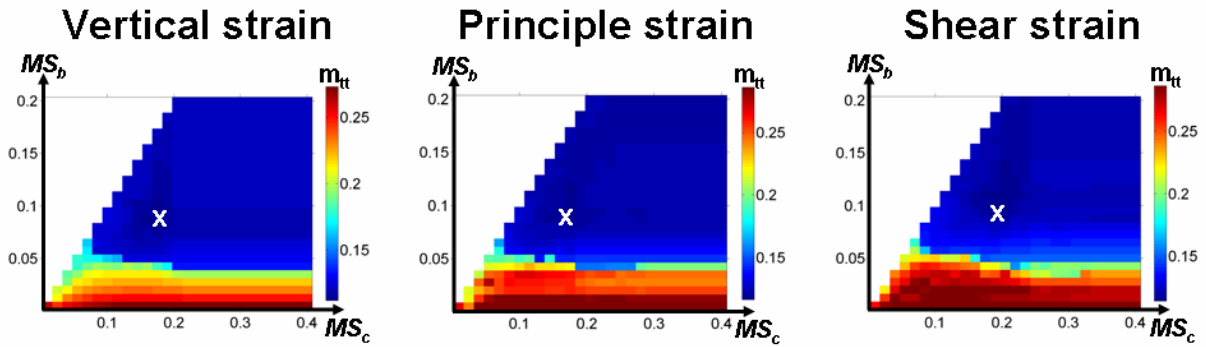


Figure III.5: Phase diagrams of the mismatch  $m_{tt}$  between experimental images and simulation results based on spatial tissue type comparison (see Methods).

$MS_c$  and  $MS_b$  denote the mechanical strain threshold for cartilage and bone formation, respectively. Each diagram was obtained by running 547 simulations with different values for  $MS_c$  and  $MS_b$  assuming periosteum and marrow space as sources of the biological potential (source type 3) and using three different mechanical stimuli: (i) absolute value of the vertical strain (left), (ii) absolute value of the maximum of the minimal and maximal principle strain (middle) and (iii) the maximal shear strain (right). The position of the minimum mismatch between experiment and simulation is marked with a white x in each phase diagram.

### Comparison based on area fractions

The next set of simulations demonstrates the importance of considering the spatial information of the various tissue types for validating computer simulations and not only the amount of the tissues. Again, different realisations of mechanobiological regulation were tested by varying the thresholds for cartilage and bone formation ( $MS_c$  and  $MS_b$ ). The phase diagram shows the mismatch based on the experimental area fractions of the different tissues (fibrous tissue, cartilage, and bone),  $m_{area}$  (Figure III.6a). The smallest mismatch between experiment and simulation (indicated

by the white cross in the magnified phase diagram) was below 0.014 or 1.4%. This value is very low indicating a very “good” simulation of the healing progression. This impression is corroborated by the plot of the time development of the different tissue area fractions (Figure III.6a). For all three tissue types, the experimentally measured area fractions (circles) are met by computational prediction (lines). However, looking in detail at the progression of healing as reflected by the time-evolving tissue type patterns, crucial shortcomings of the simulated healing could be observed: the simulation run (i) showed too early formation of cartilage, i.e. at stage II, (ii) did not show periosteal bridging of the callus via cartilage, but via bone at stage III and (iii) did not show a shift of the cartilage towards the centre of the fracture gap between stage III and stage IV.

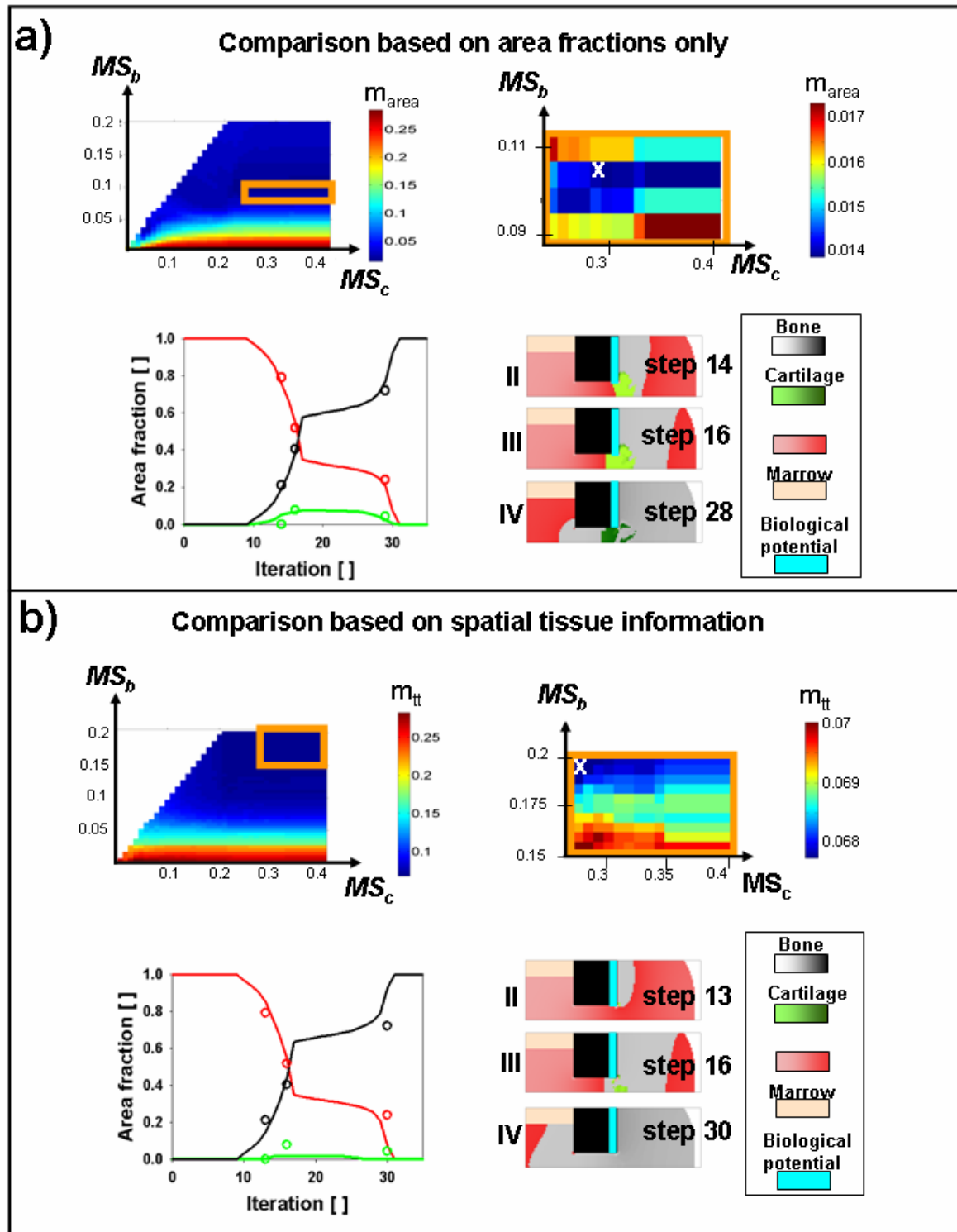


Figure III.6: Two phase diagrams of the mismatch between simulation and experiment

a) Phase diagram of the mismatch between simulation and experiment based on the comparison of tissue area fractions only. In the simulations it was assumed that the maximal shear acts as mechanical stimulus and that the periosteum is the main source of the biological potential (source type 1). The position of the minimum mismatch between experiment and simulation is marked with a white x. For the simulation run corresponding to the x, the time development of area fractions (bottom: experimental data as circles, simulated development as lines) and the images at the three time points of best agreement are shown (right). In Fig. b the

same information is presented for the case, when the comparison between experiment and simulation is based on the full spatial information of the tissue arrangements of the images.

### Comparison based on images or spatial information

In the last set of simulations presented in this thesis, the influence of the source of the biological potential on the progression of healing was studied. The growth of the hard callus could be predicted in good agreement with the animal experiment, assuming the periosteum being the main source (source type 1). The phase diagram based on the tissue mismatch between experiment and simulation,  $m_{tt}$ , showed again that good agreement is only obtained for values of  $MS_b$  larger than 0.05 (Figure III.6b). Simulations with values of  $MS_b$  below 0.02 and  $MS_c$  above 0.04 predicted a non-union with cartilage remaining in the callus. The dark blue area in the phase diagram marks the region of good agreement between experiment and simulation, which is, once  $MS_b$  is above 0.1, remarkably independent of the chosen values for  $MS_c$  and  $MS_b$ . The minimal value of  $m_{tt}$  was 0.067 (at  $MS_c = 0.26$ ,  $MS_b = 0.195$ ) meaning that less than 7% of the pixels were not in agreement on average (Figure III.6b). The values of  $m_{tt}$  in the marked region around the minimal  $m_{tt}$  varied less than 1%. While the hard callus was well described, the simulations did not show the conspicuous formation of the cartilage at the periosteal side of the callus. Figure III.7, left, demonstrates this by means of a phase diagram, which displays only the mismatch of pixels with cartilage in the experimental and computational images. The disagreement is due to too little cartilage formed in the simulation too close to the fracture gap. Analyses of the simulations indicated that the reason for this disagreement is that the biological potential is distributed too homogeneously within the callus leading to a “premature” decision towards intramembranous ossification instead of a delayed decision towards endochondral ossification.

This observation was confirmed by simulations, where a sharper front of the biological potential was created by making the periosteum an extra-potent source. This was realized by increasing the values of the potential at the periosteum from 1 to 10. About two thirds of the cartilage region of the experimental and simulated image overlapped at stage III, when assuming no additional biological source from the marrow (source type 2). The agreement of the predicted cartilage could be further improved under the assumption that also the bone marrow acts as a considerable source of biological potential (source type 3). In this case, the overlap of correctly predicted cartilage pixels for the best simulation increased to about three fourths (Figure III.7, middle, white cross marks the values for  $MS_c$  and  $MS_b$  for the best simulation). The assumed biological source at the interface marrow/callus has the objectionable effect of an extensive bone formation at the endosteal side even at early stages in the healing process, which was not observed in the sheep

experiment. A further modification of the strength of the biological sources was carried out to resolve the dilemma of predicting correctly either the hard callus formation or the cartilage formation. Still, an extra-potent source at the periosteum was assumed but the potency of the assumed source at the marrow was reduced by a factor 10 (source type 4). As a result, the bridging of the callus gap via cartilage is retained (Figure III.7, right), but the endosteal bone formation is delayed to later stages.

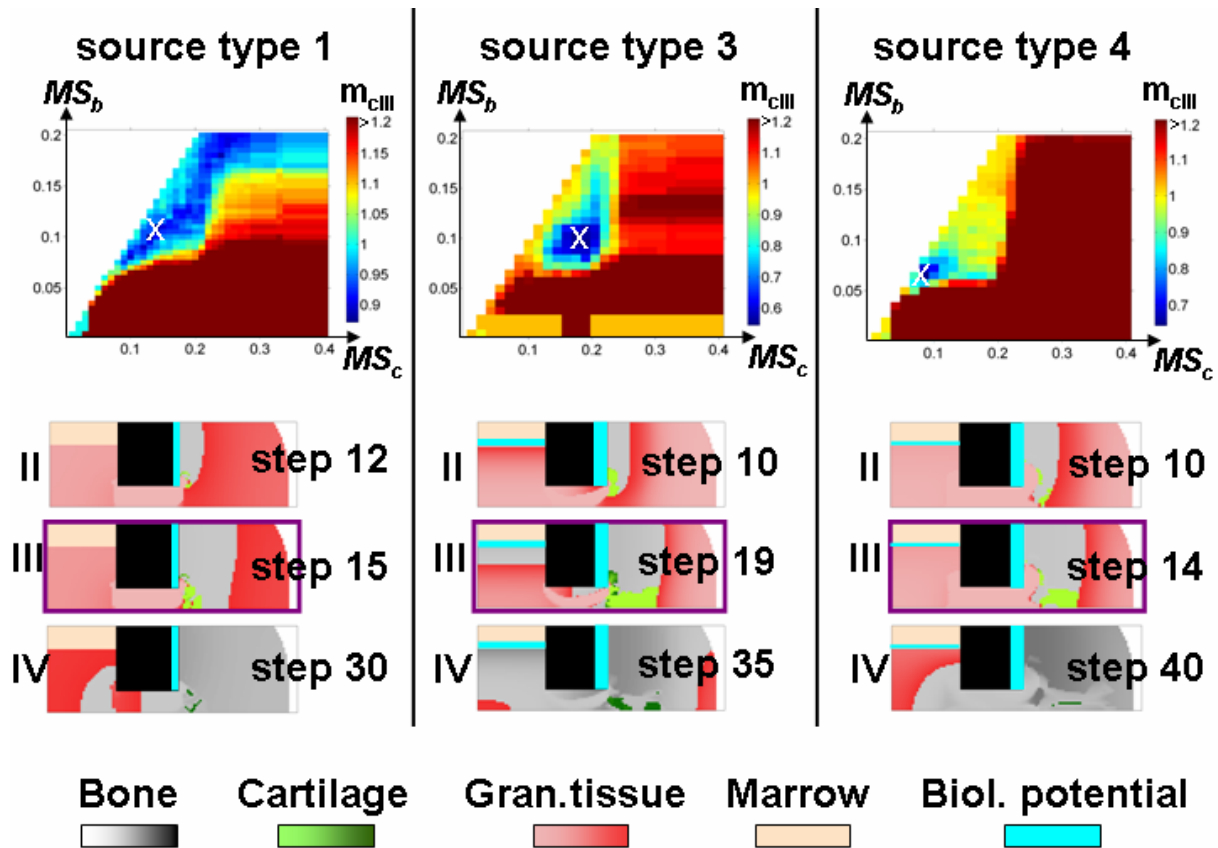


Figure III.7: Phase diagrams of the mismatch of cartilage pixels between simulation and experimental stage III, assuming maximal shear as mechanical stimulus.

The white x marks the best fits. Additionally, the images of the best simulations (according to the cartilage match at stage III) are shown. Left: source type 1 (low gradient of the biological potential, starting from the peristeum). Middle: source type 3 (high gradient of biological potential and additional source at the callus/marrow interface). Right: source type 4 (high gradient of biological potential and additional low source at callus/marrow interface).

Table 4 summarizes the results of the agreement between experiment and simulation for the different hypotheses, from where the callus is biologically stimulated (source types 1-4). As further criteria the endosteal bone formation, the periosteal bridging via cartilage and the shift of the cartilage at later stages (between stage III and IV) are listed. Source type 4 shows the best overall agreement to the experimental histological images although other assumption of the source perform better for specific aspects of the healing process (source type 1 for hard callus formation, for

example). None of the investigated assumptions, however, could reproduce the shift of the cartilage towards the fracture gap.

**Table 4: Overview of different values describing the mismatch between simulation and experiment for the best simulations.**

The lower the value of the mismatch  $m$  the better the agreement between simulation and experiment;  $m_{tt}$  is the mean value of the tissue type mismatch for all three compared stages,  $m$  is the mean value of the tissue type mismatch including bone density for all three compared stages,  $m_{cIII}$  is the mismatch of the cartilage pixels at stage III and  $m_{cIV}$  is the mismatch of the cartilage pixels at stage IV. The two mechanical thresholds for the according simulation is given in the parenthesis ( $MS_c$ ,  $MS_b$ ). The boxes highlighted with grey represent the best simulation runs according to the different quantified  $m$ -values.

	$m_{tt}$	$m$	$m_{cIII}$	$m_{cIV}$	Bone growth	Cartilage bridging	Cartilage shift
<b>Source type 1</b> (low source at periosteum)	<b>0.0678</b>	<b>0.2229</b>	<b>0.9261</b>	<b>0.7361</b>			
	$MS_c$ : 26%, $MS_b$ : 19.5%	$MS_c$ : 26%, $MS_b$ : 19.5%	$MS_c$ : 14%, $MS_b$ : 11%	$MS_c$ : 25-34%, $MS_b$ : 11%	Yes	No	No
<b>Source type 2</b> (high source at periosteum)	<b>0.0693</b>	<b>0.2261</b>	<b>0.6440</b>	<b>0.9513</b>			
	$MS_c$ : 20.5%, $MS_b$ : 20%	$MS_c$ : 20.5%, $MS_b$ : 20%	$MS_c$ : 8.5, 6.5%)	(many)	Yes	Yes	No
<b>Source type 3</b> (high source at periosteum and marrow)	<b>0.1141</b>	<b>0.2886</b>	<b>0.5451</b>	<b>0.8750</b>			
	$MS_c$ : 20.5%, $MS_b$ : 10.25%	$MS_c$ : 19%, $MS_b$ : 9.5%	$MS_c$ : 19%, $MS_b$ : 9.5%	$MS_c$ : 34%, $MS_b$ : 8.75%	No	Yes	No
<b>Source type 4</b> (high source at periosteum, low at marrow)	<b>0.0690</b>	<b>0.2254</b>	<b>0.6440</b>	<b>0.9375</b>			
	$MS_c$ : 20.5%, $MS_b$ : 20%	$MS_c$ : 20.5%, $MS_b$ : 20%	$MS_c$ : 8.5%, $MS_b$ : 6.5%	$MS_c$ : 17.5%, $MS_b$ : 5.75%	Yes	Yes	No

## 7.6. Conclusions

The complexity of the bone healing process with its multifaceted influencing factors (the "diamond concept" (Giannoudis et al. 2007) names only the four most important: growth factors, scaffolds, mesenchymal stem cells and mechanical environment) makes a comprehensive modelling of the whole process unfeasible. In particular the lack of quantitative information about the temporal-spatial distribution of growth factors and different cell populations within the callus suggests strongly a phenomenological model approach. The parameters in the model were reduced to a minimum, summarizing, for example, the biological factors like mesenchymal stem cell migration, growth factors and others, into a scalar "biological potential". Although, influencing factors such as growth factors are therefore not explicitly modelled, it has to be emphasized that they are implicitly part of the model in the sense of a "mean field" description. Based on nanoindentation experiments and histological images maturation rates of the different tissues can be reasonably well



estimated. In essence, the model then includes as unknown parameters only the threshold values of the mechanical stimulus and the migration velocity of the biological potential, which determines the connection between real and computational time.

The quantification of animal experiments and a reduction of the model complexity leads to the favourable situation, where computational modelling can show its full potential: (i) to explain a complex data set with a simple model and (ii) to perform parameter studies to understand the full behaviour of the model. Only when the model cannot explain satisfactorily the experimental data set, a refinement of the model seems appropriate.

The applied model is a mechanobiological model, i.e. a more accurate biomechanical description of the (soft) tissues is of minor importance, since it is unknown how the mechanical input is processed by the cells. In the model, tissue differentiation is controlled via a single mechanical stimulus. The simulations demonstrated that the choice of the stimulus (vertical, principal or shear strain) has a minor influence on the progression of healing. Although probably cells are sensitive to a multitude of biophysical stimuli, the simulations showed that a single mechanical stimulus is sufficient to describe the time evolution of the tissue patterns. However, the choice of the strain type could become important for the simulation outcome when either non-idealized geometry or load is modelled, anisotropic material properties are used or low mechanical thresholds are included, e.g. for modelling bone resorption.

This model differs from other models by the decision to not apply rules of mixtures. In those cases, each element is populated with different types of cells which produce different tissue matrix. The element is then partially fibrous tissue, cartilage and bone and the element's elastic modulus is averaged. Within this model, every element is assigned to one phenotype which enables the direct comparison with the histological data. Furthermore, this also enables to differentiate between the two important paths of bone formation, the intramembraneous and endochondral ossification. This distinction of bone formation has not been differentiated so precisely so far. The element's tissue type has been assigned according to the element's elastic modulus or the predominating cell type within a region. Due to the rule of mixture, no intramembraneous ossification has been modelled (direct bone formation) but only endochondral ossification (formation of cartilage first which is then replaced by bone).

Simulations of bone healing face the problem of to define a simulation time. In particular, parameters such as maturation rates and cell migration have to be

quantified. However, they are only estimated input values. Additionally, the transient mechanical boundary conditions are only estimations because of experimental constrictions. These inaccuracies impede a precise definition of simulation time. This issue could be addressed by (i) using “self scaling” mechanical loads and (ii) searching “flexible in simulation time” for the best simulation run result by means of area fractions or healing patterns. Of course, it has to be ensured that the area fractions or healing patterns are reproduced in the experimentally observed order.

Concerning the source of the cells (or the more general, the biological potential), the two main results of the simulational work are stated below.

Firstly, the strength of the source has to be stronger at the periosteum than at the marrow space to be in accordance with an early periosteal bone formation and a delayed endosteal bone formation.

Secondly, a standard diffusion approach is not adequate to describe the periosteal bridging of the hard callus via cartilage. Better agreement with the experiment is obtained, when the front of the biological potential proceeding into the callus is steeper than it would develop from normal diffusion. A reason for this observation could be that (stem) cell migration is indeed a directed process in contrast to simple diffusion as a passive transport. Furthermore, the inclusion of multiple factors in the biological potential, which have to be simultaneously present to promote cell differentiation, could also lead to a more distinct separation between biological “active” and “passive” areas in the callus.

This computational work demonstrated that a comparison between experiment and simulation based only on area fraction of the different tissue types is insufficient for a validation of the model approach. Not surprisingly, essential information is contained in the “where” and “when” the different tissues are formed within the callus. Assuming maximal shear strain as the mechanical stimulus, and the sources of the biological potential at the periosteum (strong) and the marrow space (weak), disagreement between experiment and simulation evaluated by the percentage of pixels was lower than 7%. Taking into account that inevitably the experimental images are based on a small number of animals (which is in any case large compared to other animal experiments) and that the procedure to obtain the averaged images cannot be without ambiguity (Vetter et al. 2010a), this disagreement is satisfactory. Estimated values for the thresholds of the mechanical stimulus for cartilage ( $MS_c$ ) and bone formation ( $MS_b$ ) are, 12%  $\pm$  3% and 7%  $\pm$  1%. The interfragmentary strain theory (Perren and Cordey 1980) predicts cartilage formation for strains under 10% ( $MS_c$ ) and bone formation under 2% ( $MS_b$ ). One of the mechanobiological models of Isaksson and co-authors assumed the octahedral

strain as stimulus (Isaksson et al. 2006). The formation of cartilage and endochondral ossification was assumed for strains between 2.5 and 5%. Intramembranous ossification for immature bone was predicted for strains between 0.05% and 2.5% and intramembranous ossification of mature bone between 0.005% and 0.05%. Compared to these values, the results of the current study are higher but in the same strain range. The comparison with other simulation work is not straight forward as the simulations assume two mechanical stimuli for the regulation of tissue adaptation.

One feature of the experimental histological images was not observed in any of the simulations: the shift of the cartilage towards the fracture gap between stage III and stage IV in the healing process. The described simulations in this chapter have neither considered granulation tissue nor the process of bone resorption in order to reduce the number of mechanical thresholds by neglecting  $MS_t$  and  $MS_r$  of the mechanobiological model (Figure III.2). Especially, the process of bone resorption could influence the way of how cartilage forms. However, it remains as a challenge for future computational work to understand which biological motivated refinement of the model can be connected to this feature of the cartilage development during healing.

## IV. Simulating a self-healing material

In this last part of the thesis, the process of bone healing is investigated as a model system of a self-healing material (van der Zwaag 2007). The biological specifics, such as endochondral and intramembranous ossification, were disregarded. Compared to the mechanobiological model (Chapter 7.2), a more general model was set up which focuses only on how the local stiffening (or change of the local material property) is regulated and how this regulation influences the healing progression. The different types of biological cells were replaced by dynamical sensors (including a “repair unit”), which feel and respond to (bio)physical stimulation. A common type of sensor was assumed which means that all sensors followed the same behaviour. The model can be interpreted as the inverse problem of a fracture model (Hansen 2005). This terminology is reasonable, since beside of the model approach, simplifications are made, which are common in fracture models.

The questions asked with this approach were: how do sensors (or cells) have to respond to a (bio)physical stimulation in order to achieve an indirect way of healing by the formation of material bridge exterior to the gap? When does direct healing of the gap occur without this “detour”? And, in particular, how important is the influence of the local material environment (e.g. the local stiffness of the material) on the behaviour or sensitivity of the sensors?

In the model, there was no distinction between the phenotype of different materials. Accordingly, the tissue could be characterized only by its material property, which was a single scalar quantity. Each element changed its material property depending only on the local physical stimulus and its material property. The model did not distinguish between different cell types but assumed a common, dynamic sensor which could adapt its behaviour on the local material properties. Compared to the mechanobiological approach (see Chapter 7.2), the model gained generality by abolishing thresholds for the stimulation ( $ms_1$ ,  $ms_2$ ). The thresholds were replaced by a single response or feedback function  $f$ , which describes the local change of the material property as a function of the (bio)physical stimulus and the material property itself.

While the other parts of this thesis are under review or in the process of submitting, this last part of the thesis reports about work still under progress.

## 8. Exploring the cell sensitivity

The assumed response of cells to (bio)physical stimulation is the core of all iterative tissue adaptation simulations (Figure IV.1, left). The response can be modelled as the change of a local material property, e.g. the stiffness of the tissue. Generally, a positive or a negative response is possible, meaning either a local formation and maturation of a certain material, or a local resorption and de-maturation of material. Instead of modelling different cell types, the new model employs sensors (black boxes). The sensors feel the local environment and react accordingly in terms of changing the local material properties. The sensors are located at each site within the fracture area. The response of the sensors is defined by the feedback function  $f$ , which describes the material net-maturation depending on the actual stimulation in terms of the change of the local material properties (Figure IV.1, right).

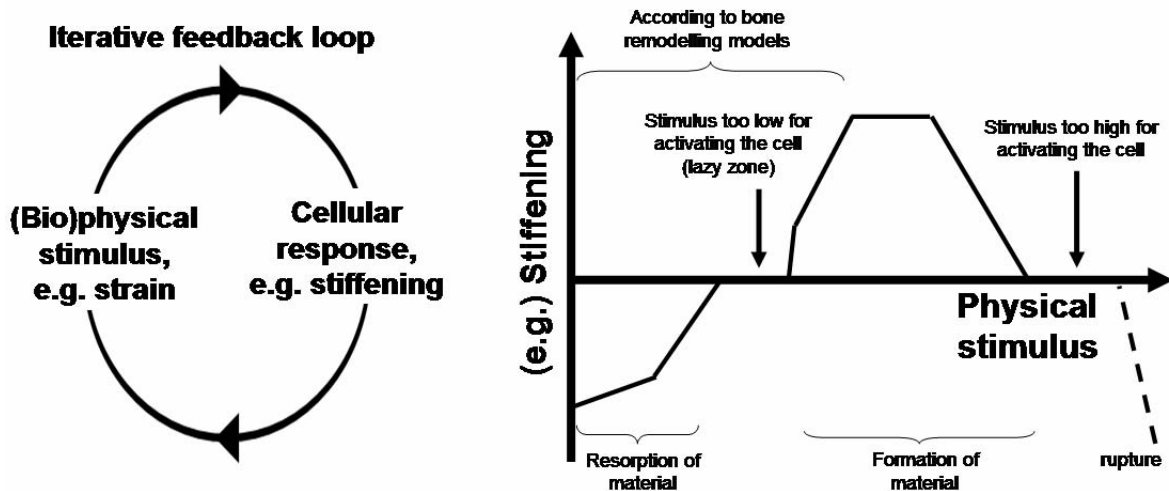


Figure IV.1: Schematic of tissue adaptation models.

Left: Feedback loop of a (bio)physical stimulus onto the cellular process (response of the cells to the stimulation). In iterative tissue adaptation models, the response is the formation or resorption of tissue and is, accordingly, modelled by a change of the local material property. Right: Feedback function which describes the change of the material properties by adding (formation) of new material or removing (resorption) of material depending on the amount of physical stimulation. The part of the area with low values of stimulation is derived from existing models of bone remodelling (Huiskes et al. 2000; Frost 2003; Weinkamer et al. 2004).

Existing models of bone remodelling were used (Huiskes et al. 2000; Frost 2003; Weinkamer et al. 2004) as a baseline for the feedback function  $f$  of the sensors. In case of very low stimulation, the models assume a net removal of bone material (Figure IV.1, right) because the material is not required from a mechanical viewpoint. For an intermediate amount of stimulation, new material is added resulting in a local stiffening. Some authors assume a "lazy zone" between the region of stimuli for bone resorption and formation (Frost 2003) resulting in no change of the amount of bone

material. In the case of bone healing, regions of very high stimulation can occur, e.g. in the fracture gap. Therefore, the feedback function has to be extended. Sensors which can not sustain the local stimulus do not produce new material. For even higher stimulation (or strains), the material would rupture (which is not investigated in the current model).

The shape of the feedback function  $f$  was assumed to be common for all sensors. However, dynamic sensors were assumed meaning that the sensors could adapt their behaviour to the material property of their surrounding material. The feedback function of the dynamical sensor was scaled vertically and horizontally according to a "set point" which depended on the local material property.

### 8.1. Reduction of the model complexity

The investigations in this chapter investigate the stiffening of the callus and do not aim to simulate "real" fracture healing with different tissue types. The complexity of the model could be reduced by:

- Substituting the mechanical system with a heat transfer system (see also Chapter 8.2 for details)
- Elements strictly defined by one material property (Conductivity  $L$ )
- Every element acts only on the amount of stimulation and its conductivity  $L$  (no biological potential)
- Usage of dimensionless parameters
- No bone resorption for the basic models

The static mechanical problem was replaced by a steady state heat transfer problem (described in detail in the Chapter 8.2). As there is no more distinction between different tissue types, the material is fully described by its material property (Figure IV.2). For the mechanical system it is the elastic modulus, for the heat transfer system, it is in an equivalent way the thermal conductivity  $L$ . The mechanical strain, stimulus in the previous model, is replaced by the gradient of the temperature field in the heat transfer system.

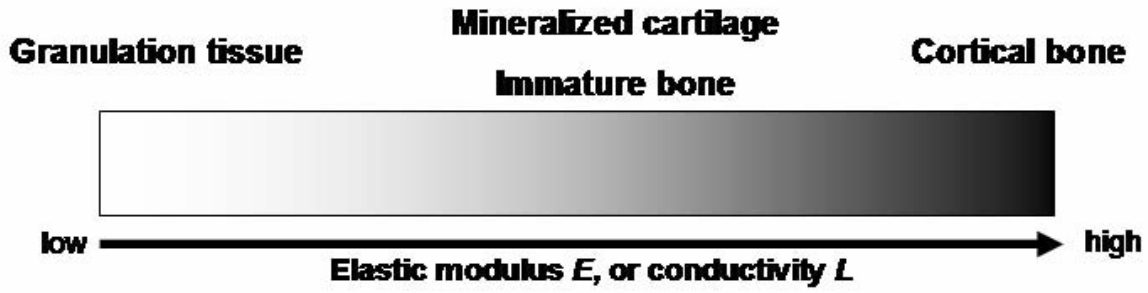


Figure IV.2: Schematic of the reduction of the complexity of the problem (indirect healing of a fracture gap).

The mechanical system of the mechanobiological model (Chapter 7) is replaced by a steady state heat transfer problem (Torquato 2001). The equivalent to the mechanical stiffness is the conductivity in the heat transfer problem. In the new model, only the material property determines the tissue type. Accordingly, there is no more distinction between mineralized cartilage (endochondral ossification) and immature bone (intramembranous ossification).

As a further reduction of the problem, the local influence of the biology was neglected. In the case of the mechanobiological model, that means that the biological potential was assumed to be homogeneously distributed within the callus. In other words, only the biophysical stimulation drives the tissue adaptation and each local element of the model acted in a common way on the stimulation.

## 8.2. Substitution of the mechanical system

In the mechanobiological model (Chapter 7), the mechanical system had to be solved in order to calculate the strains. A standard way to reduce the mathematical complexity is to rewrite a (steady state) mechanical problem (24),(25) as a problem of (steady state) heat transfer (26),(27) to reduce the rank of the tensors of the parameters (Torquato 2001). The material property tensor is reduced from a tensor of rank 4 (mechanical stiffness  $C$ ) to a tensor of rank 2 (conductivity  $L$ ). The strain tensor  $\varepsilon$  and the stress tensor  $\tau$  of rank 2 are reduced to the according vectors (gradient of the temperature  $T$  and heat flow  $j$ ).

$$\underline{\underline{\tau}}(\vec{x}) = \underline{\underline{C}}(\vec{x}) \cdot \underline{\underline{\varepsilon}}(\vec{x}) \quad (24)$$

$$\vec{\nabla} \cdot \underline{\underline{\tau}} = 0 \quad (25)$$

$$\underline{j}(\vec{x}) = \underline{L}(\vec{x}) \cdot \nabla T(\vec{x}) \quad (26)$$

$$\vec{\nabla} \cdot \underline{j} = 0 \quad (27)$$

$\tau$	Mechanical stress
$C$	Mechanical stiffness
$\varepsilon$	Mechanical strain

$j$	Heat flux
$L$	Conductivity
$T$	Temperature

For the modelling, linear elastic and isotropic behaviour is assumed. Accordingly, the material properties  $C$  in a mechanical system can be described by two material parameters, the elastic modulus and the Poisson ratio. In the case of heat transfer, the material parameter is the (scalar) conductivity  $L$ .

A scalar value or stimulus is desired by iterative tissue adaptation models in order to decide on local tissue maturation. In the mechanical system (Chapter 7), the strains were assumed to act as stimulus. The strain tensor is of rank 2 and has, therefore, three invariants. The question, which one of the invariants or even combinations of these invariants to use as stimulus, is open and different invariants have been investigated in literature. In the heat transfer system, the equivalent to the strains (the gradient field of the temperature) is a vector. Accordingly, the definition of the stimulus becomes straight forward and the length of the vector was chosen as scalar stimulus. The maturation of the material is modelled by an increase of the local conductivity  $L$ .

In the heat transfer problem, there are two unknown parameters (temperature  $T$  and heat flow  $j$ ) and two equations available (26),(27). The initial conductivity field  $L$  is given, there are no sources of heat flow within the modelled geometry (27) and the values of either the heat flow or the temperature on the boundaries are known.

### 8.3. Implementation and dimensionless parameters

The steady state heat flux problem was solved by a commercial FE program (ABAQUS v6.6, Hibbit Karlsson & Sorensen, Inc., RI, USA). The iterative adaptation of the elements was carried out by an external routine written in MATLAB (The Mathworks Inc., v 7.1). A two dimensional quadratic lattice model was implemented with 60 times 80 elements. The geometry and boundary conditions of the system (Figure IV.3) were motivated by the mechanobiological model of bone healing (Chapter 7). A constant heat influx  $j_{in}$  onto the cortex (equivalent to the applied force in the mechanical simulations) was assumed and the bottom temperature was set to a constant value  $T_{bottom}$  (equivalent to symmetrical boundary conditions along the horizontal axis in the mechanical simulations).



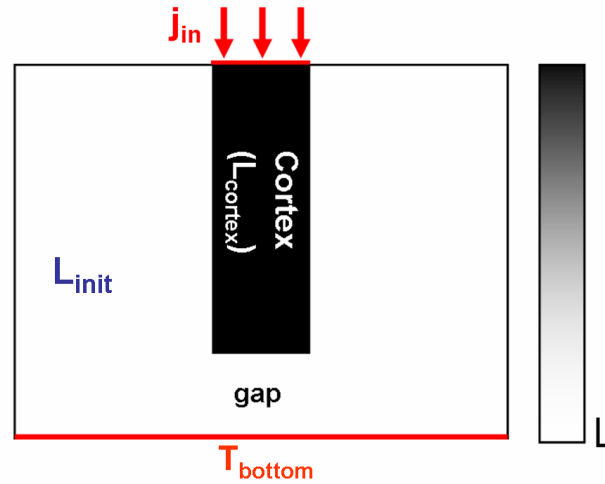


**Figure IV.3: Scheme of the geometry** (vertical axis-symmetry is assumed) and the applied initial and boundary conditions. The elements of the cortex have a high conductivity ( $L_{\text{cortex}}$ ), the other elements are initialized with a low conductivity  $L_{\text{init}}$ .

### Dimensions of the parameters

Reference values for the different parameters have to be defined in order to compute with dimensionless parameters. The model describes a process of bridging or healing in terms of an increase of the conductivity of the elements. As reference conditions, the initial conditions were chosen (initial callus conductivity, mean initial stimulus within the callus, fixed temperature at the bottom of the system).

- Conductivity  $L$

The conductivity can vary over four orders of magnitude from the lowest values describing granulation tissue (with an elastic modulus of 1 MPa) to the highest values describing cortex material (20 GPa). The dimensionless conductivity  $L_d$  is given in units of the initial material (28). Therefore, the initial conductivity in the callus is equal to 1 which results in a dimensionless conductivity of the cortex of 20,000.

$$L_d(\vec{x}) = \frac{L(\vec{x})}{L_{\text{init}}} \quad (28)$$

$L_d$	Dimensionless conductivity
$L$	Conductivity of an element
$L_{\text{init}}$	Initial conductivity of the elements within the callus

- Temperature  $T$

The temperature  $T_d$  is made dimensionless by relating it to the fixed temperature at the bottom of the system (29). The nodes at the bottom of the system are therefore set to 1 according to equation (29).

$$T_d(\vec{x}) = \frac{T(\vec{x})}{T_{bottom}} \quad (29)$$

$T_d$	Dimensionless temperature
$T$	Calculated temperature of an element
$T_{bottom}$	Fixed temperature at the bottom

- Physical stimulus  $S$

As physical stimulus  $S$  which regulates the behaviour of the black box (sensor/repair unit), the absolute value of the gradient of the temperature  $T_d$  is chosen (30). In the mechanical system, the equivalent to  $S$  is an invariant of the strain tensor. The mean initial stimulus within the callus,  $S_0$ , is one main net property of the initial environment (31). The dimensionless physical stimulus  $S_d$  is calculated by relating the local stimulus to  $S_0$  (32).

$$S(\vec{x}) = |\text{grad}(T_d(\vec{x}))| \quad (30)$$

$$S_0 = \frac{1}{N} \sum_{\vec{x}_i \in \text{callus}} S_{init}(\vec{x}_i) \quad (31)$$

$$S_d(\vec{x}) = \frac{S(\vec{x})}{S_0} \quad (32)$$

$S$	Physical stimulus
$S_0$	Mean physical stimulus in the callus at time step 0
$S_d$	Dimensionless stimulus
$N$	Number of the quadratic elements in the callus

### 8.4. Feedback of the system

Biological cells do not only feel their local mechanical stimulation, e.g (Perren 1979), but also their local environment. In particular, *in vitro* studies showed that cells feel the stiffness of the substrate which they were seeded onto (Discher et al. 2005; Engler et al. 2006; Schneider et al. 2007). Different cell types are mechanically stimulated in different strain ranges. For example, fibroblasts “like” strains in an order of magnitude of about 10% to produce fibrous tissue, while osteoblasts like several hundreds of microstrains (roughly about 0.05%) to lay down osteoid. Cells at sites with low local stiffness (e.g. fibroblast surrounded by fibrous tissue) add material which contributes to a smaller increase of stiffness compared to the increase

of cells in the region of high stiffness (e.g. osteoblasts). This is because fibroblasts lay down fibrous tissue which does not mature strongly (in absolute numbers) compared to the osteoid which mineralizes and increases its stiffness strongly (in absolute numbers).

The new model uses these facts as a “guide” for the behaviour of the dynamical sensors. Accordingly, the sensors are differently “sensitive” depending on the material they sit on. Furthermore, they change the local material properties in a different (absolute) amount. This is modelled by a feedback function, which does not only depend on the local stimulus but also on the local conductivity  $L$ . Figure IV.4 shows an example for a basic (rectangular) feedback function  $f$  neglecting any resorption. It was assumed that the feedback function  $f$  has the same shape for all sensors. In other words, the feedback function  $f$  was a family of parametric functions.

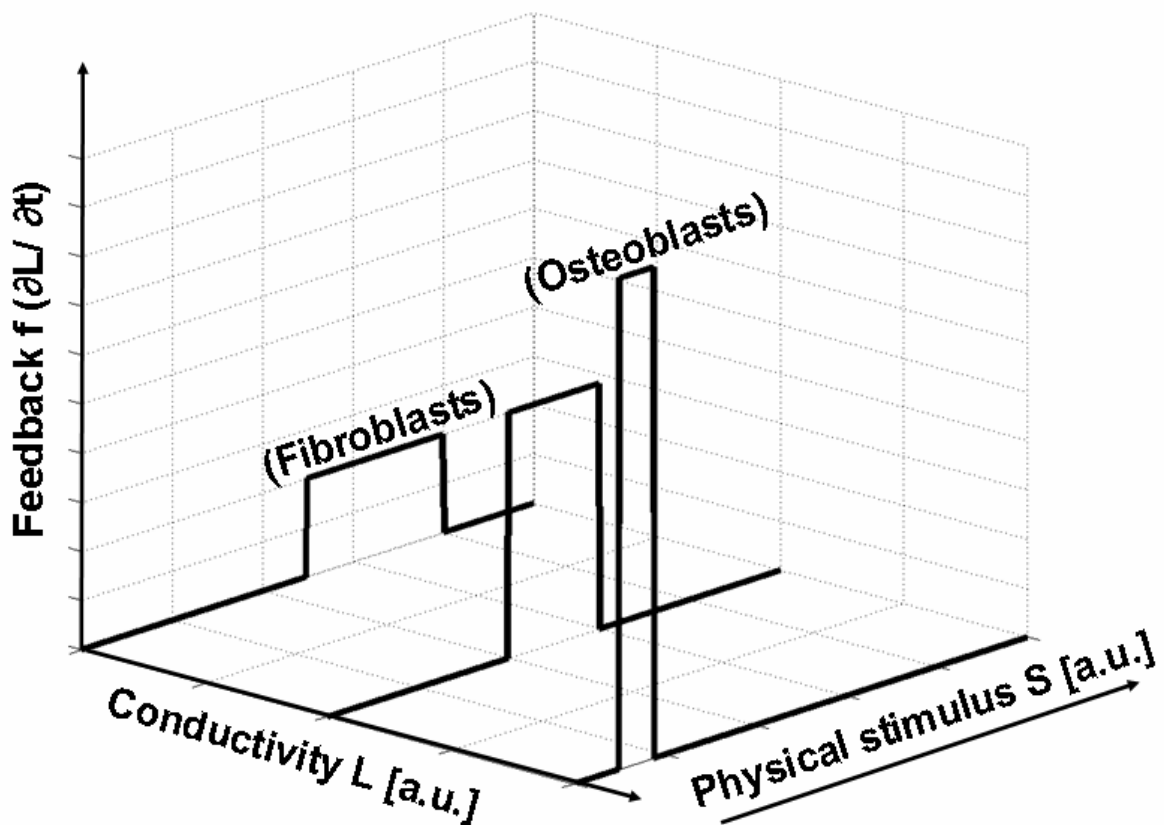


Figure IV.4: Example for a basic feedback function of the dynamic sensors (comprising a sensor and a repair unit) on the local (bio)physical stimulus and the conductivity.

In this model, the feedback is the change of the local conductivity  $L$ . The shape of the feedback function is assumed to be independent of conductivity. However, the sensors become more sensitive to the local stimulus the higher the conductivity of their surrounding material is (schematically shown for the case of bone healing by fibroblasts and osteoblasts). Furthermore, dynamic sensors surrounded by material with higher conductivity were assumed to change the local material properties more. The actual feedback function depending on  $L$  can

be found by horizontal and vertical scaling of the basic function (e.g, the feedback function for fibroblasts).

### Scaling of the feedback function $f$

The next step is to define the feedback function depending on the conductivity  $L$  and the stimulus  $S_d$ . To do so, the assumed basic function  $f$  was scaled in vertical and horizontal direction (33). The vertical scaling (scaling along  $f$ -axis) can be carried out by multiplication with an amplitude  $A$ . The sensor "sensitivity"  $z$ , which depends on the local conductivity  $L$ , is a useful parameter for the horizontal scaling (scaling along  $S$ -axis) of the feedback function. A linear dependency between the stimulus and the sensor sensitivity was assumed (33).

$$f(A, S_d, z) = A(L) \cdot f(S_d \cdot z(L)) \quad (33)$$

$A$  Amplitude of the feedback function  $f$

$S_d$  Dimensionless stimulus

$z$  Dimensionless sensitivity of the sensor as a function of the local conductivity  $L$

Next, the dependency of the sensor sensitivity  $z$  on the local conductivity  $L$  has to be quantified. To do so, the estimated ranges of a stimulation known by mechanobiological studies were "translated" into the according dimensionless parameters of the heat transfer model (Table 5). The stiffness (described by the elastic modulus  $E_{mat}$ ) of the tissues is known and the according range of positive mechanical stimulation (described by a mean strain  $\varepsilon$ ) to form new material was estimated. The dimensionless parameters of the conductivity  $L_d$  and stimulation  $S_d$  were calculated by defining the initial condition as equal to 1 (see also previous section for the definition of the dimensionless parameters). A cell or sensor which adds material to existing cortical bone requires 1/600 of the stimulation of a sensor adding initial (granulation) tissue, for example. The cell sensitivity was defined as the inverse of this estimated stimulus set point  $S_d$ . Accordingly, the cell sensitivity  $z$  of osteoblasts was estimated to be 600 times higher than the sensitivity of cells forming granulation tissue.

**Table 5: Overview of the material properties and the according stimuli in bone healing.**

The first two rows list the mechanical properties of the tissues (see Chapter 6.2) and the preferred strain ranges depending on the tissue. The values were estimated according to the results of Chapter 6.5 and (Perren and Cordey 1980; Claes and Heigele 1999; Isaksson et al. 2006). The next two rows show the according dimensionless parameters for a representation of the healing process in a heat transfer system, the dimensionless conductivity  $L_d$  and the preferred dimensionless physical stimulus  $S_d$ . The last row shows the sensitivity of the sensors (or cells) depending on their material (or tissue). The sensitivity is the inverse of the preferred dimensionless stimulus.

System	Property	Granulation tissue	Fibrous tissue	Cartilage	Immature Bone	Cortical bone
Mechanics	$E_{mat}$ [Pa]	$1 \cdot 10^6$	$2 \cdot 10^6$	$1 \cdot 10^7$	$5 \cdot 10^8$	$2 \cdot 10^{10}$
	$\varepsilon$ [ ]	$3 \cdot 10^{-1}$	$2 \cdot 10^{-1}$	$1 \cdot 10^{-1}$	$1 \cdot 10^{-2}$	$5 \cdot 10^{-4}$
Heat transfer	$L_d$ [ ]	1	2	10	500	20000
	$S_d$ [ ]	1	2/3	1/3	1/30	1/600
	$z$ [ ]	1	1.5	3	30	600

The estimated dependency of the sensitivity  $z$  of the local conductivity  $L_d$  (Table 5) could be well fitted by a power law (Figure IV.5). This fit was used to calculate the sensor sensitivity in the computer simulations in order to model a gradual adaptation of the dynamic sensors.

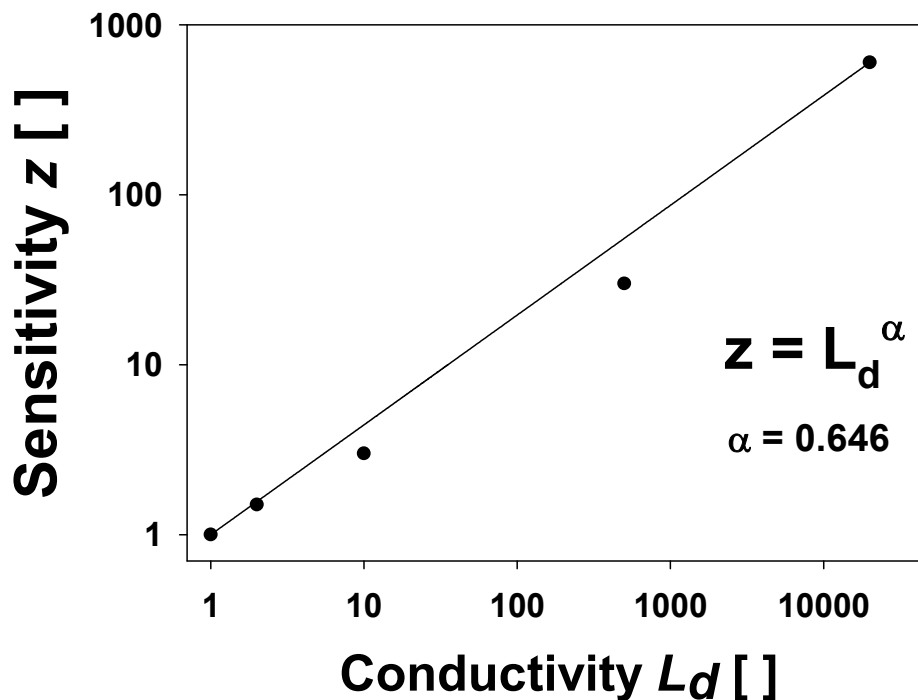


**Figure IV.5: Estimated dependency of the sensor's sensitivity  $z$  towards biophysical stimulation and the local material property (conductivity  $L$ ) of the sensor's environment. The more sensitive the sensor is the lower is the required biophysical stimulation.**

A vertical scaling (scaling in  $f$ -axis) can be carried out by multiplication with an amplitude  $A$  (33). This would require an estimated dependency between amplitude  $A$  of the function and the conductivity  $L$ . To circumvent this problem, the feedback was not calculated in absolute values (maturation rates) but as a percentage change in the local conductivity (34). This replaces the vertical scaling of a feedback function  $f$  for a model which applies maturation rates ( $dL/dt$ ) and no maturation rates have to be defined. Accordingly, the time is considered dimensionless (35). A test step carried out to calculate a new conductivity field. The result was scaled according to a desired maximal local change in conductivity. For the current study, the maximal value of the change was set to 5% ( $\Delta f_{d,max} = 0.05$ ). For the basic rectangular feedback function, stimulated elements added 5% to their current value of conductivity, while un-stimulated elements remained their value.

$$\frac{\partial}{\partial t}(\ln(L_d)) = \frac{\partial}{\partial t}\left(\frac{\Delta L_d}{L_d}\right) = f_d(S_d \cdot L_d^\alpha) \quad (34)$$

$$\Delta t_d = \frac{f_d(S_d \cdot L_d^\alpha)}{\Delta f_{d,max}} \quad (35)$$

$f_d$	dimensionless feedback (change of conductivity in per cent of the actual value of conductivity)
$S_d$	Dimensionless stimulus
$L_d$	Dimensionless conductivity
$\alpha$	Coupling between sensor sensitivity and local conductivity (0.646)
$t_d$	Dimensionless time
$\Delta f_{d,max}$	Maximal change in dimensionless conductivity per step

### 8.5. Results

Several simulations of the model with different feedback functions were run all with the assumption of an inert cortex (changes in the conductivity  $L$  were only allowed within the callus). First, a rectangular feedback function was tested as a basic model without resorption. Before running the simulations, the initial stimulus  $S_d$  was calculated and investigated (Figure IV.6, left). The mean stimuli at three different regions were used as "landmarks" (reference values). These landmarks were used for defining the two thresholds ( $S_{d1}$ ,  $S_{d2}$ ) of the rectangular functions (Figure IV.6, right). The landmarks were: the mean stimulus in the fracture gap (about 4 times as big as the initial mean stimulus  $S_0$ ), the outer fringe of the gap (about 1.3 times larger as  $S_0$ ), and the outer corner at the top (about 1% to 5% of  $S_0$ ). The investigated threshold values for the simulations were: 0.06, 0.5, 1.0, 1.3, 2, 4 and 5 times the value of  $S_0$ .

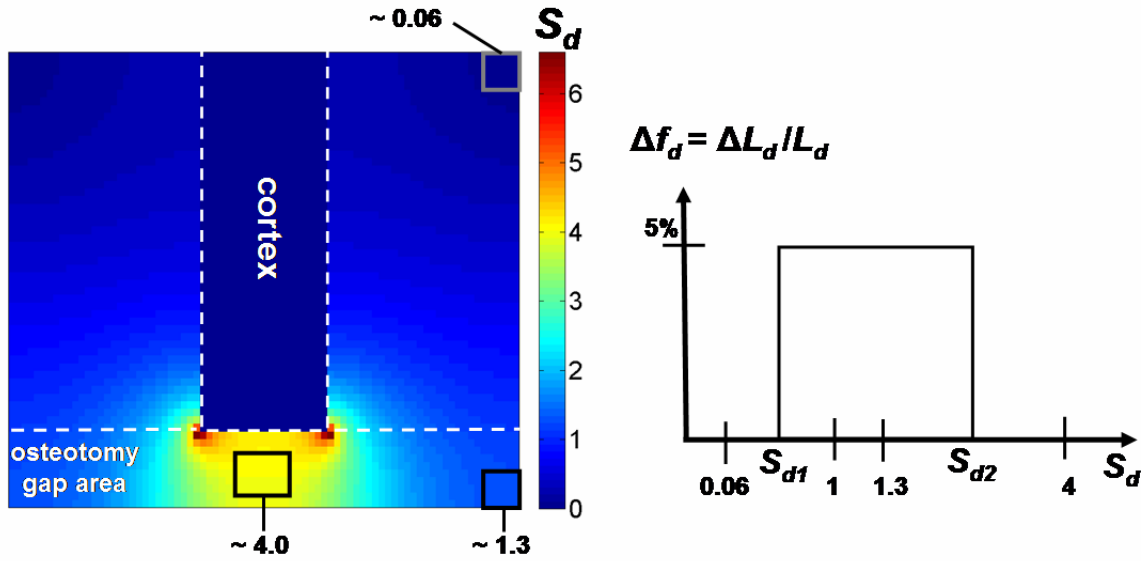
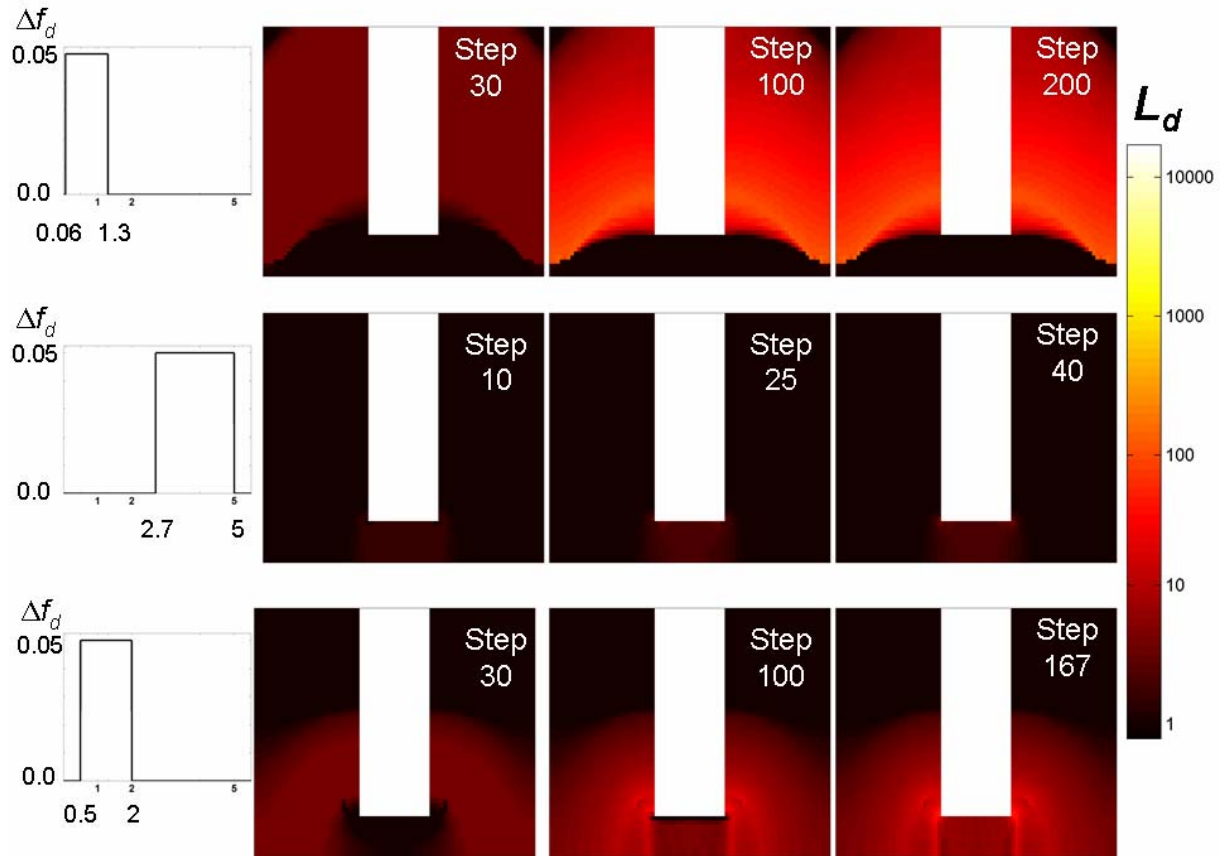


Figure IV.6: Dimensionless stimulus  $S_d$  at the initial time point.

The dimensionless stimulus is calculated by referring the actual stimulus  $S$  to the mean stimulus within the callus at the initial time point  $S_0$  ( $S_d = S/S_0$ ).

First, simulations were carried out without coupling of the feedback function and the local conductivity ( $\alpha = 0$ , see Eq. (35)). The simulations showed three main types of healing depending of the actual rectangular feedback function (Figure IV.7). The gap did not bridge at all for values of  $S_{d2} = 1.3$  or smaller (Figure IV.7, top). The initial stimulus was too high for the sensors within the gap and the formation of additional material was found only above the gap. This additional material leads to a decrease of the stimulus within the gap by increasing the area of load transmission. However, the decrease of the stimulus was not sufficient to allow a maturation of any element within the gap area (the stimulus remained higher than  $1.3 \cdot S_d$  within the gap). For threshold values around the initial stimulus in the fracture gap (Figure IV.7, middle), only the interfragmentary gap increased its conductivity. With this increase the stimulus in the interfragmentary gap became quickly smaller than the lower threshold  $S_{d1}$  ( $2.7 \cdot S_d$ ) and the bridging stopped. The simulations with a positive feedback around the initial mean stimulus within the callus  $S_0$  showed the most similarities to indirect bridging (Figure IV.7, bottom). However, the development of the callus stopped after 167 steps as every sensor received a stimulus below  $S_{d1}$  ( $0.5 \cdot S_d$ ).



**Figure IV.7: Simulations *without* coupling between feedback and local material properties. Different ways of gap bridging depending on the according feedback function (left). Top: no bridging of the gap, middle: direct bridging of the gap; bottom: indirect bridging of the gap**

Next, the simulations were carried out with coupling of the feedback function and the local conductivity ( $\alpha = 0.646$ , see Eq. (35)) and the same three types of healing were found (Figure IV.8). With coupling, the simulations did not stop as the sensors adapted to their local material (dynamic sensors). No bridging was found for low positive feedback but, compared to the case without coupling, a more distinct gap was simulated (Figure IV.8, top). Direct bridging of the gap was found for threshold values around the initial stimulus in the gap (Figure IV.8, middle). The initial stimulated elements within the gap increased their conductivity and the applied horizontal scaling of the feedback function (sensitiveness of the sensors to the local conductivity) ensured that the feedback was positive for the simulated healing time. Simulations with a positive feedback around the initial mean stimulus within the callus  $S_0$  showed the most similarities to indirect bridging (Figure IV.8, bottom). After an increase of  $L_d$  at the outer gap area, also  $L_d$  within the fracture gap began to increase. After 200 steps, the gap was bridged in the gap and, additionally, by an arch outside the fracture gap. The rectangular function caused the demand on a very small increase of the time step  $\Delta f_d$ . Simulations with  $\Delta f_d$  of 5% still showed some local effects of the choice of the time step (Figure IV.8, bottom). Smoothing the



feedback function results in a faster convergence of the solution and allows a higher values of  $\Delta f_d$  (Figure IV.9, top). To summarize this first investigations, a reasonable range for a positive feedback was estimated to be between  $0.5 S_0$  and  $2 S_0$ .

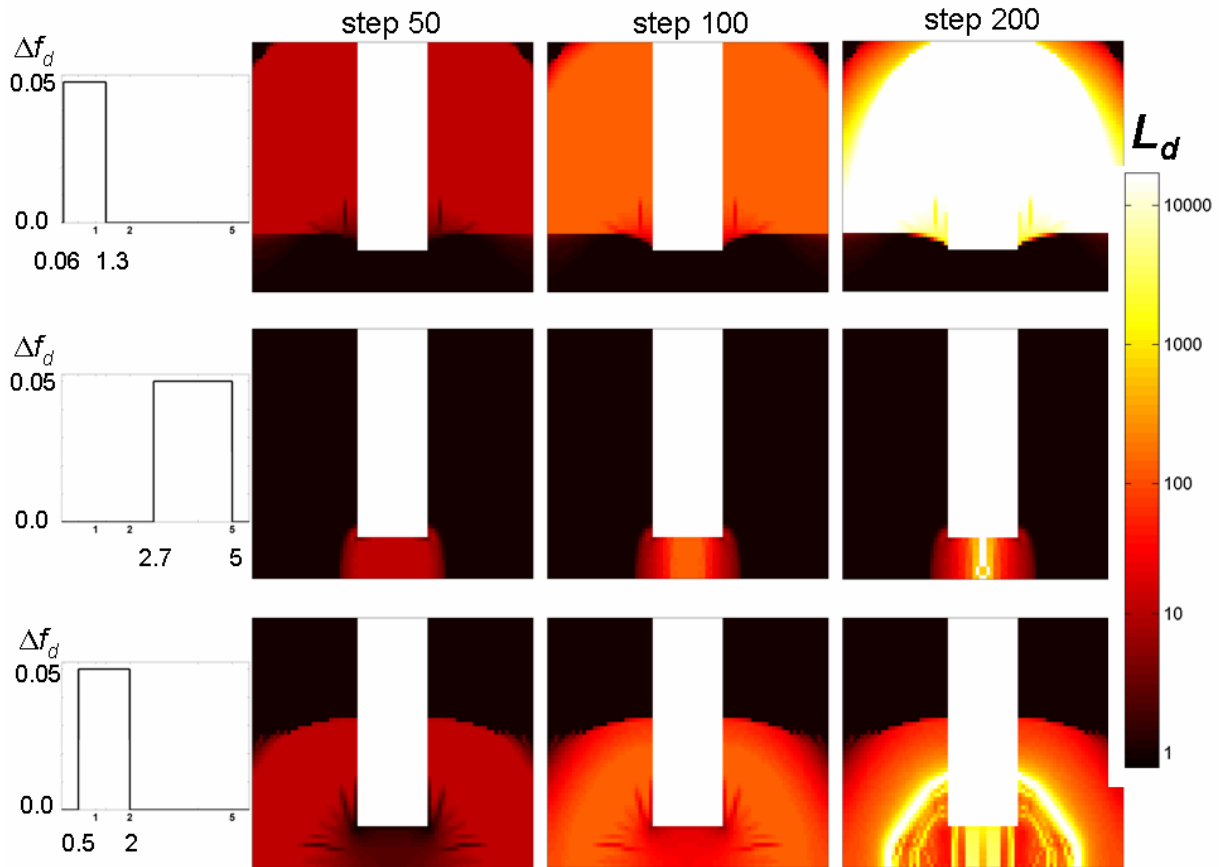


**Figure IV.8: Simulations *with* coupling between feedback and local material properties. Different ways of gap bridging depending on the according feedback function (left). Top: no bridging of the gap, middle: direct bridging of the gap; bottom: indirect bridging of the gap**

Finally, the influence of resorption was investigated. A positive feedback between values of 0.5 and 2 was assumed. The maximal increase and decrease in conductivity per step was assumed to be 5%. For comparison, the result for a “smoothed” rectangular feedback function (including a starting and ending ramp) without resorption is shown in Figure IV.9, top. Two simulations including the possibility of resorption were carried out to investigate the influence of a lazy zone (Figure IV.9, middle and bottom). In both simulations, the influence of the resorption was not very high. The simulation with lazy zone started the resorption from a stimulus below  $0.1 S_0$  (Figure IV.9, middle). The result of this simulation was very similar to the results without resorption. The effect of resorption became visible at the late stage of healing (see step 200, white arrow) when the outer area of the formed callus started to resorb. The simulation without lazy zone (Figure IV.9, bottom) showed resorption

## 8. Exploring the cell sensitivity

of the outer area of the callus starting early during the simulated healing progression (see step 50, white arrow). Additionally, this simulation showed a wider and less distinct bridging for both, the bridging in the gap region as well as the outside arch (see step 200, black arrows).

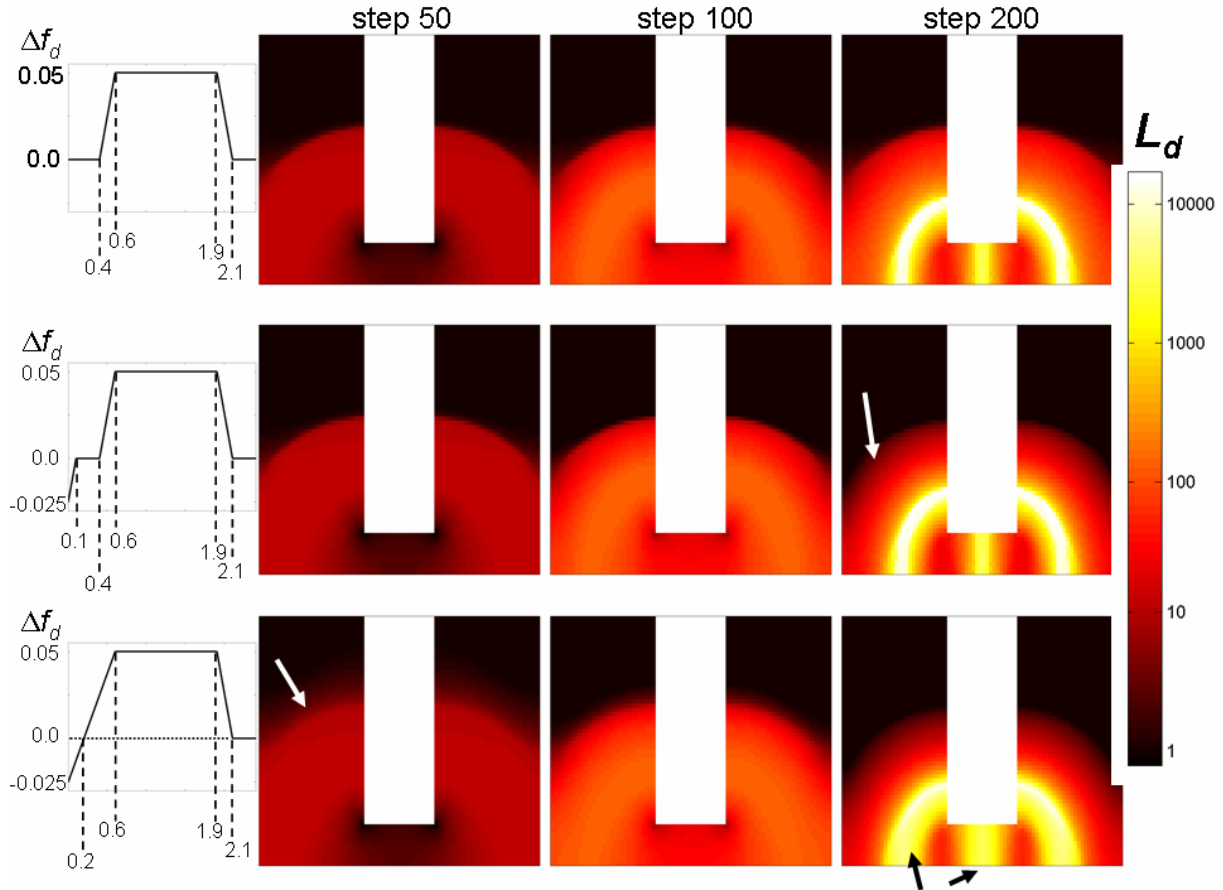


**Figure IV.9: Simulations (with coupling between feedback and local material properties) with a positive maximal feedback between  $0.6 S_0$  and  $1.9 S_0$ .**

A reference simulation was carried out without resorption (top). The second simulation assumed a lazy zone between resorption and formation of material (middle) and the third simulation was carried out without the lazy zone (bottom).

To quantify the interfragmentary changes, the development of the mean value of the stimulus  $S_d$  within the interfragmentary gap was investigated. Figure IV.10 shows this development for an indirect healing simulation (the first simulation in Figure IV.9). The decrease was very fast and in a semi-logarithmic plot almost linear. The initial value of the mean  $S_d$  was about 4 and decreased to about 1/1000 ( $S_d = 0.0035$ ) of the initial value after 200 steps.

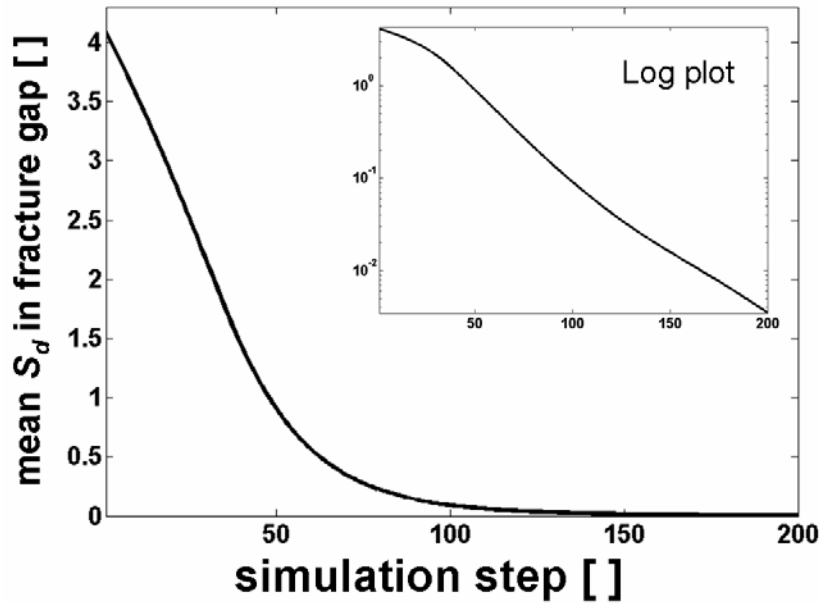


Figure IV.10: Development of the mean value of the stimulus  $S_d$  within the fracture gap (for the simulation at the top in Figure IV.9).

The mean  $S_d$  within the gap corresponds to the interfragmentary movement (IFM) in bone healing simulations.

### 8.6. Conclusions

This part investigated a material which has self healing capacity due to sensors which include repair units. The sensors were black boxes. The approach was driven and applied to bone fracture healing. However, the implemented model is not restricted to bone healing. The model incorporates a continuous adaptation of the sensors to their local environment in terms of the local material property  $L$ . This adaptation is not gradual for the case of bone healing. More likely, a certain site of the fracture with certain cells of a certain cell type is filled with more and more cells of a different cell type, which then influence the local change of the material property.

For the investigated basic behaviour (represented by basic feedback functions) of the sensors, it was found that the coupling between the sensor behaviour or “sensitivity” and the local material property was elementary for the healing progression. The choice of the initial set point of the dynamic sensors (represented by the choice of the two thresholds of a rectangular feedback function) was found to be crucial for the healing progression. An indirect bridging of the gap (= first, increase of the conductivity *outside* the fracture gap, then increase of the conductivity *within* the fracture gap) was found for a set point around the initial mean stimulus within the callus.

The simulations could reproduce an indirect bridging of the gap in a basic way. The difference between the conductivity within the cortical gap and the rest of the osteotomy gap area was not very high. The overall stiffening pattern of bone healing could be roughly simulated even without the influence of biological parameters. The development of the interfragmentary movement (*IFM*) depends strongly on the callus stiffness. Accordingly, also the current, very basic model was able to simulate the decrease of *IFM* over time as observed in animal experiments. This suggests that mechanobiological simulations need additional parameters to be validated with such as tissue type patterns. This is of particular importance as the *IFM* is difficult to measure accurately in an animal study.

The approach of assuming a common feedback function could be linked back to the mechanobiological approach from Chapter 7. The conclusions of the investigation of the mechanobiological model raised the idea to model the endochondral and intramembranous ossification separately. A suitable feedback function could be the input to an adapted mechanobiological model (Figure IV.11). The adapted model would still distinguish stringently between the different cell types but the previously used thresholds would be replaced by feedback functions, scaled according to the tissue.

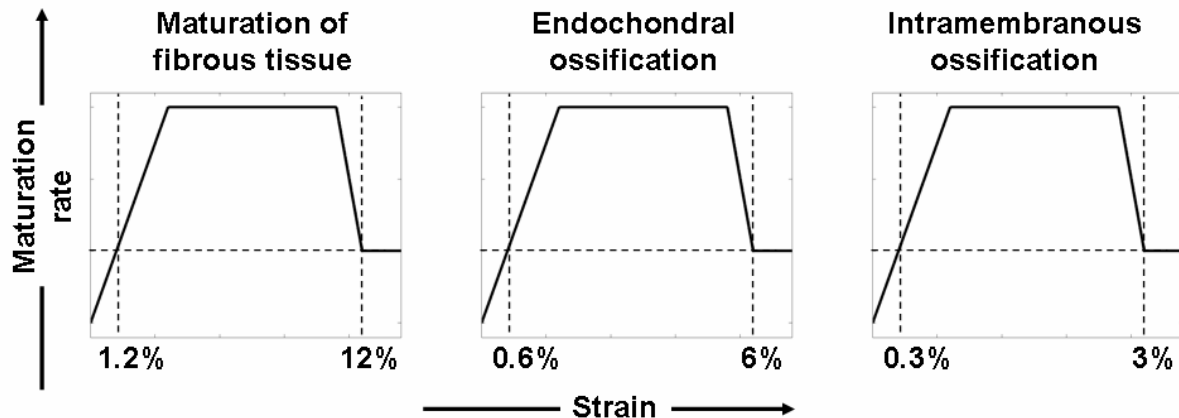


Figure IV.11: Incorporation of the investigated feedback function into the mechanobiological model of Chapter 7.

The mechanobiological model is refined by modeling bone formation separately for endochondral and intramembranous ossification. The maturation rates (for fibrous tissue and cartilage) and the transient maturation function for bone could be substituted by a percentaged increase of the local stiffness (as it was done in this current model) to reduce the complexity.

## 9. Summary and outlook

### Summary

Existing simulations of bone healing showed the general potential to explain the healing progression by employing mechanobiological theories. However, *quantitative* validation of the simulation results has been carried out mainly by comparing the *in silico* interfragmentary movement (*IFM*) or the *in silico* stiffness of the callus with the experimentally observed values. It has to be mentioned that additional *un-quantified* validations have been carried out, e.g. by comparing the tissue type development in the callus with experimentally derived impressions about the tissue type composition of the callus as the healing proceeds. This lack of comparison with experimental results is in a striking disproportion to the complexity of the used computer models.

To overcome this problem, the **first part** of this thesis started with the calculation of a *quantified* "norm" healing progression in terms of tissue type patterns described by a succession of six images ("snapshots"). The first bridging of the gap occurred by cartilage formation on the periosteal side of the callus. On the subsequent snapshot the cartilage region was found shifted towards the intercortical gap and the gap was bridged by bone on the periosteal and endosteal side. The six images provided the main experimental base for the further *in silico* work, and was extensively used for the comparison with the dynamical computer simulations.

In the **second part**, the six images of the norm healing and further experimental data on the mechanical properties were used to set up a model of the fracture callus, which considered the mechanical heterogeneity of the hard callus. Using the finite element method, it was found that this the mechanical heterogeneity of the hard callus (caused by local stiffening of the bone material and densification) influences strongly the local strains within the callus. One conclusion of this part of the work was therefore that the time-evolution of the mechanical properties of the newly formed bone should be modelled also in a dynamical simulation of bone healing. A second conclusion was obtained by a mechanobiological interpretation of the obtained strain distributions within the callus. The application of only one invariant of the strain tensor as mechanical stimulus showed good capability to explain the tissue differentiation on the periosteal and intercortical region of the callus.

In the **third part** of the thesis, a basic phenomenological model with a minimum set of simulation parameters was set up to dynamically simulate bone healing. Parameter studies have been performed by varying the two mechanobiological key parameters of the model: the threshold of the mechanical stimulus for bone and

cartilage formation, respectively. The basic model could explain the hard callus formation and the periosteal bridging by cartilage. A sharp gradient of the biological potential, which diffused into the callus, was found to be crucial to reproduce the periosteal cartilage bridging *in silico*. However, the shift of the cartilage during the healing progression could not be explained.

The **fourth part** analysed the healing process as a kind of converse problem of a fracture model. Accordingly the model did not include any biological influencing factors, but concentrated on the feedback between the local stimulation of the material and its healing response. The general way how the callus stiffens ("indirect healing" via exterior bridging) during bone healing could be simulated. An adaptation of the cells ("dynamical sensors") to their local material environment was crucial for simulating an indirect healing. The important conclusion is here that indirect healing can occur in a simulation model without resorting to an additional biological influence.

### Outlook

Two main limitations of this work are: (i) the experimental data is in 2D and the simulations assume rotational symmetry of the callus and (ii) the experimental data and the simulations are only based on a single animal species, namely sheep. It is known that the tissue distribution within the fracture callus is not rotational symmetric (Gerstenfeld et al. 2006) and that the way bone heals depends on the animal species (Mehta et al. 2008). The step from 2D to 3D is straight forward, however, it requires an increased amount of work. Besides longitudinal sections, also some transversal histological sections have to be evaluated to obtain a 3D averaged norm healing progression. The simulations and the comparison method between experiment and simulation can also be extended to 3D without the assumption of any symmetry. The averaging method can be used to evaluate experiments on other large and small animals. Firstly, this would enable the comparison of the progress of tissue patterns between different experiments on the same animals. Therefore, pathologies in the process of healing would be easier to identify. And secondly, it would clarify, which features of the healing process are specific for a given animal species and which are more general features of the healing process and should therefore be also transferable to humans.

Regarding the mechanobiological model itself, a variety of refinements is possible. However, any refinement should be in the spirit of the applied modelling approach, i.e. to explain new experimental observations. Any refinement should be phenomenological due to the lack of cellular data and data about signalling factors

within the callus. Two possible model refinements are: (i) including a separate mechanical threshold for the endochondral ossification and (ii) incorporating the influence of the local material stiffness on the cell behaviour. The first refinement is straight forward. The current model assumes that, in order to allow endochondral or intramembranous ossification to happen, the local strain has to be below a common value of strain. Endochondral ossification can probably occur under higher mechanical strains compared to intramembranous ossification. Possibly this refinement would allow a better description of the cartilage formation and resorption at intermediate stages of healing. The second refinement addresses the experimental observation that cells feel the stiffness of their surrounding tissue and the stiffness influences the cell behaviour (Engler et al. 2006). This cell behaviour can be incorporated in a phenomenological model approach by assuming an inertia of the modelled maturation processes. After a maturing element has reached some "inertia" point, the maturation of an element proceeds to the next tissue level even without any activating mechanical stimulation. The inertia point can be, for example, the mean value of the elastic modulus of the element's current tissue and the elastic modulus of the tissue, which the element matures to. For example, the inertia point of a maturing fibrous tissue element would be 6 MPa (the elastic modulus of unmaturing fibrous tissue is 2 MPa, the elastic modulus of cartilage is 10 MPa).

The investigation from the fourth part of this thesis provides a way to address further basic questions. Some of the main interesting questions are:

- How does the resorption of the cortex (as seen experimentally) influence the stiffening pattern within the callus?
- How does the stiffening pattern change when the cortex is thicker, the load smaller and the gap wider?
- Does a stress-driven feedback produce similar results compared with the investigated feedback of a combination of strain and material property?
- Considering a time-dependent load on the cortex: which load function optimizes the healing in terms of the fastest possible regeneration?

The last question is of clinical relevance. The question that arises from animal experiments is how to optimize the fracture fixation during the healing process. The analysis of the healing patterns (Chapter 5.2 and 5.6) and an *in vivo* study on sheep (Goodship et al. 1998) showed that a variable fixator rigidity can increase the speed of healing. An initially less rigid fixation of the fracture seems to be beneficial followed by more rigid fixation in the later healing phase. The precise timing of this flexible fixation is unknown and could be investigated *in silico*. Assuming a certain feedback

function to regulate the local healing response, the unknown would be the load function, which causes the fracture to heal fastest. Optimal control theory provides the theoretical framework to find the unknown load function.

Finally, the information and ideas found by this general model can be important input for the mechanobiological modelling. The optimized load function can be tested with the mechanobiological model *in silico*. The feedback behaviour of cells from Part IV can be used as a guide to replace the cell specific threshold values for mechanical stimulation, e.g.  $MS_b$ , with a smooth function.



## References

- Ament, C. and Hofer, E. P. (2000). "A fuzzy logic model of fracture healing." J Biomech **33**(8): 961-968.
- Andreykiv, A., van Keulen, F. and Prendergast, P. J. (2008). "Simulation of fracture healing incorporating mechanoregulation of tissue differentiation and dispersal/proliferation of cells." Biomechanics and Modeling in Mechanobiology **7**(6): 443-461.
- Auer, J. A., Goodship, A., Arnoczky, S., Pearce, S., Price, J., Claes, L., Von Rechenberg, B., Hofmann-Amttenbrinck, M., Schneider, E., Muller-Terpitz, R., Thiele, F., Rippe, K. P. and Grainger, D. W. (2007). "Refining animal models in fracture research: seeking consensus in optimising both animal welfare and scientific validity for appropriate biomedical use." Bmc Musculoskel Dis **8**: -.
- Augat, P., Burger, J., Schorlemmer, S., Henke, T., Peraus, M. and Claes, L. (2003). "Shear movement at the fracture site delays healing in a diaphyseal fracture model." J Orthop Res **21**(6): 1011-1017.
- Bailon-Plaza, A. and van der Meulen, M. C. H. (2001). "A mathematical framework to study the effects of growth factor influences on fracture healing." J Theor Biol **212**(2): 191-209.
- Bailon-Plaza, A. and van der Meulen, M. C. H. (2003). "Beneficial effects of moderate, early loading and adverse effects of delayed or excessive loading on bone healing." J Biomech **36**(8): 1069-1077.
- Barnes, G. L., Kakar, S., Vora, S., Morgan, E. E., Gerstenfeld, L. C. and Einhorn, T. A. (2008). "Stimulation of fracture-healing with systemic intermittent parathyroid hormone treatment." J Bone Joint Surg Am **90A**: 120-127.
- Bishop, N. E., van Rhijn, M., Tami, I., Corveleijn, R., Schneider, E. and Ito, K. (2006). "Shear does not necessarily inhibit bone healing." Clin Orthop Relat R(443): 307-314.
- Bolander, M. E. (1992). "Regulation of Fracture Repair by Growth-Factors." P Soc Exp Biol Med **200**(2): 165-170.
- Bonnarens, F. and Einhorn, T. A. (1984). "Production of a standard closed fracture in laboratory animal bone." J Orthop Res **2**(1): 97-101.
- Bostrom, M. P. G. (1998). "Expression of bone morphogenetic proteins in fracture healing." Clin Orthop Relat R(355): S116-S123.
- Bottlang, M., Mohr, M., Simon, U. and Claes, L. (2008). "Acquisition of full-field strain distributions on ovine fracture callus cross-sections with electronic speckle pattern interferometry." J Biomech **41**(3): 701-705.
- Brighton, C. T. and Hunt, R. M. (1986). "Histochemical-Localization of Calcium in the Fracture Callus with Potassium Pyroantimonate - Possible Role of Chondrocyte Mitochondrial Calcium in Callus Calcification." J Bone Joint Surg Am **68A**(5): 703-715.
- Buckwalter, J. A. (1996). Healing of the musculoskeletal tissues. Rockwood and Green's Fractures in Adults. C. A. e. a. Rockwood. Philadelphia, Lippincott-Raven: pp. 261-304.
- Carter, D. R. and Beaupre, G. S. (1999). "Linear elastic and poroelastic models of cartilage can produce comparable stress results: a comment on Tanck et al. (J Biomech 32 : 153-161, 1999)." J Biomech **32**(11): 1255-1256.
- Carter, D. R., Beaupre, G. S., Giori, N. J. and Helms, J. A. (1998). "Mechanobiology of skeletal regeneration." Clin Orthop Relat R(355): S41-S55.

- Carter, D. R., Blenman, P. R. and Beaupre, G. S. (1988). "Correlations between Mechanical-Stress History and Tissue Differentiation in Initial Fracture-Healing." J Orthop Res **6**(5): 736-748.
- Carter, D. R. and Hayes, W. C. (1978). "Compressive Behavior of Trabecular Bone." J Biomech **11**(4): 209-209.
- Checa, S. and Prendergast, P. J. (2009). "A Mechanobiological Model for Tissue Differentiation that Includes Angiogenesis: A Lattice-Based Modeling Approach." Ann Biomed Eng **37**(1): 129-145.
- Claes, L., Augat, P., Suger, G. and Wilke, H. J. (1997). "Influence of size and stability of the osteotomy gap on the success of fracture healing." J Orthop Res **15**(4): 577-584.
- Claes, L., Eckert-Hubner, K. and Augat, P. (2003). "The fracture gap size influences the local vascularization and tissue differentiation in callus healing." Langenbecks Arch Chir **388**(5): 316-322.
- Claes, L. E. and Heigele, C. A. (1999). "Magnitudes of local stress and strain along bony surfaces predict the course and type of fracture healing." J Biomech **32**(3): 255-266.
- Claes, L. E., Heigele, C. A., Neidlinger-Wilke, C., Kaspar, D., Seidl, W., Margevicius, K. J. and Augat, P. (1998). "Effects of mechanical factors on the fracture healing process." Clin Orthop Relat R(355): S132-S147.
- Claes, L. E., Wilke, H. J., Augat, P., Rubenacker, S. and Margevicius, K. J. (1995). "Effect of Dynamization on Gap Healing of Diaphyseal Fractures under External Fixation." Clin Biomech **10**(5): 227-234.
- Coles, C. P. and Gross, M. (2000). "Closed tibial shaft fractures: Management and treatment complications. A review of the prospective literature." Can J Surg **43**(4): 256-262.
- Colnot, C. (2009). "Skeletal Cell Fate Decisions Within Periosteum and Bone Marrow During Bone Regeneration." J Bone Miner Res **24**(2): 274-282.
- Cowin, C. C. (2001). Bone Mechanics Handbook, 2nd edition. New York, Informa Healthcare.
- Cruess, R. L. and Dumont, J. (1975). "Fracture Healing." Can J Surg **18**(5): 403-&.
- Cullinane, D. M., Salisbury, K. T., Alkhiary, Y., Eisenberg, S., Gerstenfeld, L. and Einhorn, T. A. (2003). "Effects of the local mechanical environment on vertebrate tissue differentiation during repair: does repair recapitulate development?" J Exp Biol **206**(14): 2459-2471.
- Currey, J. D. (2006). Bones: Structure and Mechanics, 1st edition. New Jersey, Princeton University Press.
- Discher, D. E., Janmey, P. and Wang, Y. L. (2005). "Tissue cells feel and respond to the stiffness of their substrate." Science **310**(5751): 1139-1143.
- Duda, G. N., Eckert-Hubner, K., Sokiranski, R., Kreutner, A., Miller, R. and Claes, L. (1998). "Analysis of inter-fragmentary movement as a function of musculoskeletal loading conditions in sheep." J Biomech **31**(3): 201-210.
- Duda, G. N., Taylor, W. R., Winkler, T., Matziolis, G., Heller, M. O., Haas, N. P., Perka, C. and Schaser, K. D. (2008). "Biomechanical, microvascular, and cellular factors promote muscle and bone regeneration." Exerc Sport Sci Rev **36**(2): 64-70.
- Dunlop, J. W. C., Hartmann, M. A., Brechet, Y. J., Fratzl, P. and Weinkamer, R. (2009). "New Suggestions for the Mechanical Control of Bone Remodeling." Calcified Tissue Int **85**(1): 45-54.

- Einhorn, T. A. (1998). "The cell and molecular biology of fracture healing." Clin Orthop Relat R **355**: S7-S21.
- Engler, A. J., Sen, S., Sweeney, H. L. and Discher, D. E. (2006). "Matrix elasticity directs stem cell lineage specification." Cell **126**(4): 677-689.
- Epari, D. R. (2006). The Mechanobiology of Diaphyseal Secondary Bone Healing - Chapter 5, TU Berlin.
- Epari, D. R., Schell, H., Bail, H. J. and Duda, G. N. (2006a). "Instability prolongs the chondral phase during bone healing in sheep." Bone **38**(6): 864-870.
- Epari, D. R., Taylor, W. R., Heller, M. O. and Duda, G. N. (2006b). "Mechanical conditions in the initial phase of bone healing." Clin Biomech **21**(6): 646-655.
- Eriksen, E. F., Melsen, F., Sod, E., Barton, I. and Chines, A. (2002). "Effects of long-term risedronate on bone quality and bone turnover in women with postmenopausal osteoporosis." Bone **31**(5): 620-625.
- Fratzl, P., Gupta, H. S., Paschalis, E. P. and Roschger, P. (2004). "Structure and mechanical quality of the collagen-mineral nano-composite in bone." J Mater Chem **14**(14): 2115-2123.
- Fratzl, P. and Weinkamer, R. (2007). "Nature's hierarchical materials." Prog Mater Sci **52**(8): 1263-1334.
- Frost, H. M. (2003). "Bone's mechanostat: A 2003 update." Anat Rec Part A **275A**(2): 1081-1101.
- Fung, Y. C. (2004). Introduction - A sketch of the history and scope of the field. Biomechanics - Mechanical Properties of Living Tissue. Berlin, Springer.
- Galilei, G. (1638). Discorsi e dimostrazioni matematiche, intorno a due nuove scienze. Leiden, Lowys Elsevier
- Gao, H. J., Ji, B. H., Jager, I. L., Arzt, E. and Fratzl, P. (2003). "Materials become insensitive to flaws at nanoscale: Lessons from nature." P Natl Acad Sci USA **100**(10): 5597-5600.
- Garcia, P., Holstein, J. H., Maier, S., Schaumloffel, H., Al-Marrawi, F., Hannig, M., Pohlemann, T. and Menger, M. D. (2008). "Development of a reliable non-union model in mice." J Surg Res **147**(1): 84-91.
- Gardner, M. J., van der Meulen, M. C. H., Demetrakopoulos, D., Wright, T. M., Myers, E. R. and Bostrom, M. P. (2006). "In vivo cyclic axial compression affects bone healing in the mouse tibia." J Orthop Res **24**(8): 1679-1686.
- Gardner, T. N., Evans, M. and Simpson, H. (1998). "Temporal variation of applied inter fragmentary displacement at a bone fracture in harmony with maturation of the fracture callus." Med Eng Phys **20**(6): 480-484.
- Gardner, T. N., Hardy, J., Evans, M. and Kenwright, J. (1997). "Temporal changes in dynamic inter fragmentary motion and callus formation in fractures." J Biomech **30**(4): 315-321.
- Geris, L., Sloten, J. V. and Van Oosterwyck, H. (2009). "In silico biology of bone modelling and remodelling: regeneration." Philos T R Soc A **367**(1895): 2031-2053.
- Geris, L., Vander Sloten, J. and van Oosterwyck, H. (2008). An integrated mathematical modelling framework for the study of bone fracture healing. 16th ESB Congress, Journal of Biomechanics, 41(S1).
- Gerstenfeld, L. C., Alkhiary, Y. M., Krall, E. A., Nicholls, F. H., Stapleton, S. N., Fitch, J. L., Bauer, M., Kayal, R., Graves, D. T., Jepsen, K. J. and Einhorn, T. A. (2006). "Three-dimensional reconstruction of fracture callus morphogenesis." Journal of Histochemistry & Cytochemistry **54**(11): 1215-1228.

- Gerstenfeld, L. C., Cullinane, D. M., Barnes, G. L., Graves, D. T. and Einhorn, T. A. (2003). "Fracture healing as a post-natal developmental process: Molecular, spatial, and temporal aspects of its regulation." J Cell Biochem **88**(5): 873-884.
- Giannoudis, P. V., Einhorn, T. A. and Marsh, D. (2007). "Fracture healing: The diamond concept." Injury **38**: S3-S6.
- Gibson, L. J. (2005). "Biomechanics of cellular solids." J Biomech **38**(3): 377-399.
- Gibson, L. J. and Ahsby, M. F. (1999). Cellular solids, structure and properties, 2nd edition. Cambridge, UK, Cambridge University Press, p. 510.
- Glowacki, J. (1998). "Angiogenesis in fracture repair." Clin Orthop Relat R(355): S82-S89.
- Gomez-Benito, M. J., Garcia-Aznar, J. M., Kuiper, J. H. and Doblare, M. (2006). "A 3D computational simulation of fracture callus formation: Influence of the stiffness of the external fixator." Journal of Biomechanical Engineering-Transactions of the Asme **128**(3): 290-299.
- Goodship, A. E., Cunningham, J. L. and Kenwright, J. (1998). "Strain rate and timing of stimulation in mechanical modulation of fracture healing." Clin Orthop Relat R(355): S105-S115.
- Goodship, A. E., Watkins, P. E., Rigby, H. S. and Kenwright, J. (1993). "The Role of Fixator Frame Stiffness in the Control of Fracture-Healing - an Experimental-Study." J Biomech **26**(9): 1027-1035.
- Greiner, S., Kadow-Romacker, A., Wildernann, B., Schwabe, P. and Schmidmaier, G. (2007). "Bisphosphonates incorporated in a poly(D,L-lactide) implant coating inhibit osteoclast like cells in vitro." J Biomed Mater Res A **83A**(4): 1184-1191.
- Gruber, R., Koch, H., Doll, B. A., Tegtmeier, F., Einhorn, T. A. and Hollinger, J. O. (2006). "Fracture healing in the elderly patient." Exp Gerontol **41**(11): 1080-1093.
- Gupta, H. S., Seto, J., Wagermaier, W., Zaslansky, P., Boesecke, P. and Fratzl, P. (2006). "Cooperative deformation of mineral and collagen in bone at the nanoscale." P Natl Acad Sci USA **103**(47): 17741-17746.
- Haas, N. P. (2000). "Callusmodulation - Fiktion oder Realität?" Der Chirurg **71**: 987-988.
- Hansen, A. (2005). "Physics and fracture." Comput Sci Eng **7**(5): 90-95.
- Harrison, L. J., Cunningham, J. L., Stromberg, L. and Goodship, A. E. (2003). "Controlled induction of a pseudarthrosis: A study using a rodent model." J Orthop Trauma **17**(1): 11-21.
- Heim, A. J., Matthews, W. G. and Koob, T. J. (2006). "Determination of the elastic modulus of native collagen fibrils via radial indentation." Appl Phys Lett **89**(18): -.
- Hente, R., Fuchtmeier, B., Schlegel, U., Ernstberger, A. and Perren, S. M. (2004). "The influence of cyclic compression and distraction on the healing of experimental tibial fractures." J Orthop Res **22**(4): 709-715.
- Hollinger, J. and Wong, M. E. K. (1996). "The integrated processes of hard tissue regeneration with special emphasis on fracture healing." Oral Surg Oral Med O **82**(6): 594-606.
- Höntzsch, D. (1997). "Fixateur-externe-Montagen mit dem AO-Rohrsystem." OP-Journal **13**: 18-21.

- Hori, R. Y. and Lewis, J. L. (1982). "Mechanical-Properties of the Fibrous Tissue Found at the Bone-Cement Interface Following Total Joint Replacement." J Biomed Mater Res **16**(6): 911-927.
- Huiskes, R., Ruimerman, R., van Lenthe, G. H. and Janssen, J. D. (2000). "Effects of mechanical forces on maintenance and adaptation of form in trabecular bone." Nature **405**(6787): 704-706.
- Huiskes, R., Weinans, H. and Vanrietbergen, B. (1992). "The Relationship between Stress Shielding and Bone-Resorption around Total Hip Stems and the Effects of Flexible Materials." Clin Orthop Relat R(274): 124-134.
- Ilizarov, G. A. (1989). "The Tension Stress Effect on the Genesis and Growth of Tissues .1. The Influence of Stability of Fixation and Soft-Tissue Preservation." Clin Orthop Relat R(238): 249-281.
- Isaksson, H., van Donkelaar, C. C., Huiskes, R. and Ito, K. (2008a). "A mechano-regulatory bone-healing model incorporating cell-phenotype specific activity." J Theor Biol **252**(2): 230-246.
- Isaksson, H., van Donkelaar, C. C., Huiskes, R., Yao, J. and Ito, K. (2008b). "Determining the most important cellular characteristics for fracture healing using design of experiments methods." J Theor Biol **255**(1): 26-39.
- Isaksson, H., van Donkelaar, C. C. and Ito, K. (2009). "Sensitivity of tissue differentiation and bone healing predictions to tissue properties." J Biomech **42**(5): 555-564.
- Isaksson, H., Wilson, W., van Donkelaar, C. C., Huiskes, R. and Ito, K. (2006). "Comparison of biophysical stimuli for mechano-regulation of tissue differentiation during fracture healing." J Biomech **39**(8): 1507-1516.
- Jager, I. and Fratzl, P. (2000). "Mineralized collagen fibrils: A mechanical model with a staggered arrangement of mineral particles." Biophys J **79**(4): 1737-1746.
- Jagodzinski, M. and Krettek, C. (2007). "Effect of mechanical stability on fracture healing - an update." Injury **38**: S3-S10.
- Jakob, F., Seefried, L., Ebert, R., Eulert, J., Wolf, E., Schieker, M., Bocker, W., Mutschler, W., Amling, M., Pogoda, P., Schinke, T., Liedert, A., Blakytyn, R., Ignatius, A. and Claes, L. (2007). "Fracture healing in osteoporosis." Osteologie **16**(2): 71-84.
- Javadieh, F., Bayat, M., Abdi, S., Mohsenifar, Z. and Razi, S. (2009). "The Effects of Infrared Low-Level Laser Therapy on Healing of Partial Osteotomy of Tibia in Streptozotocin-Induced Diabetic Rats." Photomed Laser Surg **27**(4): 641-646.
- Kaspar, K., Matziolis, G., Strube, P., Senturk, U., Dormann, S., Bail, H. J. and Duda, G. N. (2008). "A New Animal Model for Bone Atrophic Nonunion: Fixation by External Fixator." J Orthop Res **26**(12): 1649-1655.
- Kenwright, J. and Goodship, A. E. (1989). "Controlled Mechanical Stimulation in the Treatment of Tibial Fractures." Clin Orthop Relat R(241): 36-47.
- Klein, P., Schell, H., Streitparth, F., Heller, M., Kassi, J. P., Kandziora, F., Bragulla, H., Haas, N. P. and Duda, G. N. (2003). "The initial phase of fracture healing is specifically sensitive to mechanical conditions." J Orthop Res **21**(4): 662-669.
- Kratzel, C., Bergmann, C., Duda, G., Greiner, S., Schmidmaier, G. and Wildemann, B. (2008). "Characterization of a rat osteotomy model with impaired healing." Bmc Musculoskel Dis **9**: -.
- Kuiper, J. H., Ashton, B. A. and Richardson, J. B. (2000). Computer simulation of fracture callus formation and stiffness restoration. 12th Conference of European Society of Biomechanics, Dublin.

- Kuiper, J. H., Richardson, J. B. and Ashton, B. A. (1996). Mechanical signals in early fracture callus. 10th Conference of the European Society of Biomechanics, Leuven.
- Lacroix, D. and Prendergast, P. J. (2002). "A mechano-regulation model for tissue differentiation during fracture healing: analysis of gap size and loading." J Biomech **35**(9): 1163-1171.
- Lambers, F. M., Kuhn, G., Gerhard, F. A. and Muller, R. (2009). "In vivo micro computed tomography allows monitoring of load induced microstructural bone adaptation." Bone **44**(2): S300-S300.
- Leong, P. L. and Morgan, E. F. (2008). "Measurement of fracture callus material properties via nanoindentation." Acta Biomater **4**(5): 1569-1575.
- Lienau, J., Schell, H., Duda, G. N., Seebeck, P., Muchow, S. and Ball, H. J. (2005). "Initial vascularization and tissue differentiation are influenced by fixation stability." J Orthop Res **23**(3): 639-645.
- Lienau, J., Schmidt-Bleek, K., Peters, A., Haschke, F., Duda, G. N., Perka, C., Bail, H. J., Schutze, N., Jakob, F. and Schell, H. (2009). "Differential Regulation of Blood Vessel Formation between Standard and Delayed Bone Healing." J Orthop Res **27**(9): 1133-1140.
- Lill, C. A., Winterstein, E., Eckhardt, C., Rahn, B., Goldhahn, J. and Schneider, E. (2003). "Quantification of histomorphometric and structural bone changes in a sheep model for fracture treatment in osteoporotic bone." Vet Comp Orthopaed **16**(4): 243-249.
- Liu, Y., Manjubala, I., Epari, D. R., Roschger, P., Schell, H., Fratzl, P. and Duda, G. N. (2009a). Influence of fixator stability on mechanical competence of healing callus - a nanoindentation study in a sheep osteotomy model. Poster presentation. Symposium: Biomechanics and Biology of Bone Regeneration. Berlin.
- Liu, Y., Manjubala, I., Roschger, P., Epari, D. R., Schell, H., Duda, G. N. and Fratzl, P. (2009b). "Size and habit of mineral particles in bone and mineralized callus during sheep bone healing." J Bone Miner Res **under review**.
- Locke, M. (2004). "Structure of long bones in mammals." J Morphol **262**(2): 546-565.
- Lynch, J. R., Taitsman, L. A., Barei, D. P. and Nork, S. E. (2008). "Femoral nonunion: Risk factors and treatment options." J Am Acad Orthop Sur **16**(2): 88-97.
- Madison, M. and Martin, R. B. (1993). Fracture healing. Operative Orthopaedics. M. W. Chapman. Philadelphia, Lippincott: pp. 221-228.
- Malizos, K. N. and Papatheodorou, L. K. (2005). "The healing potential of the periosteum Molecular aspects." Injury **36**: 13-19.
- Manjubala, I., Liu, Y., Epari, D. R., Roschger, P., Schell, H., Fratzl, P. and Duda, G. N. (2009). "Spatial and temporal variations of mechanical properties and mineral content of the external callus during bone healing." Bone **45**(2): 185-192.
- McKibbin, B. (1978). "Biology of Fracture Healing in Long Bones." J Bone Joint Surg Br **60**(2): 150-162.
- Mehta, M., Schell, H., Kaspar, K. and Duda, G. N. (2008). "Differences in the healing pathways: Rat model vs. sheep model." Calcified Tissue Int **82**: S71-S72.
- Mehta, M., Strube, P., Perka, C. and Duda, G. N. (2009). "Influence of gender and mechanical stability on bone defect healing: Males show a stronger biological response than females." Bone **44**(2): S264-S264.

- Mollon, B., da Silva, V., Busse, J. W., Einhorn, T. A. and Bhandari, M. (2008). "Electrical Stimulation for Long-Bone Fracture-Healing: A Meta-Analysis of Randomized Controlled Trials." J Bone Joint Surg Am **90A**(11): 2322-2330.
- Morgan, E. F., Bayraktar, H. H. and Keaveny, T. M. (2003). "Trabecular bone modulus-density relationships depend on anatomic site." J Biomech **36**(7): 897-904.
- Morgan, E. F., Gleason, R. E., Hayward, L. N. M., Leong, P. L. and Palomares, K. T. S. (2008). "Mechanotransduction and fracture repair." J Bone Joint Surg Am **90A**: 25-30.
- Morgan, E. F., Longaker, M. T. and Carter, D. R. (2006). "Relationships between tissue dilatation and differentiation in distraction osteogenesis." Matrix Biology **25**(2): 94-103.
- Owen, M. (1970). "The origin of bone cells." International Review of Cytology **28**: 213-238.
- Park, S. H., O'Connor, K., McKellop, H. and Sarmiento, A. (1998). "The influence of active shear or compressive motion on fracture-healing." J Bone Joint Surg Am **80A**(6): 868-878.
- Park, S. H. and Silva, M. (2004). "Neuromuscular electrical stimulation enhances fracture healing: results of an animal model." J Orthop Res **22**(2): 382-387.
- Pauly, S., Luttosch, F., Morawski, M., Haas, N. P., Schmidmaier, G. and Wildemann, B. (2009). "Simvastatin locally applied from a biodegradable coating of osteosynthetic implants improves fracture healing comparable to BMP-2 application." Bone **45**(3): 505-11.
- Pauwels, F. (1960). "Eine neue Theorie über den Einfluß mechanischer Reize auf die Differenzierung im Stützgewebe." Z Anat Entwicklungsgeschichte **121**: 478-515.
- Perez, M. A. and Prendergast, P. J. (2007). "Random-walk models of cell dispersal included in mechanobiological simulations of tissue differentiation." J Biomech **40**(10): 2244-2253.
- Perren, S. M. (1979). "Physical and Biological Aspects of Fracture-Healing with Special Reference to Internal-Fixation." Clin Orthop Relat R(138): 175-196.
- Perren, S. M. and Cordey, J. (1980). The concept of interfragmentary strain. Current Concepts of Internal Fixation of Fractures. H. K. Uthoff. Berlin, Springer-Verlag: 67-77.
- Peterlik, H., Roschger, P., Klaushofer, K. and Fratzl, P. (2006). "From brittle to ductile fracture of bone." Nat Mater **5**(1): 52-55.
- Prendergast, P. J., Huiskes, R. and Soballe, K. (1997). "Biophysical stimuli on cells during tissue differentiation at implant interfaces." J Biomech **30**(6): 539-548.
- Reginster, J. Y. and Burlet, N. (2006). "Osteoporosis: A still increasing prevalence." Bone **38**(2): 4-9.
- Reichert, J. C., Saifzadeha, S., Wullschlegel, M. E., Epari, D. R., Schutz, M. A., Duda, G. N., Schell, H., van Griensven, M., Redl, H. and Hutmacher, D. W. (2009). "The challenge of establishing preclinical models for segmental bone defect research." Biomaterials **30**(12): 2149-2163.
- Reilly, D. T. and Burstein, A. H. (1975). "Elastic and Ultimate Properties of Compact Bone Tissue." J Biomech **8**(6): 393-&.
- Rhineland, F. W. (1968). "Normal Microcirculation of Diaphyseal Cortex and Its Response to Fracture." J Bone Joint Surg Am **A 50**(4): 784-&.

- Rho, J. Y., Kuhn-Spearing, L. and Zioupos, P. (1998). "Mechanical properties and the hierarchical structure of bone." Med Eng Phys **20**(2): 92-102.
- Richards, M., Goulet, J. A., Weiss, J. A., Waanders, N. A., Schaffler, M. B. and Goldstein, S. A. (1998). "Bone regeneration and fracture healing - Experience with distraction osteogenesis model." Clin Orthop Relat R(355): S191-S204.
- Robling, A. G., Castillo, A. B. and Turner, C. H. (2006). "Biomechanical and molecular regulation of bone remodeling." Annu Rev Biomed Eng **8**: 455-498.
- Ryaby, J. T. (1998). "Clinical effects of electromagnetic and electric fields on fracture healing." Clin Orthop Relat R(355): S205-S215.
- Schaffler, M. B. and Burr, D. B. (1988). "Stiffness of Compact-Bone - Effects of Porosity and Density." J Biomech **21**(1): 13-16.
- Schell, H., Epari, D. R., Kassi, J. P., Bragulla, H., Bail, H. J. and Duda, G. N. (2005). "The course of bone healing is influenced by the initial shear fixation stability." J Orthop Res **23**(5): 1022-1028.
- Schell, H., Lienau, J., Epari, D. R., Seebeck, P., Exner, C., Muchow, S., Bragulla, H., Haas, N. P. and Duda, G. N. (2006). "Osteoclastic activity begins early and increases over the course of bone healing." Bone **38**(4): 547-554.
- Schell, H., Thompson, M. S., Bail, H. J., Hoffmann, J. E., Schill, A., Duda, G. N. and Lienau, J. (2008). "Mechanical induction of critically delayed bone healing in sheep: Radiological and biomechanical results." J Biomech **41**(14): 3066-3072.
- Schindeler, A., Morse, A., Harry, L., Godfrey, C., Mikulec, K., McDonald, M., Gasser, J. A. and Little, D. G. (2008). "Models of tibial fracture healing in normal and Nf1-deficient mice." J Orthop Res **26**(8): 1053-1060.
- Schmidt-Bleek, K., Schell, H., Kolar, P., Pfaff, M., Perka, C., Buttgerit, F., Duda, G. and Lienau, J. (2009). "Cellular Composition of the Initial Fracture Hematoma Compared to a Muscle Hematoma: A Study in Sheep." J Orthop Res **27**(9): 1147-1151.
- Schneider, A., Richert, L., Francius, G., Voegel, J. C. and Picart, C. (2007). "Elasticity, biodegradability and cell adhesive properties of chitosan/hyaluronan multilayer films." Biomed Mater **2**(1): S45-S51.
- Seto, J., Gupta, H. S., Zaslansky, P., Wagner, H. D. and Fratzl, P. (2008). "Tough lessons from bone: Extreme mechanical anisotropy at the mesoscale." Adv Funct Mater **18**(13): 1905-1911.
- Setton, L. A., Mow, V. C., Muller, F. J., Pita, J. C. and Howell, D. S. (1997). "Mechanical behavior and biochemical composition of canine knee cartilage following periods of joint disuse and disuse with remobilization." Osteoarthritis Cartilage **5**(1): 1-16.
- Sfeir, C., Ho, C., Doll, B. A., Azari, K. and Hollinger, J. O. (2005). Fracture Repair. Bone Regeneration and Repair. J. R. Lieberman and G. E. Friedlaender. Totowa, Humana Press Inc.: 21-43.
- Strube, P., Sentuerk, U., Riha, T., Kaspar, K., Mueller, M., Kasper, G., Matziolis, G., Duda, G. N. and Perka, C. (2008). "Influence of age and mechanical stability on bone defect healing: Age reverses mechanical effects." Bone **42**(4): 758-764.
- Sturmer, E. K., Seidlova-Wuttke, D., Sehmisch, S., Rack, T., Wille, J., Frosch, K. H., Wuttke, W. and Sturmer, K. M. (2006). "Standardized bending and breaking test for the normal and osteoporotic metaphyseal tibias of the rat: Effect of estradiol, testosterone, and raloxifene." J Bone Miner Res **21**(1): 89-96.



- Tarr, R. R. and Wiss, D. A. (1986). "The Mechanics and Biology of Intramedullary Fracture Fixation." Clin Orthop Relat R(212): 10-17.
- Thompson, M. S., Schell, H., Lienau, J. and Duda, G. N. (2007). "Digital image correlation: A technique for determining local mechanical conditions within early bone callus." Med Eng Phys **29**(7): 820-823.
- Toben, D., Metha, M., Schell, H., Kolanczyk, M., Mundlos, S. and Duda, G. (2009). "Fracture healing in the mouse - The NF1wflox/floxPrx1Cre mouse as a pseudarthrosis model in neurofibromatosis 1." Bone **44**(2): S275-S276.
- Torquato, S. (2001). Random Heterogeneous Materials: Microstructure and Macroscopic Properties. Berlin, Springer.
- Utvag, S. E., Grundnes, O. and Reikeraas, O. (1996). "Effects of periosteal stripping on healing of segmental fractures in rats." J Orthop Trauma **10**(4): 279-284.
- van der Meulen, M. C. H. and Huiskes, R. (2002). "Why mechanobiology? A survey article." J Biomech **35**(4): 401-414.
- van der Zwaag, S., Ed. (2007). Self Healing Materials - An alternative approach to 20 centuries of Materials Science. Springer Series in Material Science. Berlin, Springer.
- Vetter, A., Epari, D. R., Seidel, R., Schell, H., Fratzl, P., Duda, G. N. and Weinkamer, R. (2010a). "Temporal tissue patterns in bone healing of sheep." J Orthop Res **DOI 10.1002/jor.21175**.
- Vetter, A., Liu, Y., Witt, F., Manjubala, I., Fratzl, P., Duda, G. N. and Weinkamer, R. (2010b). "The mechanical heterogeneity of the hard callus influences the local strains during bone healing " J Biomech (**under review**).
- Victoria, G., Petrisor, B., Drew, B. and Dick, D. (2009). "Bone stimulation for fracture healing: Whats all the fuss." Indian J Orthop **43**(2): 117-120.
- Vincent, J. F. V. (1990). Structural biomaterials. Princeton, Princeton University Press.
- Waarsing, J. H., Day, J. S., van der Linden, J. C., Ederveen, A. G., Spanjers, C., De Clerck, N., Sasov, A., Verhaar, J. A. N. and Weinans, H. (2004). "Detecting and tracking local changes in the tibiae of individual rats: a novel method to analyse longitudinal in vivo micro-CT data." Bone **34**(1): 163-169.
- Watson, M. A., Mathias, K. J. and Maffulli, N. (2000). "External ring fixators: an overview." P I Mech Eng H **214**(H5): 459-470.
- Webb, J. C. J. and Tricker, J. (2000). "A review of fracture healing." Curr Orthopaed **14**(6): 457-463.
- Wei, X. C., Rasanen, T. and Messner, K. (1998). "Maturation-related compressive properties of rabbit knee articular cartilage and volume fraction of subchondral tissue." Osteoarthr Cartilage **6**(6): 400-409.
- Weiner, S. and Wagner, H. D. (1998). "The material bone: Structure mechanical function relations." Annu Rev Mater Sci **28**: 271-298.
- Weinkamer, R., Hartmann, M. A., Brechet, Y. and Fratzl, P. (2004). "Stochastic lattice model for bone remodeling and aging." Phys Rev Lett **93**(22): -.
- Wendeberg, B. (1961). "Mineral metabolism of fractures of the tibia in man studied with external counting of strontium." Acta Orthopaedics Scandinavica Suppl. **52**(1-79).
- Willenegger, H., Perren, S. M. and Schenk, R. (1971). "Primary and Secondary Healing of Bone Fractures." Chirurg **42**(6): 241-&.

- Woesz, A., Stampfl, J. and Fratzl, P. (2004). "Cellular solids beyond the apparent density - an experimental assessment of mechanical properties." Adv Eng Mater **6**(3): 134-138.
- Wolff, J. (1892). Das Gesetz der Transformation der Knochen. Berlin, Hirschwald.
- Yamada, H. (1970). Strength of Biological Materials. Baltimore, Williams and Wilkins.
- Yamagishi, M. and Yoshimura, Y. (1955). "The biomechanics of fracture healing." J Bone Joint Surg **37A**: 1035-1068.
- Yoo, J. U., Barthel, T. S., Nishimura, K., Solchaga, L., Caplan, A. I., Goldberg, V. M. and Johnstone, B. (1998). "The chondrogenic potential of human bone-marrow-derived mesenchymal progenitor cells." J Bone Joint Surg Am **80A**(12): 1745-1757.
- Zysset, P. K. (2003). "A review of morphology-elasticity relationships in human trabecular bone: theories and experiments." J Biomech **36**(10): 1469-1485.

## Appendix

### Appendix to Chapter 7.4

Overview of the values describing the mismatch between simulation and experiment

Firstly, only the area fractions,  $a$ , of the three occurring tissue types in the callus, fibrous tissue (ft), cartilage (c) and hard callus or bone (b), were compared. The mismatch in area fractions for each stage,  $m_{area, stage}$  was obtained by summing the difference of the area fractions for each tissue type,  $tt$ , and calculating the mean value (Eq. A1). The mean value of the three  $m_{area, stage}$  values,  $m_{area}$  (Eq. A2) was calculated to describe the mismatch of a complete simulation run.

Secondly, the spatial information of the images was considered by a pixel-to-pixel comparison between two images. Three scalar quantities were calculated based on such a one-to-one comparison between pixels in the experimental and the simulated image. The first quantity,  $p_{tt}$ , considered only the tissue type and was "1" for pixels with a mismatch in tissue type, and "0" for matching tissue type (Eq. A3). The second quantity,  $p$ , took into account that elements of the hard callus contain additional information, their bone area fraction,  $BA/TA$ . A straightforward extension of the pixel-to-pixel comparison, resulting in  $p_{tt}$ , is to calculate the difference in the  $BA/TA$  values in the case that both compared pixels have the tissue type bone (Eq. A4). To emphasize the importance of amount and location of the formed cartilage, a third quantity,  $p_c$  was calculated, which takes only the mismatching cartilage pixels into account. Accordingly,  $p_c$  is defined as 0 if both compared pixels were cartilage or both pixels were not cartilage, otherwise  $p_c$  is 1 (Eq. A5).

The mismatching pixels for each image were summed up and divided by the total number of pixels in the callus to quantify the pixel-based mismatch of experimental and simulated image. This was carried out for all three types of comparison (Eq. A6 – Eq. A8) resulting in the quantified mismatch for a stage  $m_{comparison, stage}$ . In the case of cartilage comparison, the sum over all  $p_c$  was normalized by the number of cartilage pixels in the experimental image in order to quantify the cartilage mismatch for an image (Eq. A8). In order to quantify the mismatch of a simulation run, the average of the three compared healing stages were calculated resulting in the value  $m_{comparison}$  (Eq. A9 – Eq. A11).

$$m_{area,stage} = \frac{1}{3} \cdot \sum_{tt=1}^3 |a_{tt,exp} - a_{tt,sim}| \quad (A1)$$

$$m_{area} = \frac{1}{3} \cdot \sum_{stage=II}^{IV} m_{area,stage} \quad (A2)$$

$$p_{tt} = \begin{cases} 0 & \text{Both pixels the same type} \\ 1 & \text{Pixels different type} \end{cases} \quad (A3)$$

$$p = \begin{cases} 0 & \text{Both pixels the same type} \\ 1 & \text{Pixels different type} \\ |(BA/TA)_{sim} - (BA/TA)_{exp}| & \text{Both pixels bone} \end{cases} \quad (A4)$$

$$p_c = \begin{cases} 0 & \text{Both pixels no cartilage or both pixels cartilage} \\ 1 & \text{Otherwise} \end{cases} \quad (A5)$$

$$m_{tt,stage} = \frac{1}{N_{callus}} \cdot \sum_{i=1}^N p_{tt}^i \quad (A6)$$

$$m_{stage} = \frac{1}{N_{callus}} \cdot \sum_{i=1}^N p^i \quad (A7)$$

$$m_{c,stage} = \frac{1}{2 N_c^{exp,stage}} \cdot \sum_{i=1}^N p_c^i \quad (A8)$$

$$m_{tt} = \frac{1}{3} \cdot \sum_{stage=II}^{IV} m_{tt,stage} \quad (A9)$$

$$m = \frac{1}{3} \cdot \sum_{stage=II}^{IV} m_{stage} \quad (A10)$$

$$m_c = \frac{1}{3} \cdot \sum_{stage=II}^{IV} m_{c,stage} \quad (A11)$$

<i>Sim</i>	Simulational value
<i>exp</i>	Experimental value
<i>a</i>	Area
<i>tt</i>	Tissue type (ft: fibrous tissue, c: cartilage, b: bone)
<i>p</i>	Error of one pixel to pixel comparison
<i>BA/TA</i>	Bone area fraction
<i>m<sub>..,II</sub></i>	Mismatch of one stage (image), here stage II
<i>m</i>	Mismatch of one simulation run
<i>N</i>	Number of compared pixels

## Glossary

Apoptosis	Programmed cell death activated by the cell itself
Angiogenesis	Formation of new blood vessels
Atrophy	The process of wasting away (shrivelling) of cells or tissue, e.g. due to malnutrition
Bone marrow	Soft and fatty tissue, containing diverse cell types, within a long bone
Callus	Tissue formed during bone healing
Chemotaxis	Phenomenon in which cells move according to certain chemicals in their environment
Chondroblast	Cartilage forming cells
Chondrogenesis	Formation of cartilage
Cytokine	Substance which carries signals locally between cells
Differentiation	Process which leads a cell to become a more specialized cell
Distal	In direction away from the body centre
Endogenous	Within the body
Endosteum	Thin layer of connective tissue on the inner surface (towards the medullary cavity) of long bones
Fibroblast	Cell which forms fibrous tissue
Fixator	Device for the fixation of a fracture
Growth factor	Biochemical cellular stimulant
Hemostasis	Process which stops the bleeding (generally by blood clotting)
Histology	Science of the anatomy of cells and tissues
Histomorphometry	Quantification of number of cells or amount of tissue
Hypertrophy	Enlargement of a cell or tissue due to increased cell activity
Hypoxic	A pathological condition in which the body as a whole or region of the body is deprived of adequate oxygen supply
IFM - Interfragmentary movement	Movement of the two fracture ends towards or

	away of each other
IFS - Interfragmentary strain	Strain within the fracture gap due to interfragmentary movement
<i>In silico</i>	In the computer, computer based
<i>In vitro</i>	In physiological conditions (outside the animal)
<i>In vivo</i>	In the living animal
Interfragmentary	Between the ends of a bone cap
Interstitial fluid	The intercellular fluid
Lateral	In direction towards the outside
Macrophage	Cells of the immune system
Medial	In direction towards the centre
Medullary cavity	Central cavity of bone shafts filled with bone marrow
Mesenchymal stem cell (MSC)	Multipotent cell which means that MSC can differentiate into more specific cells such as fibroblasts, for example
Necrotic (cell)	Premature dead cell in living tissue
Non-union	A fracture which has stopped to heal
Osteoblast	Cell which lays down osteoid
Osteogenesis	Formation of bone
Osteoid	Unmineralized, organic portion of the bone matrix that forms prior to the maturation (calcification) of bone tissue
Osteon	Cylindrical bone unit (in cortical bone)
Osteotomy	Surgical cut through a bone in order to shorten, lengthen or change the alignment of the bone
Ovine	Pertaining to the sheep
Periosteum	Thin layer of connective tissue on the outer surface of long bones
Primary bone healing	Direct healing of a thin fracture (crack) without the formation of an external callus
Proliferation	Cell reproduction by cell division
Proximal	In direction towards the body centre
Secondary bone healing	Common way of fracture healing by formation of an external callus
Tibia	Shin bone
Trauma	Injury

## List of publications

### Manuscripts:

A. Vetter, R. Seidel, D.R. Epari, H. Schell, P. Fratzl, G.N. Duda, R. Weinkamer

"Temporal tissue pattern in bone healing of sheep"

Journal of Orthopaedic Research, 2010, DOI: 10.1002/jor.21175

J. Blacklock, A. Vetter, A. Lankenau, D. Oupický, H. Möhwald

"Tuning the mechanical properties of bioresorbable multilayer films for improved cell adhesion and transfection activity"

Biomaterials, 2010, DOI: 10.1016/j.biomaterials.2010.06.002

A. Vetter, Y. Liu, F. Witt, I. Manjubala, O. Sander, D.R. Epari, P. Fratzl, G.N. Duda, R. Weinkamer

"The mechanical heterogeneity of the hard callus influences local tissue strains during bone healing"

Journal of Biomechanics (under review)

A. Vetter, F. Witt, O. Sander, G.N. Duda, R. Weinkamer

"Simulation of spatial-temporal arrangement of different tissues during bone healing"

Biomechanics and Modeling in Mechanobiology (under review)

F. Witt, A. Petersen, R. Seidel, A. Vetter, R. Weinkamer, G.N. Duda

"Endochondral ossification is driven by mechanobiological rules: validation using in-vivo histological data of medial and lateral callus formation"

Journal of Biomechanics (under review)

### Poster presentations:

A. Vetter, R. Seidel, D.R. Epari, H. Schell, P. Fratzl, G.N. Duda, R. Weinkamer (2008)

35<sup>th</sup> European Symposium on Calcified Tissues, Barcelona, Spain

"Identifying typical patterns of bone healing to understanding endogenous tissue formation", Calcified Tissue International, 2008, Volume 82, Supplement 1, S79

A. Vetter, F. Witt, D.R. Epari, R. Seidel, P. Fratzl, G.N. Duda, R. Weinkamer (2009)

4<sup>th</sup> International Conference on Computational Bioengineering, Bertinoro (Flore), Italy

"Temporal patterns of different tissue types during fracture healing: experiment vs. simulation", Book of Abstracts p. 170

### Talks:

A. Vetter, R. Seidel, D.R. Epari, H. Schell, P. Fratzl, G.N. Duda, R. Weinkamer (2008)

35<sup>th</sup> European Clinical Symposium on Bone and Tissue Regeneration, Berlin, Germany

"Understanding bone healing patterns for different loading conditions"

A. Vetter, F. Witt, R. Seidel, P. Fratzl, G.N. Duda, R. Weinkamer (2010)

Osteologie – Interdisziplinärer Kongress, Berlin, Germany

“Quantification and simulation of different tissue type patterns during fracture healing:  
experiment vs. simulation”



**First manuscript (Vetter et al. 2010a)****Temporal tissue patterns in bone healing of sheep**

Journal of Orthopaedic Research

DOI: 10:1002/jor.21175, published online May 24, 2010

A. Vetter (1), D.R. Epari (2,3), R. Seidel (2), H. Schell (2), P. Fratzl (1), G.N. Duda (2), R. Weinkamer (1)

1. Max Planck Institute of Colloids and Interfaces, Department of Biomaterials, 14424 Potsdam, Germany

2. Julius Wolff Institut and Center for Musculoskeletal Surgery, Charité – Universitätsmedizin, 13353 Berlin, Germany

3. Institute of Health and Biomedical Innovation, Queensland University of Technology, Brisbane, Qld 4059, Australia

**Abstract**

Secondary fracture healing in long bones leads to the successive formation of intricate patterns of tissues in the newly formed callus. The main aim of this work was to quantitatively describe the topology of these tissue patterns at different stages of the healing process and to generate averaged images of tissue distribution. This averaging procedure is based on stained histological sections (2, 3, 6 and 9 weeks post-op) of 64 sheep with a 3 mm tibial mid-shaft osteotomy, stabilized either with a rigid or a semi-rigid external fixator. The averaged images were obtained for both fixation types and the lateral and medial side separately. For each case, the result of the averaging procedure was a collection of six images characterizing quantitatively the progression of the healing process. In addition, quantified descriptions of the newly formed cartilage and the bone area fractions (BA/TA) of the bony callus are presented. For all cases, a linear increase in the BA/TA of the bony callus was observed. The slope was largest in case of stiffest stabilization and lowest in case of least stiff stabilization. The obtained topological description of the progression of bone healing will allow quantitative validation (or falsification) of current mechano-biological theories.

**Keywords:** bone healing, tissue pattern, osteotomy, animal model, averaged image

## Introduction

Secondary fracture healing of long bones proceeds via the formation of a callus [1-3]. The task of the callus is to stabilize the fracture fragments resulting in a reduction of the strains in the fracture area, allowing the bone ends to be united. Usually, the process of secondary fracture healing is subdivided into three main phases [4]: the inflammatory phase, the reparative phase and the remodelling phase. These phases, however, are not well separated in time, and significant overlap can occur between them. During the inflammatory phase, vascular damage leads to haematoma formation. The reparative phase includes revascularization and the formation of fibrous tissue and cartilage, and new bone is formed at the periosteal side of the cortex by intramembranous ossification [4-6]. Soft callus bridging occurs via cartilage, which is later transformed into bone by endochondral ossification. During the remodelling phase, lamellar bone replaces woven bone, the callus is resorbed, and finally the original shape of the bone is restored [7-10].

To understand the progression of the healing process, and in particular the influence of the mechanical environment, a number of animal experiments have been performed. In these experiments, either "static" fixators with different stabilities [11-14] or "dynamic" fixators, which induce micro-movement to stimulate callus formation [15; 16] were used. These experiments demonstrated the importance of an appropriate mechanical environment to ensure union of the fracture ends and to accelerate the healing process [17].

The outcome of animal experiments is commonly reported by means of histological images at different time points post-operatively. Depending on the harvesting time, these histological sections show an intricate pattern of different tissue types including haematoma, fibrous tissue, cartilage, mineralized cartilage and the newly formed bone (as an example see Fig. 1). In order to summarize the information of a group of animals, typically only the amount of the various tissue types (area fractions) are reported as quantitative outcome [7; 12; 18; 19]. This information is limited for two reasons. Firstly, area fractions are missing important topological information, i.e. they do not provide location and distribution information. The topological information of the tissue type patterns, however, is crucial for a more profound understanding of the healing process. Secondly, individual histological sections have the disadvantage to reflect the healing situations only in single animals. It remains unclear whether they are representative for animal groups and, in addition, data on variability is lacking.

The aim of this study is to provide a quantitative description of the typical topological arrangement of the different tissue types for diaphyseal bone healing in sheep under two different fixation types. The input data comes from histological sections obtained from an experiment of 64 sheep with a tibial osteotomy treated with two different

fixators (rigid, semi-rigid). The output of the novel averaging procedure is a succession of six images, which describes the progression of healing under different loading conditions.

## **Materials and methods**

### **Animal model and histology**

Longitudinal histological sections were obtained from a previous bone healing experiment in sheep and used as input for the image analysis. The animal model has been extensively reported [5; 7] and is only briefly summarized in the next paragraph.

Sixty-four mature female Merino sheep [aged between 2.5 and 3.5 years and a mean weight of 63 ( $\pm 8$ ) kg] underwent a 3 mm tibial mid-shaft osteotomy. The sheep were subdivided into two groups of thirty-two each: the osteotomy of one group was stabilized with a “rigid” fixator (applied medially, Fig. 1), while the other was treated with a “semi-rigid” fixator resulting in two different well characterized loading conditions [7]. Eight sheep of each group were sacrificed at the harvesting time points of two, three, six and nine weeks postoperatively.

After harvesting, the callus regions of all sheep were sectioned in the frontal plane. Polymethylmetacrylate (PMMA, Technovit® 9100, Heraeus Kulzer, Germany) was used to embed the anterior portion after dehydration. Serial histological sections of 6  $\mu$ m were cut and stained either with Safranin Orange/von Kossa, Safranin Orange/Fast Green or Movat Pentachrome for distinction of newly formed bone, cartilage and haematoma, respectively.

### **Single image analysis**

The region of interest (ROI) was defined as the region of callus up to 6 mm proximal and distal from the osteotomy gap (i.e. encompassing 12 mm vertically) and the maximal callus width in the horizontal direction (Fig. 1). The ROI was divided into lateral and medial sides. Where the ROI contained an artefact, such as additional bone fragments caused by the creation of the osteotomy, the respective side was excluded from further image analysis.

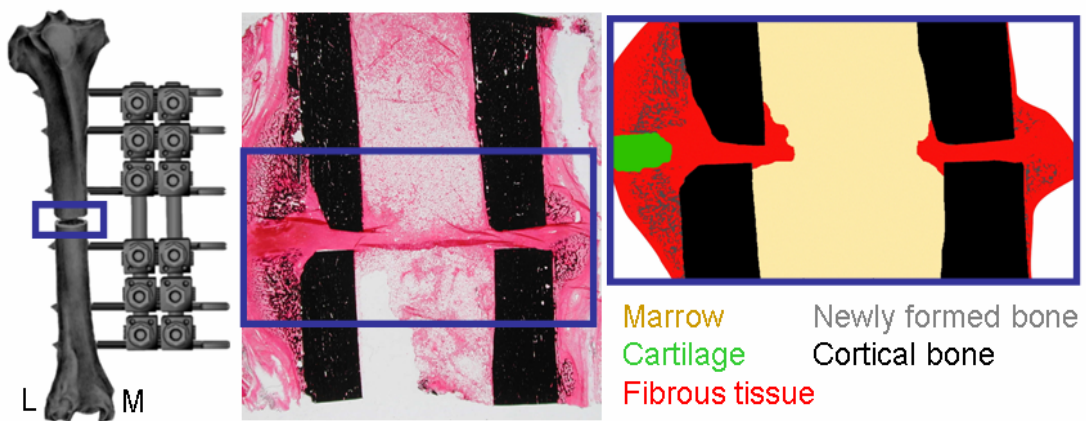


**Figure 1: Example for conversion of stained histological sections (middle) into tissue type map (right) for a 3-week post-op sheep tibia with rigid fixation.**

**The blue box denotes the region of interest (ROI). Left: schematic drawing of the rigid fixator (applied on the medial side M). Middle: Safranin Orange/von Kossa stained section. Right: converted tissue type map with colour coding given by the legend.**

The first step of the image analysis was to convert the histological images into digitized tissue type maps (Fig. 1). These tissue maps are digital images with the same pixel resolution as the original image (2048x1536 pixels). Each pixel in the image was assigned a colour corresponding to a tissue type. The staining of the tissue in the histological sections and the predominant cell type in the tissue, as identified using light microscopy, were used to distinguish the different tissue types. The following tissue types were observed: marrow, haematoma, fibrous tissue, cartilage, newly formed bone and cortical bone. For each histological section a mask for each tissue type was created with an image editing software (KS 400, Zeiss Jena, Germany) and finally assembled into tissue type maps with MATLAB (The Mathworks Inc., v 7.1) (Fig. 1).

In a second step, the information content of the tissue type maps is reduced by describing the newly formed bone locally by the ratio of bone area to tissue area (BA/TA). To do so, the region of newly formed bone was covered with overlapping squares of side length 0.5 mm. The overlap was half the length in both the horizontal and vertical directions and in each of the squares, BA/TA was calculated. A similar procedure was performed for the cortex. Its roughly rectangular cross-sectional shape was subdivided into eight different subareas according to a coarse grid (distinguishing only left and right, and four zones in the proximal-distal direction) and BA/TA was calculated in each subarea.

The areas of haematoma and cartilage, and their positions given by the centre of mass, were calculated separately for the lateral and medial sides. The shape of the haematoma and cartilage were quantified by the moment of inertia,  $I_y$ , given by,

$$I_y = \int x^2 dA \quad (1)$$

where  $x$  denotes the horizontal distance to the vertical axis running through the centre of mass, and the integration is performed over the area of haematoma and cartilage, respectively.

Furthermore, the thickness of the cortices and the bone width (defined as the width of the marrow space plus cortex thickness) were measured. The ratio of bone area over tissue area (BA/TA), i.e. the bone area fraction, of the whole bony callus and the cortex was determined using ImageJ (NIH, USA, v. 1.38). The median values of BA/TA were calculated for each harvesting time point comprising eight animals.

### **Averaging of images**

The proximal and distal side of the callus are generally similar to one another. Therefore, mirror symmetry between proximal and distal sides was assumed. The first step in the averaging procedure of the tissue type maps was to correctly superimpose the images. A vertically oriented cortex of rectangular shape was used as reference for superimposing. Differences in size of bone width were adjusted by rescaling the images by a factor defined as the ratio between each bone width and the mean bone width.

Secondly the tissue type maps had to be grouped into maps of similar topology, since averaging over images with different topology is not reasonable. Similar to the procedure used in averaging human facial features [20], the tissue maps were first classified into different developmental stages according to the observed topology of the different tissues (for the definition of the stages, see next section).

Finally, the averaging of the images was performed at each stage separately according to the respective numerical description characterising each tissue type. The newly formed bone and the cortex were described by local BA/TA values and the averaging was carried out by calculating locally the mean BA/TA values. The amount, position and shape of haematoma and cartilage areas were described by their tissue area, centre of mass and moment of inertia (Eq. 1), respectively. For these quantities, mean values were calculated and the “averaged” haematoma and cartilage were placed according to the mean values. Based on the histological data, the shape of the haematoma was assumed to be circular, while the shape of the cartilage was assumed to be elliptical.

### **Grouping of the histological sections into defined healing stages**

Instead of considering the harvesting time points as fixed and investigating the differences in the topology, an alternative viewpoint is to define criteria of the topological development of the callus. Our approach was to identify six distinct healing stages independent of the harvesting time point and to group the available

histological sections according to these healing stages. They are defined according to the topological criteria summarized in table 1 and classified according to the biological phases of healing (e.g., Sfeir and co-authors [4], see also introduction).

*Table 1: Definition of the criteria of all six observed healing stages. The right column shows their classification in the standard scheme of healing phases to describe the bone healing process (e.g., Sfeir and co-authors [4]).*

Healing stage	Topological criteria	Classification according to healing phases
Stage I	remnants of haematoma still present in the callus	late inflammatory phase
Stage II	remnants of haematoma left, cartilage not yet formed	early reparative phase
Stage III	bridging via cartilage in the outer osteotomy zone, but no bony bridging of the osteotomy gap	reparative phase
Stage IV	formation of a periosteal bony bridge between the proximal and distal parts of the osteotomy callus	late reparative phase
Stage V	formation of an endosteal bony bridge between medial and lateral parts of the osteotomy callus	early remodelling phase
Stage VI	reduced size of the hard callus, resorption of the endosteal bony bridge	remodelling phase

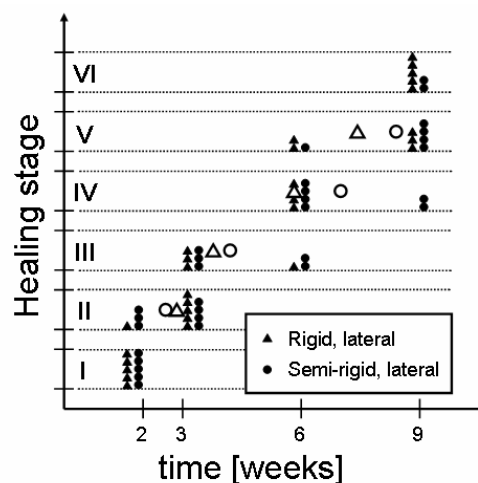


**Figure 2: Grouping of the histological images of the four harvesting time points into the six defined healing stages for the lateral side and both rigid/semi-rigid fixation.**

Every solid symbol corresponds to a histological section used for the consecutive image analysis. The open symbols denote the estimated healing time for each stage.

Fig. 2 shows the grouping of all histological images of the lateral side entering the image analysis with respect to the four harvesting time points (x-axis) and the six healing stages (y-axis). For the same harvesting time point and mechanical fixation, the inter-individual differences of the histological section were so substantial that they must be categorized into different healing stages. For example, at the harvesting time point of two weeks post-op and semi-rigid fixation, five histological sections showed remnants of haematoma, while three others did not (Fig. 2). This outcome of a histological cross-sectional study can be interpreted in two different ways. The first interpretation is that the specificities of each animal lead to a

qualitative different “healing path” reflected in a different succession of healing stages. The second interpretation is that the “healing path” as defined by the succession of the healing stages is the same for all animals. Individual differences, however, lead to a considerable difference in the speed with which this healing path is followed. Since only the second interpretation allows assigning a general succession of tissue type patterns to an animal under well-defined mechanical conditions (as aimed in this work), it is this interpretation that is assumed for the evaluation of the animal experiment. Two observations support this assumption in our study. Firstly, all defined healing stages were observed for both methods of fixation. Secondly, within one healing stage histological sections from maximal two different consecutive harvesting time points were categorized (Fig. 2).

The above described averaging method was therefore not based on the same harvesting time points, which would include all samples corresponding to symbols arranged vertically in Fig. 2. Instead, samples within the same healing stage were considered, i.e. all samples grouped horizontally. The average times of all histological sections within one healing stage were calculated (open symbols in Fig. 2) to obtain an estimated healing time for each healing stage. For example, the samples grouped into stage II (rigid fixation) consisted of one sample harvested at two weeks post-op and five samples harvested at three weeks post-op resulting in an estimated healing time for stage II (rigid fixation) of about 2.8 weeks post-op. Fig. 2 shows that stage II was reached slightly faster for semi-rigid fixation. Later healing stages, however, were attained earlier in time with the rigid fixation. Since the final stage VI only reflects the bone union, which was obtained for both fixations, the plot must not be misinterpreted as a catching up of the semi-rigid fixation group to the rigid one. The analogue classification of the medial side shows similar results.

## Results

The topological averaging process of the longitudinal histological section for each stage was performed for both the lateral and medial sides of the callus and for both rigid and semi-rigid fixations separately. The outcome was four different successions of six tissue type patterns in each case. Comparison of tissue patterns at equivalent stages in the healing process showed no *qualitative* differences in the topology between them, although *quantitative* differences in the amount of different tissues could be observed. Fig. 3 displays exemplarily the succession of tissue type patterns for the lateral side when a rigid fixation to the osteotomy was applied. The increase in bone area fraction (BA/TA) of newly formed hard callus and the decrease of BA/TA of the cortex are reflected by the gray values.

Stage I (Fig. 3, image at the top) still showed remnants of haematoma within the osteotomy gap with an area of  $0.83 \text{ mm}^2$ . The formation of new bone by

intramembranous ossification started on the periosteal surface of the osteotomy segments (area of newly formed bone:  $8.94 \text{ mm}^2$ ). At stage II intramembranous ossification continued at the periosteal side, where the width of the newly formed hard callus was largest towards the osteotomy site. In addition, new bone formation was also initiated at the endosteal side of the cortex close to the osteotomy gap. The total area of newly formed bone was  $16.8 \text{ mm}^2$ . The formation of cartilage, defining stage III, occurred at the level of the osteotomy gap, but shifted periosteally, bridging the proximal and distal osteotomy hard callus. The newly formed bone area of  $42.8 \text{ mm}^2$  was still almost exclusively at the periosteal side, only  $0.70 \text{ mm}^2$  was formed endosteally. Furthermore, first bone was formed within the osteotomy gap. At the following stage IV the cartilage area was reduced in size and had shifted centrally towards the osteotomy gap. On both the periosteal and the endosteal side, the two osteotomy ends were bridged by a bony callus. The size of this callus reached its largest value with regard to all healing stages at  $98.4 \text{ mm}^2$ , at this point, also with a significant contribution from the endosteal side ( $12.5 \text{ mm}^2$ ). At stage V, no cartilage could be observed, and the bony endosteal callus reached its largest extension, thereby establishing a connection between the medial and lateral cortices. From a total area of the newly formed bone area of  $90.9 \text{ mm}^2$ , 58.2% was found on the endosteal side. At the final stage VI, bone resorption had reduced the size of the callus to  $71.2 \text{ mm}^2$ ,  $13.1 \text{ mm}^2$  of which was on the endosteal side. The bony connection between the lateral and medial side was resorbed. Only sheep in the 9-week post-operative group reached this final healing stage.

Analysis of the formed cartilage was carried out with respect to healing stages (Table 2) and not with respect to harvesting time as previously done (Schell et al. 2005). At stage III, semi-rigid fixation led to more cartilage on the lateral side. The cartilage was slightly further towards the periphery from the osteotomy gap, compared to the rigid fixation. At stage IV, the amount of cartilage was comparable; the position, however, was clearly different. The healing path on the medial side cannot be compared for the two fixators since no histological section representative of stage III for rigid fixation could be used for the image analysis. The cartilage evolution for the semi-rigid medial case was very similar to the rigid lateral case.



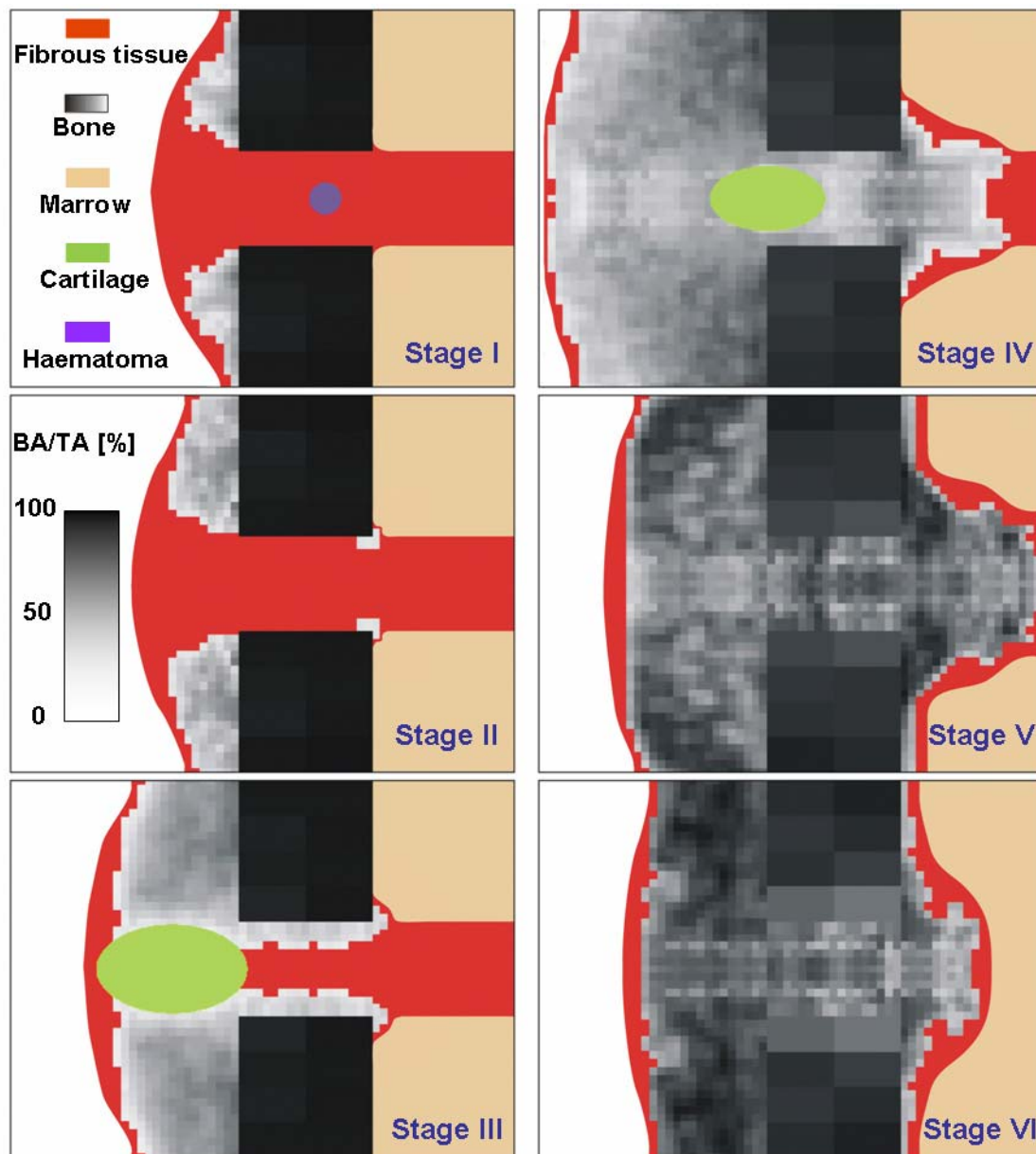


**Figure 3: Averaged histological images of bone healing in a tibia of a sheep (healing process via a succession of six healing stages).**

The images correspond to the lateral side of the tibia, i.e. opposite to the side where a rigid fixator was placed under the assumption of proximal/distal symmetry. Colours are according to the legend in the upper left plot. Different gray values correspond to different values of BA/TA. For the definition of healing stages see text.

Two opposite trends concerning the bone area fraction, BA/TA, were observed in the newly formed bone and in the cortical bone, respectively. For the newly formed hard callus, a densification occurred reflected by darker gray scales as seen in Fig. 3. Starting with stage IV, however, the BA/TA of the cortex significantly decreased making a distinction between cortex and newly formed bone more difficult. BA/TA values at the cortical ends (determined by evaluating only the two subareas closest

to the osteotomy gap, see method section) started from about 90% (stages I–III) and decreased to 83.6% at stage VI, 73.6% at stage V and 60.4% at stage VI.

The frequency distributions of the BA/TA values within the newly formed bone are plotted in Fig. 4. Both stages I and II reached maximal BA/TA values of about 50%, while the distribution does not display a clear peak structure. The growth of the callus is reflected in larger values of the distribution, whereby the distribution becomes bell-shaped starting with stage IV. The further time evolution of the distribution is a shift of the peak towards larger BA/TA values (reflecting the densification) and a reduction of the peak height (reflecting the onset of remodeling). In the final stages V and VI regions can be observed with a bone area fraction as high as 90%.

**Table 2: Area, centre of mass (CoM) and moment of inertia (Mol) of cartilage at healing stages III and IV (standard deviation in parenthesis).**

The CoM is given by its distance to the centre of the osteotomy. The moment of inertia was calculated according to equation 1. The vertical axes for calculating the Mol was placed in the centre of mass for each cartilage region in order to describe quantitatively the shape of the cartilage regions.

		Rigid		Semi-rigid	
		Lateral	Medial	Lateral	Medial
Stage III	Area [mm <sup>2</sup> ]	10.7 (2.47)		16.7 (9.33)	8.84 (2.48)
	CoM [mm]	4.25 (0.91)		4.71 (0.69)	4.32 (1.06)
	Mol [mm <sup>4</sup> ]	15.6 (9.66)		39.2 (26.4)	8.40 (5.18)
Stage IV	Area [mm <sup>2</sup> ]	5.99 (2.35)	5.45 (1.64)	4.64 (2.84)	1.82 (1.17)
	CoM [mm]	2.15 (1.59)	2.08 (0.63)	4.26 (1.23)	2.07 (1.32)
	Mol [mm <sup>4</sup> ]	4.20 (0.98)	4.95 (2.93)	8.62 (6.05)	0.90 (0.71)

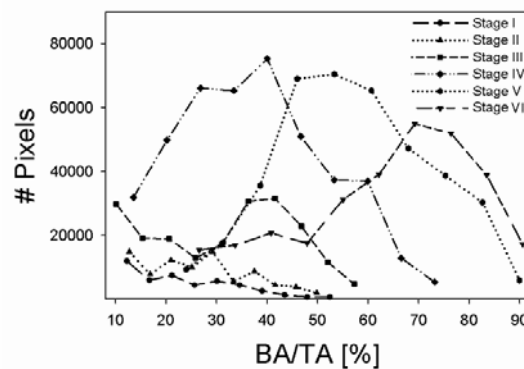


**Figure 4: Distribution of bone area fraction (BA/TA) of the newly formed bone at the six defined stages (for rigid fixation, lateral side).**

The densification over time of the hard callus (i.e. the increase of BA/TA) and the degradation of the cortex can also be determined without reference to the healing stages, but with respect to the harvesting time points (Fig. 5), since similar topology is not a prerequisite in this case. The histological sections for all four cases (rigid fixation lateral, rigid medial, semi-rigid lateral and semi-rigid medial) were analyzed separately. In all four cases, the densification data could be well fitted using a linear regression with the maximal  $r^2$ -value at 0.99 and the minimal one at 0.93 (see figure legend of Fig. 5 top). The slopes, which correspond to the densification rate of the newly formed bone, were different depending both on the fixation and the anatomical side. With the densification rate given in percent per week, the increase in BA/TA for the rigid fixations (lateral: 4.26, medial: 5.80) was higher compared to the semi-rigid cases (lateral: 4.06, medial: 5.29). For a given fixation, densification occurred faster on the medial side (i.e., the side where the fixator is placed, see Fig. 1). BA/TA values at the final nine weeks time point were around 70%. The four linear regressions of the four median values were tested to investigate if there were significantly different slopes amongst them. T-values were calculated based on the slope differences and the standard errors between regressions with regard to the median values. Significant differences in the slopes occurred for the comparison between the cases "rigid medial/semi-rigid lateral" ( $p=0.0394$ ) and "rigid medial/rigid lateral" ( $p=0.0445$ ).

In contrast to the newly formed bone, the cortical ends show a decrease in BA/TA values (Fig. 5, bottom). From an initial value of about 94% at two weeks post-op, BA/TA reduced to about 75% at nine weeks with a decrease rate of approximately 2.6% per week.

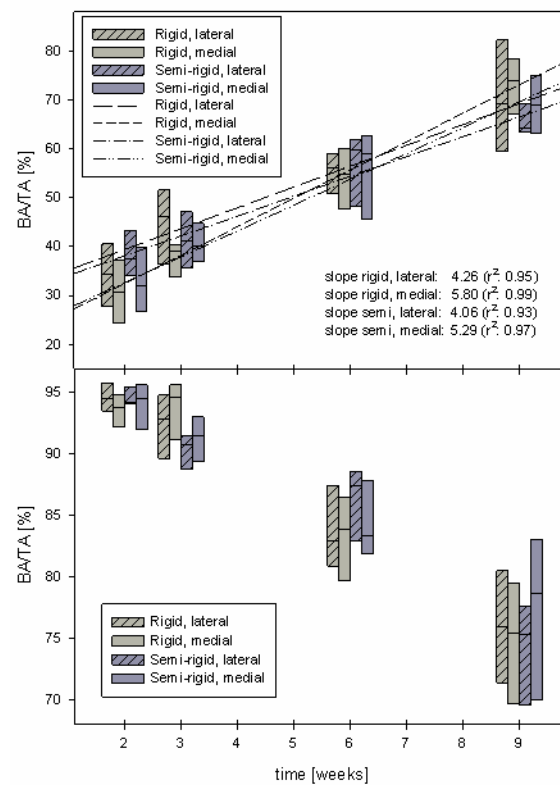


**Figure 5: Development of the bone area fraction, BA/TA, of the newly formed bony callus (top) and the cortex (bottom) as a function of the harvesting time points for the for different cases (medial/lateral and rigid/semi-rigid fixation). The boxes comprise the data from the lower to the upper quartile with the interior line indicating the median.**

## Discussion

This work introduces a new method to describe the progression of bone healing in terms of a succession of images, which reflect the topology of the different tissue types formed. These images were obtained by an averaging procedure, which allows condensing the histological information of several animals into one image. At the core of the new method is the classification of histological sections into six different healing stages of similar topology. Instead of performing the averaging over histological sections at the same harvesting time points, averaging was performed according to healing stages. This overcomes the difficulty of dealing with crucially different topologies of the tissue type patterns of different animals at the same harvesting time point. A result of this method is that for each healing stage an effective healing time can be evaluated (Fig. 2). This evaluation showed that semi-rigid fixation leads initially to a faster development, but is later overtaken by the healing process with rigid fixation. The same tendency was found by analysing the increase of the bone area fraction in the newly formed callus (Fig. 5). Although semi-rigid fixation resulted in slightly higher values for two weeks (first time point post-op), the further densification of the callus characterized by the slope of the increase

in BA/TA proceeded faster for rigid fixation. Assuming that the differences of the slope for BA/TA (Fig. 5 top) are mechanically influenced, the conclusion would be that densification proceeds fastest in later stages under a mechanically stable environment. The highest values for the slope were found for the medial side for both rigid and semi-rigid fixation, which was the same side as the external fixator. This suggests that the asymmetric stabilization by the external fixator leads to a particular stable mechanical environment on the side of the fixator (for the mechanical characterization of the fixators see [7; 8]) influencing positively the densification of the callus. Our observations are in agreement with the proposal of a fixation of variable stiffness in time. Such a fixation should initially trigger the healing process by providing a larger mechanical stimulus, but should provide later on a higher mechanical stability supporting a faster healing response. Beneficial effects of a temporally decreasing inter-fragmentary displacement during the healing process were also suggested by a similar study on sheep [21].

In conclusion, we would like to emphasize that the proposed averaging procedure not only provides a succession of images that characterized the progression of healing under a controlled mechanical environment. The image also provides quantitative information and with regards to the averaging, estimates are obtained where the largest inter-individual differences occur. In the case of the bony callus, the largest inter-individual differences are found at the outer fringe of the callus.

An immediate application of such obtained tissue type patterns is to test current mechano-biological theories. Different theories have been proposed [22-25] as to how mechanical stimuli influence cell differentiation and the formation of different tissue types during healing. More recently these theories were implemented in computer models and tested extensively [26-28]. Further progress is significantly hindered by the lack of reliable experimental data, which allow a one-to-one comparison between experimental outcome and simulation result, ideally at different time points during healing. Averaged tissue type patterns, as presented in this work, will in this way help to sharpen our understanding of which parts in the healing process are more biologically or mechanically controlled.

The averaging procedure is by no means restricted to sheep. We propose that presented (or similar) averaging methods can be used to evaluate experiments on other large and small animals. Firstly, this would enable the comparison of the progress of tissue patterns between different experiments on the same animals. Therefore, pathologies in the process of healing would be easier to identify. And secondly, it would clarify, which features of the healing process are specific for a given animal species and which are more general features of the healing process and should therefore be also transferable to humans.

## Acknowledgments

This study was supported by a grant of the German Research Foundation (Collaborative Research Centre "Biomechanics and Biology of Musculoskeletal Regeneration – From Functional Assessment to Guided Tissue Formation", SFB 760).

## References

1. Einhorn, T.A., 1998. The cell and molecular biology of fracture healing. *Clin Orthop Relat R* 355, S7-S21.
2. Claes, L.E., Ito, K., 2004. Biomechanics of fracture fixation and fracture healing. In: Mow, V.C., Huiskes, R. (Eds.), *Basic Orthopaedic Biomechanics and Mechano-Biology*. Lippincott Williams & Wilkins, London.
3. Cruess, R.L., Dumont, J., 1975. Fracture Healing. *Can J Surg* 18, 403-&.
4. Sfeir, C., Ho, C., Doll, B.A., Azari, K., Hollinger, J.O., 2005. Fracture Repair. In: Lieberman, J.R., Friedlaender, G.E. (Eds.), *Bone Regeneration and Repair*. Humana Press Inc., Totowa, pp. 21-43.
5. Epari, D.R., Schell, H., Bail, H.J., Duda, G.N., 2006. Instability prolongs the chondral phase during bone healing in sheep. *Bone* 38, 864-870.
6. Bostrom, M.P.G., 1998. Expression of bone morphogenetic proteins in fracture healing. *Clin Orthop Relat R*, S116-S123.
7. Schell, H., Epari, D.R., Kassi, J.P., et al., 2005. The course of bone healing is influenced by the initial shear fixation stability. *J Orthop Res* 23, 1022-1028.
8. Klein, P., Opitz, M., et al., 2004. Comparison of unreamed nailing and external fixation of tibial diastases - mechanical conditions during healing and biological outcome. *J Orthop Res* 22, 1072-1078.
9. McKibbin, B., 1978. Biology of Fracture Healing in Long Bones. *J Bone Joint Surg Br* 60, 150-162.
10. Rhinelander, F.W., 1968. Normal Microcirculation of Diaphyseal Cortex and Its Response to Fracture. *J Bone Joint Surg Am* 50, 784-&.
11. Goodship, A.E., Watkins, P.E., Rigby, H.S., Kenwright, J., 1993. The Role of Fixator Frame Stiffness in the Control of Fracture-Healing - an Experimental-Study. *J Biomech* 26, 1027-1035.
12. Claes, L.E., Wilke, H.J., Augat, et al., 1995. Effect of Dynamization on Gap Healing of Diaphyseal Fractures under External Fixation. *Clin Biomech* 10, 227-234.
13. Duda, G.N., Sporrer, S., Sollmann, M., et al., 2003. Interfragmentary movements in the early phase of healing in distraction and correction osteotomies stabilize with ring fixators. *Langenbecks Arch Chir* 387, 433-440.
14. Duda, G.N., Kassi, J.P., Hoffmann, J.E., et al., 2000. Mechanical performance of Ilizarov ring fixators. Influence of the frame configuration on the stiffness and consequences for the clinical application. *Unfallchirurg* 103, 839-845.
15. Goodship, A.E., Kenwright, J., 1985. The Influence of Induced Micromovement Upon the Healing of Experimental Tibial Fractures. *J Bone Joint Surg Br* 67, 650-655.
16. Hente, R., Fuchtmeier, B., Schlegel, U., et al., 2004. The influence of cyclic compression and distraction on the healing of experimental tibial fractures. *J Orthop Res* 22, 709-715.
17. Reichert, J.C., Saifzadeha, S., Wulschleger, M.E., et al., 2009. The challenge of establishing preclinical models for segmental bone defect research. *Biomaterials* 30, 2149-2163.
18. Bishop, N.E., van Rhijn, M., Tami, I., et al., 2006. Shear does not necessarily inhibit bone healing. *Clin Orthop Relat R* 443, 307-314.
19. Lill, C.A., Winterstein, E., Eckhardt, C., et al., 2003. Quantification of histomorphometric and structural bone changes in a sheep model for fracture treatment in osteoporotic bone. *Vet Comp Orthopaed* 16, 243-249.
20. Burton, A.M., Jenkins, R., Hancock, P.J.B., White, D., 2005. Robust representations for face recognition: The power of averages. *Cognitive Psychol* 51, 256-284.
21. Gardner, T.N., Evans, M., Simpson, H., 1998. Temporal variation of applied inter fragmentary displacement at a bone fracture in harmony with maturation of the fracture callus. *Med Eng Phys* 20, 480-484.
22. Pauwels, F., 1960. Eine neue Theorie über den Einfluß mechanischer Reize auf die Differenzierung im Stützgewebe. *Z Anat Entwicklungsgeschichte* 121, 478-515.
23. Yamagishi, M., Yoshimura, Y., 1955. The biomechanics of fracture healing. *J Bone Joint Surg* 37A, 1035-1068.
24. Perren, S.M., 1979. Physical and Biological Aspects of Fracture-Healing with Special Reference to Internal-Fixation. *Clin Orthop Relat R*, 175-196.
25. Carter, D.R., Beaupre, G.S., Giori, N.J., Helms, J.A., 1998. Mechanobiology of skeletal regeneration. *Clin Orthop Relat R*, S41-S55.
26. Ament, C., Hofer, E.P., 2000. A fuzzy logic model of fracture healing. *J Biomech* 33, 961-968.
27. Isaksson, H., Wilson, W., van Donkelaar, C.C., et al., 2006. Comparison of biophysical stimuli for mechano-regulation of tissue differentiation during fracture healing. *J Biomech* 39, 1507-1516.
28. Lacroix, D., Prendergast, P.J., 2002. A mechano-regulation model for tissue differentiation during fracture healing: analysis of gap size and loading. *J Biomech* 35, 1163-1171.

**Second manuscript (Vetter et al. 2010b)****The mechanical heterogeneity of the hard callus influences local tissue strains during bone healing**

To be submitted to: Journal of Biomechanics

A. Vetter (1), Y. Liu (1), F. Witt (2), I. Manjubala (1), O. Sander (4), D.R. Epari (3), P. Fratzl (1), G.N. Duda (2), R. Weinkamer (1)

1. Max Planck Institute of Colloids and Interfaces, Department of Biomaterials, 14424 Potsdam, Germany
2. Julius Wolff Institut and Center for Musculoskeletal Surgery, Charité – Universitätsmedizin, 13353 Berlin, Germany
3. Institute of Health and Biomedical Innovation, Queensland University of Technology, Brisbane, Qld 4059, Australia
4. Free University of Berlin, Institute for Mathematics, 14195 Berlin

**Abstract**

During secondary fracture healing, various tissue types including new bone are formed. The local mechanical strains play an important role in tissue proliferation and differentiation, influencing the progression of tissue patterns and the healing process. To further our mechanobiological understanding of fracture healing, a precise assessment of local strains is mandatory. Until now, finite element (FE) models have assumed homogenous material properties. With the recent quantification of both the spatial tissue patterns and the development of elastic modulus of newly formed bone during healing, it is now possible to incorporate this heterogeneity. Therefore, the aim of this study is to quantify the effect of this heterogeneity on the strain patterns at six successive healing stages.

The input data of the present work stemmed from a comprehensive cross-sectional study of sheep with a tibial osteotomy. In our FE model, each element containing bone was described by a bulk elastic modulus, which depended on both the local area fraction and the local elastic modulus of the bone material. The obtained strains were compared to the results of hypothetical FE models assuming homogeneous material properties.

It was found that the heterogeneity of the hard callus tissue considerably increased the strains within the osteotomy gap. The strain analyses indicate that the heterogeneity influences the way endochondral ossification occurs. We hypothesize that the stiffening of the hard callus is an essential factor for the shifting of the

cartilage region inwards to the osteotomy gap during healing, similar to what is reported from animal experiments.

**Keywords:** Bone healing, mechanobiology, tissue properties, finite element, shear strain, fracture callus

### Introduction

Secondary bone healing of long bones occurs in the presence of interfragmentary movement with the formation of an external callus (Willenegger et al. 1971; Cruess and Dumont 1975; Einhorn 1998; Duda et al. 2003; Claes and Ito 2004). Fracture healing begins with the inflammatory phase which includes the formation of a haematoma. During the subsequent reparative phase, revascularisation and formation of fibrous tissue, cartilage and bone (hard callus) occurs. The final bone healing phase comprises remodelling of the hard callus and restoration of the original shape of the long bone takes place (Sfeir et al. 2005). The progression of healing is characterized by an intricate time-evolving pattern of different tissues in the callus. Based on a sheep experiment and the observed tissue patterns (Klein et al. 2003; Lienau et al. 2005; Schell et al. 2005), a succession of six healing stages could be defined describing the normal bone healing in sheep (Vetter et al. 2010).

With the ongoing healing process, the bone fracture fragments are mechanically stabilized due to a consecutive stiffening of the callus. This stiffening occurs on three different hierarchical levels of the callus structure. At the macroscopical level, the growth of the callus leads to an increase in the bending stiffness especially from new material formed distant to the long bone axis. At the mesoscopical level, new material is formed within the callus, for example fibrous tissue, cartilage, mineralized cartilage and bone. Furthermore, the thickening of the trabeculae, which leads to a denser trabecular network, can be assessed to this level. At the microscopical level, the material properties of the tissues change over time, for example by incorporation of more mineral into the newly formed bone. All of these levels are of importance to investigate due to their direct relation to a reduction of the strains within the fracture area, a prerequisite for the unification of the two fracture fragments.

The information of how strains evolve over time within in the callus during healing is of particular interest since the mechanical environment influences healing as demonstrated in various experimental studies (Yamagishi and Yoshimura 1955; White et al. 1977; Kenwright and Goodship 1989; Cheal et al. 1991; Claes et al. 1998; Kaspar et al. 2005; Epari et al. 2007). The foundation of this mechanobiological influence is the mechano-responsiveness of cells allowing cells to react to local mechanical stimuli, by either differentiation, proliferation or by other



means (Klein-Nulend et al. 2005; Matziolis et al. 2006; Morgan et al. 2008; Kokkinos et al. 2009).

The aim of this work is to use recent experimental data to characterize the straining of tissues in a way that respects the heterogeneity of the material properties and tissue distribution of callus and cortex tissues. The new experimental data cover all three hierarchical levels of the callus mentioned above; macroscopical, mesoscopical and microscopical. The shape of the callus and the time-evolving pattern of different tissues were defined for six successive healing stages for sheep (Vetter et al. 2010). From the same animal experiment, the elastic modulus of the bone material was measured at different time points during healing progression (Manjubala et al. 2009). In the present study, this improved characterization of callus during the healing process was used as input for finite element (FE) calculations to obtain the local strains within the callus.

Different techniques are available to quantify tissue straining, amongst them digital image correlation (DIC) (Thompson et al. 2007) and electronic speckle pattern interferometry (ESPI) (Bottlang et al. 2008). However, ESPI requires direct observations of the deforming surface and therefore this method is limited to 2D, investigating only callus cross-sections (Zaslansky et al. 2006). Our approach can be seen as the natural extension of earlier FE calculations, which were carried out for simplified geometries of sheep osteotomies (Claes and Heigele 1999), oblique fractures (Loboa et al. 2001) and based on radiographs (Gardner et al. 2000; Gardner and Mishra 2003).

## **Material and Methods**

### **Animal model and image analysis**

The animal experiment included 64 female merino sheep with a 3 mm tibial mid-shaft osteotomy stabilized with two kinds of external fixators (Fig 1a). The animals were sacrificed two, three, six and nine weeks post-operation. Detailed report of the experiment can be found in previous work from our group (Schell et al. 2005; Epari et al. 2006) and is only briefly summarized here. Based on longitudinal histological sections of the fracture calli, an image analysis was performed to define the patterns of different tissue types during the progression of normal bone healing in sheep. The region of interest (ROI) for the image analysis had to be limited to a region, which was comprised of 6 mm in proximal and distal direction of the osteotomy gap in order to avoid the influence of the external fixator screws (Fig 1a). Depending on a specified fixator and specified side of the callus (medial or lateral), the outcome of the image analysis was a succession of six images corresponding to six consecutive healing stages (see Fig 1b for an example). The main topological characteristics of the six healing stages are summarized as follows (Vetter et al. 2010): stage I) the callus still includes remnants of haematoma, stage II) no remnants of haematoma

are present and also no cartilage yet formed, stage III) cartilage bridging of the osteotomy on the periosteal side, stage IV) the hard callus has bridged the gap, while cartilage is still present, stage V) cartilage has disappeared, a endosteal bony connection occurred horizontally and remodelling led to a decrease in callus size and stage VI) is characterised by resorption of the endosteal bony connection.

### **Heterogeneity of the elastic modulus of hard callus**

For estimating the local stresses and strains in the hard callus, the local mechanical properties have to be defined. In a porous material both the architecture and the material has to be considered. An anisotropy in the architecture, as described by a fabric tensor (Zysset 2003), result in anisotropic mechanical properties. Under assumption of structural isotropy, the elastic modulus of the hard callus viewed on the mesoscopic scale depends mainly on two quantities at two different levels of the hierarchical structure: i) on the bone area fraction  $BA/TA$  at the architectural level, and ii) on the elastic modulus of the hard callus material  $E_{mat}$  at the material level. The (bulk) elastic modulus depends crucially on the investigated length scale due to the applicability of the continuum assumption (Harrigan et al. 1988), In this study, the element size was based on the resolution of the image analysis (pixel size: 500  $\mu\text{m}$ ) (Vetter et al. 2010). According to Gibson and Ashby (Gibson and Ahsby 1999) the local (bulk) elastic modulus of the hard callus element is given by ,

$$E = E_{mat} \cdot \left( \frac{BA}{TA} \right)^\kappa \quad (1) ,$$

where  $\kappa$  is a constant exponent which has for trabecular bone a value close to 2 (Morgan et al. 2003; Gibson 2005). All quantities in the formula are a function of both space and time. During the progression of the healing for a fixed point within the hard callus,  $E_{mat}$  increases mainly due to the incorporation of more mineral into bone, and  $BA/TA$  increases since the trabecular network becomes denser.

### *Elastic modulus of the bone material*

To determine  $E_{mat}$  as a function of healing time nanoindentation experiments were performed with a scanning nanoindenter (Hysitron Inc., Minneapolis, USA) (Manjubala et al. 2009). The indentation elastic modulus  $E_{mat}$  was measure in the periosteal hard callus region adjacent to the cortex and 3 mm away from the cortex end. Four sheep per time point were measured with at least 1100 indents per animal callus, with a spacing between the indents of 20  $\mu\text{m}$ . Table 1 shows the averaged data of the elastic moduli of the bony material.

**Table 1: Elastic modulus  $E_{mat}$  of the bone material of the hard callus (with standard deviations) measured by nanoindentation (Manjubala et al. 2009). The indented region was the periosteal hard callus close to the cortex for a rigid fixation of the osteotomy.**

Time (post-op)	2 weeks	3 weeks	6 weeks	9 weeks
$E_{mat}$ [GPa]	5.14 ( $\pm 1.18$ )	7.06 ( $\pm 1.89$ )	11.04 ( $\pm 1.08$ )	11.53 ( $\pm 1.24$ )

#### *Hard callus growth and bone area fraction*

The images resulting from our previous analysis of histological sections consisting of the six healing stages (Vetter et al. 2010) were used to describe the size of the hard callus during its initial growth and later remodelling. Callus growth over time provides information when bone formation started at a specific location of the hard callus. The data on callus size was available for the six different time points or healing stages. To reproduce a more continuous growth of the callus, this data was interpolated by smoothing (Fig 1c). Based on the histological images, the bone area fraction ( $BA/TA$ ) was determined locally, using each pixel of the image. The bone area fraction of the cortex outside the ROI was set to 0.96.

#### *Mechanical characterization of the callus*

In order to calculate the local elastic modulus of the hard callus, three types of data were used and inserted into Equation (1): (i) the time evolution of  $E_{mat}$  (Table 1, linear interpolation within data points was applied), (ii) the map of when bone formation started and (iii) the local  $BA/TA$  for the six healing stages. A value slightly smaller than 2 was used for the exponent  $\kappa$  as characteristic for human (Morgan et al. 2003) and bovine bone (Gibson 2005). The used mechanical properties, including mechanical properties of other tissue types than hard callus, are summarised in Table 2. Accordingly, maps of the elastic modulus within the callus were obtained for all six healing stages (as an example, see Fig 1d).

**Table 2: Elastic modulus of the materials  $E_{mat}$ , Poisson Ratio  $\nu$ , and exponent  $\kappa$  of the different tissues within the callus.**

[a] Hori and Lewis (1982), b) Isaksson et al. (2006), c) Schaffler and Burr (1988), d) Claes and Heigele (1999), e) Morgan et al. (2003)]

Material	$E_{mat}$	$\nu$	$\kappa$
Fibrous tissue, marrow	2 MPa <sup>(a,b)</sup>	0.167 <sup>(b)</sup>	
Cartilage	10 MPa <sup>(c)</sup>	0.167 <sup>(b)</sup>	
Hard callus	time dependent, see Table 1	0.3 <sup>(d)</sup>	1.83 <sup>(e)</sup>
Cortex	20 GPa <sup>(d)</sup>	0.3 <sup>(d)</sup>	1.83 <sup>(e)</sup>

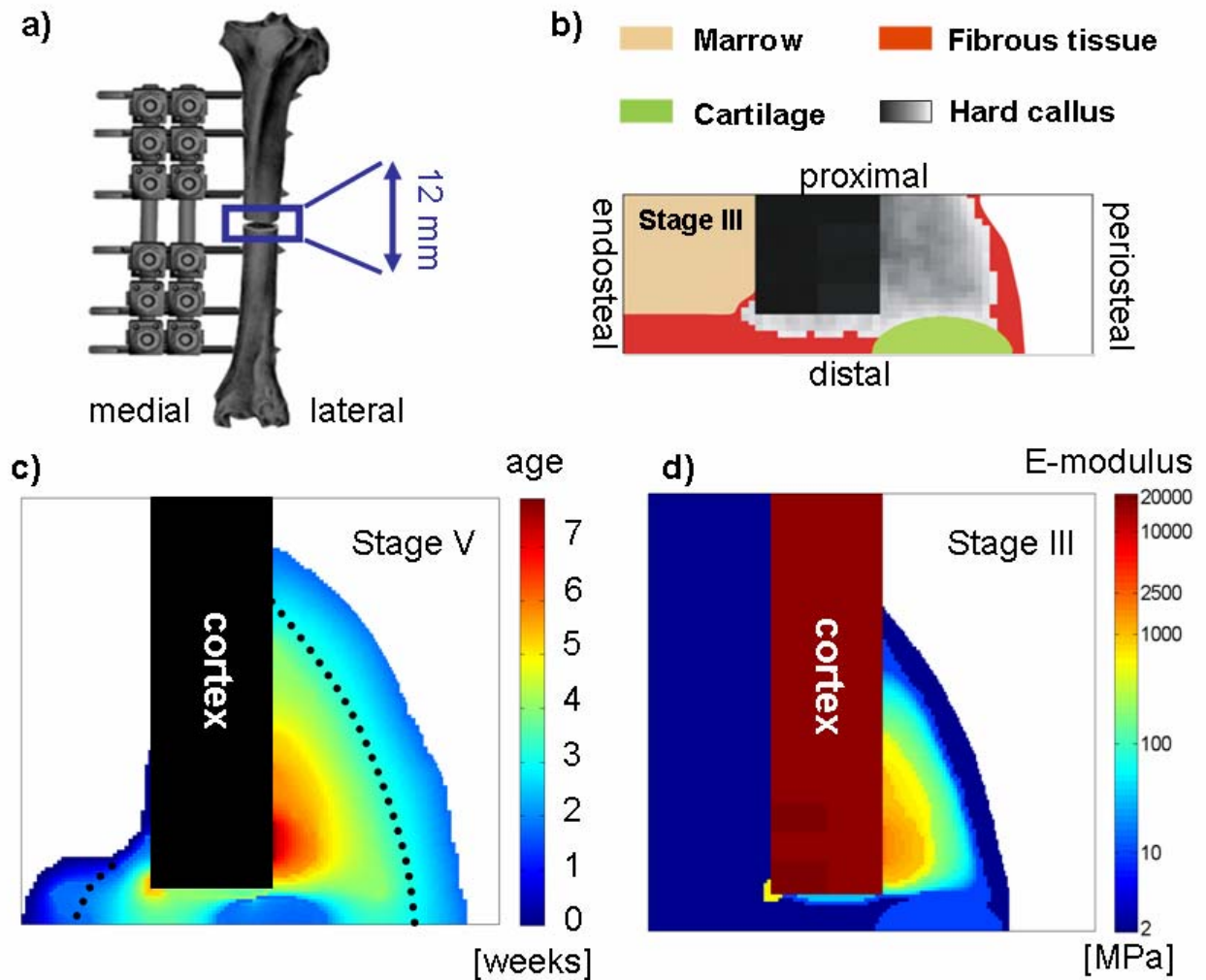


Figure 1: a) Schematic drawing of the osteotomy and positioning of the external rigid fixator, adapted from (Schell et al. 2005).

The blue frame denotes the region of interest (ROI) for the following calculations. b) Example of a tissue type map obtained from image analysis of histological sections (Vetter et al. 2010) (stage III). Horizontal axis symmetry along the osteotomy was assumed. The differences in the grey scale indicate different bone area fractions (BA/TA). c) Age map of the hard callus at stage V indicating when bone formation started within different regions in the hard callus. The dotted lines indicate the reduced size of the hard callus at stage VI due to remodelling. d) Calculated map of the elastic modulus at stage III using experimental data on the bone material and bone area fraction together with Equation (1).

### Tissue strain analyses: finite element calculations

The maps of the heterogeneous spatial distribution of the elastic modulus within the callus (Fig 1d) were used as input for the finite element (FE) calculations. For all six healing stages, the mechanical information of each pixel was imported into ABAQUS (ABAQUS v6.6, Hibbit Karlsson & Sorensen, Inc., RI, USA) as linear elastic elements. To study the influence of the elastic heterogeneity of the hard callus and the softening of the cortex ends, two *hypothetical* cases for each stage were modelled as references: i) assuming a homogeneous hard callus and ii) assuming a homogeneous

cortex. In the homogeneous hard callus, the elastic modulus of each hard callus element was set to the corresponding mean value of the hard callus (Table 3). In the homogeneous cortex, the elastic modulus of each element in the cortex was set to the corresponding cortical mean value (Table 3). After calculating these hypothetical cases, the difference between the strain distribution between heterogeneous and homogeneous case was calculated to investigate the importance of the heterogeneity of the hard callus. Rotational-symmetric boundary conditions along the vertical axis of the centre of the long bone and mirror symmetric boundary conditions along the horizontal axis (along the osteotomy cut) were applied. In each calculation approximately 10000 axis-symmetric four-node elements were used. The convergence of the FE model was tested by doubling the number of elements and using 8-node elements.

An axial force of 500 N was applied on the cortex for stages IV, V and VI, according to previous calculations (Duda et al. 1998). For stages I, II and III, the applied force had to be lowered to agree with experimentally measured maximal interfragmentary movement of 0.5 mm (Schell et al. 2008). The applied forces necessary to obtain this displacement in the model were 105.2 N, 120.7 N and 453.6 N at stages I, II and III, respectively. The calculated stress and strain tensors were reduced to a scalar quantity, which can be interpreted as a mechanical stimulus in mechanobiological simulations (Lacroix and Prendergast 2002; Bailon-Plaza and van der Meulen 2003; Isaksson et al. 2006). The results are reported for the maximal shear strain as defined by

$$\gamma_{\max} = \sqrt{(\varepsilon_x - \varepsilon_y)^2 + \gamma_{xy}^2} \quad (2)$$

where  $\varepsilon_x$ , and  $\varepsilon_y$  are the horizontal and vertical strains and  $\gamma_{xy}$  is the shear strain.

Qualitatively identical results were obtained by considering the maximum of the absolute values of maximal and minimal principal strains at each element. The FE results were imported into MATLAB (The Mathworks Inc., v 7.1) for post-processing.

## Results

### Overall stiffening of the hard callus

The hard callus increases its elastic modulus by a stiffening of the bone material and by a densification of the network of newly formed bone. New soft bone material is added constantly at the boundary of the hard callus during growth of the hard callus (stages I to IV). These three processes together result in an overall increase of the elastic modulus of the hard callus over time as described by the mean value of the (bulk) elastic moduli of all pixel elements constituting the hard callus. The remodelling of the cortex leads to a decrease of its stiffness. The values are summarized in Table 3.

**Table 3: Mean values and standard deviations of the (bulk) elastic moduli of the whole hard callus and cortex at the six healing stages.**

Stage	I	II	III	IV	V	VI
$E_{\text{hard callus}}$ [GPa]	0.129 ( $\pm 0.103$ )	0.232 ( $\pm 0.195$ )	0.537 ( $\pm 0.498$ )	1.04 ( $\pm 1.07$ )	2.69 ( $\pm 1.03$ )	4.29 ( $\pm 1.98$ )
$E_{\text{cortex}}$ [GPa]	18.38 ( $\pm 0.59$ )	18.27 ( $\pm 0.49$ )	17.93 ( $\pm 0.66$ )	15.28 ( $\pm 1.09$ )	14.30 ( $\pm 2.00$ )	13.54 ( $\pm 3.42$ )

### Frequency distribution of the strains

For each of the six healing stages, we performed calculations using three FE models resulting in 18 models. The first model at each stage used the heterogeneous hard callus data in terms of the local elastic modulus. In the second model, the hard callus at each stage was modelled as homogeneous by assigning the mean elastic modulus to each element of the hard callus (Table 3). Following the same principle, a homogeneous cortex was assumed in the third model according to the mean elastic modulus of the cortical region at each stage (Table 3). Figure 2 shows the frequency distributions of the maximal shear strains within the hard callus at stage I and stage VI, as examples of an early and a late healing stage. The distributions for the heterogeneous callus show a longer tail for large strains due to the presence of very soft material in the callus. Both distributions are strongly peaked at stage I (Fig. 2, left). The inset shows the position of the pixels of low strain. In the heterogeneous case, these pixels form a region following the half-almond shape of the callus, while in homogeneous case, they are found at maximal vertical distance from the fracture gap (Fig. 2, left, inset). At the late healing stage VI, the peak of the strain distribution is narrower for the heterogeneous callus (Fig. 2, right). For the homogeneous case, the main peak is not only broader but also a second peak appeared at higher strains. The elements corresponding to the second peak are located between the cortex ends (Fig. 2, right, inset).

### Spatial distribution of the strains

The left column of Figure 3 shows the maximal shear strain for the six successive stages of bone healing. The overall stiffening of the hard callus leads to a reduction of the strains of about 3 orders of magnitude from the initial to the final healing stage. The largest strains are found between the cortical ends and at the lower fringe of the newly formed hard callus. To highlight the differences of a more accurate mechanical description of the hard callus, the middle and the right column of Figure 3 shows the strain differences between the heterogeneous case and the hypothetical reference cases of a homogeneous hard callus or a homogeneous cortex, respectively. At early stages of healing, the influence of the callus heterogeneity resulted in higher strain differences compared to the influence of

cortex heterogeneity (note the different orders of magnitude in the plots). Starting from stage V, the influences of the heterogeneities of the callus and the cortex are of comparable magnitude (Fig. 3).

In comparison with the homogeneous callus (Fig. 3, middle) the region of the periosteally newly formed bone close to cortex is lower strained in the heterogeneous case. However, two regions can be observed where the strains are increased in the heterogeneous case: (i) the region at the lower fringe of the hard callus and (ii) the region between the cortical ends. The semi-logarithmic plot of the mean strain of all the pixels in the region between the cortex ends (Fig. 4) emphasizes the higher strains present in the heterogeneous case. The slight increase from stage I to stage III is the effect of the increased external loading. Worth noticing is the difference of the strains within the cartilage, in particular at stage III. While the outer part has lower local strains for the heterogeneous callus (greenish colours), the reddish colour indicates higher strains for the inner part. The same behaviour can be observed when the maximal shear strains for both cases are plotted along a horizontal cut or line scan through the cartilage (Fig. 5, left).

The influence of the cortex heterogeneity was most predominant within the cortex itself (Fig. 3, images in the right column). Higher strains were found within the cortex close to its ends at stages IV, V and VI, but lower strains were found further away from the gap (see also Fig 5, right). At stage IV, the strains within the cartilage are slightly decreased by the cortex heterogeneity, but the increase due to the callus heterogeneity is about two orders of magnitude larger.

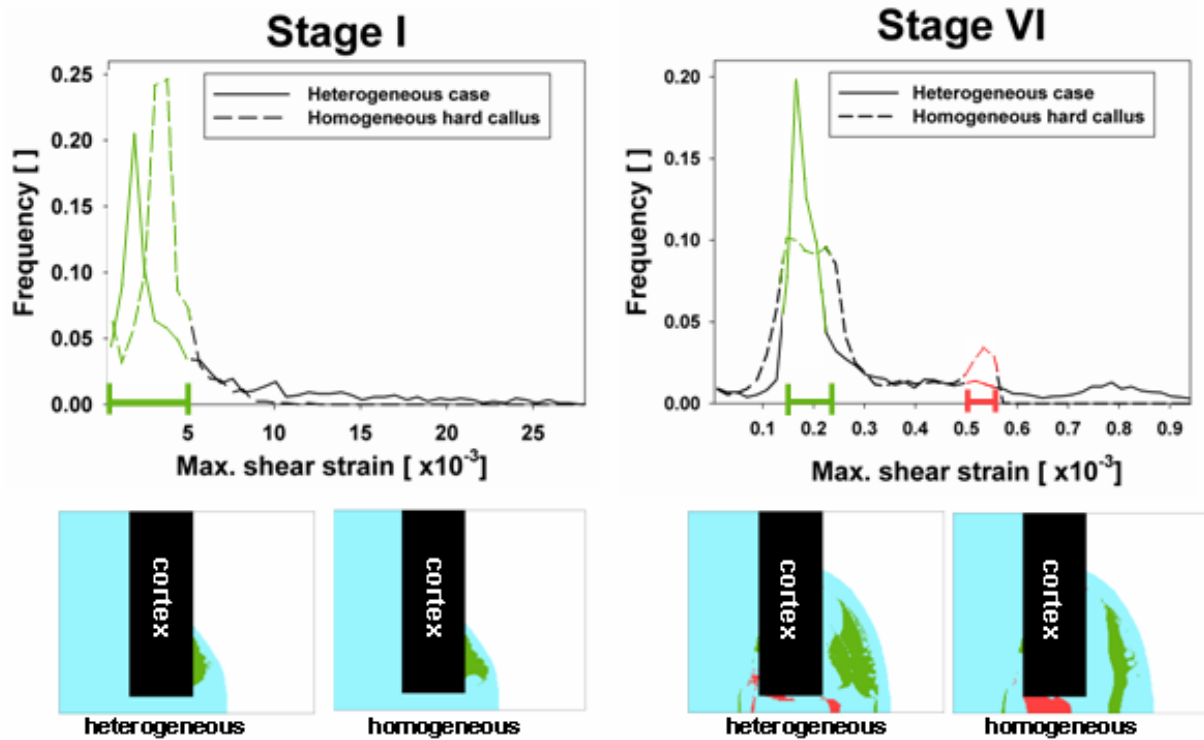


Figure 2: Frequency distributions of the maximal shear strains within the hard callus at stage I (left) and stage VI (right).

The heterogeneous description of the hard callus is compared with a hypothetical case assuming a homogeneous hard callus with a mean elastic modulus. The figures below show these pixels within the callus, which contribute to the peaks in the frequency distribution. In the plots, strain ranges around the peak are marked in the same colour as in the insets.



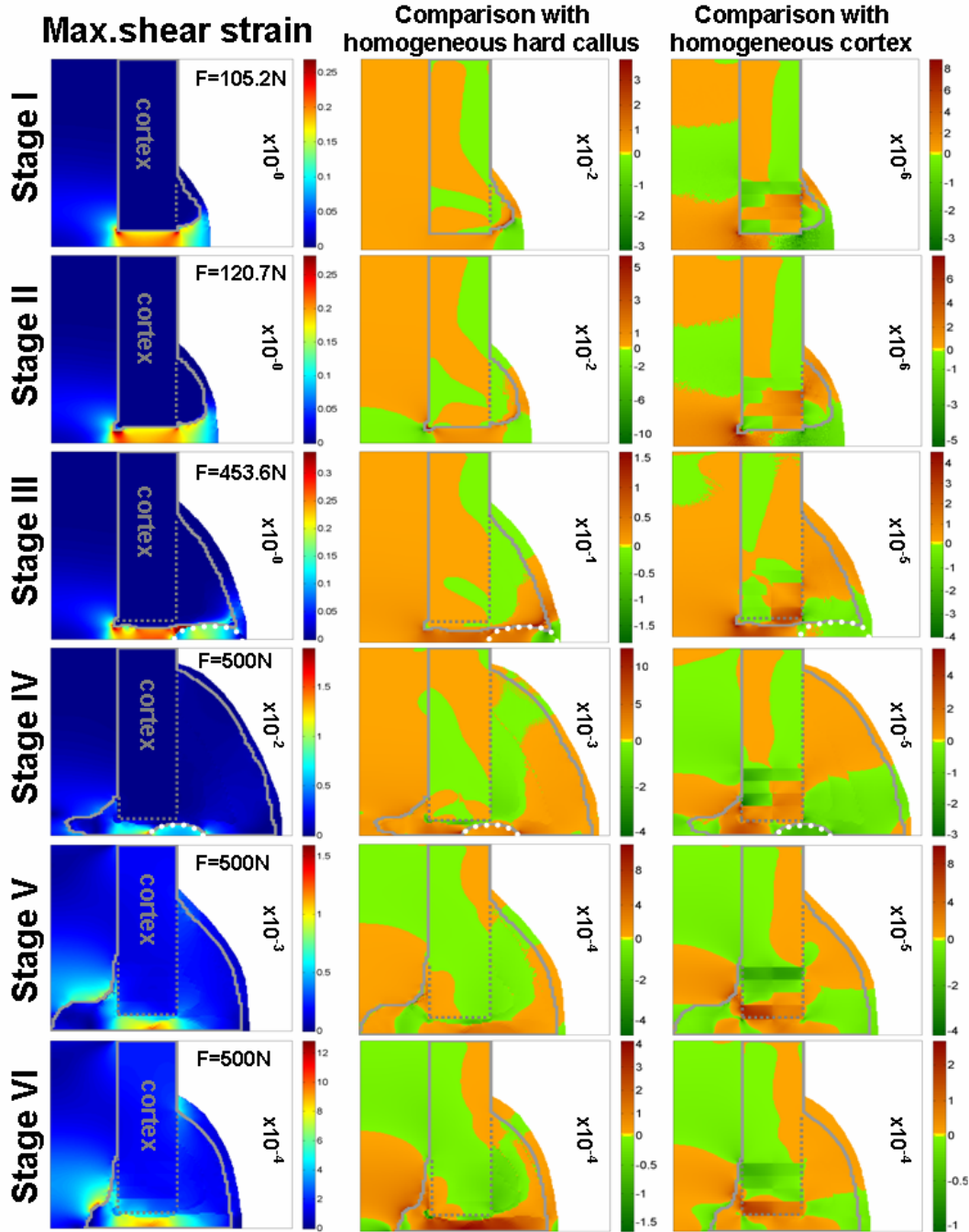


Figure 3: Spatial distributions of the maximal shear strain (left) and comparison between the heterogeneous case two homogeneous cases as reference.

Left column of images: maximal shear strains calculated for six different stages during bone healing considering the heterogeneity of the stiffness of the hard callus and cortex. Middle column of the images: strain differences of the heterogeneous case and a hypothetical homogeneous hard callus. Right column of images: strain differences of the heterogeneous case and a hypothetical homogeneous cortex. In the comparison between heterogeneous and homogeneous cases, areas with reddish colours indicate higher strains in the heterogeneous case while greenish colours indicate higher strains in the homogeneous case. Grey lines indicate the boundaries of the cortex and the hard callus. The regions of cartilage at stage III and stage IV are marked with a white dotted line. The orders of magnitude of the displayed values are provided on the right of each image. All values are given in dimensionless units of strain. To transform to  $\mu$ -strain values, the given values have to be multiplied by  $10^6$ .

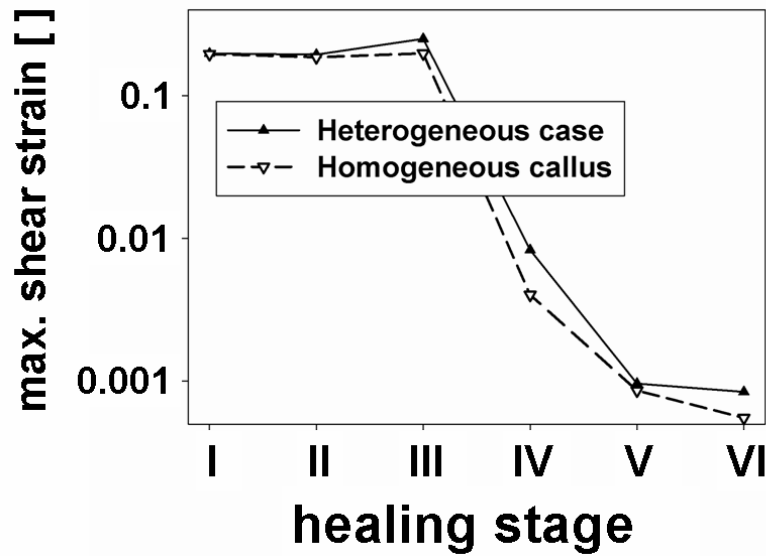


Figure 4: Semi-logarithmic plot of the maximal shear strains within the fracture gap at the six healing stages.

The values are means of all the pixels below the end of the cortex. The values are given in dimensionless units of strain. To transform to  $\mu$ -strain values, the given values have to be multiplied by  $10^6$ .

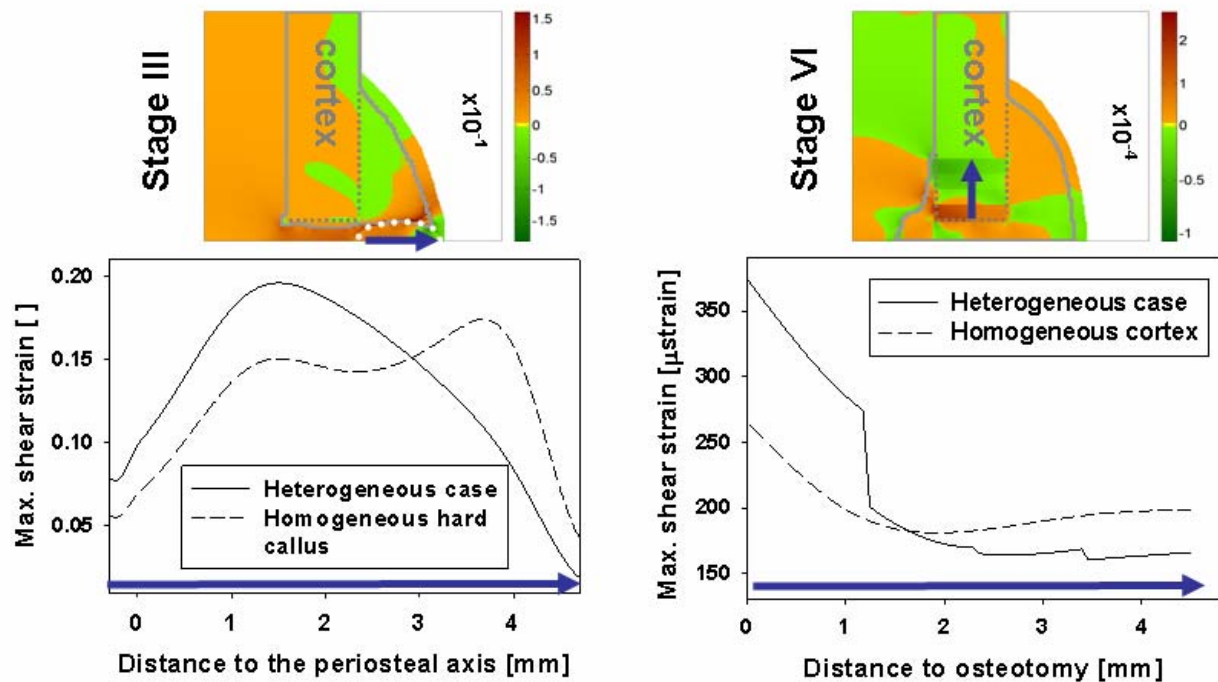


Figure 5: Comparison between the maximal shear strains for the heterogeneous case and the hypothetical case of a homogeneous hard callus along a line scan through the cartilage at stage III (left) and along a line scan through the cortex at stage VI (right), as indicated by the blue arrows.

## Discussion

Due to a lack of experimental data, finite element analyses on fracture calli typically assumed a single value for the elastic modulus of the hard callus, or distinguished a few regions of differently matured bone (Claes and Heigele 1999; Gardner et al. 2000; Gardner and Mishra 2003). In this work we demonstrated how the comprehensive characterization of material properties of a sheep callus at different length scales can be used to improve the understanding of tissue straining within the callus. However, as unavoidable for computational studies, the following points have to be emphasized as main limitations. Although the performed FE calculation is three-dimensional, the computational model is based on two-dimensional longitudinal histological sections of the callus with the additional assumption of radial symmetry. Experimental three-dimensional data of the callus showing the spatial arrangement of the different tissue types, for example obtained by serial sectioning (Gerstenfeld et al. 2006), is still very rare. They show that radial symmetry is a rather crude approximation of reality. The positioning of the Schanz screws of the external fixator in the vicinity of the osteotomy gap, also limited the area of the callus, which can be used for this computational study. Looking at the interpretation of the measured material properties of the newly formed bone at different times post-operatively, we assume that they are representative for the whole hard callus. Furthermore, the anisotropy of the materials (Fratzl and Weinkamer 2007; Seto et al. 2008) were neglected as in most computational studies. Potential refinements of the model are to use models for the soft tissues which go beyond linear elasticity (Huang et al. 2003; Kim and Srinivasan 2005) and to consider the anisotropy. Since new animal experiments show that fracture healing can be different in small and large animals (Mehta et al. 2008), and specifically also in humans, it has to be emphasized that this computational study is based on data of sheep with a 3 mm tibial osteotomy (Schell et al. 2005; Epari et al. 2006; Manjubala et al. 2009; Vetter et al. 2010).

Using a Gibson-Ashby formula (Equation 1) for porous materials, the calculations showed a strong increase in the mean elastic stiffness of the hard callus over time, starting with a mean elastic modulus of only 130 MPa at the first healing stage (corresponding to 2 weeks post-op) and ending with 4.3 GPa at stage VI (corresponding to 9 weeks post-op). The elastic heterogeneity of the hard callus was particularly high for stages I-IV. For these stages, the standard deviations of the elastic moduli were about the same range as the mean values (Table 3).

The general pattern of the spatial strain distributions is similar to former computational results (Claes and Heigele 1999). The strains within the hard callus (bone) are within the range of strains measured in un-fractured long bones of sheep during walking (200-1200  $\mu$ strain) (Lanyon et al. 1982; Skerry and Lanyon 1995).

To better understand the significance of the elastic heterogeneity, we compared the calculated strains for this heterogeneous case with a situation where, either the hard callus or the cortex had a single mean value of the elastic modulus. Interestingly, this broader distribution of the elastic moduli in the heterogeneous case was not reflected in a broader distribution of the strains for later stages of the hard callus evolution (Fig. 2, right). Calculating the full strain field within the callus demonstrated that the strains are higher between the cortex ends and at the lower boundary of the hard callus when compared to the case of a homogeneous hard callus.

The differences in strain distribution due to the heterogeneity of the hard callus can have important implications when considering standard mechanobiological theories of fracture healing. While the mechanobiological argumentation is based usually on “static” strains, it is implicitly assumed that temporal changes in the strain are the more important stimulus for cells in the tissue (Robling et al. 2006). In this study, we considered static strains since a transformation in estimated strain rates is straightforward (Huiskes 2000). As an example for the influence of the callus heterogeneity, endochondral ossification (transformation of cartilage into bone) between stage III and IV is discussed. According to mechanobiological theories, the local shear strain has to be lower than a certain threshold to allow endochondral ossification of the cartilage (Bailon-Plaza and van der Meulen 2003; Isaksson et al. 2006; Geris et al. 2009). Assuming a threshold of the maximal shear strain of 7.5% (Bailon-Plaza and van der Meulen 2003; Isaksson et al. 2006), Figure 6 shows the cartilage regions that are below this threshold in blue (and therefore will undergo endochondral ossification). The mechanical heterogeneity of the callus favours an ossification from the outside to the inside (Fig. 5, looking from the right to the left side). Under the assumption of a homogeneous hard callus, an ossification starting from both sides would occur. In this way, the mechanical heterogeneity has important influence on the direction of how endochondral ossification proceeds. Small differences in the initial phase of endochondral ossification can have large effects on the advance of healing as time proceeds. We hypothesize that this influence of the heterogeneity of the callus on the cartilage could be the driving force of the shift of the cartilage towards the fracture gap as observed in animal experiments (Schell et al. 2008; Lienau et al. 2009; Vetter et al. 2010).

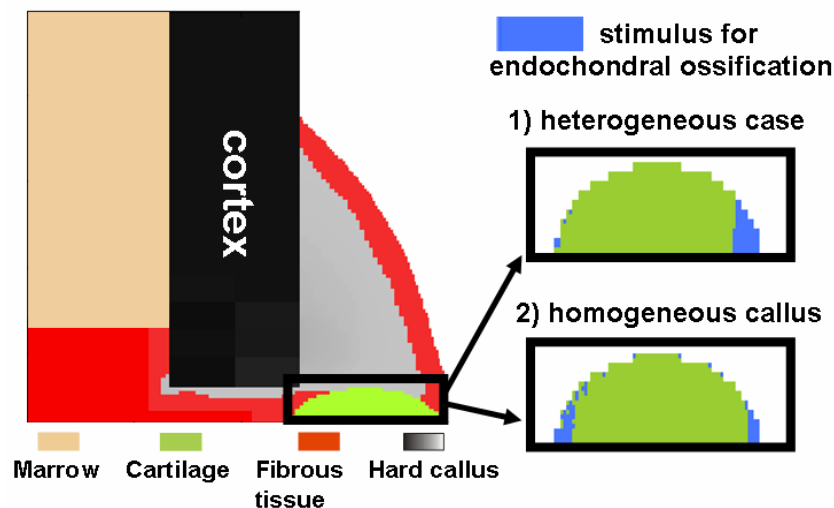


**Figure 6: Influence of the hard callus heterogeneity on the mechanical stimulus (max. shear strain) within the cartilage region at stage III.**

The blue regions show the areas of strains lower than 0.075 which are assumed to be the maximal strain sustainable for cartilage experiencing endochondral ossification.

## Acknowledgments

This study was supported by a grant of the German Research Foundation (Collaborative Research Centre "Biomechanics and Biology of Musculoskeletal Regeneration – From Functional Assessment to Guided Tissue Formation", SFB 760).

## References

- Bailon-Plaza, A. and van der Meulen, M. C. H. (2003). "Beneficial effects of moderate, early loading and adverse effects of delayed or excessive loading on bone healing." *Journal of Biomechanics* **36**(8): 1069-1077.
- Bottlang, M., Mohr, M., Simon, U. and Claes, L. (2008). "Acquisition of full-field strain distributions on ovine fracture callus cross-sections with electronic speckle pattern interferometry." *Journal of Biomechanics* **41**(3): 701-705.
- Cheal, E. J., Mansmann, K. A., Digioia, A. M., Hayes, W. C. and Perren, S. M. (1991). "Role of Interfragmentary Strain in Fracture-Healing - Ovine Model of a Healing Osteotomy." *Journal of Orthopaedic Research* **9**(1): 131-142.
- Claes, L. E. and Heigele, C. A. (1999). "Magnitudes of local stress and strain along bony surfaces predict the course and type of fracture healing." *Journal of Biomechanics* **32**(3): 255-266.
- Claes, L. E., Heigele, C. A., Neidlinger-Wilke, C., Kaspar, D., Seidl, W., Margevicius, K. J. and Augat, P. (1998). "Effects of mechanical factors on the fracture healing process." *Clinical Orthopaedics and Related Research*(355): S132-S147.
- Claes, L. E. and Ito, K. (2004). *Biomechanics of fracture fixation and fracture healing. Basic Orthopaedic Biomechanics and Mechano-Biology*. V. C. Mow and R. Huijskes. London, Lippincott Williams & Wilkins.
- Cruess, R. L. and Dumont, J. (1975). "Fracture Healing." *Canadian Journal of Surgery* **18**(5): 403-408.
- Duda, G. N., Eckert-Hubner, K., Sokiranski, R., Kreutner, A., Miller, R. and Claes, L. (1998). "Analysis of inter-fragmentary movement as a function of musculoskeletal loading conditions in sheep." *Journal of Biomechanics* **31**(3): 201-210.
- Duda, G. N., Sporrer, S., Sollmann, M., Hoffmann, J. E., Kassi, J. P., Khodadadyan, C. and Raschke, M. (2003). "Interfragmentary movements in the early phase of healing in distraction and correction osteotomies stabilize with ring fixators." *Langenbecks Archives of Surgery* **387**(11-12): 433-440.
- Einhorn, T. A. (1998). "The cell and molecular biology of fracture healing." *Clinical Orthopaedics and Related Research* **355**: S7-S21.
- Epari, D. R., Kassi, J. P., Schell, H. and Duda, G. N. (2007). "Timely fracture-healing requires optimization of axial fixation stability." *Journal of Bone and Joint Surgery-American Volume* **89A**(7): 1575-1585.
- Epari, D. R., Schell, H., Bail, H. J. and Duda, G. N. (2006). "Instability prolongs the chondral phase during bone healing in sheep." *Bone* **38**(6): 864-870.
- Fratzl, P. and Weinkamer, R. (2007). "Nature's hierarchical materials." *Progress in Materials Science* **52**(8): 1263-1334.
- Gardner, T. N. and Mishra, S. (2003). "The biomechanical environment of a bone fracture and its influence upon the morphology of healing." *Medical Engineering & Physics* **25**(6): 455-464.
- Gardner, T. N., Stoll, T., Marks, L., Mishra, S. and Tate, M. K. (2000). "The influence of mechanical stimulus on the pattern of tissue differentiation in a long bone fracture - an FEM study." *Journal of Biomechanics* **33**(4): 415-425.
- Geris, L., Sloten, J. V. and Van Oosterwyck, H. (2009). "In silico biology of bone modelling and remodelling: regeneration." *Philosophical Transactions of the Royal Society a-Mathematical Physical and Engineering Sciences* **367**(1895): 2031-2053.

- Gerstenfeld, L. C., Alkhiary, Y. M., Krall, E. A., Nicholls, F. H., Stapleton, S. N., Fitch, J. L., Bauer, M., Kayal, R., Graves, D. T., Jepsen, K. J. and Einhorn, T. A. (2006). "Three-dimensional reconstruction of fracture callus morphogenesis." *Journal of Histochemistry & Cytochemistry* **54**(11): 1215-1228.
- Gibson, L. J. (2005). "Biomechanics of cellular solids." *Journal of Biomechanics* **38**(3): 377-399.
- Gibson, L. J. and Ahsby, M. F. (1999). *Cellular solids, structure and properties*, 2nd edition. Cambridge, UK, Cambridge University Press, p. 510.
- Harrigan, T. P., Jasty, M., Mann, R. W. and Harris, W. H. (1988). "Limitations of the Continuum Assumption in Cancellous Bone." *Journal of Biomechanics* **21**(4): 269-275.
- Hori, R. Y. and Lewis, J. L. (1982). "Mechanical-Properties of the Fibrous Tissue Found at the Bone-Cement Interface Following Total Joint Replacement." *Journal of Biomedical Materials Research* **16**(6): 911-927.
- Huang, C. Y., Soltz, M. A., Kopacz, M., Mow, V. C. and Ateshian, G. A. (2003). "Experimental verification of the roles of intrinsic matrix viscoelasticity and tension-compression nonlinearity in the biphasic response of cartilage." *Journal of Biomechanical Engineering-Transactions of the Asme* **125**(1): 84-93.
- Huiskes, R. (2000). "If bone is the answer, then what is the question?" *Journal of Anatomy* **197**: 145-156.
- Isaksson, H., Wilson, W., van Donkelaar, C. C., Huiskes, R. and Ito, K. (2006). "Comparison of biophysical stimuli for mechano-regulation of tissue differentiation during fracture healing." *Journal of Biomechanics* **39**(8): 1507-1516.
- Kaspar, K., Schell, H., Seebeck, P., Thompson, M. S., Schutz, M., Haas, N. P. and Duda, G. N. (2005). "Angle stable locking reduces interfragmentary movements and promotes healing after unreamed nailing - Study of a displaced osteotomy model in sheep tibiae." *Journal of Bone and Joint Surgery-American Volume* **87A**(9): 2028-2037.
- Kenwright, J. and Goodship, A. E. (1989). "Controlled Mechanical Stimulation in the Treatment of Tibial Fractures." *Clinical Orthopaedics and Related Research*(241): 36-47.
- Kim, J. and Srinivasan, M. A. (2005). "Characterization of viscoelastic soft tissue properties from in vivo animal experiments and inverse FE parameter estimation." *Medical Image Computing and Computer-Assisted Intervention - Miccai 2005, Pt 2* **3750**: 599-606.
- Klein-Nulend, J., Bacabac, R. G. and Mullender, M. G. (2005). "Mechanobiology of bone tissue." *Pathologie Biologie* **53**(10): 576-580.
- Klein, P., Schell, H., Streitparth, F., Heller, M., Kassi, J. P., Kandziora, F., Bragulla, H., Haas, N. P. and Duda, G. N. (2003). "The initial phase of fracture healing is specifically sensitive to mechanical conditions." *Journal of Orthopaedic Research* **21**(4): 662-669.
- Kokkinos, P. A., Zarkadis, I. K., Panidis, T. T. and Deligianni, D. D. (2009). "Estimation of hydrodynamic shear stresses developed on human osteoblasts cultured on Ti-6Al-4V and strained by four point bending. Effects of mechanical loading to specific gene expression." *Journal of Materials Science-Materials in Medicine* **20**(3): 655-665.
- Lacroix, D. and Prendergast, P. J. (2002). "A mechano-regulation model for tissue differentiation during fracture healing: analysis of gap size and loading." *Journal of Biomechanics* **35**(9): 1163-1171.
- Lanyon, L. E., Goodship, A. E., Pye, C. J. and Macfie, J. H. (1982). "Mechanically Adaptive Bone Remodeling." *Journal of Biomechanics* **15**(3): 141-154.
- Lienau, J., Schell, H., Duda, G. N., Seebeck, P., Muchow, S. and Ball, H. J. (2005). "Initial vascularization and tissue differentiation are influenced by fixation stability." *Journal of Orthopaedic Research* **23**(3): 639-645.
- Lienau, J., Schmidt-Bleek, K., Peters, A., Haschke, F., Duda, G. N., Perka, C., Bail, H. J., Schutze, N., Jakob, F. and Schell, H. (2009). "Differential Regulation of Blood Vessel Formation between Standard and Delayed Bone Healing." *Journal of Orthopaedic Research* **27**(9): 1133-1140.
- Lobao, E. G., Beaupre, G. S. and Carter, D. R. (2001). "Mechanobiology of initial pseudarthrosis formation with oblique fractures." *Journal of Orthopaedic Research* **19**(6): 1067-1072.
- Manjubala, I., Liu, Y., Epari, D. R., Roschger, P., Schell, H., Fratzl, P. and Duda, G. N. (2009). "Spatial and temporal variations of mechanical properties and mineral content of the external callus during bone healing." *Bone* **45**(2): 185-192.
- Matziolis, G., Tuischer, J., Kasper, G., Thompson, M., Bartmeyer, B., Krockner, D., Perka, C. and Duda, G. (2006). "Simulation of cell differentiation in fracture healing: Mechanically loaded composite scaffolds in a novel bioreactor system." *Tissue Engineering* **12**(1): 201-208.
- Mehta, M., Schell, H., Kaspar, K. and Duda, G. N. (2008). "Differences in the healing pathways: Rat model vs. sheep model." *Calcified Tissue International* **82**: S71-S72.
- Morgan, E. F., Bayraktar, H. H. and Keaveny, T. M. (2003). "Trabecular bone modulus-density relationships depend on anatomic site." *Journal of Biomechanics* **36**(7): 897-904.
- Morgan, E. F., Gleason, R. E., Hayward, L. N. M., Leong, P. L. and Palomares, K. T. S. (2008). "Mechanotransduction and fracture repair." *Journal of Bone and Joint Surgery-American Volume* **90A**: 25-30.
- Robling, A. G., Castillo, A. B. and Turner, C. H. (2006). "Biomechanical and molecular regulation of bone remodeling." *Annual Review of Biomedical Engineering* **8**: 455-498.
- Schaffler, M. B. and Burr, D. B. (1988). "Stiffness of Compact-Bone - Effects of Porosity and Density." *Journal of Biomechanics* **21**(1): 13-16.
- Schell, H., Epari, D. R., Kassi, J. P., Bragulla, H., Bail, H. J. and Duda, G. N. (2005). "The course of bone healing is influenced by the initial shear fixation stability." *Journal of Orthopaedic Research* **23**(5): 1022-1028.
- Schell, H., Thompson, M. S., Bail, H. J., Hoffmann, J. E., Schill, A., Duda, G. N. and Lienau, J. (2008). "Mechanical induction of critically delayed bone healing in sheep: Radiological and biomechanical results." *Journal of Biomechanics* **41**(14): 3066-3072.
- Seto, J., Gupta, H. S., Zaslansky, P., Wagner, H. D. and Fratzl, P. (2008). "Tough lessons from bone: Extreme mechanical anisotropy at the mesoscale." *Advanced Functional Materials* **18**(13): 1905-1911.
- Sfeir, C., Ho, C., Doll, B. A., Azari, K. and Hollinger, J. O. (2005). Fracture Repair. *Bone Regeneration and Repair*. J. R. Lieberman and G. E. Friedlaender. Totowa, Humana Press Inc.: 21-43.
- Skerry, T. M. and Lanyon, L. E. (1995). "Interruption of Disuse by Short-Duration Walking Exercise Does Not Prevent Bone Loss in the Sheep Calcaneus." *Bone* **16**(2): 269-274.
- Thompson, M. S., Schell, H., Lienau, J. and Duda, G. N. (2007). "Digital image correlation: A technique for determining local mechanical conditions within early bone callus." *Medical Engineering & Physics* **29**(7): 820-823.
- Vetter, A., Epari, D. R., Seidel, R., Schell, H., Fratzl, P., Duda, G. N. and Weinkamer, R. (2010). "Temporal tissue patterns in bone healing of sheep." *Submitted to JoR*.
- White, A. A., Panjabi, M. M. and Southwick, W. O. (1977). "Effects of Compression and Cyclical Loading on Fracture Healing - Quantitative Biomechanical Study." *Journal of Biomechanics* **10**(4): 233-239.
- Willenegger, H., Perren, S. M. and Schenk, R. (1971). "Primary and Secondary Healing of Bone Fractures." *Chirurg* **42**(6): 241-&.

- Yamagishi, M. and Yoshimura, Y. (1955). "The biomechanics of fracture healing." Journal of Bone and Joint Surgery **37A**: 1035-1068.
- Zaslansky, P., Friesem, A. A. and Weiner, S. (2006). "Structure and mechanical properties of the soft zone separating bulk dentin and enamel in crowns of human teeth: Insight into tooth function." Journal of Structural Biology **153**(2): 188-199.
- Zysset, P. K. (2003). "A review of morphology-elasticity relationships in human trabecular bone: theories and experiments." Journal of Biomechanics **36**(10): 1469-1485.

## **Danksagung**

First of all, I have to say thank you to my supervisor Dr. Richard Weinkamer or as he likes to be called, Ricci. His office door was always open for me and he always tried to help me when I had questions or problems. He would never let me leave his office without giving me advice and most of the times also some inspiration which I would have never had dreamt of before I went to his office. If curiosity is the main prerequisite for good research, Ricci is perfectly suited to be a researcher. Independently from the topic of seminars and talks, Ricci sits attentively on his seat, takes notes and finally asks an intelligent question after the talk. I guess this is one reason for his inspirational ideas. Also very inspiring were the meetings with Professor Fratzl who was my main supervisor. Thank you a lot, Peter! I have to say thanks to Professor Duda for making this thesis possible by creating the whole structure of the research project (SFB 760 - Musculoskeletal Regeneration). Without the comprehensive experimental work, this theoretical thesis would not have solid ground. Finally, I have to thank Professor Sokolov for taking time to be a referee of this thesis.

I want to say thank you to my co-workers too. Oliver Sander did a great job in adopting the Finite Element code (DUNE) according to our needs. During our tries to make the code run on different machines, I learned not to underestimate the own will of computers. Thanks a lot to Devakar Epari for discussions on Skype and commenting on the introduction of the thesis. Thanks to Robin Seidel, Hanna Schell and again Devakar for helping me with the biology and in identifying the different cells in the histology lab! Yifei Liu spent a lot of time on the nanoindenter which turned out to have also an own will similar to my computers. Thanks for putting a huge effort into the experiments and taking you the time for explaining me the experiments and results! Finally, I want to thank Anne Beyreuther and Florian Witt for the technical support and tips and the discussions.

Finally, my thanks go to the whole department of Biomaterials! It was a relaxing and very productive work atmosphere with many creative minds and at least one more Bavarian, thanks Caro! Thanks also to a new (also Bavarian) colleague: Philip Kollmannsberger for reading the thesis and the helpful comments! Another thank you goes to Manav. You always helped me when I had some questions on the differences between the healing of large and small animals. And at least, we made it once together to the library to write on our theses. I also want to say thank you to my parents who always supported me during my studies! And last but not least, a huge thank you goes to my girlfriend Jeni. Thanks for reading through all the stuff I wrote and for being great and putting up with me in times of thesis writing! Hereby, I also promise to take more care of the apartment again and we will have some real nice dinner in Greece soon!



## **Eidesstattliche Erklärung**

Hiermit versichere ich, Andreas Christian Vetter, geboren am 29.08.1980, dass ich die vorliegende Dissertation zum Thema „Mechanobiology of Healing and Regeneration of Bone“ selbständig verfasst habe, keine anderen als die von mir angegebenen Quellen und Hilfsmittel benutzt und wörtlich übernommene Ausführungen in der Arbeit als solche gekennzeichnet habe.

Potsdam, 8. April 2010